Drying behavior of concrete : application to nuclear waste packages

Ginger El Tabbal

UNIVERSITÉ PARIS-EST

Université Paris-Est

Laboratoire Navier – Ecole des Ponts Paris Tech
Eléctricité de France

Thèse présenté en vue de l'obtention du titre
de docteur de l'université Paris-Est

Par : Ginger El Tabbal

DRYING BEHAVIOR OF CONCRETE: APPLICATION TO NUCLEAR WASTE PACKAGES

Soutenu le 02/10/2020

M. Jan Carmeliet	Rapporteur
M. Fréderic Skoczylas	Rapporteur
M. Patrick Dangla	Directeur de thèse
M. Alain Sellier	Examinateur
M. Farid Benboudjema	Examinateur
M. Benoit Coasne	Examinateur
M. Matthieu Vandamme	Co- directeur de thèse
Mme Marina Bottoni	Encadrante

Acknowledgments

I would like to express my sincere acknowledgments to my advisors Marina Bottoni, Sylvie Granet, Patrick Dangla and Matthieu Vandamme. I thank you for your continuous support during my PH.D, for your motivation and enthusiasm but also for your remarkable knowledge. I could not have imagined having better advisors and mentors during my thesis' years.

Beside my advisors, i would like to thank the rest of my thesis' committee: Prof. Carmeliet, Prof. Skoczylas, Prof. Benboudjema, Prof. Sellier and Dr. Coasne. I thank you for your insightful comments and your exceptional questions. My sincere aknowledgments goes to Prof. Benboudjema who has shared in previous meetings his thoughts and remarks regarding my thesis. The latter have helped me straighten out my work.

Let me also thank EDF for having me as a member of their group during the last 3 years. This made me benefice from an exceptional experience in an outstanding work environment. I thank exceptionally, my future colleagues at the civil engineering laboratory of MMC – EDF. Their experimental work constituted a major important part of my thesis' work. My sincere acknowledgment goes to Laurent Charpin, Jean-Luc Adia, Patrick Semété and François Soleilhet. Moreover, i would like to thank the GDR project manager at EDF Jeremy Buttin, for sharing his wide knowledge on the project's context, objectives and perspectives.

In addition, i would like to thank all of my friends for their continuous support especially during my last year. Thank you for being there for me everytime i needed you. A special thanks for my friends who have brought joy and fun to this experience: Hiba El Arja, Mihaja Razafimbelo, Luis Alvarez Sanchez, Christelle Bou Malham and Roy Chaaya. But also a special thanks to my fiancée and future life partner Joe Akiki for his continuous love and motivation.

Finally, i would like to thank all the members of my family for their support and motivation thorough my life and especially during my thesis' years. Even thought you were far away, you were always in my thoughts.

Abstract

EDF is currently working on multiple projects concerning the durability of concrete structures. Among these projects, a research program focuses in particular on the drying behavior of a high-performance concrete used as a shell for nuclear waste packages. The package of interest noted as $C1PG^{SP}$, will be at first conserved in a storage facility and then disposed of at Cigéo, i.e. the future underground disposal facility for long term radioactive waste in France.

During the storage phase, the "F44Adj" concrete shells will be submitted to relative humidity that could be lower than 50% and a relatively high ambient temperature (attaining 50°C). Under these conditions, the impact of drying has to be evaluated and EDF is required to verify the package against the risk of cracking of the concrete shell due to structural restraining of strains.

The overall objective of this thesis is to provide a new valid poromechanical model that can be used to study the risk of cracking of the concrete shell caused by the restriction of drying shrinkage.

Previous modelling works based on a classical Thermo-Hydro-Mechanical (THM) formalism have shown the need of a better understanding of the drying behavior of concrete, in particular for what concerns the hydromechanical coupling. As a matter of fact, the THM models based on the poromechanical works of Biot, Terzaghi and then Coussy et al. (2003), are proven to be only valid for a relative humidity higher than 50% (Wyrzykowski et al., 2017). In this thesis, we propose a new poromechanical model that extends and adapts those models to a lower relative humidity. This result is obtained by introducing the mechanism of adsorption of water molecules on the pores surface and its effect on the hydro-mechanical coupling.

Apart from the hydromechanical coupling, the drying kinetics of the concrete impacts the kinetics of shrinkage. The existing models of water transfer are examined and discussed with respect to their applicability to high-performance concretes (such as the F44Adj). Hence, two chapters of this thesis are devoted to the water retention phenomenon and to the transfer properties of the concrete.

Finally, material properties are necessary to accurately model the drying behavior of the F44Adj concrete. For this reason, EDF has established an experimental program in order to obtain the data necessary to calibrate the transfer parameters as well as to validate the proposed poromechanical model. Hence, a large section of each chapter is dedicated to the description and analysis of experimental results, then to calibration of the model parameters.

The proposed model is finally applied to simulate the drying of the $C1PG^{SP}$ package under storage conditions; results are compared with those obtained in older simulations performed at EDF.

Résumé

EDF travaille actuellement sur de multiples projets concernant la durabilité des structures en béton. Parmi ces projets, un programme de recherche se concentre notamment sur le comportement au séchage d'un béton à haute performance utilisé pour la fabrication de coques pour des colis de déchets radioactifs. Le colis d'intérêt, noté C1PG^{SP}, sera dans un premier temps conservé dans une installation d'entreposage, puis stocké à Cigéo, le futur centre de stockage souterrain pour les déchets radioactifs de moyenne et haute activité à vie longue en France.

Pendant la phase d'entreposage, la coque constituée de béton "F44Adj" (formulation EDF) sera soumise à une humidité relative qui pourrait être inférieure à 50% et à une température ambiante relativement élevée (pouvant atteindre 50°C). Dans ces conditions, l'impact du séchage sur les propriétés mécaniques du béton doit être vérifié. EDF est ainsi tenue de vérifier que le colis ne présente pas de risque de fissuration de la coque en béton lié à une restriction structurelle des déformations.

L'objectif global de cette thèse est de fournir un nouveau modèle poromécanique qui étudie le risque de fissuration du béton causé par le retrait de séchage.

Des travaux de modélisation antérieurs basés sur un formalisme thermo-hydro-mécanique (THM) classique ont montré la nécessité d'une meilleure compréhension du comportement au séchage du béton. En effet, les modèles THM basés sur les travaux poromécaniques de Biot, Terzaghi et puis Coussy et al. (2003) se sont avérés valables uniquement pour des humidités relatives supérieures à 50% (Wyrzykowski et al. 2017). Dans le cadre actuel de la thèse, il s'agit donc d'étendre et d'adapter ces modèles pour des humidités plus faibles. Cette adaptation passe par l'introduction dans le modèle des phénomènes d'adsorption des molécules d'eau à la surface des pores du béton et par la prise en compte de son effet sur le couplage hydro-mécanique.

La cinétique de séchage du béton a un impact sur la cinétique de retrait de dessication. Les modèles de transfert existants sont examinés et discutés quant à leur applicabilité aux bétons à hautes performances (tels que le béton F44Adj). Ainsi, deux chapitres de cette thèse sont consacrés au phénomène de rétention d'eau et aux propriétés de transfert du béton.

Enfin, la connaissance des propriétés du béton F44Adj sont nécessaires pour modéliser correctement le comportement au séchage. Pour cette raison, EDF a mis en place un programme expérimental afin de fournir les données nécessaires à la calibration des paramètres de transfert, ainsi que pour valider le modèle poromécanique proposé. Ainsi, une grande partie de chaque chapitre est consacrée à la description et à l'analyse des résultats expérimentaux, puis à la calibration des paramètres du modèle.

Le modèle proposé est finalement appliqué à la simulation du séchage d'un colis C1PG^{SP} ; les résultats obtenus avec ce nouveau modèle sont comparés à ceux issus de simulations plus anciennes réalisées par EDF.

Résumé long

En France, les colis en béton sont largement utilisés pour le conditionnement de différents types de déchets radioactifs, en conformité avec les spécifications d'acceptation des colis dans les centres de stockage de surface exploités par l'Andra (Agence nationale française de gestion des déchets radioactifs).

EDF met ainsi déjà en œuvre, depuis de nombreuses années et en toute sûreté, des colis de déchets en béton pour la gestion des déchets issus de l'exploitation des centrales nucléaires et de leur démantèlement. L'un de ces colis, noté le colis C1PG est reconnu par l'Andra comme offrant un niveau élevé de résistance mécanique répondant aux spécifications en matière de confinement de la radioactivité. La coque extérieure du colis est réalisée en béton armé à haute performance (béton « F44Adj », notation EDF), dont la formulation a été développée dans les laboratoires internes d'EDF. Cette formulation répond à l'ensemble des exigences requises par l'Andra pour le stockage de déchets de faible et moyenne activité à vie courte (destinés au CSA, Centre de Stockage de l'Aube). Aujourd'hui, il est également prévu d'utiliser c pour le stockage de déchets de moyenne activité à vie longue. Dans ce cas, avant d'être stockés à Cigéo, le centre de stockage géologique des déchets radioactifs vie longue en France, ces colis seront entreposés une fois produits dans l'Installation de Conditionnement et d'Entreposag des Déchets Activés (ICEDA, installation EDF dont la mise en service est prévue en 2020). Cette installation permettra à EDF de fournir à ces colis un conditionnement adapté et une gestion sûre en attendant leur évacuation vers Cigéo.

Entre le moment où les colis sont produits, et celui où ils peuvent être évacués vers Cigéo, l'entreposage à ICEDA peut durer jusqu'à cinquante ans. On estime que lorsque la zone d'entreposage sera pleine de colis de déchets, l'exothermie des déchets radioactifs pourra conduire à une température maximale autour des colis d'environ 50°C et à une humidité relative minimale de 30%. Après l'entreposage, les colis de béton seront soumis à une température et une humidité moins contraingante

à l'intérieur des alvéoles de stockage à Cigéo durant la période d'exploitation puis de stockage réversible. Cette période est aujourd'hui estimée aux alentours de 100 ans, au cours de laquelle le béton doit toujours offrir des propriétés de confinement conformes aux futures spécifications d'acceptation des colis. Pendant cette période maximale de 150 ans (entreposage et stockage réversible), le béton séchera et vieillira dans ces conditions spécifiques d'exploitation (température relativement élevée et faible humidité relative). De telles conditions pourraient entraîner un retrait par dessiccation et donc des contraintes dont l'impact sur l'état du béton (e.g. apparition éventuelle de fissuration) est à vérifier. Par conséquent, EDF doit démontrer la capacité de l'enveloppe de béton à résister à ces conditions et à conserver ses propriétés mécaniques dans le temps.

Dans ce contexte, l'objectif global de cette thèse est de fournir des éléments de compréhension des phénomènes de séchage et du risque de fissuration de la coque en béton causé par la restriction des déformations de retrait de dessication. Le but final est de de démontrer la capacité des colis à répondre aux exigences futures.

Le séchage du béton est le principal phénomène qui sera étudié dans le cadre de ce travail. En effet, ce séchage peut conduire à du retrait et donc à des contraintes importantes si les déformations de retrait sont restreintes. Le séchage doit donc être étudié avec soin car, s'il est surestimé, tant en termes de cinétique que d'amplitude, les contraintes seront également surestimées. Cela peut conduire à terme à un surdimensionnement des dimensions de la coque en béton, ou, dans notre contexte industriel, à une conclusion erronée concernant l'évolution des propriétés du colis dans le temps.

Deux aspects importants doivent être explorés dans ce travail. Le premier est la cinétique de séchage, principalement contrôlée par la condition limite considérée et les paramètres de transfert du matériau tels que la perméabilité. De plus, un autre paramètre du matériau qui peut affecter sa cinétique de séchage est la courbe de rétention d'eau, c'est-à-dire la relation entre le degré de saturation et la pression capillaire ou l'humidité relative. Il convient donc de garantir que le modèle de transfert

considéré, avec les paramètres de transfert requis, est capable de décrire le séchage du béton sur toute la gamme des humidités relatives d'intérêt (entre 100% et 30%) et jusqu'à une température de 50°C.

Le deuxième aspect est la description correcte du comportement mécanique de la coque en béton. Ceci nécessite un modèle poromécanique adapté. Dans la littérature, on trouve différents modèles poromécaniques basés, entre autres, sur les travaux de Terzaghi, Biot (1941) puis Coussy (2003). Un modèle, basé sur ces derniers travaux, est actuellement implémenté dans *Code_Aster*, le logiciel scientifique utilisé et développé à EDF. Néanmoins, il a été démontré que ces modèles ne décrivent pas correctement l'évolution des contraintes de retrait au séchage pour une humidité relative inférieure à 40% - 50%. Ceci peut s'expliquer par le fait que ces modèles négligent l'effet de l'eau adsorbée à la surface des pores. Par conséquent, dans le travail actuel, ces modèles sont étendus et adaptés à des humidités relatives plus faibles, descendant jusqu'à 30%.

Le travail numérique à réaliser dans le cadre de la thèse nécessite un certain nombre de données expérimentales. Ces données permettent notamment l'évaluation des paramètres de transfert du béton considéré et la validation du modèle poromécanique qui est développé. La majorité des essais expérimentaux ont été réalisés parallèlement à cette thèse dans les laboratoires internes d'EDF (laboratoire de Génie Civil d'EDF R&D, au département Matériaux et Mécanique des Composants, et les laboratoires du département Technique de réalisation et Expertise en Géologie et Génie civil (TEGG) de la Direction de l'Ingénierie d'EDF). D'autre part, certains essais expérimentaux ont également été réalisés au LMDC (Laboratoire des Matériaux et Durabilité des Constructions, INSA Toulouse) et au laboratoire LaM^{cube} de l'Université de Lille – Centrale Lille. Les essais expérimentaux réalisés dans un laboratoire interne d'EDF R&D ont été initiés en 2017-2018. Ces derniers consistent d'abord en des essais de rétention d'eau réalisés en adoptant deux méthodes de mesure différentes : la méthode de la solution saline saturée (SSS) et la méthode de la sorption dynamique de vapeur (DVS). D'autre part, des expériences de perte de masse et de retrait par séchage ont également été réalisées sur des échantillons de F44Adj à EDF R&D. Ces dernières sont menées dans des conditions thermo-

hydriques externes de T=50°C et à une humidité relative de 30%. Ces conditions sont choisies comme étant des conditions enveloppes et pénalisantes, représentatives des conditions d'entreposage puis de stockage des colis C1PG^{SP}. A des fins de comparaison, les essais sont également effectués en conditions ambiantes classiques, avec *T*=20°C et une humidité relative de 50%. L'essai effectué au laboratoire LaM^{cube} de l'Université de Lille consiste à mesurer la perméabilité à l'eau du béton. Enfin, les essais effectués au LMDC et décrits dans ce manuscrit consistent principalement à mesurer le retrait endogène du béton F44Adj. Ils s'inscrivent par ailleurs dans une campagne expérimentale plus large qui n'est pas l'objet principal de ce travail.

Le travail effectué dans le cadre de la présente thèse sera synthétisé dans six chapitres. Outre un chapitre introductif, les chapitres 2 à 4 couvrent les différents aspects phénoménologiques décrivant le comportement de séchage du béton. Ces aspects comprennent : la rétention d'eau et la caractérisation des pores du béton, les modèles de transfert d'humidité et enfin la modélisation du retrait au séchage par une nouvelle approche poromécanique. Le chapitre 5 est consacré à une application industrielle : il consiste en une simulation numérique du colis pendant sa phase de stockage. Enfin, le chapitre 6 présente les conclusions et perspectives de ce travail.

L'objectif principal du chapitre 2 est de déterminer et modéliser la courbe de rétention d'eau représentative du béton étudié. Cette courbe est une donnée importante pour différents modèles poromécaniques. Le chapitre commence par un travail bibliographique présentant les phénomènes de rétention d'eau dans le béton. Les méthodes expérimentales ainsi que les modèles numériques décrivant la rétention d'eau du matériau cimentaire sont détaillés. Il est également montré que les courbes de rétention peuvent être utilisées comme données pour de multiples méthodes pour caractériser la distribution de la taille des pores du matériau telles que la méthode B.E.T (Brunauer et al., 1938) et la méthode BJH (Barrett et al., 1951). Cela sera d'une importance notable pour l'établissement d'un modèle poromécanique adapté à la structure poreuse du béton (voir chapitre 4). Une deuxième partie de ce chapitre présente les essais expérimentaux de désorption d'eau sur le béton

F44Adj. Les essais ont été réalisés par deux techniques différentes : la méthode des solutions salines saturées (SSS) et la méthode de désorption dynamique de vapeur (Dynamic Vapor Sorption, DVS). Enfin, le besoin d'un modèle numérique capable de bien représenter la courbe de rétention d'eau nécessite une évaluation et une révision du modèle de Van Genuchten (1980). Ce modèle est couramment utilisé dans la littérature et est mis en œuvre dans *Code_Aster*. Après avoir présenté l'isotherme de désorption expérimentale du béton à haute performance F44Adj ainsi que d'autres isothermes de désorption expérimentales de bétons à haute performance issues de la littérature (section 2.3.1), il s'est avéré que le modèle de Van Genuchten nécessite une modification. En effet, ce modèle impose pour une humidité relative h_R =100% un degré de saturation égal à 1. Les observations expérimentales conduisent néanmoins à une conclusion différente : placer un échantillon dans un environnement avec une humidité relative de 100% n'impose pas la saturation de tous les pores du matériau. Ainsi, ces observations expérimentales ont montré l'importance dans le modèle de Van Genuchten d'un paramètre additionnel S_{100} indiquant la saturation maximale de l'échantillon à 100% d'humidité relative.

Le chapitre 3 est dédié à la modélisation de la cinétique de séchage du béton. Ce chapitre détaille tout d'abord les lois de transfert utilisées pour décrire la perméabilité, la diffusion de la vapeur d'eau et d'autres modes de transfert. Des méthodes numériques et expérimentales pour évaluer ces paramètres de transfert sont ensuite présentées. Une attention particulière est accordée à l'évaluation de la perméabilité du béton et aux conditions limites de transfert. Une deuxième partie décrit deux essais expérimentaux différents. Le premier vise à mesurer la perméabilité à l'eau du béton F44Adj. Cet essai est réalisé dans le laboratoire LaM^{cube}. Le deuxième consiste à évaluer la cinétique de séchage tout en séchant différentes géométries d'échantillons de béton F44Adj dans différentes conditions ambiantes. Ce dernier essai fournit des courbes expérimentales de perte de masse. Les courbes ainsi obtenues sont utilisées au moyen d'une analyse inverse effectuée avec le modèle THM de Code_Aster, ce qui permet d'identifier les paramètres de transfert du béton F44Adj.

Certaines modifications du modèle de transfert ont été proposées et mises en œuvre dans le code, comprenant une nouvelle expression pour la perméabilité relative cohérente avec les modifications apportées au modèle de Van Genuchten ainsi que l'implémentation d'une condition d'échange à la surface de l'échantillon. Différentes simulations ont été effectuées pour deux couples de conditions opératoires ((T=20°C, h_R = 50%) et (T=50°C, h_R = 30%)) et pour différentes géométries d'échantillons testées. Les simulations ont permis d'étudier l'impact de la condition aux limites d'échange, l'impact des paramètres figurant dans l'expression de la perméabilité relative, l'impact des phénomènes de diffusion sur le séchage du béton et ont enfin permis de calibrer les paramètres du modèle. Il a été constaté qu'une condition aux limites de Dirichlet est la condition limite optimale pour simuler la cinétique de séchage du béton objet de l'étude. Toutes les simulations présentées ont permis de conclure que la cinétique de séchage du béton à (T=20°C, h_R = 50%) est décrite de manière optimale par une perméabilité intrinsèque de 4.10^{-24} m^2. La cinétique de séchage à (T=50°C, h_R = 30%) est décrite de façon optimale par une perméabilité intrinsèque de 4.510^{-22} m^2.

Le chapitre 4 contient principalement une description complète des mécanismes de retrait de séchage. Un nouveau modèle poromécanique décrivant le retrait de dessication des milieux poreux non saturés pour une large gamme d'humidité relative est proposé. Basé sur une approche thermodynamique, le modèle dérivé permet de prendre en compte diverses contributions, notamment la pression capillaire, l'adsorption d'eau et l'effet de Shuttleworth (1950). La plupart des paramètres d'entrée du modèle est liée à l'évolution du volume et de la surface des pores non saturés au cours de la désaturation. Ces paramètres sont évalués par des méthodes couramment utilisées pour la caractérisation de la distribution des pores : les techniques B.E.T (Brunauer et al. 1938) et BJH (Barrett et al. 1951). Les autres paramètres d'entrée, plus liés au couplage hydromécanique (comme le coefficient de Biot et un paramètre qui régit l'ampleur de l'effet Shuttleworth) sont calibrés par des données expérimentales de retrait séchant. Ce modèle est d'abord validé pour divers matériaux poreux : une pâte de ciment, un béton à haute performance et un verre Vycor. Finalement, il a été montré que

le modèle peut décrire le retrait séchant d'une façon assez satisfaisante tout en considérant un seul paramètre de recalage : le coefficient de Biot.

Le modèle proposé a été implémenté dans *Code_Aster*. Les résultats numériques de ce modèle sont comparés aux résultats expérimentaux obtenus par des essais de retrait séchant réalisés sur le béton F44Adj. D'une manière générale, le modèle est capable de décrire l'évolution des déformations de retrait de séchage. Par conséquent, dans le chapitre suivant, une application industrielle sur le colis est réalisée tout en utilisant le nouveau modèle poromécanique.

Ainsi, les travaux cités pécédemment sont utilisés pour modéliser le comportement au séchage des colis $C1PG^{SP}$ dans les conditions spécifiques précédemment décrites. Le chapitre 5 présente une simulation du comportement au séchage du colis en béton en utilisant le nouveau modèle poromécanique mis en place, et ceci pour une durée de 150 ans (incluant donc la période d'entreposage et de stockage réversible). Pour cette simulation sont utilisés tous les paramètres hydro-mécaniques déjà introduits dans les chapitres 2, 3 et 4. Les résultats de la simulation, en termes de contraintes et de déformations, sont comparés à ceux obtenus avec le modèle de Coussy et al. (2003). Le nouveau modèle montre que, dans la coque en béton, les contrainte hydrauliques, les contraintes effectives et les déformations sont plus faibles que celles obtenues en utilisant le modèle de Coussy et al. (2003). Finalement, le risque de fissuration de la coque est évalué en se basant sur un critère de rupture de Rankine, selon lequel une fissure apparait lorsque la contrainte en un point est supérieure à la résistance en traction du béton. Durant la période de 150 ans étudiée, nous ne prévoyons pas un risque de propagation de fissure traversante toute l'épaisseur de la coque ou du bouchoun en béton.

Summary

Notations

$\emptyset$	*Porosity*
V_p	*Volume of pores*
V_t	*Total volume of the sample*
V_w	*Volume of water in pores*
m_w	*Mass of water*
ρ_w	*Density of liquid water*
m_{sat}	*Mass of saturated sample*
m_{dry}	*Mass of dried sample*
w	*Water content*
h_R	*Relative humidity*
$m(h_R)$	*Mass of the sample at a relative humidity* h_R
S_w	*Experimental degree of saturation*
$S_{w,ini}$	*Initial degree of saturation*
$\sigma_{w/nw}$	*Surface stress between a wetting and a non-wetting phase*
θ	*Wetting angle*
P_{nw}	*Pressure of non-wetting phase*
P_w	*Pressure of wetting phase*
r_{ms}	*Radius of the meniscus*
r_p	*Radius of the pore*
d	*Diameter of the pore*
P_c	*Capillary pressure*
$P_{vp,sat}$	*Saturated vapor pressure*
P_{vp}	*Vapor pressure*
R	*Constant of ideal gas (8.314 J/Kg/K)*
T	*Ambient temperature (K)*
M_w^{mol}	*Molar mass of liquid water*
r_k	*Kelvin's radius*
r	*Distribution function*
C	*B.E.T constant*
w_m	*Water content necessary to cover a monolayer surface of adsorbed molecules*
S_{BET}	*Specific surface area of the material determined by the B.E.T method*
S_{BJH}	*Specific surface area of the material determined by the B.J.H method*
N_A	*Number of Avogadro (6.022* 10^{23} *molecules/mol),*
V_M	*Molar volume of water*

A_m	*Average area occupied by one molecule of the adsorbate*
t	*Thickness of the adsorbed layer*
S_e	*Effective saturation*
w_r	*Residual water content of the dried sample*
w_s	*Water content of the saturated sample*
α, n, m	*Van Genuchten three parameters*
S_r	*Residual saturation*
P_r	*Characteristic capillary pressure intervening in the Van Genuchten equation*
Δm	*Variation of mass*
$m(t)$	*Mass of the sample at a time t*
m_{ini}	*Initial mass of the sample*
ρ_{dry}	*Dry density of the sample*
ρ_{sat}	*Saturated density of the sample*
$m_{under\ water}$	*Mass of the sample measured when immersed in water*
$\Delta\rho_{ini-sat}$	*Relative variation between the initial and saturated density*
$\Delta\rho_{ini-dry}$	*Relative variation between the initial and dry density*
w_{DVS}	*Water content obtained with the DVS technique*
w_{SSS}	*Water content obtained with the SSS technique*
j	*Phase j*
M_j	*Mass flow of the j^{th} phase*
l	*Characteristic length*
η_j	*Dynamic viscosity of the liquid or gas (for j=L or j=G)*
K_{eff}	*Effective permeability of the material*
K_L	*Intrinsic liquid permeability of the material*
K_G	*Intrinsic gas permeability of the material*
K_{rl}	*Liquid relative permeability of the material*
K_{rg}	*Gas relative permeability of the material*
P_j	*Pressure of the liquid or gas (for j=L or j=G)*
F_m	*Mass gravity force*
λ_j^H	*Hydraulic conductivity of the liquid or gas (for j=L or j=G)*
l_m	*Average free path of the gas molecules*
Kn	*Knudsen number*
g	*Molar flux density*
D_{vp}	*Water vapor diffusion coefficient*
R_M	*Millington's diffusion resistance factor*
M_{vp}^{mol}	*Molar mass of water vapor*

D_{vp}^{eff}	*Effective water vapor diffusion coefficient*
β_d	*Knudsen's reductive factor*
h_w^m	*Specific mass enthalpy*
s_{vp}^m	*Specific mass entropy*
g_i	*Specific free energy of Gibbs*
L	*Latent heat of vaporization*
C_w^P	*Specific mass heat at a constant pressure of water*
C_{vp}^P	*Specific mass heat at a constant pressure of water vapor*
δ	*Water vapor permeability*
δ_v	*Thickness of the boundary layer*
E_v	*Evaporation flux*
h_ρ	*Mass exchange coefficient*
h_T	*Heat exchange coefficient*
Le	*Lewis' number*
λ_{vp}	*Thermal conductivity of water vapor*
ρ_{vsat}	*Mass density of saturated vapor*
P_d	*Disjoining pressure*
γ	*Surface energy*
ε	*Volumetric drying shrinkage strains*
k_d	*Hydric compressibility coefficient*
σ'	*Effective stress*
σ	*Total stress*
σ_f	*Hydraulic stress*
b	*Biot coefficient*
K_b	*Elastic bulk modulus*
K_s	*Elastic bulk modulus of the solid skeleton*
χ	*Bishop parameter*
π	*Equivalent pore pressure*
N_α	*Number of moles (per unit volume)of the constituent found in the phase α*
N_{ex}	*Number of moles(per unit volume) in excess placed at an adsorbing interface*
μ	*Chemical potential*
λ_B	*Proportionality factor of Bangham's law*
$F_{sk}; F_{sol}; F_{int}$	*Helmholtz energies (per unit volume) of the solid skeleton, the solid matrix and the interfaces*
U	*Energy contribution of the interfaces in the works of (Coussy et al., 2003)*
F_{ex}	*Helmholtz energy (per unit volume) of an interface when excess fluid molecules are adsorbed*

$A_{S/F}$	*Surface area (per unit volume) of the solid/liquid interface*
σ_s	*Surface stress*
A_{def}	*Contribution to the increase of the interface surface area due to a deformation (per unit volume)*
A_{cre}	*Contribution to the increase of the interface surface area due to an addition of new fluid moles(per unit volume)*
Γ	*Density of excess moles at the interface (per unit surface)*
P_a	*Pressure related to a surface adsorption effect*
σ_a	*Surface stress related to a surface adsorption effect*
φ	*Increment in the Lagrangian porosity*
ϕ_0	*Initial porosity*
ϕ_j	*Parial porosities of the fluid phase*
S_L	*Lagrangian volume fraction of the saturated pores*
S_G	*Lagrangian volume fraction of the unsaturated pores*
δW	*quantity of mechanical work exchanged with the external environment*
σ	*Stress developed in the porous volume*
V_0	*Initial undeformed volume*
A_0	*Total surface area of the pores (per unit volume)*
ω_G	*Lagrangian surface fraction of the unsaturated pores*
γ_0	*Surface energy density prior to deformation and without adsorbed moles*
π_L	*Liquid contribution to the equivalent pore pressure*
π_G	*Gas contribution to the equivalent pore pressure*
$\left(\frac{\partial \gamma}{\partial \varepsilon_s}\right)\Big\vert_{\mu}$	*Shuttleworth parameter*
ε_d	*Drying shrinkage strain*
ε_a	*Autogenous shrinkage strain*
ε_{d+a}	*Total (drying + autogenous) shrinkage strain*

Chapter 1

Introduction

List of Figures

1.1. Industrial context

Radioactive waste management is a major issue for nuclear industry. France has defined and implemented public policy on radioactive waste, in a legislative framework established in 1991 (Bataille act). Since this time, Andra (French National Agency for Radioactive Waste Management) is in charge of long-term radioactive waste management on the French territory. At short term, producers (mainly EDF) are responsible of their radioactive wastes.

Radioactive wastes are classified - according to French laws - using two criteria:

- their level of radioactivity, which characterizes the activity of radionuclides present in the waste and which is divided into 4 categories: high level activity waste (HLW), intermediate level activity waste (ILW), low activity level (LLW), and very low activity;
- their life duration: short life (SL) for waste with a radioactive element content of less than or equal to 31 years; long life (LL) for waste with a radioactive element content of more than 31 years.

The radioactive wastes currently produced by EDF (Eléctricité de France) are 90% short lived and 10% long lived. While the short lived wastes constitute approximately 945000 m^3, long lived wastes constitute: 3880 m^3 of HLW, 43000 m^3 of ILW and 93700 m^3 of LLW. Those radioactive wastes are made up of operational wastes from the 58 reactors currently under operation in France and of dismantlement wastes from nine reactors of EDF that are being dismantled.

In France, concrete packages are widely used for the packing of various types of radioactive waste. The use of concrete packages is in compliance with waste acceptance specifications for existing surface repository operated by Andra, the French National Radioactive Waste Management Agency. The requirements these packages should meet are the following:

- The ability to confine the radionuclides within the package during storage and disposal phase of the packages;
- High mechanical strength, preventing significant concrete cracks of occurring and thus preventing the dissemination of radioactive material in case of an incident during transport or handling;
- A good chemical resistance under the repositories conditions. This includes the resistance of the concretes to carbonation, alkali and internal sulfate reactions but also resistance of steel to corrosion.

EDF has already successfully implemented concrete-based waste packages for the management of both operating and dismantling waste produced respectively during the lifetime of EDF nuclear power plants (NPP) and during their dismantlement. One type of these packages, the “C1PG” package (Fig. 1-1), is recognized by Andra as offering a high level of mechanical strength and meeting the specification regarding confinement. The C1PG package is used on EDF Nuclear Power Plants sites to pack Low and Intermediate Level Short-Lived Waste, for transportation and final disposal at the CSA (Centre de Stockage de l’Aube) which is a surface storage center commissioned in 1992. The external shell of the C1PG is made of high-performance reinforced concrete (“F44Adj” concrete, EDF notation), whose formulation has been developed in internal laboratories of EDF. Those concrete packages meet the specifications previously listed and required by Andra: high mechanical strength, resistance to chemical reactions such as carbonation, alkali and internal sulfate reactions.

Fig. 1-1 – The C1PG^{SP} nuclear waste package

In addition to this short-lived waste, activated metallic waste classified as ILW-LL (Intermediate-Level Long Lived Waste) has been and will be generated during the operation and dismantlement of nuclear facilities. Those which have been already produced are currently stored in nuclear power plant's pools, while the dismantling waste is starting to be produced, as dismantling operations are moving forward. In France, the reference solution for such Long Lived waste management is a deep geological disposal, in the future French radioactive waste disposal facility Cigéo (Fig. 1-2). This project, managed by the French National Radioactive Waste Management Agency (Andra), is planned to be built in the North East of France, at the border of the Meuse and Haute-Marne departments. This area allows the implementation of disposal cells at about 500m depth in a thick (130 m) and very low permeability (of approximately 10^{-20} m^2) clay layer.

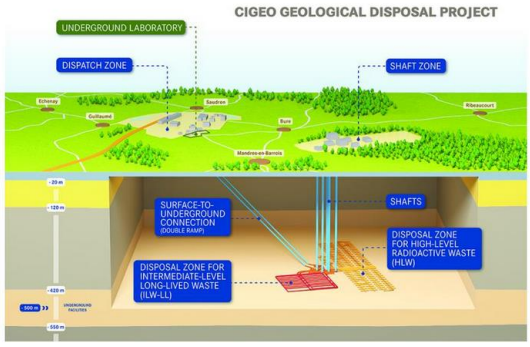

Fig. 1-2 – Cigéo disposal project – (Andra, 2020)

According to the current reference planning, the Cigéo project will be commissioned around 2030-2035. The operational phase of the facility is planned to last a total of hundred years. The disposal is designed to allow further package retrieval during their hundred years of disposal in the geological repository. Hence, the period of hundred years must be reversible.

To allow EDF to provide this activated metallic waste with a suitable packaging and a safe manage while waiting for the commissioning of Cigéo, a Conditioning and Storage Facility for Activated Nuclear Waste (ICEDA) has been built on Bugey Nuclear Power Plant site (see Fig. 1-3This facility will be commissioned in 2020. ICEDA is designed to receive, cut, pack and store this activated metallic waste. Strong of its experience managing of the Short-Lived waste, EDF chose, in accordance with the latest standards and Andra's waste specifications for Cigéo (still currently being discussed as the facility has not been commissioned yet), to dispose these wastes in a very similar package design to that of the C1PG packages. This package called the C1PG^{SP}, uses the same geometry and high performance concrete formulation as the Short-Lived wastes packages. However, the suffix SP ("sans polystyrène") means that the package design for Long-Lived waste has been slightly modified in regards to the initial C1PG, by removing a polystyrene layer that could be degraded by the higher level of radioactivity shown by Long-Lived waste than by Short-Lived waste.

Contrary to the C1PG packages already used in the CSA disposal, the C1PG^{SP} packages properties are not completely validated according to the ANDRA's requirements: these packages are still in discussion.

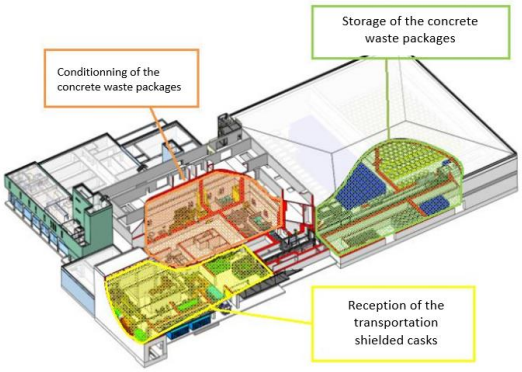

Fig. 1-3 – ICEDA Facility (EDF, 2020)

Within ICEDA:

- Activated metallic waste is received in transportation shielded casks and is extracted from the casks;
- The waste is cut into pieces that are compliant with the C1PG^{SP1} concrete shell size;
- These pieces are placed in a metallic basket, then grouted with cement matrix (Fig. 1-4);
- The metallic basket is placed in the F44Adj high performance reinforced concrete shell, and the space between the basket and the shell is filled with the same cementitious grout;
- The package is finally closed with an F44Adj concrete cap.

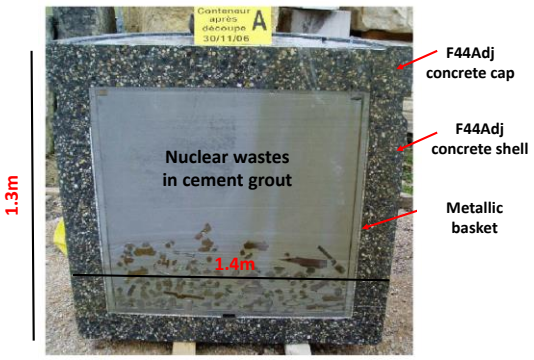

Fig. 1-4 – Transversal section of the C1PG^{SP} package

Once the packages are produced, they will be placed in a dedicated storage area in the facility. Depending on when the packages are produced, and when they can be evacuated towards Cigéo, their storage at ICEDA can last up to fifty years. According to EDF estimations, while making the conservative hypothesis that the storage area is full with waste packages, the exothermicity of the radioactive waste may lead to a maximum temperature around the packages of about 50°C and a minimum of 30% relative humidity. After storage, the concrete shell will potentially be submitted to a lower temperature and higher humidity within the disposal cell during the hundred years of the operational and reversibility phase of Cigéo.

During this maximum of 150 years of storage and disposal, the concrete will dry and age under these specific operating conditions (relatively high temperature and low relative humidity). These conditions have not been studied previously in the frame of surface disposal. Such conditions could lead to significant shrinkage strains by desiccation due to the small value of relative humidity that is

reached. If the latter strains are restrained, this can lead to significant stresses that could make the concrete crack. In the case of the concrete package, this restraining is partially caused by the steel basket that prevents the shell from freely deforming under desiccation.

Therefore, EDF is required to demonstrate the ability of the concrete shell to withstand the storage and disposal conditions and to keep its excellent mechanical properties overtime. Subsequently, the overall objective of this thesis is to provide elements of understanding the drying phenomena and the risk of cracking of the concrete shell caused by the restriction of drying deformations, in order to demonstrate the ability of packages to meet the requirements of future disposal.

1.2. Scientific context and research methodology

The drying behavior of the concrete is the main phenomenon that will be studied in this work. As previously said, drying can lead to drying shrinkage strains and therefore to significant stresses if the strains are restrained. Drying must therefore be studied carefully in order to ensure that the package will maintain its mechanical strength during the storage and disposal duration. Moreover, if this drying is overestimated, in terms of kinetics as well as in terms of strains amplitude, the stresses occurring will also be overestimated. This can lead eventually to an oversizing of the concrete shells dimensions, or, in our industrial context, to an inaccurate conclusion regarding the modification of the package properties over time.

The goal of this thesis is to model the dessication behavior of the $C1PG^{SP}$ package. Two aspects are to be carefully explored in this thesis:

- A major importance is given to correctly describe the mechanical behavior of the concrete shell. For that purpose, a corresponding model is needed. A model, based on the poromechanical works of Terzaghi, Biot (1941) and Coussy (2003), is currently implemented in *Code_Aster*, the scientific in-house software used and developed at EDF. Nevertheless, it has been shown that those models fail to describe the evolution of drying shrinkage strains for a relative humidity lower than 40% - 50% (Wyrzykowski et al., 2017). Therefore, in the current work, a major issue is to extend and adapt those models for lower humidities (down to 30%).
- The second aspect is the drying kinetics primarily controlled by the considered boundary conditions and the material transfer parameters. In the current framework, it should be guaranteed that the considered transfer model with the required transfer parameters is able to describe the drying of the concrete over the entire range of relative humidities and up to a temperature of 50°C.

The assessment of the model parameters and its validation require a number of experimental data. Therefore, an experimental campaign has been carried out by multiple laboratories under the framework of this thesis. The majority of the experimental tests were done in internal laboratories of EDF. Some tests were also executed in the LMDC (Laboratoire des Matériaux et Durabilité des Constructions, INSA Toulouse) and the LaM^{cube} laboratory (Université de Lille – Ecole Centrale de Lille).

The experimental tests performed at EDF R&D were initiated in 2017-2018. The tests consisted first in water retention measurements executed on F44Adj samples while adopting two different measuring methods: the saturated salt solution (SSS) method and the dynamic vapor sorption (DVS) method; at the same time, mass loss experiments and drying shrinkage experiments were also executed. All experiments are conducted under an external thermo hydric condition of T=50°C and a relative humidity of 30%. These conditions are chosen adequately to the most penalizing storage

conditions of the C1PG^{SP} packages, as described in section 1.1. For the purpose of comparison, the tests are also carried out under an ambient condition of T=20°C and a relative humidity of 50%, more commonly studied in the literature. It is important to note that all the previously cited experiments were finalized, except for the water retention experiments that are still ongoing and will be completed over the 2020-2021 period.

Regarding the test done at the LaM^{cube} laboratory, it consists in a direct measurement of the water permeability of the F44Adj concrete. Finally, the tests executed at the LMDC consisted in measuring both the shrinkage and creep of the F44Adj concrete. In this manuscript, only the corresponding autogenous shrinkage tests on the F44Adj concrete are used.

1.3. Thesis outline

This manuscript is organized in six chapters. The current chapter and chapter 6 constitute respectively the introduction and a presentation of conclusions and perspectives of this work. Chapters 2 to 4 cover each of the various phenomenological aspects describing the concrete drying behavior: the water retention and pores characterization of concrete, the moisture transfer and the drying shrinkage. Moreover, Chapter 4 presents a new poromechanical approach for describing the drying shrinkage on a large range of relative humidity. Chapter 5 is dedicated to an industrial application consisting in a numerical simulation of the C1PG^{SP} waste package during its storage phase.

The main aim of chapter 2 is to determine the appropriate water retention curve of the studied concrete. In fact, this curve is a major input for various poromechanical models. Chapter 2 begins with a bibliographical work introducing the water retention phenomena in concrete and the models used to describe it. A second part of this chapter is dedicated to the description of the experimental water desorption tests on the F44Adj concrete performed at the MMC (Matériaux et Mécanique des composants) laboratory of EDF. Finally, the need of a correct numerical model of the water retention curve requires an evaluation and a review of the Van Genuchten (1980) model. Indeed, this model is commonly used and implemented in *Code_Aster* (www.code-aster.org).

Chapter 3 deals with the modelling of the concrete drying kinetics. This chapter details at first the physical models found in the literature and usually adopted to describe various transfer modes in the concrete. A second part consists in describing drying experimental tests done at the MMC laboratory for evaluating this kinetic and a water permeability test done at the LaM^{cube} laboratory. The drying tests on samples of the F44Adj concrete under different tested conditions provided us with experimental mass loss curves. These curves are then used in the final part of chapter 3 for an inverse analysis using *Code_Aster*. This numerical analysis will help to identify correctly the transfer parameters of the concrete F44Adj.

Chapter 4 is dedicated to drying shrinkage. It describes the physical mechanisms behind it and the more common models of the literature. Then, a new poromechanical model describing the drying shrinkage of unsaturated porous media for a large range of relative humidity is proposed. Based on a thermodynamical approach, the derived model allows to account for various contributions to the stress development. Under the current framework, this model has been implemented in *Code_Aster*. This model is firstly validated for multiple porous materials from the literature: a cement paste, a high-performance concrete and a porous glass. The numerical results are compared with experimental results obtained with drying shrinkage tests on the F44Adj concrete.

At last, the previous works are used to model the drying behavior of the C1PG^{SP} package under the specific storage and disposal conditions. The corresponding numerical results are shown in chapter 5. Finally, chapter 6 presents the experimental and numerical simulations conclusions and perspectives of this work.

Chapter 2

Water retention and characterization of pores size distribution in concrete

List of Figures

List of Tables

In order to estimate the drying evolution of the shell, the moisture behavior of concrete should be known and accurately modelled. This chapter focuses in particular on the characterization of the porous system of the concrete as well as on finding a proper numerical model that could describe its water retention curve. i.e., the relation between the degree of saturation (or water content) and relative humidity. This water retention curve is a mandatory input for many classical poromechanical models.

We begin by referring to the literature in order to state the most important methods for characterizing the porous structure of the concrete (section 2.1.5). A literature survey allows us to find a certain number of mathematical expressions that could describe the water retention curve of the concrete (section 2.1.6). In a second step, the experimental campaign that allowed us to obtain the water retention curve of the F44Adj concrete is detailed in section 2.2. Finally, a proper numerical model for calibrating those curves on a large range of relative humidity is introduced (section 2.3).

2.1. State of the art

2.1.1. Generalities on concrete

Concrete is a porous material formed by a cementitious matrix, aggregates (sand, gravel…) and by voids or "pores" of different sizes. Cement, at the base of the matrix, is a binder composed of numerous constituents (alite, belite...) which react as soon as they come into contact with water. All of these reactions, known as hydration reactions, can be characterized by three main phases: the dissolution of oxides into ions, the precipitation of hydrates and diffusion (Mounanga, 2003). Once the concentration of ions (Ca^{2+}, OH^{-}...) in solution reaches a certain threshold, the hydrate precipitation phase begins, accompanied by heat production. This phase corresponds to the setting of the cement paste. As the paste sets, a layer of hydrates develops around the grains of binder, slowing down the diffusion of water. The kinetics of hydration are reduced.

The main products of hydration are hydrates, which are mainly in the form of calcium silicate hydrates C-S-H and portlandite $Ca(OH)_2$. Other products may also be present as simple hydrates (binding only with hydrogen molecules) such as aluminum hydroxide AlOH and silica acid $Si(OH)_4$, binary hydrates (binding with a second guest of molecules other than hydrogen) such as hydrated calcium aluminates $Ca_nAl(OH)_m$ or ternary hydrates (ettringite, hydrated calcium monosulphate aluminate) (Baroghel-Bouny,1994).

2.1.2.1

2.1.2. Porous structure of concrete

Pores and water in concrete

The geometry of the pore space in concrete can be complex and can include pores of various shapes and sizes, connected or not (Fig. 2-1).

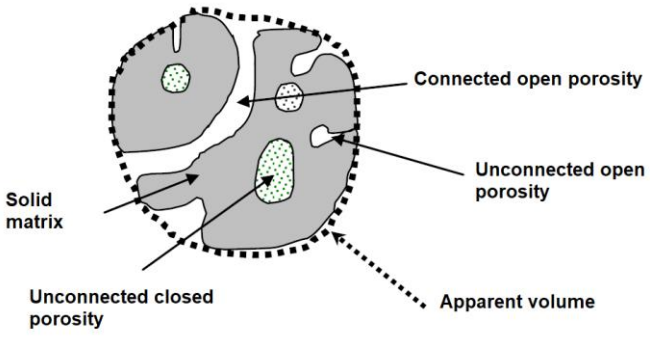

Fig. 2-1– Porous structure (adapted from Ollivier and Torrenti (2008))

It should be noted that unconnected pores, which do not communicate with each other, do not participate in the transfer phenomena. For this reason only connected porosity will be considered from now on.

Water in the pores of cementitious materials can be found under different forms (Baroghel-Bouny, 1994):

- **Chemically bound water**: this water is present in the hydrates produced during the hydration of cement. It only evaporates at high temperatures and such conditions can cause irreversible damage because the structure of the hydrates is modified.
- **Adsorbed water**: this water is physically bound to the solid pore walls under the effect of intermolecular forces. The structure of C-S-H particules is similar, according to Feldman and Sereda (1968) and Powers and Brownyard (1947), to a stack of sheets or leaves (Fig. 2-2). The average thickness of a layer of H_2O adsorbed on the surface of a C-S-H sheet is about 3Å (=0.3 nm). This water could be adsorbed on the outer surface of C-S-H in the interparticular space or inter-crystallite pores (space between two particles of C-S-H). On the other hand, water can be adsorbed between the C-S-H leaves in the intra-crystalliste pores (pores of sub-nanometric small size) in the form of 2 molecular layers (Baroghel-Bouny, 1994). This water is called interleaf water.
- **Free water**: this water is mainly found in pores of a bigger size than those found at the C-S-H scale. These pores are called capillary pores (Fig. 2-2 - left). The free water is most probably a water that can be completely evaporated by the drying of the concrete.

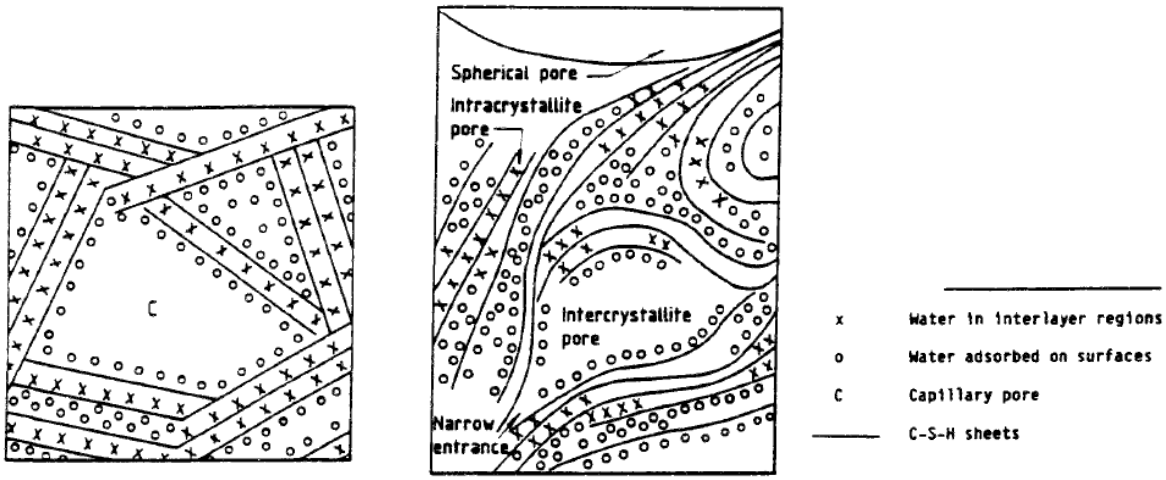

Fig. 2-2- Water in pores (Baroghel-Bouny, 1994): left, the Powers and Brownyard (1947) C-S-H representation – right, the Feldman and Sereda (1968) C-S-H representation

It is useful to classify pores in cementitious materials according to their size, as there are implications on the shape of retention curves and on water transport properties. The usual classification according to the IUPAC (1994)(International Union of Pure and Applied Chemistry) distinguishes between:

- **Micropores** with a size smaller than 2 nm.
- **Mesopores** with a size between 2 and 50 nm.
- **Macropores** with a size larger than 50 nm.

In the micropores domain, all water molecules are at a distance of less than 1nm from any atom of solid. Water molecules cannot be treated as a continuous medium: their study is a matter of molecular dynamics. The notion of pressure becomes problematic and the intermolecular forces exerted by the solid wall play a key role in the behavior of water molecules. In a micropore, water

molecules are either under a chemically bonded or physically adsorbed form.. Micropores may also be referred to as "hydrate pores" or “interparticular spacing between C-S-H sheets”.

The mesopores domain is entered when there is large enough space to harbor a significant amount of water in the liquid state due to its weak interactions with the pore walls. Water in such pores could be found in an adsorbed form or in a bulk (free) form. The free liquid contained in these pores is commonly called capillary, i.e. the water behavior is mainly determined by capillarity (see section 2.1.3). This capillary domain includes macro and mesoporous bodies, and excludes microporous solids. A limit is established between meso and macropores which is of the order of 50 nanometers. In macropores, the fraction of adsorbed water becomes negligible compared to the fraction of free water.

The term “capillary” voids or pores is also used by some authors to refer to both macropores and a mesopore margin above 10 nm (Fig. 2-3).

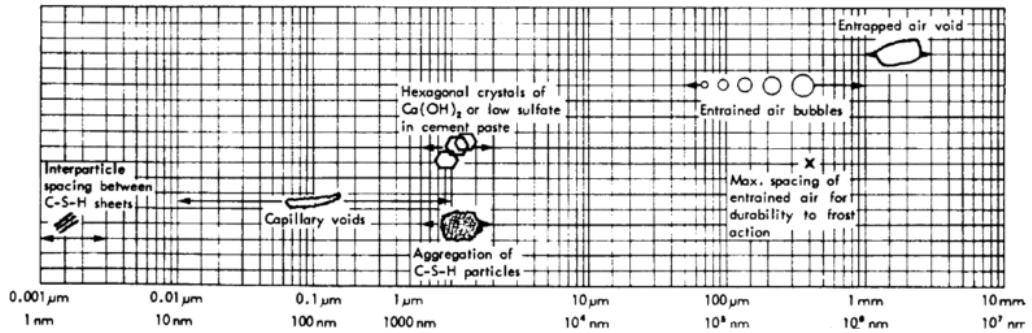

Fig. 2-3 - Size of solid phase constituents (aggregates, crystals) and pores size of a hydrated cement paste (Mehta, 1986)

2.1.2.2. Porosity, water content and degree of saturation

The porosity ($\emptyset$) of a material is defined by the ratio between the volume V_p of interconnected pores and the total volume V_t (pores volume + solid matrix volume).

$$\emptyset = \frac{V_p}{V_t} \tag{2-1}$$

This definition of porosity does not take into account the complexity of the geometry of the pore space, such as shape and pore size distribution. Other notions (such as permeability or water retention curves) complete the description of voids, when it comes to defining the transfer properties of the medium or its thermo-hygral equilibrium with the environment. These notions will be explained in more details in section 2.1.4 and in Chapter 3.

The porosity of an ordinary concrete is of the order of 15% at 28 days, that of a high-performance concrete is of 10 to 12% and that of a very high-performance concrete can vary between 7 and 9% (Ollivier & Torrenti, 2008).The most widespread method to measure porosity of a cementitious material is by saturating the sample with a liquid under vacuum, such as water or ethanol. After saturation, the entire pore volume is occupied by the liquid, so that the volume of pores is equal to the volume of water in the material V_w and we can write:

$$V_p = V_w = \frac{m_w}{\rho_w} = \frac{m_{sat} - m_{dry}}{\rho_w} \tag{2-2}$$

where m_w is the mass of water, ρ_w is the density of liquid water, m_{sat} is the mass of the saturated sample and m_{dry} is the mass of the dry sample. The saturation and drying techniques of samples will be further discussed in this chapter. Replacing equation (2-2) in (2-1), we obtain:

$$\emptyset = \frac{m_{sat} - m_{dry}}{\rho_w V_t} \tag{2-3}$$

This way, only the porosity accessible to that particular liquid is measured, so that some difference exists in principle between various employed substances, which can access different porosities.

Various definitions are used in the literature to characterize the amount of water in a sample, such as the water content *w* and the degree of saturation S_w. The water content w is defined as the ratio between the mass of water contained in the material and the mass m_{dry} of the material in the dry state:

$$w = \frac{m - m_{dry}}{m_{dry}} \tag{2-4}$$

with m being the mass of the sample at the measured state. The experimental degree of saturation S_w of a porous material is the ratio of the volume of water in the pores in the considered state to the total volume of the void or pores. It is easily shown that it can be expressed in terms of mass as given in equation (2-5) (while considering that the density of water in pores under its different forms is the same):

$$S_w = \frac{m - m_{dry}}{m_{sat} - m_{dry}} \tag{2-5}$$

From the definitions of the saturation and water content, it appears that they depend on two reference states namely the dry and saturated states. Some clarifications must thus be added to this point. In fact, knowing that the method of measuring the dry mass of the samples affects directly the calculation of moisture content and saturation levels (Wyrzykowski et al., 2017), the choice of an appropriate drying and saturation method is a major issue to be considered. The definition of the dry state of a material differs from one author to another. Some authors consider that the drying should be done at a temperature of 105 °C, which is the temperature necessary for the departure of free water (also indicated in the norm NF P18-459). Mjahad (2012) uses drying at 60°C for all the tests, noting that a temperature of 105°C can cause micro-cracking in the tested sample. Baroghel-Bouny(2007) considers that the dry mass is that which corresponds to the mass of the sample for a relative humidity near 0%. Given that a 0% of relative humidity is generally difficult to establish (depending on the technique used to fix an ambient relative humidity), the author used instead a relative humidity of 3% to define the dry state of the material.

For the measurement of the saturated mass, the sample is placed under water in a vacuum sealed bell. This operation allows it to be fully saturated while avoiding the existence of air bubbles in the sample. Its mass increases until it stabilizes. Baroghel-Bouny (2007) indicates that it is necessary to have a stable material unaffected by chemical reactions such as hydration during sorption/desorption experiments. For this reason, the author suggests that a maturation phase under water is necessary before starting the tests. An average duration of 6 months to 1 year is usually adopted depending on the formulation of the material (depending on the duration of almost complete hydration).

2.1.3. Liquid interfacial equilibrium (Laplace's Law) and thermodynamic equilibrium (Kelvin's Law)

Unsaturated concrete is a porous medium consisting of three phases (Fig. 2-4 - left):

- The solid (s) phase: constituted by the porous matrix
- The liquid (l) phase contained in the pores
- The gas (g) phase: moist air (dry air + water vapor) contained in the pores.

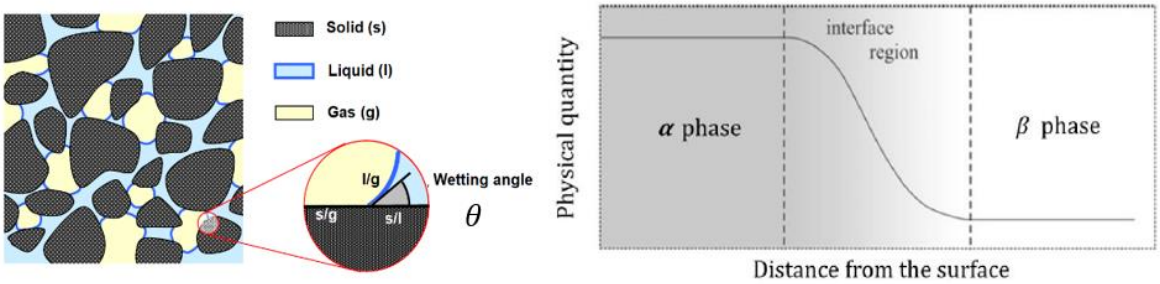

Fig. 2-4 - Phases and interfaces in a porous system – adapted from Daian (2013)

It should be noted that between the previously considered phases α (gas or liquid phase) and β (the solid surface of the pores), there exists a transition zone or interface region (Fig. 2-4- right) in which the composition is not homogeneous and does not correspond to those of α and β (Maugis, 1980). To model this system, Gibbs (1928) proposed to define an ideal system with an interface Σ located in the transition zone and to assume that the composition of the nearby phases remains homogeneous until reaching this surface.

In an unsaturated porous medium occupied by a liquid and a gaseous phase, liquid/gas, solid/gas and solid/liquid interfaces are considered to be present (Fig. 2-4- right). The angle in Fig. 2-4 is called a wetting angle θ. Its value is limited by the value of 0° in the case of a perfect wetting and by 180° in the case of zero wetting. Fluids are usually classified according to the value of θ: when $\theta \leqslant 90^\circ$, the fluid is "wetting" with respect to the solid surface; on the contrary, the fluid is called "non-wetting" if $\theta > 90°$. In the case of cementitious materials, their solid surface is said to be hydrophilic i.e. when exposed to liquid water the latter is the wetting phase (with θ=0°) and the gas is the non-wetting phase.

Laplace's law (equation (2-6)) describes the interfacial equilibrium between two fluids: a wetting w (e.g. liquid water) and a non-wetting nw (e.g. gas) one. In fact, any element at the interface between two fluids is in equilibrium under the effect of surface stresses $\sigma_{nw/w}$ acting on its perimeter and under pressure forces P_{nw} and P_w acting on either side of its interface (Fig. 2-5).

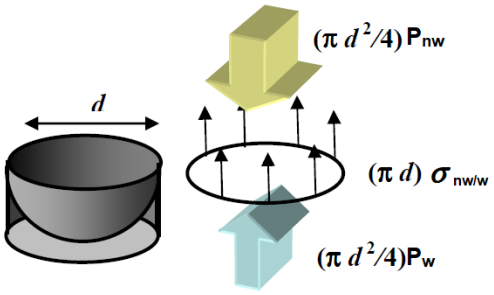

Fig. 2-5 - Laplace Law applied on a spherical meniscus of a pore (Daian, 2013)

In the particular case of a cylindrical pore, we can define a radius r_p of the pore and a diameter d. When gravity forces are negligible (i.e. for sizes below the capillary length), the meniscus is a portion of sphere and a radius r_{ms} can therefore be defined (Fig. 2-6).

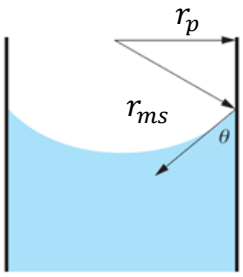

Fig. 2-6 – Schematic of a cylindrical pore

The Laplace equation is then given by equation (2-6):

$$P_{nw} - P_w = \frac{2\sigma_{nw/w}}{r_{ms}} = \frac{2\sigma_{w/nw}\cos\theta}{r_p} = \frac{4\sigma_{w/nw}\cos\theta}{d} \quad (2\text{-}6)$$

where $\sigma_{w/nw}$ is the surface stress between wetting and non-wetting fluid. For the liquid water / air interface, the interfacial tension $\sigma_{L/G}$ is 0.072 N/m^2 (Coussy, 2010). In equation (2-6), the difference between the pressure of a non-wetting phase and that of the wetting phase appears: this pressure difference is called the "capillary" pressure P_C.

In the case of a vertical capillary tube in contact with a liquid wetting the solids wall, the water rises in the capillary until it stabilizes. According to the law of hydrostatics, the pressure of the liquid P_L under the meniscus can be calculated as given by equation (2-7) (where ρ_L is the density of the liquid, g is the acceleration of gravity and h height to which the liquid rises under the effect of interfacial tensions):

$$P_L = \rho_L g h \quad (2\text{-}7)$$

By applying equation (2-6) for the case of liquid water and gas and combining it with equation (2-7), we arrive at Jurin's law which makes it possible to calculate the height h often referred to as the "water column":

$$h = \frac{2.\sigma_{L/G}}{\rho_L\, g\, r_p} = \frac{P_C}{\rho_L\, g} \quad (2\text{-}8)$$

By equating the chemical potential of the water in the gas phase and in the liquid phase, the Kelvin's Law is derived expressing the thermodynamic equilibrium between the two phases at a certain temperature and (derivation found in (Coussy, 2010)) written as:

$$P_C = P_G - P_L = -\,R\,T\,\frac{\rho_w}{M_w^{mol}}\,ln(h_R) \quad (2\text{-}9)$$

where P_G is the pressure of the gas phase is, P_L is the pressure of the liquid phase, R is the constant of ideal gases, T is the ambient temperature, M_w^{mol} the molar mass of the liquid water.

2.1.4. Sorption and desorption in porous materials

The relative humidity h_R at a temperature T is defined as the ratio between the vapor pressure P_{vp} and the saturated vapor pressure $P_{vp,sat}(T)$. When the relative humidity of the environment where the material is laid increases, the material adsorbs water: this is the phenomenon of sorption. In turn,

the decrease in relative humidity leads to a loss of water mass from the sample: this is called desorption. With each change in ambient relative humidity, the sample evolves transiently and eventually stabilizes: at this point there is no more gain or loss of mass of the sample therefore the latter, which is in thermo-hydric equilibrium with the environment. If, at constant temperature, an initially saturated material is gradually dried (or a dry material is gradually saturated) and the equilibrium points (w, h_R) or (S_w, h_R) are plotted, a desorption isotherm (or a sorption isotherm) is obtained

For certain applications, often for soils, sorption and desorption curves are obtained by imposing a capillary pressure at the edge of the specimen by a drainage test, and that by controlling the liquid and the air pressure - (Daian, 2013). In that case, the experimental curve is more properly expressed as a function of P_C. Usually for concrete, sorption or desorption curves are obtained by exposure to a given relative humidity: we will focus then hereafter on that kind of test.

2.1.4.1. Sorption mechanisms

When a material is submitted to an increase of relative humidity, small pores start at first to get filled with water. In the low relative humidity range, the large specific surface area of a cementitious material plays an important role and thus surface adsorption is the predominant filling mechanism. This adsorption could be either characterized by a monolayer or by multilayers of adsorbed fluid (Fig. 2-7(a), (b)). At higher relative humidities, bigger pores start to get filled with water. In such pores, the phenomenon of capillary condensation occurs (Fig. 2-7-(c)), with coalescence of adsorbed layers and formation of liquid water.

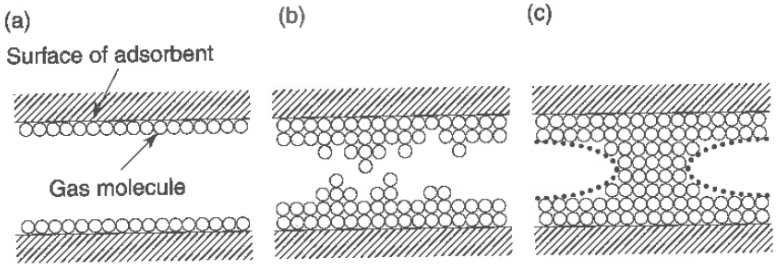

Fig. 2-7 – (a) Monolayer adsorption (b) Multilayer adsorption (c) Capillary condensation (Aligizaki, 2006)

Many have discussed the applicability of the Laplace Law (equation (2-6)) to concrete, given that its derivation arises from the conservation of linear momentum across a curved meniscus separating the wetting and non-wetting phases. However, the existence of such a stable meniscus (such in Fig. 2-7-(c)) in single nanometer sized pores has been frequently debated and denied (Beltzung and Wittmann, 2005; Pellenq et al., 2009). Therefore, the validity of the Laplace Law can be admitted to stand to the mesopores limit. On the other hand, Kelvin's equation remains valid irrespectively of the size of the meniscus (i.e. irrespective of the pores size) (Rahman and Grasley, 2017) due to the fact that this relation can be derived through purely thermodynamic considerations via a Gibbs-Duhem state equation. Therefore, Kelvin's equation is considered to be applicable even when monolayer adsorption or multilayer adsorption occurs. In the case where both equations (2-6) and (2-9) are accepted we can write the Kelvin-Laplace equation:

$$r_k = -\frac{2\sigma_{L/G} M_w^{mol}}{R\,T\,\rho_w\,ln(h_R)} \tag{2-10}$$

The Kelvin radius r_k corresponds to the smallest pore emptied at a fixed relative humidity value. All pores with a radius r_p such that $r_p < r_k$ are saturated with liquid water, while those with a radius r_p such that $r_p > r_k$ are not yet saturated.

2.1.4.2. Ink bottle effect and delayed desorption (cavitation and pore blocking)

The sorption / desorption isotherms depend on the porous structure of the material. Moreover, as can be seen in Fig. 2-8, the sorption and desorption isotherms are generally not identical for a cementitious material.

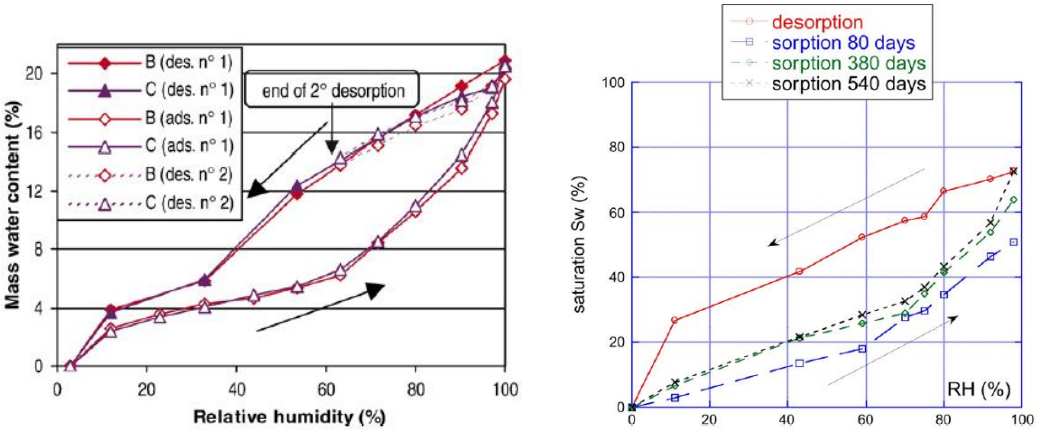

Fig. 2-8- Sorption and desorption isotherms for a high performance concrete studied in (right) Chen et al.(2012) and for an ordinary concrete (B) and cement paste (C) studied by Baroghel-Bouny (2007) – (left)

A hysteresis is observed between these two curves. This hysteresis is usually remarkable in the mid-range of relative humidity (Baroghel-Bouny, 2007) where capillary condensation mechanisms are most important. In this mid-range, one of the reasons behind this hysteresis is the "ink bottle" effect (Mcbain, 1935), also called “pore blocking”. This effect is related to the presence of a neck between two connected pores. During sorption, the filling of water is controlled by the pore radius, noted φ_1. During drying or desorption, the departure of water from the pore depends essentially on the radius of the throat, noted φ_2 in Fig. 2-9. The fluid remains trapped in the throat until the vapor pressure becomes low enough to empty the adjacent pore. Consequently, during desorption, the relative humidity at which a pore empties may be smaller than the relative humidity at which, during sorption, the same pore becomes saturated. This behavior leads to a hysteresis.

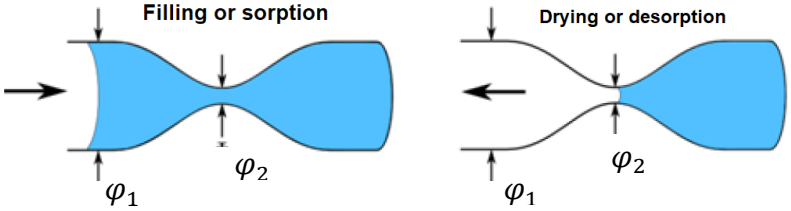

Fig. 2-9- Schematic of the “ink-bottle” (or “pore blocking”) effect - (Mjahad, 2012)

As for the observation of a sudden drop in the desorption branch near 40% (see Fig. 2-8-left), this is explained by the occurrence of a phenomenon known as “cavitation” Maruyama et al. (2018): “during desorption, the surface tension acting on the meniscus causes negative pressure in the condensed liquid water. This negative pressure stretches the liquid water entrapped in the pores. When water vapor is more stable than liquid water (which is the fact for any relative humidity lower than 100%), the nucleation of a bubble of the vapor phase in the liquid phase - a phenomenon known as cavitation - can occur”. The cavitation phenomenon occurs especially when the liquid pressure becomes larger (in absolute value) than a threshold value, hence when the relative humidity becomes smaller than a threshold value. Although Nguyen et al. (2011) proposed that the drop observed during desorption at a relative humidity near 35%-40% could be attributed to pore blocking, (Maruyama et al., 2018) provide strong evidence that this drop is in fact due to cavitation of the pore water.

During desorption, depending on the conditions and on the pore structure, pores can hence empty through cavitation of the pore or through movement of the air-water interface (see Fig. 2-10). Note that cavitation can only be observed if, during desorption, at the relative humidity at which cavitation is expected to occur, there is still liquid water present in the porosity, which is at 35%-40% relative humidity, this can only be the case if there is a pore blocking effect (see Fig. 2-10 - left).

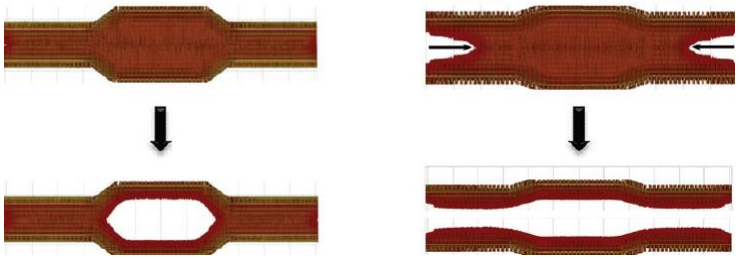

Fig. 2-10 – Two manners how, during desorption, a pore can empty: (left) through cavitation and (right) through movement of the air-water interface. Adapted from Nguyen et al. (2011)

As for the low range of relative humidity ($h_R \approx$ 10-20%) a hysteresis could also be observed in the case of cementitious materials. Baroghel-Bouny (2007) links this possible formation of a hysteresis to a modification of the nanostructure of C-S-H and hence of the microstructure of the material. Indeed after the first desorption of the material, when the relative humidity becomes very low ($h_R \approx$ 10-20%), the departure of physically bound water from the C-S-H could cause a "pore collapse", i.e. a collapse of small pores, making it difficult for water to re-soak the latter (see Fig. 2-8 - left) . Baroghel-Bouny (1994) showed that for sorption/desorption tests done on cement pastes in with an inert gas (ex: nitrogen) no hysteresis occurred in this low range of relative humidity.

2.1.5. Characterization of the pore space

The porous distribution of a porous material can be obtained with various porosimetry techniques (thermoporosimetry, NMR, mercury intrusion, sorption isotherms based techniques.), imaging techniques (optical microscopy, scanning electron microscopy SEM or MEB, X-ray tomography, MRI...). Fig. 2-11 represents some of the multiple techniques and their limits in accessing different pore sizes. In this section, we describe commonly used porous characterization methods for cementitious materials that are based on the sorption/desorption phenomena.

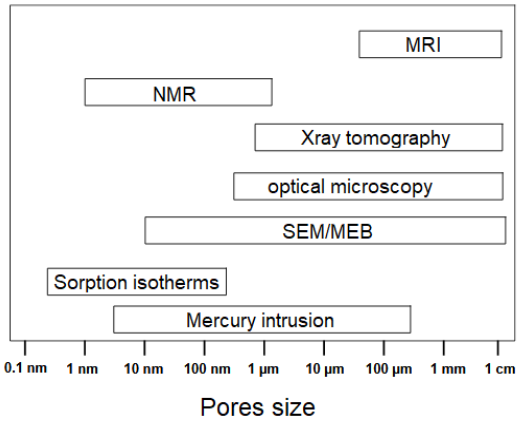

Fig. 2-11 – Techniques for porous characterization - (Jaffel, 2007)

2.1.5.1. Mercury intrusion technique

Mercury is a non-wetting fluid, which prevents it from penetrating the porosity of cementitious materials spontaneously (unlike water). The mercury injection pressure is applied to a sample that has been previously dried and increased up to 200 to 400 MPa. The radius of the accessible pores is measured for each imposed pressure level: the higher the injection pressure is, the smaller the size of

the penetrated pores is. By supposing cylindrical pores, the equation relating the injection pressure to the pore size is obtained by simply applying Laplace's law as follows:

$$P_{Hg\ liquid} - P_{Hg\ gaz} = \frac{2\,\sigma_{Hg}\cos\theta}{r_p} \tag{2-11}$$

where σ_{Hg} is the surface tension of mercury between liquid mercury and vapor mercury (approx. 0.485 N/m (Daian, 2013)), θ is the wetting angle between liquid mercury and cement (about 50 degrees (Daian, 2013)), $P_{Hg\ liquid}$ is the pressure of the liquid mercury (which is the non-wetting fluid) and $P_{Hg\ gaz}$ is the pressure of the mercury vapor, usually neglected (so that $P_{Hg\ gaz}$=0, which simplifies eq. (2-11)). During the test, the volume of mercury injected into the material is measured as a function of the pressure and thus of the pore radius. This knowledge gives access to the increment of pores volume with respect to a given increment of pore radius. Once the test is over and the total amount of injected mercury is known, it is also easy to estimate the total porosity.

An example of the results of a mercury porosimetry test for a CEM I and a CEM V high performance concrete is shown in Fig. 2-12 where the cumulative volume of mercury injected is plotted against the pore diameter (blue curves); the plot is usually logarithmic on the abscissas. A different visualization (in red) of the pore size distribution can be made by plotting on the ordinate axis the derivative of the injected mercury volume with respect to the logarithm of the pore radius $dV_{Hg}/(dlog(d))$. This curve allows us to easily identify the main pores families from peaks, which indicate an increased intrusion of mercury over a range of pore radii.

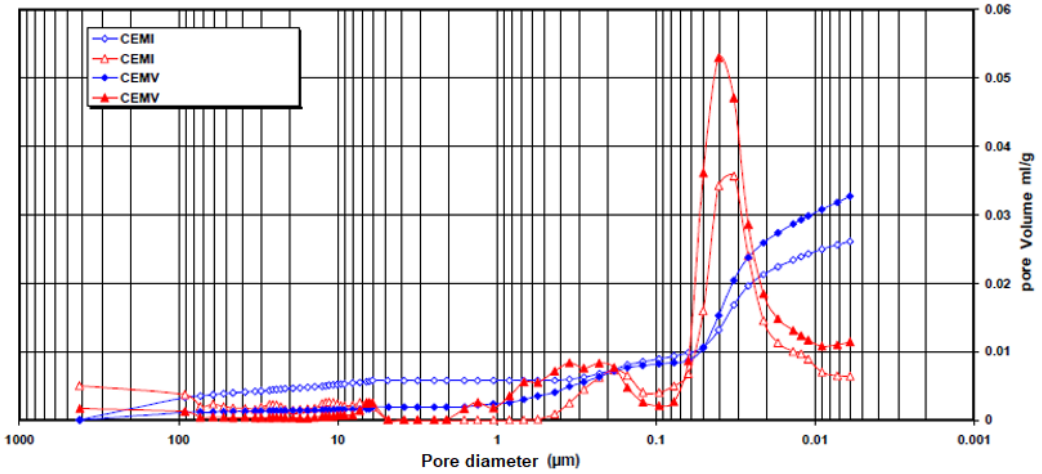

Fig. 2-12 – Mercury intrusion test results for a high-performance concrete - (Chen, 2013)

With respect to other methods, mercury porosimetry has several drawbacks, among which:

- Modification of the microstructure and pore distribution of the test material due to recommended pre-drying (Gallé, 2001).
- Mercury injection pressures limited to 400 MPa (device limitation) , which limits the access to pores smaller than approximately 3 nm in size. For concrete, this can lead to erroneous results especially in the mesopore and micropore range. Indeed, the access of mercury to certain areas of the pore network is controlled by the smallest entry diameter of pores.
- Samples introduced into the device should be of relatively small size (device limitation), of the order of magnitude of the centimeter (J.F. Daian, 2013). This may cause a lack of representativeness in the case of concrete which is a highly heterogeneous material and whose RVE is more on the order of the decimeter.

Mercury injection is commonly adopted but this does not make it representative of the porosity accessible to water, which is our quantity of interest for concrete drying.

2.1.5.2. Methods based on a sorption/desorption isotherm

The isothermal sorption method consists in exposing a sample to an atmosphere rich of a certain gas and measuring the quantity of absorbed gas, which gives the saturation to that substance.

The method is applied using for example water vapor or nitrogen. In the case of nitrogen, the sample, which has been previously dried, is placed in a climatic chamber and the pressure of the gas is gradually increased; moreover, the gas is used at a temperature close to that of its liquefaction (77 °K i.e. -196.15 °C) to allow the pores to be filled with a liquid of a given density. Fig. 2-13 illustrates a sorption/desorption curve obtained with nitrogen: the quantity of gas adsorbed as a function of increasing relative pressure (equilibrium vapor pressure (noted as p) divided by the saturating vapor pressure (noted as p_0)).

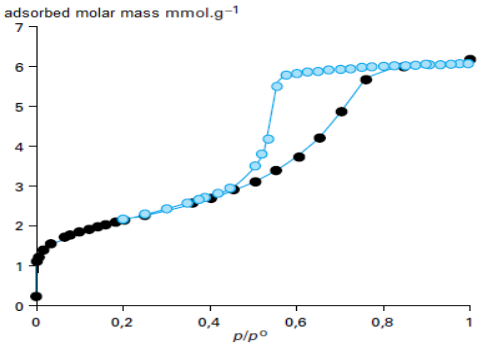

Fig. 2-13 – Sorption/desorption isotherm of N_2 on a Vycor glass - (Rouquerol, 2003)

In the case of water, the method consists in exposing the sample to a given atmosphere, at a given relative humidity and temperature, and so to a given vapor pressure. The procedure is repeated for different vapor pressures, obtaining in practice a sorption/desorption isotherm.

The pore size distribution is estimated by processing data from sorption or desorption isotherms. For instance, using water desorption isotherms. Rougelot et al.(2009) identified the pore size distribution for cement pastes and mortars. Hence, a distribution function called r is defined as follows:

$$r(h_R) = \frac{dS_w}{dh_R} \cong \frac{S_w\left(h_R^i\right) - S_w\left(h_R^{i+1}\right)}{\left(h_R^i\right) - \left(h_R^{i+1}\right)} \tag{2-12}$$

with $S_w\left(h_R^i\right)$ the degree of water saturation corresponding to the relative humidity h_R^i of the i-th desorption step. This distribution function could be also written in terms of the pores radii through the Kelvin-Laplace law. This allows for the definition of another distribution function (again called "r"):

$$r(h_R) = \frac{dS_w}{d(r_p)} \cong \frac{S_w\left(h_R^i\right) - S_w\left(h_R^{i+1}\right)}{\left(r_p^i\right) - \left(r_p^{i+1}\right)} \tag{2-13}$$

Equation (2-13) leads to a representation similar to that obtained with mercury porosimetry (Fig. 2-12), allowing for an easy identification of peaks of the pore size distribution. However, it is important to note that in this method, the thickness of an adsorbed water layer is not taken into consideration. For a better identification of the pore distribution, one could also apply the B.J.H calculation method (Barrett et al., 1951) which again is based on the Kelvin-Laplace law but takes into account the presence of the adsorbed layers on the pore surface. This method will be introduced posteriorly in this section.

The B.E.T theory

Because of its simplicity and ability to represent multiple types of isotherms, the B.E.T (Brunauer et al., 1938) method is one of the most used method for the analysis of the specific surface area of cementitious materials (Aligizaki, 2006). The BET theory describes multi-molecular adsorption on solid surfaces. This theory assumes that there is no adsorbate-adsorbate interaction between molecules of the same layer. It also assumes that the adsorption of the first layer of water or gas molecules (i=0) occurs with an interaction energy E_0, while the adsorption of all remaining layers (i>1) occurs with an energy equal to the liquefaction energy E_L (bulk liquid energy). As the relative pressure increases, the theory considers that the number of adsorbate layers becomes infinite therefore from a theoretical point view this method is only valid for non-porous materials (where the only phenomenon to occur is surface adsorption on the external surface of the material).

The described hypotheses lead to the following relationship (Baroghel-Bouny, 1994):

$$\frac{P}{V(P_0-P)} = \frac{1}{V_m C} + \frac{C-1}{V_m C}\frac{P}{P_0} \tag{2-14}$$

with V and V_m respectively the specific(per gram of adsorbent) total adsorbed volume of gas and the volume necessary to cover the surface of a monolayer , P and P_0 the gas pressure and the gas pressure at saturation, C a constant linked to the heat of adsorption of the surface adsorbed molecules E_0 and to the liquefaction energy E_L. For water adsorption tests, equation (2-14) can also be written as a function of the relative humidity, of the water content w and of the monomolecular water content w_m instead of the specific gas volume (Chen et al., 2012) and (Daian, 2013):

$$\frac{h_R}{w(h_R-1)} = \frac{1+(C-1)h_R}{C\ w_m} \tag{2-15}$$

From the desorption isotherm $w(h_R)$, when plotting $\frac{h_R}{w(h_R-1)}$ against h_R, if the BET theory is applicable, a linear relationship must be obtained. A slope of $(C-1)/(C\ w_m)$ and an intercept of $1/(Cw_m)$ are assessed so that the two constant parameters C and w_m can be calculated. In most cases, the BET theory applies in the region of h_R between 0.05 and 0.35 (Aligizaki, 2006). Indeed, in this region, the assumptions on which the theory is based are most likely to be verified.

Once the parameter w_m is calculated, one can compute the specific area of the material S_{BET} as follows (Baroghel-Bouny, 1994):

$$S_{BET} = \frac{N_A\ A_m\ V_m}{V_M} \tag{2-16}$$

where V_m the volume of water (in m^3/g) corresponding to the value of w_m , N_A is the number of Avogadro, V_M is the molar volume of water (18.10^{-6} m^3/mol (NIST Chemistry WebBook, 2018)) and A_m is the average area occupied by one molecule of the adsorbate. The latter was estimated for water molecules in Baroghel-Bouny (1994) and Hagymassy et al. (1969) according to the empirical relation (for a temperature of 20°C, the value of 10.6 $Å^2$ is obtained):

$$A_m = 1.091\left[\frac{M_w^{mol}}{N_A\rho_w}\right]^{2/3} \tag{2-17}$$

To give an idea of the values of the specific surface area of concrete, Chen et al. (2012) and Baroghel-Bouny (1994) both applied the B.E.T technique to a water desorption isotherm for a CEMI high performance concrete .

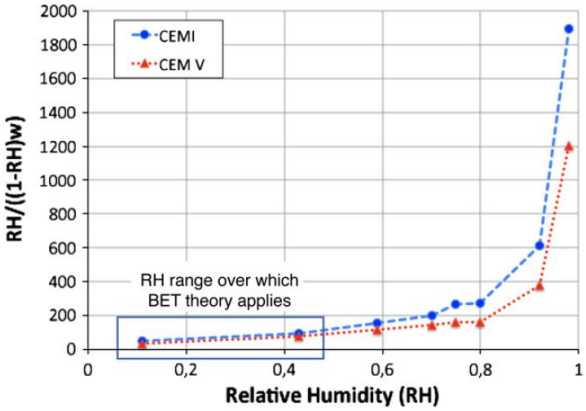

Fig. 2-14 – B.E.T technique applied to a high-performance concrete studied in Chen et al.(2012)

Chen et al. (2012) calculated a specific surface of 18 m^2/g (see Fig. 2-14), close to the specific surface of 20 m^2/g calculated by Baroghel-Bouny (1994).

Baroghel-Bouny (1994) also compared the specific surface area of a cement paste obtained with water vapor adsorption to that determined by nitrogen adsorption: results were on the order of 123 m^2/g with water vapor and 72 m^2/g with nitrogen. This difference is explained by the small size of water molecules with respect to the nitrogen molecules which allows the molecule to be more accessible to surface and pores volume.

The B.J.H method

The BJH method is a step-by-step method proposed by Barrett et al.(1951) to take into account the thickness of the adsorbed layers. Accordingly, a correction to the pore diameter is added in before computing the pore diameter again with the Kelvin-Laplace formulaa and the pores are again assumed to be cylindrically shaped. In their paper, the authors used nitrogen to obtain the experimental sorption isotherms but the method is in principle applicable also to water sorption or desorption isotherms..

A scheme of the BJH idealized desorption process is given in Fig. 2-15. At a given relative humidity, the material loses an amount of fluid that corresponds to the two following contributions:

- A loss in the amount of condensed fluid in pores with radii equal to r_p which is the sum of a Kelvin-Laplace radius noted r_k and the thickness of an adsorbed fluid layer t.
- A decrease of the thickness of the adsorbed layer for pores with a radius bigger than r_p

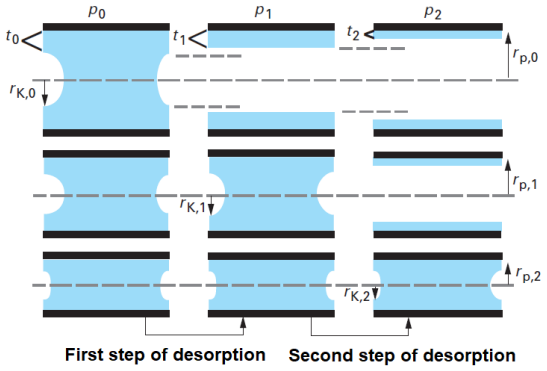

$r_{p,0} = r_{K,0} + t_0$; $r_{p,1} = r_{K,1} + t_1$; $r_{p,2} = r_{K,2} + t_2$

Fig. 2-15- Desorption stages following the BJH method - (Rouquerol, 2003)

Considering the desorption isotherm $w(h_R)$ or $S_w(h_R)$ of the studied material as an initial input, the BJH method calculates the volume of desorbed fluid between two consecutive steps n-1 and n.

This volume is noted as $\delta V_{w,n} = V_{w,n-1} - V_{w,n}$. Using the corresponding pore size $r_{p,n}(h_R)$, the method computes an increment in the volume and surface of desaturated pores (noted $\delta V_{p,n}$ and $\delta a_{p,n}$ respectively), corresponding to a relative humidity step δh_R. The expression of $\delta V_{p,n}$ is given by equation (2-18) where $\overline{r_{p,n}}$ is the average radius of pores between two consecutive steps, $\delta t_n = t_{n-1} - t_n$ is the increment of the adsorbed layer thickness and $\delta a_{p,i} = 2\delta V_{p,i}/\overline{r_{p,i}}$ is the solid surface area under the assumption of cylindrical pores:

$$\delta V_{p,n} = \left(\frac{\overline{r_{p,n}}}{\overline{r_{p,n}} - t_n}\right)^2 [\, \delta V_{w,n} - \delta t_n \sum_{i=1}^{n-1} \delta a_{p,i}(1 - \frac{t_n}{\overline{r_{p,i}}})] \qquad (2\text{-}18)$$

The total area $\sum_i \delta a_{p,i}$ calculated at the final stage of the computation corresponds to a specific surface area S_{BJH} of the material calculated with the BJH method. This area should be compared to the specific surface area S_{BET} assessed with the BET method. In fact, the two estimated area should be close (by 10% (Rouquerol, 2003)) to guarantee the consistency of the BJH method.

The cylindrical pore configuration considered in the BJH method could seem far from the actual pore configuration of cementitious materials. Nevertheless, this method has been used by various authors to determine the pore size of such materials (Baroghel-Bouny, 1994, 2007; Rahoui, 2018; Robens et al., 2002). In fact, as indicated by Baroghel-Bouny (2007), this method remains useful at least for comparative studies.

In the BJH method, the thickness of the adsorbed fluid layers as a function of the relative humidity is a necessary input. In the original paper, Barrett et al. (1951) assumed that the thickness of these layers is equal to that of an adsorbed layer on a flat free surface of a non-porous material. This thickness can be determined by multiple empirical relations, assessed from experimental curves, such as those proposed by de Boer and Lippens (1965), Halsey (1948), Hagymassy et al. (1969) among others. These relations are usually presented by a curve (named "t-curve") linking the adsorbed fluid thickness to its partial pressure. The "t-curves" given by de Boer and Lippens (1965), Halsey (1948) and Harkins and Jura (1944) were assessed from nitrogen adsorption experiments on various non-porous material e.g. zinc oxide, silver etc.

On another hand, there exist in the literature "t-curves" assessed from water vapor sorption experiments, such as those provided by Hagymassy et al. (1969), providing curves for different non-porous materials (silica gel, quartz, calcite, etc.) as adsorbent; the adsorbate was water in all cases. These non-porous materials are distinguished by their different adsorbate-adsorbent interaction energy, which is usually characterized by the BET constant *C*. Consequently, for a porous material, the corresponding 't-curve' described by a similar constant *C* should be selected. The number of layers provided by the Hagymassy et al. (1969) curve is generally multiplied by 3 Å (which is supposed to be the thickness of a monomolecular layer of water (Baroghel-Bouny, 1994)) to obtain the corresponding thickness (Fig. 2-16).

Independently from the the BET constant C, Badmann et al.(1981) provided a relation linking the thickness t to the relative humidity: $t(h_R) = K_1 + K_2 \ln(-\ln(h_R))$ where K_1 and K_2 are two constants that could be fitted on the experimental sorption isotherm of a material. In the case of raw-cements, Badmann et al. (1981) indicated the values K_1 =0.385 nm and K_2= -0.189 nm.

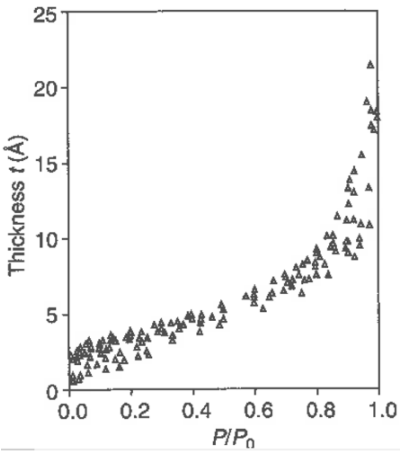

Fig. 2-16 –The‘t-curve’ given by Hagymassy et al. (1969) from Aligizaki (2006)

2.1.6. Numerical models for water retention curves

In this section we will describe commonly used numerical models for water retention available in the literature. The experimental water retention tests procedures might be different (relative humidity or fluid pressure control). It is therefore necessary to be vigilant while choosing the corresponding water retention numerical model. Several numerical models in the literature are known to describe sorption/desorption isotherms of porous materials (Brooks and Corey, 1964; Durner, 1994; Van Genuchten, 1980).

One of the commonly used numerical models is the Pickett model. Pickett (1945) modified the BET model (equation (2-15)) and proposed a 4 parameters fitting model that takes into account the monolayer and multilayer adsorption. Hence the model is a priori designed for adsorbed water but not for free water. This model is presented by equation (2-19) where C, w_m, are the two previously introduced BET parameters, D is a positive parameter and p is the maximal number of layers which can form:

$$w(h_R) = Cw_m \frac{h_R\left(1-h_R^p\right) + Dp(1-h_R)h_R^p}{(1-h_R)[(1-h_R) + C\left(h_R + h_R^p\right)]} \tag{2-19}$$

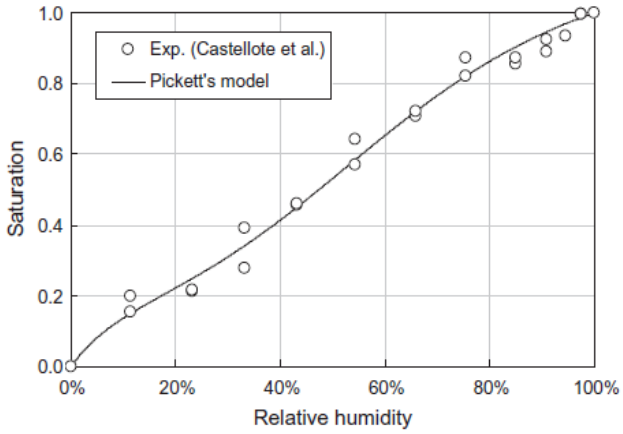

Fig. 2-17 - The Pickett (1945) model used to fit Casrellote et al. experimental data in Poyet (2013)

In its initial form, this model was written by the author in terms of water content. However, it was then written and used by Poyet (2013) in terms of the degree of saturation. This model (Fig. 2-

17) showed a successful representation of experimental water retention curves of cementitious materials in Drouet et al. (2015) and Poyet (2013). This model was used by the previous authors only for fitting purposes without verifying the physical meaning of its parameters.

Later on, the BET model was also modified by Brunauer et al. (1969). The BSB model (for Brunauer, Skalny and Bodor) which is a 3 fitting parameter model is also known as the GAB model (for Guggenheim (Guggenheim, 1966), Anderson (Anderson, 1946) and de Boer (Boer, 1953)). This model permitted to extend the applicability of the BET model to high relative humidities (Zou et al., 2016). The model is represented in equation (2-20) with C, k, w_m the three fitting parameters (when k =1, one recover the BET model):

$$w(h_R) = \frac{C\ k\ w_m h_R}{(1 - k\ h_R)[1 + (C - 1)k\ h_R]} \tag{2-20}$$

It was recently used by Poyet and Charles (2009) and Brue et al. (2012) to model water retention curves of concretes. It was shown by Brue et al. (2012) that the parameters of the GAB model does not always present a physical meaning. As a matter of fact, Brue et al. (2012) used this model to model water retention curves of a high performance concrete CEMI and CEMI V at different temperatures (20°C shown in Fig. 2-18 left, 50° and 80°C). The authors tried to give a physical interpretation for the models parameters by calculating the number of absorbed layers ($n = w/w_m$) from the fitted parameters at different temperatures.

For a CEMI, the GAB model gave a bigger number of adsorbed layers when T°$= 50°C$ and $h_R > 0.35$ than the number of adsorbed layer at 20°C (Fig. 2-18 - right). The same result is observed when T°$= 80°C$ for the whole range of relative humidity. As noted by the authors, the latter results are not exactly physical as this number is supposed to decrease with a higher temperature and lower relative humidity. Therefore, it has been deduced that the model could have a physical meaning only when T°$\leq 50°C$ and $h_R < 0.35$.

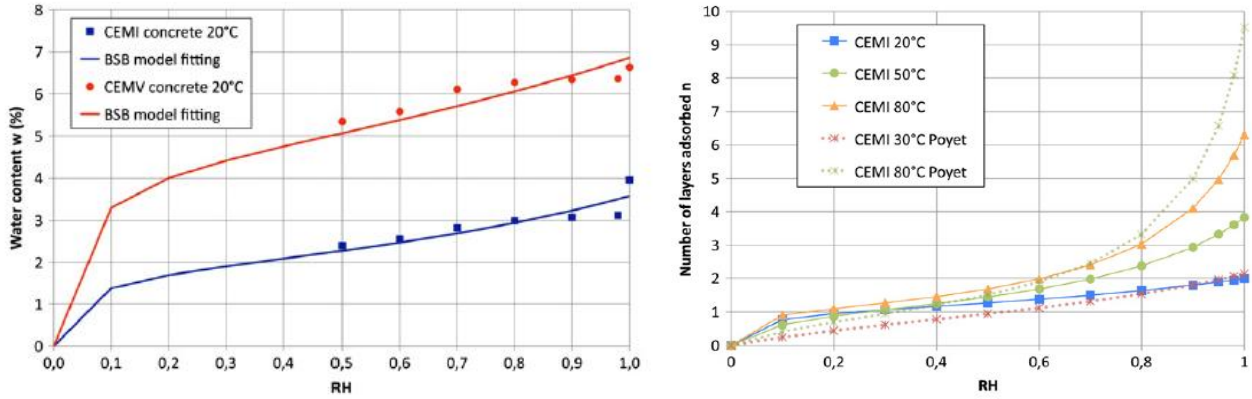

Fig. 2-18 – left: the BSB or GAB model used by Brue et al. (2012) to model the desorption isotherm of a high-performance CEM I concrete at 20°C - right: number of adsorbed layers

More recently, the numerical model of Van Genuchten (1980) was developed. The Van Genuchten model (Van Genuchten and Nielsen, 1985; Van Genuchten, 1980), was originally developed for soils but it was also widely applied for cementitious materials (Carlier and Burlion, 2010; Poyet, 2016). In its initial form, this model has been proposed to model drainage tests, where capillary pressure (liquid and gas pressure) is imposed on one end of the sample as an experimental boundary condition. Thus, the model can be expressed in an equivalent way as a function depending on the water column h or the capillary pressure P_C both linked by Jurin's law:

$$S_e = \frac{w - w_r}{w_s - w_r} = (1 + (\alpha h)^n)^{-m} \quad (2\text{-}21)$$

S_e is the dimensionless water content or effective saturation as defined by Van Genuchten (1980), w_r is the residual moisture content of the dried sample, w_s the water content of the saturated sample, α, n, m are the model parameters with $n \geq 1$. We can observe that Van Genuchten (1980) introduced the concept of residual water content. This refers to the presence of water in the dry sample, so that S_e= 0 for $w = w_r$. Moreover, the maximum saturation S_e=1 is obtained for for $w = w_s$, w_s being the extreme point of the desorption isotherm. Equivalently, one can formulate equation (2-21) as a function of the capillary pressure and the degree of saturation $S_w = w/w_s$. This has been done previously by many authors as Kébré et al. (2013) and Poyet (2016). Hence, h is replaced by the expression given by Jurin law (equation (2-8)). $S_r = w_r \,/\, w_s$ is the residual saturation. We find:

$$S_e = \frac{S_w - S_r}{1 - S_r} = \left(1 + \left(\frac{P_C}{P_r}\right)^n\right)^{-m} \quad (2\text{-}22)$$

Van Genuchten's work has also concerned hydraulic transfer properties (covered in chapter 3). In this framework, in accordance with the works of Mualem (1976), he proposes the following relationship: $= 1 - 1/n$. This relationship limits the number of parameters needed but it is alleged to limit the flexibility of the model (Van Genuchten and Nielsen, 1985). Moreover, other authors such as Kébré et al. (2013) insist on the fact that the independence between *m* and *n* is necessary for a flexibility that describe the behavior of certain materials (such as soils). On another hand, it should be noted that Poyet (2016) used equation (2-22) to fit water retention curves of hardened cement pastes at different temperature (going from 10°C to 75°C). It has been observed by the author that the parameter *m (*or *n)* had a constant value regardless of the temperature considered.

In the current framework, we are interested in the mechanisms solicited by water vapor sorption in a humid environment, for this reason the logical variable to express the experimental retention curves with is the relative humidity, i.e. the variable controlled in the experiment. For the same reason, in practice several authors like Carlier and Burlion (2010) and Morandeau et al. (2014) express Van Genuchten's model as a function of relative humidity using Kelvin's law (2-9), with the following formulation:

$$S_e = \frac{S_w - S_r}{1 - S_r} = (1 + (-c \ln(h_R))^{\mathrm{n}})^{-\mathrm{m}} \quad (2\text{-}23)$$

It is important to note that in the previous equation: when $h_R \to 1$, $S_e = 1$ and when $h_R \to 0$, $S_e = 0$.

The limitation of the Van Genuchten (1980) model for cementitious materials has been highlighted by Carlier and Burlion (2010). In fact, by carrying out desorption tests on mortars and cement pastes, the authors showed that the Van Genuchten model is insufficient to describe the behavior of these materials, over the whole saturation range tested. Therefore, the authors used an alternative model to model water retention: the Durner (1994) model. This model combines as many Van Genuchten curves as the number of identified pore modes. Thus, the Durner relation given by (2-24) is a combination of the Van Genuchten relation, weighted by w_i parameters (with $\sum_{i=1}^{k} w_i = 1$):

$$S_e = \sum_{i=1}^{k} w_i \left(1 + \left(-c_i \, ln(HR)\right)^{n_i}\right)^{-m_i} \quad (2\text{-}24)$$

Durner's model has also recently been used to model water retention of other porous materials such as soils (Alfaro Soto and Chang, 2015) and multiple types of wood (Kang and Chung, 2009). However, in spite of its efficiency, it should be note that the Durner model could present a large number of parameters to fit. The interest of its use would appear remarkable only in the case where a large number of desorption experimental points is available.

2.1.7. Conclusions

The modelling of water transfer inside the concrete depends on the microstructure of this porous material. In this section (section 2.1), the porous structure of concrete and the difference between the various forms of water (bound, adsorbed, free) present in the latter are introduced.

On another hand, the various phenomena (sorption and desorption) that take place when the concrete is exposed to a humid environment were explained. It was shown that when a surface of a solid is exposed to a moist air, the number of water molecules to be gained/lost by the surface is a function of the partial pressure of water vapor (i.e. relative humidity). The sorption or desorption phenomena can be described using corresponding isotherms that allow to characterize the thermo hydric equilibrium state of the material.

Based on sorption and desorption isotherms, multiple methods for the characterization of the pore sizes distribution of porous materials were detailed in section 2.1.5.2. Finally, numerous models for the representation of those isotherms found in the literature are presented in section 2.1.6. Among those models, the Van Genuchten (1980), Durner (1994), GAB and Pickett models were presented since they have previously made it possible to describe the desorption of cementitious materials in a fairly representative manner

2.2. Experimental desorption isotherm of the F44Adj concrete

The experimental tests presented in this section are part of the large experimental campaign mentioned in Chapter 1 in order to verify the acceptability for storage of the C1PG^{SP} packages and more specifically to characterize the F44Adj concrete properties. The tests presented in this section were carried out at the civil engineering laboratory of EDF R&D, MMC department, located at Les Renardières, Moret-sur-loing, France.

The main aim of the tests presented in this section is to determine experimental desorption isotherms of the F44Adj concrete, since they are a major input data for modelling its hygral behavior. To that purpose, two commonly known water vapor sorption/desorption techniques were used. The first one employs saturated salt solutions (SSS), the second one is the Dynamic Vapor Sorption (DVS) technique. Both tests were carried out at a room temperature of 20°C and then at a controlled temperature of 50°C.

2.2.1. Material composition and conditioning

The tested material is the F44Adj concrete used for the fabrication of the C1PG^{SP} packages. The material composition is given by Table 2-1.

Constituents	Composition (kg/m^3)
CEMI 52.5 N	400
Silica fume	40
Filler C4	15
Sand BB 2/4	146
Sand HN 0.6/1.6	234
Sand HN 0.4/0.8	117
Sand HN 31	117
Sand HN38	117
Gravel 2/8	255
Gravel 8/19	890
Superplasticizer	3.8
Water	138

Table 2-1 – Composition of F44Adj concrete

A total number of 30 concrete samples with a dimension of 7x7x28(cm) were fabricated on 06/2017 at the EDF – MMC Laboratories. These samples were used for multiple tests in the above described experimental campaign. Once unmolded, the samples were put in autogenous conditions: they were covered with a sealed bag and then placed in two hermetically sealed containers (Fig. 2-19). Five of those samples (used for this desorption test) stayed in autogenous conditions for 371 days. This period is supposed to be sufficient to ensure a complete hydration of the concrete. Indeed, a similar duration for concrete maturation has been used by Baroghel-Bouny et al. (1999). The author, after measuring the evolution of the internal relative humidity inside a high performance concrete for a period of two years, showed that no remarkable evolution of the latter is seen after 1 year.

The main reason behind the choice of an autogenous conservation before running the experimental tests was to represent at best the drying state of the real concrete package before being disposed of at the storage facility. Another important choice had to be made regarding the time between the pouring of the concrete samples and the beginning of the experimental tests.

Fig. 2-19 – Autogenous conditioning of concrete samples

2.2.2. Measurement of desorption isotherm with saturated salt solution (SSS) technique

2.2.2.1. Sample fabrication

Regarding the experimental desorption tests, once received at the EDF-MMC laboratory. 5 samples of 7x7x28(cm) were used and cut into 36 samples of 7x7x1(cm) and 12 samples of 7x7x3(cm) before being used for the characterization of the concrete with the saturated salt solution technique. Each 28 cm height sample was cut into multiple 1 cm or 3 cm height samples using a circular saw blade. The sawing of samples was carried out smoothly to avoid as much as possible damaging the material (i.e. micro cracks formation).

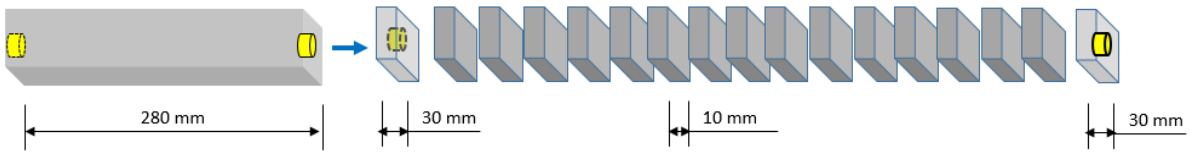

Fig. 2-20 - Fabrication of 7x7x1(cm) samples

In this study, the chosen thickness of the samples (1 or 3 cm) may appear far from the usually recommended thickness (3 times bigger than the biggest granulate which gives a minimum of 5 cm thickness). However, the 1cm thickness of the samples was chosen to obtain moisture equilibrium in a reasonable duration. The 3cm thickness was chosen for representativity comparison purposes. Small samples thicknesses (down to 1cm) for water vapor sorption tests were also used by Baroghel-Bouny et al.(1999) for similar purposes.

For the purpose of verifying whether the fabrication process of the small samples induced or not some micro-cracking of the concrete prior to the running of the tests, the porosity and dry/saturated densities of these samples are assessed at the end of the tests. The latter are compared to the porosity and density of an intact 7x7x28cm sample that was kept in autogenous conditions for 530 days.

2.2.2.2. Method description

In a general way, water sorption technique using saturated salt solutions (described in the international standard NF EN ISO 1257 (2013) consists in putting an initially saturated, or balanced at a given relative humidity sample in a hermetic desiccator in which the atmosphere is confined to a controlled constant relative humidity using saturated salt solutions. At a given temperature, the relative humidity is usually imposed by increasing (in the case of sorption) or decreasing (in the case of desorption) steps. For each step, the tested samples are periodically weighed until reaching a constant mass (hydric equilibrium). Given that the time needed to reach this equilibrium can be relatively long depending on the imposed increment of relative humidity, in this experimental campaign, it was chosen to submit simultaneously different sets of samples to different relative humidities. Therefore, each desiccator contained a certain saturated salt solution imposing a certain value of relative humidity. In this campaign, the water vapor sorption tests were carried out at two test temperatures: 20°C and 50°C. For that purpose, two climatic chambers for controlling the temperature were used (Fig. 2-21). In each climatic chamber, were placed different desiccators with saturated salt solutions.

Fig. 2-21 – Two climatic chambers used to regulate temperature for the water vapor sorption tests

For the temperature of 20°C, the chosen fixed relative humidities are (98%, 85%, 69%, 58%, 33%, 11%) and for the temperature of 50°C we chose (96%, 81%, 64%, 50%, 30%, 11%). Each relative humidity was fixed inside one desiccator that contained: 3 samples with a thickness of 1 cm and 1 sample with a thickness of 3 cm. The running of simultaneous sorption tests allowed to reduce the experiment time. However, it should be noted that this could induce some test variability given that different samples of the material were tested each time.

The relative humidity within every desiccator depends on the salt concentration of each salt solution. The value of the equilibrium theoretical relative humidity at saturation for various salts at various temperatures is given in Fig. 2-22. It should be noted that the norm NFX15-119, 1999) indicates a temperature variation tolerance of 2°C in the test room and an uncertainty of relative humidity of around 2% to 4%. The temperature condition was monitored and was insured for the entire campaign. In addition, the hygrometry of the saline solutions was controlled using a Rotronic sensor at start-up (at the preparation of solutions), during and at the end of the tests, which made it possible to verify the quality of the salt solutions. Relative humidity values in all desiccators are in compliance with the expected value ranges.

It should be noted that the choice of an initial autogenous state for the tests implies the non-knowledge of the initial relative humidity and the initial saturation state of the samples. However, the initial saturation or water content level could be calculated at the end of the tests by measuring the mass at saturation of each sample in addition to the mass at the dry state. This point will be detailed furtherly in this section.

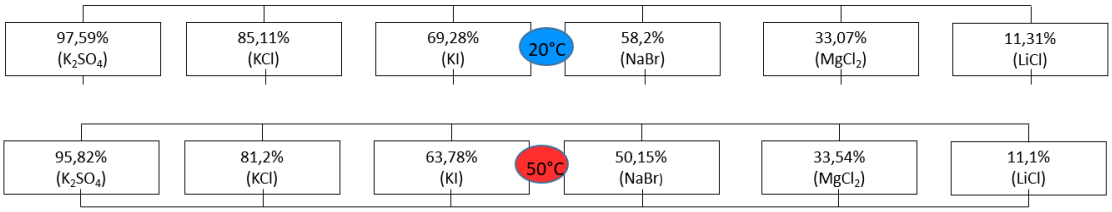

Fig. 2-22 – Theoretical relative humidity at solubility for different used salts at various temperatures

2.2.2.3. Relative mass variations

Using the periodical weighing of the samples, we could temporarily calculate the mean relative mass variation ($\Delta m/m_{ini}$) of the samples following the relation:

$$\frac{\Delta m(t)}{m_{ini}} = \frac{m(t) - m_{ini}}{m_{ini}} \tag{2-25}$$

where $m(t)$ is the mass of the sample at a time *t*, for a fixed temperature and relative humidity and m_{ini} the initial mass of the sample. The results for every temperature and the various studied relative humidities are given in Fig. 2-23 and Fig. 2-24.

We could observe that Fig. 2-23 and Fig. 2-24 show that, for a given relative humidity when the temperature increases the relative mass loss increases (for a relative humidity of 11%, this mass loss is of 2% at a temperature of 20°C, compared to a 2.5% at a temperature of 50°C). This observation shows that, when the temperature increases, the concrete is expected to lose a bigger amount of water. A possible explanation to this phenomenn is given in Drouet et al. (2015) and Poyet and Charles (2009), which link this behavior not only to changes of water properties (density) under the effect of temperature but also to "thermal desorption". This means that, when the temperature increases, we observe a shift of equilibrium between liquid water and vapor towards a bigger partial pressure.

The mass loss kinetic is at its maximum in the first days then it progressively decreases until reaching equilibrium. However, it could be also seen that, at a given relative humidity, the mass reaches equilibrium faster when temperature increases. Indeed, when a relative humidity of 11% is fixed, it takes approximately 200 days to lose 2% of relative mass at a temperature of 20°C. The same amount of relative mass is lost in 13 days at a temperature of 50°C.

The profiles in Fig. 2-23 and Fig. 2-24 make it possible to consider visually a satisfactory steady state for some of the fixed relative humidities in terms of relative mass variation. A calculated criterion to determine whether the equilibrium state has been reached or not can be found in the literature. However this criterion may differ from an author to another. In fact, (Baroghel-Bouny, 1994) states that the mass variation must be lower than 1 mg during three consecutive weeks for a sample with an initial mass bigger than 8g. Daian (1986) indicates a mass variation less than 10 mg in 25 days. Sémété et al.(2017) use a criterion ε_{crit} based on the approach of Johannesson and Janz (2002):

$$\varepsilon_{crit} = \frac{\Delta m(t)}{\Delta t} / m_{ini} \tag{2-26}$$

According to Sémété et al. (2017), based on various experimental observations, this criterion ranged between 2.10^{-4} and 5.10^{-4} (%/day) depending on the author. In the current tests, the criterion of 5.10^{-4} was adopted for all samples at the various relative humidities and temperatures. This criterion was only reached for the relative humidities of (98%, 85%, 69%) at the temperature of 20°C and of (81%, 33%,11%) at the temperature of 50°C. Therefore, in the current framework, only the corresponding equilibrated points will be considered. As for the other fixed relative humidities, the tests are still running until the equilibrated state is reached. The corresponding results will be used in a framework beyond that of the thesis.

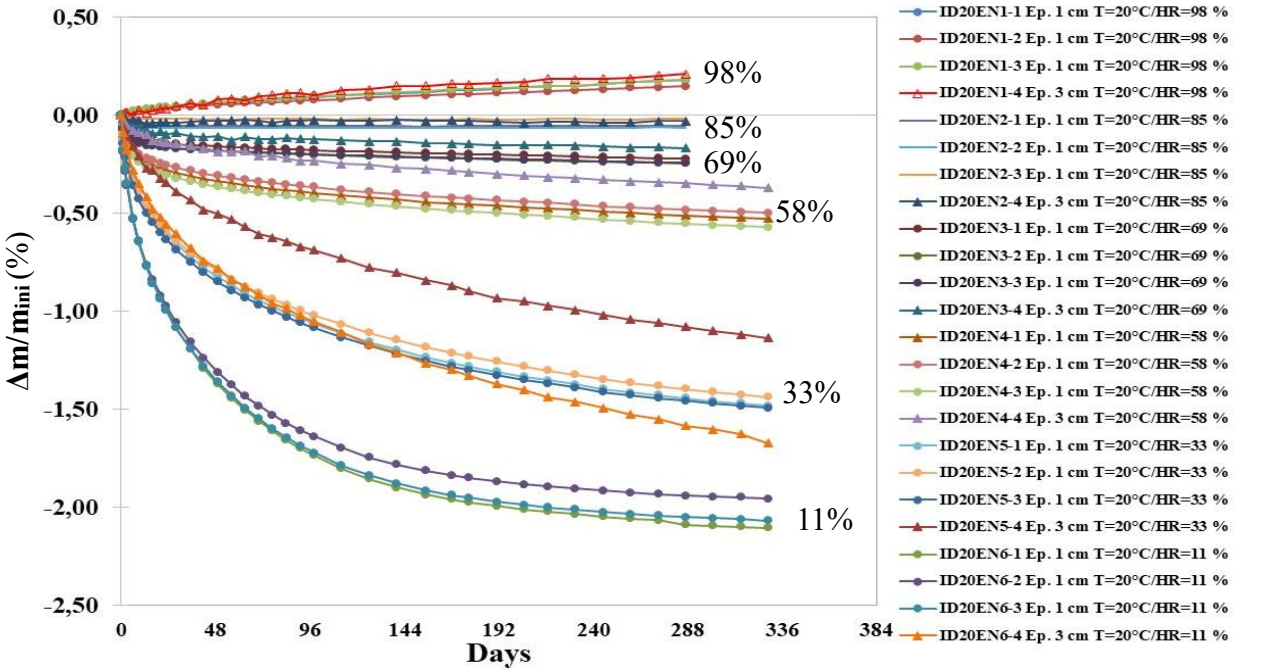

Fig. 2-23 - Mean relative mass variation of the 7x7x1cm and 7x7x3cm samples at the temperature of 20°C

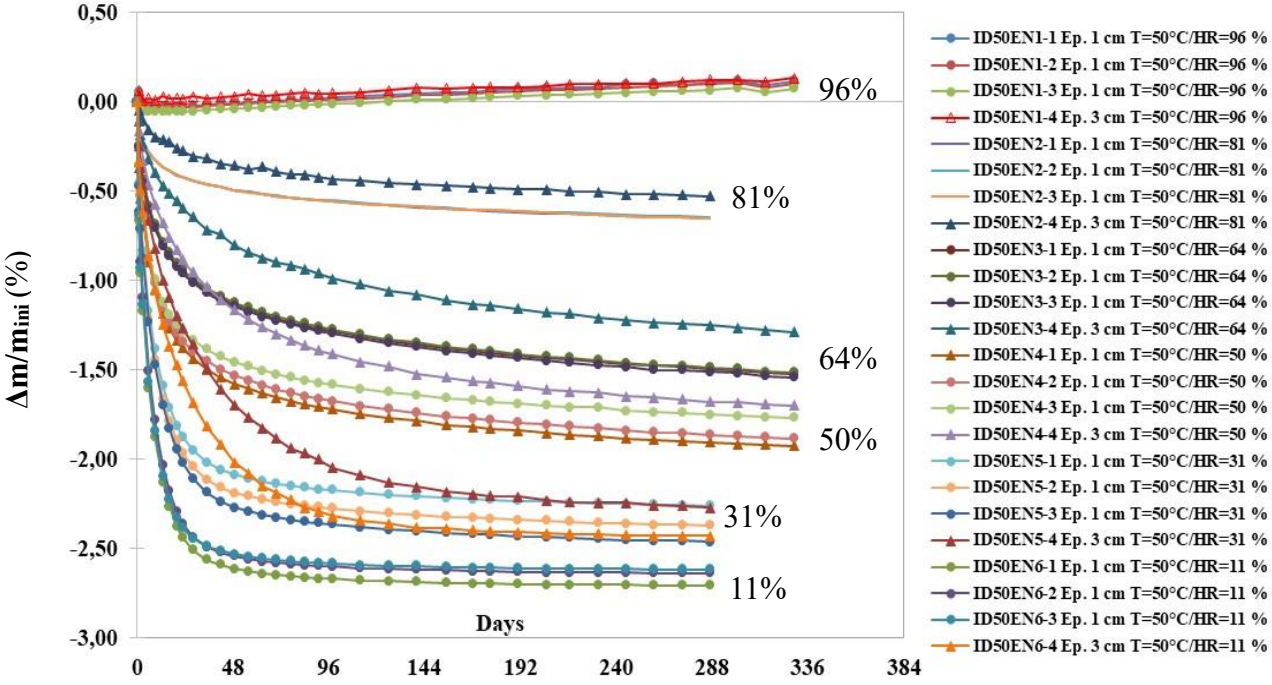

Fig. 2-24 - Mean relative mass variation of the 7x7x1cm and 7x7x3cm samples at the temperature of 50°C

Finally, it is important to note that for a temperature of 20°C and a relative humidity of approximately 85%, the concrete neither loses nor gains any amount of water. This could lead to the conclusion that the initial autogenous state corresponds, at a temperature of 20°C, to a relative humidity of 85%. On another hand, for the temperature of 50°C, the initial autogenous state will correspond to a relative humidity between 81% and 96%.

2.2.2.4. Concrete desorption isotherm – water content vs relative humidity

The results are given in this section in terms of the water content w. However, it should be noted that the poromechanical models ((Biot, 1941); (Coussy et al., 2003)) require transfer equations to be written in terms of the saturation degree S_w. The concrete desorption isotherm function of S_w will be given later in this section (section 2.2.2.6).

The water content for each thermo hydric equilibrium state could be calculated using equation (2-4). This assessment could be made only if the dry masses of the multiple samples are at disposal. For that purpose, once the desorption tests are accomplished, the samples were saturated in a vacuum sealed container and then the mass of the saturated samples is measured. The samples are then submitted to an oven drying under a temperature of 60°C and then under 105 ℃. After each oven drying, the samples were weighed. For each drying temperature, when the absolute change in mass is less than 0.05% between two 24-hour weighing operations, the dry mass of the sample is considered to be reached (Protocol of GranDubé (Arliguie, 2007)).The drying temperature of 60°C gave, for some of the samples tested previously at a temperature of 50°C, inconsistent values of their dry mass , which sometimes appears to be bigger than the equilibrated mass of the sample at 50°C due to measurement errors. Such values could lead to negative values for the calculated water content. Therefore, it was decided that under the current framework and given that tests for a temperature close to 60°C (T=50°C) have to be done, only the dry mass at 105°C will be considered for further calculations. Moreover, it is important to note that a drying temperature of 105°C is also indicated in the norm NF P18-459 (2010).

The equilibrated water contents for the equilibrated relative humidity levels and temperatures of 20°C and 50°C are given in Fig. 2-25. In Fig. 2-25, for each relative humidity and temperature, the mean calculated value of the water content for the three samples of 1cm thickness is presented and compared to that of the 3cm sample. As it could be seen, both values are very close. This could be a possible indication of a good representativity of the 1cm samples thickness. However, this claim will be furtherly discussed in the following section. It is important to note that the calculated water contents of saturation for a relative humidity near 98% and for T=20°C represent a sorption equilibrium state of the concrete rather than a desorption state. Therefore, in all further presented isotherms, this equilibrated point will be presented with a different (orange) color than those of the other equilibrated points.

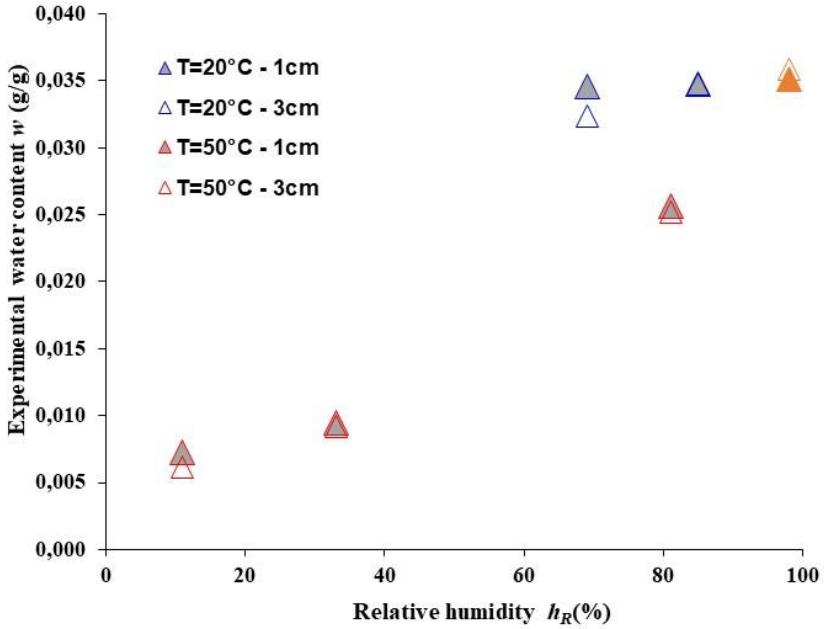

Fig. 2-25 – Desorption isotherms $w(h_R)$ of the F44Adj concrete at a temperature of 20° and 50°C

2.2.2.5. Porosity and density assessment

Once the samples are dried at the end of the SSS tests and weighed, the samples are saturated in a vacuum sealed container and then the mass of the saturated samples is measured. Once both the dry mass and saturated mass are measured, we can then calculate the corresponding porosity $\emptyset$, dry densities ρ_{dry} and saturated densities ρ_{sat} of each sample. Let us remind that the porosity can be determined with equation (2-3) with V_t the volume of the sample equal to $\frac{1}{\rho_w}(m_{sat} - m_{under\ water})$ and $m_{under\ water}$ being the mass of the sample measured when the latter is immersed in water. Thus we can write:

$$\emptyset = \frac{m_{sat} - m_{dry}}{m_{sat} - m_{under\ water}} \tag{2-27}$$

The corresponding values of the porosities and densities for the 7x7x1 and 7x7x3 samples tested at 20°C and 50°C are given respectively by Table 2-2 and Table 2-3.

	Mean values for 7x7x1 samples			Values for the 7x7x3 samples		
T = 20°C	$\emptyset$	ρ_{dry}(kg/m^3)	ρ_{sat}(kg/m^3)	$\emptyset$	ρ_{dry}(kg/m^3)	ρ_{sat}(kg/m^3)
h_R = 98%	9.13	2395	2483	9.05	2382	2473
h_R= 85%	9.24	2386	2476	8.67	2381	2468
h_R= 69%	9.65	2368	2466	8.53	2384	2470

Table 2-2 - Porosity, dry and saturated densities of the 7x7x1/3cm samples tested at 20°C

	Mean values for 7x7x1 samples			Values for the 7x7x3 samples		
T = 50°C	$\emptyset$	ρ_{dry}(kg/m^3)	ρ_{sat}(kg/m^3)	$\emptyset$	ρ_{dry}(kg/m^3)	ρ_{sat}(kg/m^3)
h_R= 81%	9.12	2400	2491	8.68	2393	2480
h_R=33%	9.38	2389	2483	9.20	2387	2479
h_R= 11%	9.52	2384	2479	8.87	2406	2495

Table 2-3- Porosity, dry and saturated densities of the 7x7x1/3cm samples tested at 50°C

As we could see, when submitted to a same thermos-hydric condition, the relative difference between the porosities of the 1cm thickness samples and those of 3cm is in average 5% with a bigger porosity for the 1cm samples. This difference is of 0.08% for the saturated density and of 0.07% for the dry density with a bigger saturated and dry density for the 1cm samples.

As for the 7x7x28 sample that was kept in autogenous conditions for the whole time of test and that was not submitted to any fabrication (sawing) process, its corresponding measured porosity is 7.5%, the dry saturated density is 2432 kg/m^3 and the saturated density is 2509 kg/m^3. At first, we can try explaining the difference of approximately 28% found in terms of porosities, between the biggest porosity of the 7x7x1cm samples and that of the 7x7x28cm intact sample, by the fact that the 7x7x1cm samples once sawed, were submitted to drying conditions during a certain amount of time contrary to the 7x7x28cm sample kept sealed in autogenous conditions.

Under the latter storage conditions, the 7x7x28cm sample might mature faster than the smaller samples. This can result in a porosity of the 7x7x28cm samples smaller than that of the 7x7x1cm and 7x7x3cm samples. If the difference observed in terms of porosity is only linked to the degree of hydration of the compared samples, then we expect an identical porosity for the 7x7x28cm ($\emptyset$ = 7.5%) and for the 7x7x1cm (or 7x7x3cm) samples submitted to a relative humidity of 85% , which corresponds approximately to an autogenous condition (see section 2.2.2.3). By referring to Table 2-2, we observe that this is not the case: the 7x7x1cm samples present an average porosity of 9.24% and the 7x7x3cm sample presents a porosity of 8.67%. The latter observation drives us to search for other possible explanations for the found differences.

In what follows, two possible explanations (scenarios) for the inconsistencies of the results are given: the first one is linked to a probable insufficient drying and saturation of the 7x7x28cm sample and the second one is a probable micro-cracks formation in the small samples following their fabrication process (sawing). The impact of the two considered scenarios on the results of this test is given in the following section. Corresponding corrections are eventually proposed in section 2.2.2.6.

2.2.2.6. Correction of the desorption isotherm – degree of saturation vs relative humidity

According to what has been said previously, in this section we compare two possible scenarios that could be responsible for the difference seen in terms of porosity and densities between the 7x7x1cm, 7x7x3cm and 7x7x28cm samples.

Scenario 1: Insufficient drying and saturation of the 7x7x28cm

This scenario considers that the dried or saturated mass of the 7x7x28cm sample was not correctly assessed. In fact, a sample (regardless of its dimension) is considered to be dried or saturated in this experimental campaign once the absolute variation in mass between two consecutive measures separated by 24 hours is 0.05%. Our hypothesis in this scenario is that due to its bigger size, the 7x7x28cm sample was not completely dried/saturated once the criterion is reached. The wrong assessment of the dried and saturated mass of this sample will lead to a wrong assessment of the calculated porosity. In the purpose of verifying this statement, we compare the initial, saturated, dry density and porosity of the 7x7x28cm sample with those of a 7x7x3cm sample and a 7x7x1cm sample submitted to a temperature of 20°C and a relative humidity of 85% (corresponding approximately to an autogenous condition – see section 2.2.2.3):

Sample	$\rho_{ini}(kg/m^3)$	$\rho_{sat}(kg/m^3)$	$\Delta\rho_{ini-sat}(\%)$	$\rho_{dry}(kg/m^3)$	$\Delta\rho_{ini-dry}(\%)$	∅
7x7x28cm	2503	2509	0.24	2432	-2.8	7.5%
7x7x3cm	2461	2468	0.28	2381	-3.2	8.67%
7x7x1cm	2468	2477	0.36	2383	-3.4	9.43%

Table 2-4 – Comparison between the porosity and density of a 7x7x28cm sample and a 7x7x1(3)cm sample

In Table 2-4, $\Delta\rho_{init-sat}$ is the relative variation between the initial and saturated density of the sample and is calculated as follows: $\Delta\rho_{init-sat} = \left(\frac{\rho_{sat}-\rho_{ini}}{\rho_{ini}}\right)$. Moreover, $\Delta\rho_{init-dry}$ is the relative variation between the initial and dry density of the sample and is calculated as follows: $\Delta\rho_{init-dry} = \left(\frac{\rho_{dry}-\rho_{ini}}{\rho_{ini}}\right)$. As we can observe, the absolute value of relative variations between the initial and saturated state and between the initial and dry state increase when the sample has a smaller size. This could verify that the 7x7x3cm and 7x7x28cm samples may have not been fully dried and fully saturated.

While considering that the 7x7x1cm samples have been fully saturated and dried, we aim to correct the porosities and densities of the 7x7x3cm samples and the 7x7x28cm sample. In what follows (equation (2-28)), we show this correction applied to the 7x7x28cm sample. The same correction was also applied on the 7x7x3cm sample. According to equation (2-3), we write:

$$\emptyset_{7x7x28,corr} = \frac{\rho_{sat,corr} - \rho_{dry,corr}}{\rho_w} \tag{2-28}$$

$\rho_{sat,corr}$ and $\rho_{dry,corr}$ are the corrected saturated and dry density of the 7x7x28cm sample. We consider that, in perfect drying/saturation conditions, this sample must loose/gain the same amount of water loosed/gained while drying/saturating the 7x7x1cm sample. Those densities are calculated as follows:

- $\rho_{sat,corr} = \rho_{ini,7x7x28} + 0.36\%\rho_{ini,7x7x28} = 2512$ kg/m^3. 0.36% is the average relative amount of water gained by the 7x7x1cm samples while being saturated (see Table 2-4).
- $\rho_{dry,corr} = \rho_{ini} - 3.4\%\rho_{ini} = 2417$ kg/m^3. 3.4% is the average relative amount of water lost by the 7x7x1 samples while being dried (see Table 2-4).
- This will lead to $\emptyset_{7x7x28,corrected} = 9.5\%$ which is equal to that of the 7x7x1 sample (see Table 2-4).

This scenario indicates that the criterion for saturating and drying the samples bigger than the 7x7x1cm samples was not strict enough which led to samples which were not yet saturated/dried. Indeed, a wrong criterion may lead to an under-estimation of the porosity and an overestimation of the degree of saturation (where the saturated and dry masses intervene).

The desorption isotherm in terms of the degree of saturation, for the 7x7x1cm samples, will be calculated with equation (2-5). As for the 7x7x3cm samples, their corrected saturation degree is calculated according to equation (2-5) in terms of densities (see equation 2-29):

$$S_{w,corr} = \frac{\rho(h_R) - \rho_{dry,corr}}{\rho_{sat,corr} - \rho_{dry,corr}} \tag{2-29}$$

$\rho_{sat,corr}$ and $\rho_{dry,corr}$ are the corrected saturated densities of the 7x7x3cm samples (as corrected before for the 7x7x28cm sample), $\rho(h_R) = \rho_{ini} + \Delta\rho(t) = \rho_{ini} + \frac{\Delta m(h_R)}{V_0}$ with $\Delta m(h_R)$ the measured mass loss (or gain) of the 7x7x3cm in order to reach equilibrium and V_0 the volume of the sample. The corrected desorption isotherms for both temperatures of 20°C and 50°C are given in Fig. 2-26. In Fig. 2-26, are presented the average degrees of saturation for both thicknesses (1cm and 3cm).

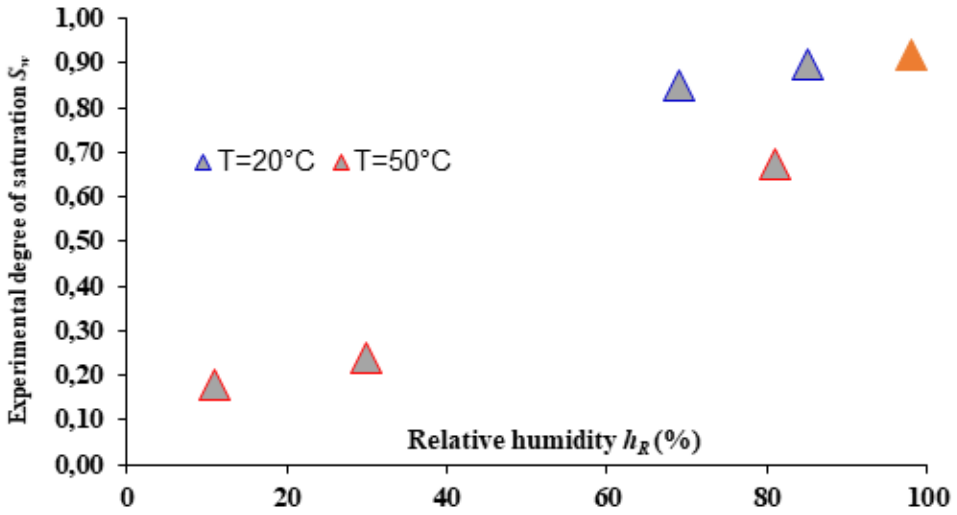

Fig. 2-26 – Desorption isotherms $S_w(h_R)$ of the F44Adj concrete at a temperature of 20° and 50°C

Scenario 2: Micro-crack formation in the 7x7x1cm and 7x7x3cm samples

This scenario considers that a probable micro-crack formation in the small samples (due to their fabrication process) might have been the main reason for the difference observed in terms of porosity and densities between the sawed small samples and the 7x7x28cm sample. In fact, if we consider that a small micro-crack of volume V_{crack} was formed at the beginning of the desorption tests in the 7x7x1cm and 7x7x3cm samples, this will eventually lead to a bigger measured value for the saturated mass of those samples at the end of the desorption test and a bigger measured value for the volume of this sample (see Fig. 2-27).

In Fig. 2-27, $m_{sat,0}$ and V_0 are respectively the saturated mass and the volume measured at the end of the desorption test, of a 7x7x1cm(or 7x7x3cm) sample where no micro-crack is present; whereas $m_{sat,7x7x1/3}$ and $V_{7x7x1/3}$ are the saturated mass and the volume, measured at the end of the desorption test, of a 7x7x1cm(or 7x7x3cm) sample where a micro-crack is present;

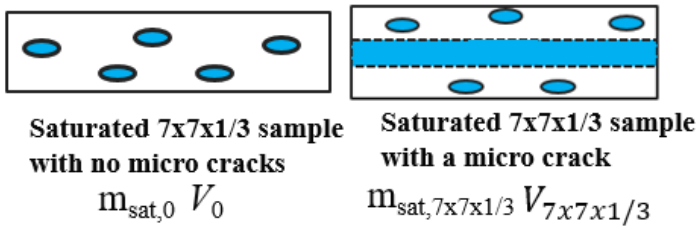

$$m_{sat,7x7x1/3} = m_{sat,0} + \rho_w \cdot V_{crack}$$
$$V_{7x7x1/3} = V_0 + V_{crack}$$

Fig. 2-27 – Impact of a micro-crack formation on the saturated mass and the volume of a 7x7x1 or a 7x7x3 sample

Eventually, those measurements could lead to an overestimation of the porosity (where the value of the saturated mass intervenes) and an underestimation of the saturated density (where both the values of the saturated mass and the volume of the sample intervene). To verify such an allegation, let us consider that the 7x7x3cm sample submitted to a 98% relative humidity and a temperature of 20°C presented at the beginning of the tests a micro-crack with a volume of x% of the initial (before any cracking occurred) volume V_0 of this sample (see Fig. 2-27). This sample presents the measured initial mass $m_{i,7x7x3}$, saturated mass $m_{sat,7x7x3}$, dry mass $m_{dry,7x7x3}$ and volume V_{7x7x3}, given in Table 2-5.

$m_{i,7x7x3}$(kg)	$m_{sat,7x7x3}$(kg)	$m_{dry,7x7x3}$(kg)	$m_{under\ water\ 7x7x3}$(kg)	V_{7x7x3}(mm^3)
0.363	0.364	0.351	0.218	147000

Table 2-5 - Mass and volume of a 7x7x3 sample

For instance, let us consider that the volume of the micro-crack is of 1.5% V_0 *(x = 1.5),* hence we could estimate from Table 2-5 a value for V_0 and $m_{sat,0}$(the saturated mass if no cracking occurred) by writing:

- $m_{sat,7x7x3} = m_{sat,0} + \rho_w \cdot 0{,}015 \cdot V_0$
- $V_{7x7x3} = V_0 + 0{,}015 \cdot V_0$
- $m_{under\ water,0} = m_{sat,0} - \rho_w \cdot V_0$

The above estimations lead to $m_{sat,0}$ = 0.362 kg, $m_{under\ water,0}$ = 0.21 kg and V_0 = 144827 mm^3. By using equation (2-27) and considering that the measurement of the dry mass m_{dry} is not affected by the micro crack, the calculated values ($m_{sat,0}$, $m_{under\ water,0}$) will lead to a porosity of 7.6% and saturated density $\rho_{sat} = m_{sat,0}/V_0$ =2504 kg/m^3. The latter two values are very close to the porosity and saturated density of the 7x7x28cm intact sample (see Table 2-4). This could verify that a micro-crack (with a certain volume x%.V_0) formed while fabricating the 7x7x3cm or 7x7x1cm samples could eventually lead to an increase of the measured porosity and a decrease in the measured saturated density.

The comparison of porosities and densities done in this section, allows us to conclude that one should be careful while measuring them on samples that have been subjected earlier to either a fabrication process or to a drying/wetting test. This could lead to a wrong assessment of their values, especially if the sample developed some micro-crack during the fabrication process or during the drying test. Moreover, one should be careful while calculating furtherly a degree of saturation for similar samples. As a matter of fact, a wrong assessment of the saturated mass of a sample can lead to erroneous values for the measured saturation degree. According to equation (2-5), the calculation

of the degree of saturation of each of the 7x7x1cm and 7x7x3cm samples is done with the following equation:

$$S_{w,7x7x1/3} = \frac{m(h_R)_{7x7x1/3} - m_{dry,7x7x1/3}}{m_{sat,7x7x1/3} - m_{dry„7x7x1/3}} \quad (2\text{-}30)$$

For further comparison purposes, we write equation (2-5) in terms of mass densities (by dividing all masses with the corresponding measured volume of the 7x7x1cm and 7x7x3cm samples noted as $V_{7x7x1/3}$):

$$S_{w,7x7x1/3} = \frac{\rho(h_R)_{7x7x1/3} - \rho_{dry,7x7x1/3}}{\rho_{sat,7x7x1/3} - \rho_{dry„7x7x1/3}} \quad (2\text{-}31)$$

However, consistently with the considered scenario 2, the measured volume of the samples $V_{7x7x1/3}$ and their measured saturated mass $m_{sat,7x7x1/3}$ accounts for a certain volume of micro-cracks which leads to an erroneous value of $S_{w,7x7x1/3}$. Therefore, if we aim to calculate a correct value for the degree of saturation, $m_{sat,7x7x1/3}$ should be substituted by $m_{sat,0}$ in equation (2-30) and then all masses should be divided by a volume V_0 (the volume excluding the volume of the micro-cracks):

$$S_{w,corr} = \frac{\frac{m(h_R)_{7x7x1/3}}{V_0} - \frac{m_{dry,7x7x1/3}}{V_0}}{\frac{m_{sat,0}}{V_0} - \frac{m_{dry,7x7x1/3}}{V_0}} \quad (2\text{-}32)$$

The terms in equation (2-32) are the densities of the 7x7x1cm and 7x7x3cm samples if no micro-cracks have occurred. We consider that saturated and dry densities present in equation (2-32) are equal to those of the 7x7x28cm sample kept in autogenous conditions and so equation (2-32) is written as:

$$S_{w,corr} = \frac{\rho_{corr}(h_R) - \rho_{dry,endo}}{\rho_{sat,endo} - \rho_{dry,endo}} \quad (2\text{-}33)$$

with $\rho_{dry,endo}$ the dry density of the 7x7x28 sample kept in autogenous conditions (equal to 2432 kg/m^3), $\rho_{sat,endo}$ its saturated density (equal to 2504 kg/m^3), $\rho_{corr}(h_R)$ is the corrected density at equilibrium for an imposed value of relative humidity of the 7x7x1cm or 7x7x3cm samples. $\rho_{corr}(h_R)$ is written as:

$$\rho_{corr}(h_R) = \frac{m(h_R)_{7x7x1/3}}{V_0} \quad (2\text{-}34)$$

$m(h_R)_{7x7x1/3}$ is the mass of each sample when the equilibrium state is reached (evaluated from the SSS tests - Fig. 2-23 and Fig. 2-24). Unlike the volume of the samples, this mass $m(h_R)_{7x7x1/3}$ is not corrected due to the presence of micro cracks. In fact, we consider that the micro-cracks (big pores) in contact with the moist air remains free of water during the whole tests and thus does not participate in the mass equilibrium of water in the sample. As for V_0, an estimation could be done from the initial state of the samples while taking:

$$V_0 = \frac{\rho_{ini,endo}}{m_{ini}} \quad (2\text{-}35)$$

$\rho_{ini,endo}$ is the initial density of the 7x7x1/3 sample (considered to be equal to that of the autogenous sample = 2504 kg/m^3) and m_{ini} the measured mass of the 7x7x1/3 sample at the beginning of the tests. For each equilibrated state and each sample of 7x7x1cm and 7x7x3cm, equations (2-33), (2-34) and (2-35) are applied.

The average obtained desorption isotherm for both thicknesses (in terms of the degree of saturation) at T=20°C and T=50°C is given by Fig. 2-28. In Fig. 2-28, is presented also the standard-deviation between the two thicknesses that appears to be very small.

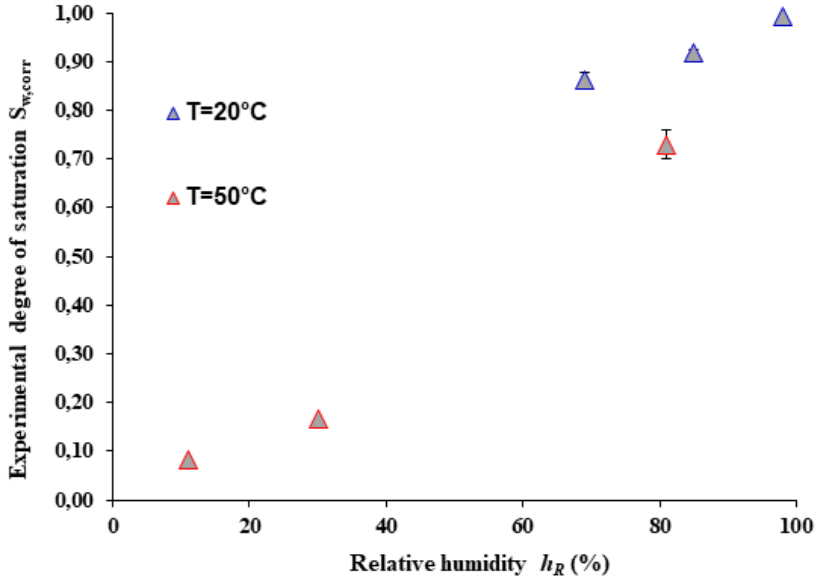

Fig. 2-28 – Corrected desorption isotherms of the F44Adj concrete at T=20°C and 50°C in case of micro crack formation in the 7x7x1cm and 7x7x3cm samples

For calculation purposes, Fig. 2-27 and Fig. 2-28 will be completed by experimental data points from literature in section 2.3.

2.2.3. Measurement of desorption isotherm with dynamic vapor sorption (DVS) technique

2.2.3.1. Sample fabrication

Two 7x7x28cm F44Adj concrete samples that were previously kept in autogenous conditions were used in order to carry out the DVS tests. Each sample was respectively used to prepare concrete powders for the 20°C and 50°C test. It is important to note that for the use of the DVS test on cementitious materials, the main difficulties identified are carbonation and the representativeness of the samples. Regarding the first difficulty, the laboratory is equipped with a Glove Box for preparing powder samples under an inert atmosphere. This glove box is entirely filled with nitrogen gas to avoid the carbonation phenomena. Once the powders are prepared and before beginning the test, deionized water is added to the powders until supernatant water appears.

2.2.3.2. Method description

The DVS balance is an experimental device equipped with a microbalance which allows continuous mass measurement of a sample of material, which in our case of application is previously reduced to powders (a few dozen of milligrams). The microbalance can measure masses up to 1 g and mass changes up to ±150 mg. Fig. 2-29 shows the DVS balance of the EDF R&D laboratory. The microbalance is located in a temperature and humidity controlled chamber (Fig. 2-29 - right). The temperature can be set between 20°C and 85°C and is generated in the entire incubator of the DVS balance. The relative humidity is generated in the test chamber containing the microbalance. For this

purpose, during the test, the sample is exposed to a mixture of dry gas and humidified gas (nitrogen in our case), by passing through a water tank, which generates a relative humidity between 98% and 0%. The condition of 0% relative humidity is obtained using a dry gas. The use of nitrogen as a gas avoids parasitic carbonation during testing of sensitive materials like cementitious ones. It is important to check that, when a given temperature and relative humidity are imposed, the correct value is actually measured in the chamber. Therefore, the DVS has been equipped with a remote acquisition system, consisting of a ROTRONIC sensor installed in the incubator of the DVS balance, a transmitter for recording the measured values of relative humidity and temperature in the incubator and a YOKOGAWA recorder.

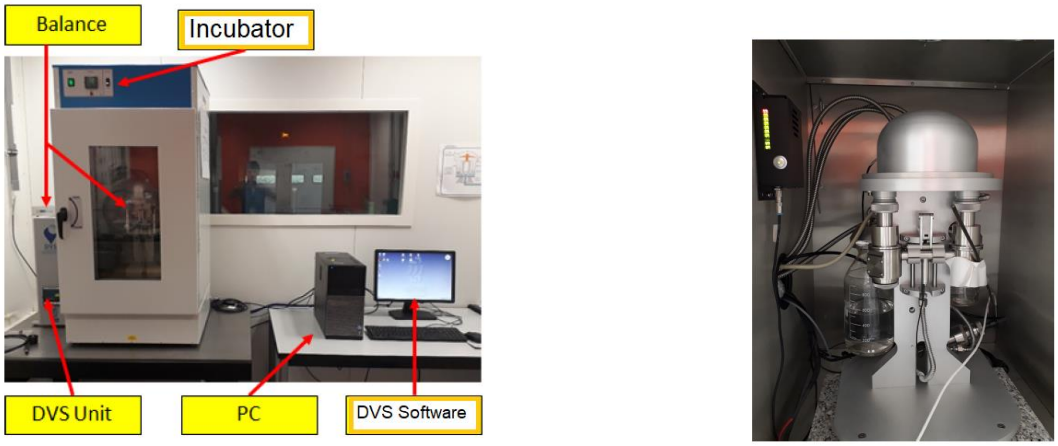

Fig. 2-29 - DVS balance from EDF R&D's GC laboratory. On the overview (left) the term"Balance" refers to the mass data acquisition in the DVS unit and to the microbalance located inside the incubator (right).

2.2.3.3. Experimental protocol

Once the powders are fabricated and introduced in the test chamber, a first relative humidity level of 98% (maximum capacity of the DVS balance) is imposed for a period of 2 days, prior to the launch of the other desorption stages. This provision ensures the removal of the supernatant water brought during the initial saturation of the powder sample. The following stages are driven by an equilibrium criterion in terms of the variation of relative mass per unit of time (given by equation (2-26)). Indeed, equilibrium for a fixed relative humidity is considered to have been reached when the rate of mass change becomes less than 10^{-4} %/min (Poyet et al., 2016). This criterion must be respected for a certain amount of time, in this case 10 mins, and at every instant. This criterion made it possible to optimize the quality and duration of the test. In equation (2-26), m_{ini} represents the initial mass of the sample (considered as the mass at the end of the first 2-day stage at 98% relative humidity). A near zero relative humidity is imposed for 2 days to ensure the best possible drying of the sample, as the dry mass value is used as a reference for the calculation of the isotherm. The calculation of the isotherm is first given in this section in terms of the water content according to equation (2-4) where the mass of the dry sample is its mass at approximately 0% of relative humidity.

2.2.3.4. First desorption isotherm–water content vs relative humidity

The Fig. 2-30 (left) shows the evolution of the mass of one of the samples with respect to the imposed relative humidity for the temperature of 20°C. The effectiveness of the first stage can be seen, with a significant loss of mass corresponding to the elimination of the supernatant water introduced when the sample was previously saturated. In addition, we could visually check the correct mass evolution for the following humidity levels. Fig. 2-30 (right) shows the average water content DVS isotherm obtained with 2 powder samples. Fig. 2-31 shows the DVS results obtained for the temperature of 50°C and for two tested powders that gave similar results.

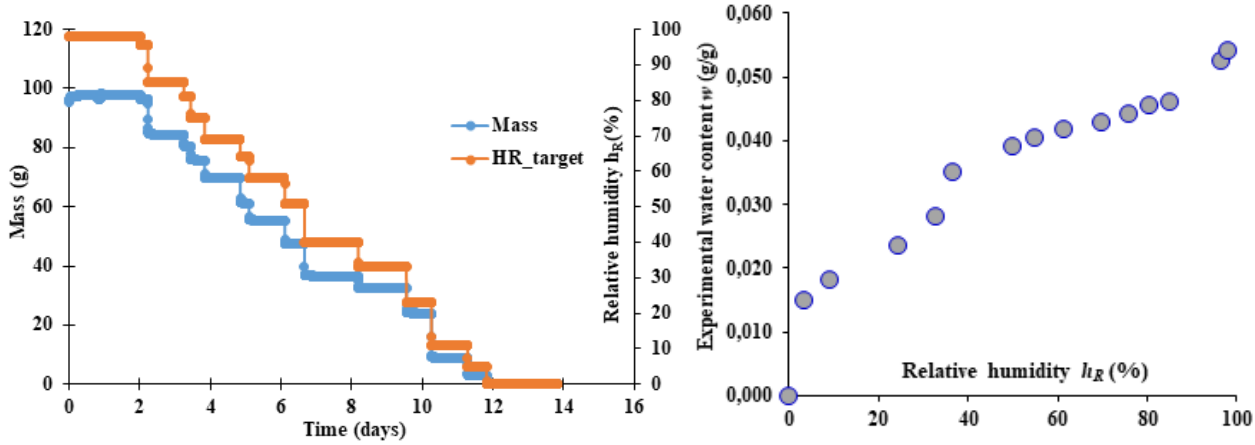

Fig. 2-30 – (left) mass loss (right) DVS desorption isotherm of the F44Adj concrete at T= 20°C

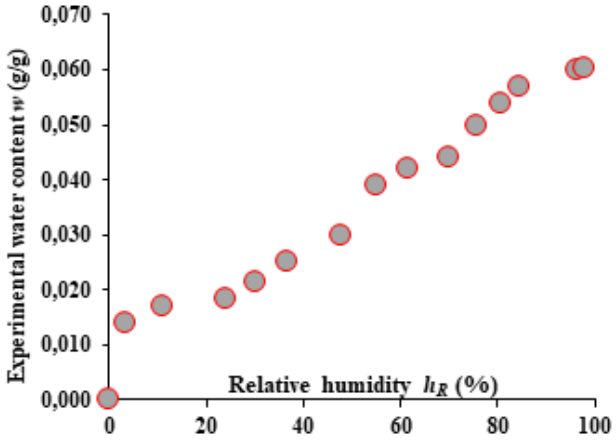

Fig. 2-31–DVS desorption isotherm of the F44Adj concrete at T= 50°C

2.2.4. Comparison of the desorption isotherms obtained with the SSS and the DVS techniques

Once the DVS desorption isotherms are obtained in terms of water content $w(h_R)$, the results are compared with those obtained with the SSS technique. As we can see (Fig. 2-32), for both temperatures, the results $w(h_R)$ obtained with the DVS differ from those obtained with the SSS technique. This may be due to a problem of representativeness of the concrete powder sample used in the DVS technique. This difference was also seen in the works of (Poyet et al., 2016) who suggested to correct this difference by re-calibrating the DVS isotherm with an equilibrated point obtained with the SSS. In their work, Poyet et al. (2016) used an SSS equilibrated point at a relative humidity of 55% to correct the DVS points. The authors wrote that for any relative humidity, the following correction according to equation (2-36) should be done:

$$w_{DVS,corrected}(h_R) = \frac{w_{DVS}(h_R)}{w_{DVS}(h_R = 55\%)} . w_{SSS}(h_R = 55\%) \qquad (2\text{-}36)$$

In the case of this experimental campaign, given that at T=20°C, the point that was the closest to equilibrium obtained with the SSS technique is for a relative humidity of 85%, the latter point (for a chosen thickness of 1cm) is used for the recalibration of the DVS curve (Fig 2-32 – left). At T=50°C, the point corresponding to 81% (for a chosen thickness of 1cm) was used for the recalibration of the DVS curve (Fig 2-32 – right).

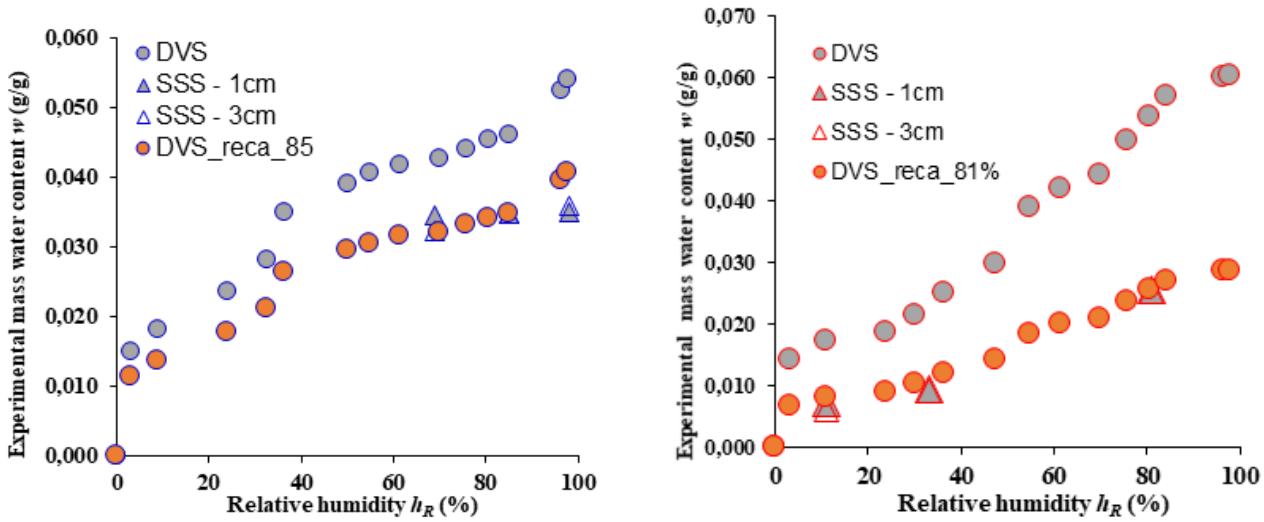

Fig. 2-32 - The DVS isotherm $w(h_R)$ compared with the SSS isotherm for the temperature of T=20°C (left) – and for T=50°C (right)

We proceed to the assessment of the previous DVS isotherms in terms of a saturation degree. This can be done using the formula ($S_w = w \cdot \rho_{dry}/\emptyset \cdot \rho_w$) with ρ_{dry} and $\emptyset$ the porosity of the concrete. In this section, we show the transition from the water content to the degree of saturation only for the scenario 1 of the insufficient saturation and drying of the 7x7x28cm sample (refer to section 2.2.2.6 – Correction of the desorption isotherm). Thus we consider an average porosity $\emptyset$ of 9.2% and an average dry density of 2390 kg/m^3.The result is shown in Fig. 2-33.

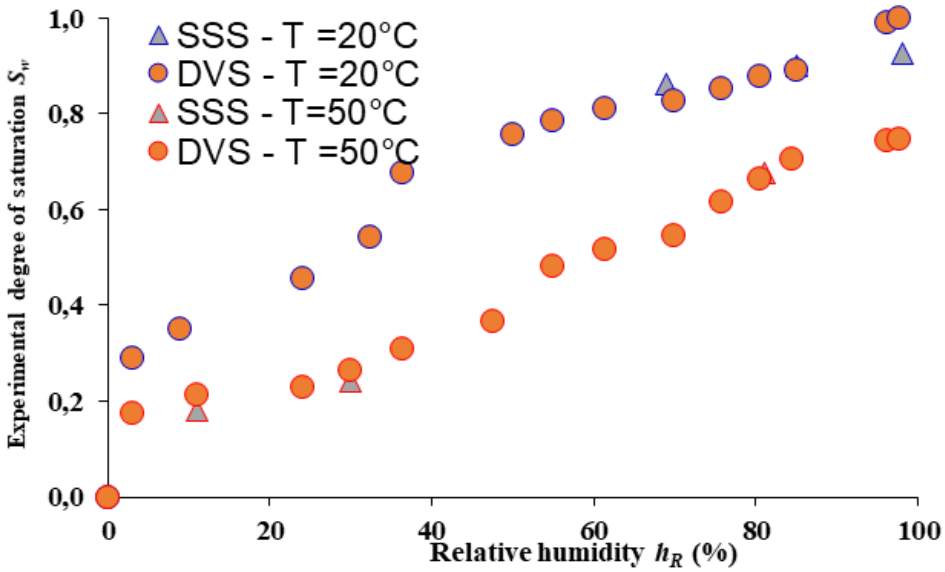

Fig. 2-33 - The DVS isotherm $S_w(h_R)$ compared with the SSS isotherm for the temperature of T=20°C and T=50°C – scenario 1 of the insufficient saturation

Regarding the second considered scenario 2 of micro-cracks formation in the 7x7x1cm and 7x7x3 cm samples, the DVS desorption isotherm in terms of $S_{w,corr}(h_R)$ is shown in Appendix 1.

2.2.5. Conclusions

The experimental desorption test carried out in the EDF-MMC Laboratory for the characterization of the F44Adj concrete at temperatures of 20°C and 50°C were detailed in this section. Two methods were adopted for this purpose: a first method based on the use of salt saturated solutions (SSS) and a second method based on the use of a dynamic vapor sorption (DVS) apparatus.

The samples used for the SSS method were fabricated from 7x7x28cm samples and presented thicknesses of 1cm and 3cm. Those thicknesses were chosen in order to try to obtain a complete desorption isotherm in a reasonable duration. The porosities and densities (dry and saturated) of the 7x7x1 cm and 7x7x3 cm samples were measured at the end of the desorption tests and compared to those of an intact 7x7x28cm sample that was submitted neither to a fabrication process nor to a drying one. Differences between the compared porosities and densities were noted. Two possible explanations for those differences (scenarios) were proposed: scenario 1 of a possible micro-crack formation of the 7x7x1cm and 7x7x3cm samples due to their fabrication process and scenario 2 of a possible insufficiency of saturation and drying of the 7x7x28 cm sample. For each of the latter scenarios, corresponding corrections (section 2.2.2.6) were proposed and led to two possible desorption isotherms. An accurate choice between the latter two scenarios will be done in chapter 3 based on additional experimental data.

As for the DVS test, it was shown that the desorption isotherm obtained with this method is different from that obtained with the SSS method. Therefore, as proposed by Poyet et al.(2016), each DVS curve was re-calibrated based on an equilibrated SSS point.

2.3. Modification of the Van Genuchten model

The main purpose of this section is to find an appropriate model to describe the desorption isotherms of the high-performance concrete F44Adj. Various water retention models have been introduced in section 2.1.6. among which the model of Van Genuchten (1980). A major emphasis will be given in this section to this latter model, given that it has been widely used in the literature to model the desorption isotherms of porous materials: soils, concrete, etc. Moreover, this model is commonly used and implemented in *Code_Aster*. We aim therefore to test this model on different desorption isotherms of high performance concretes among which that of the F44Adj concrete.

2.3.1. Experimental observations on high-performance concrete data sets from literature

In this section are detailed various desorption tests taken from the literature and carried out on concretes having a formulation as similar as possible to that of the F44Adj concrete. Therefore, the data presented corresponds to high performance concretes. The experimental data presented will be used to test, calibrate and modify the Van Genuchten (1980) model before using it to model the water retention curve of the F44Adj concrete. This will allow us to verify the general validity of this model on various different tested high-performance concretes.

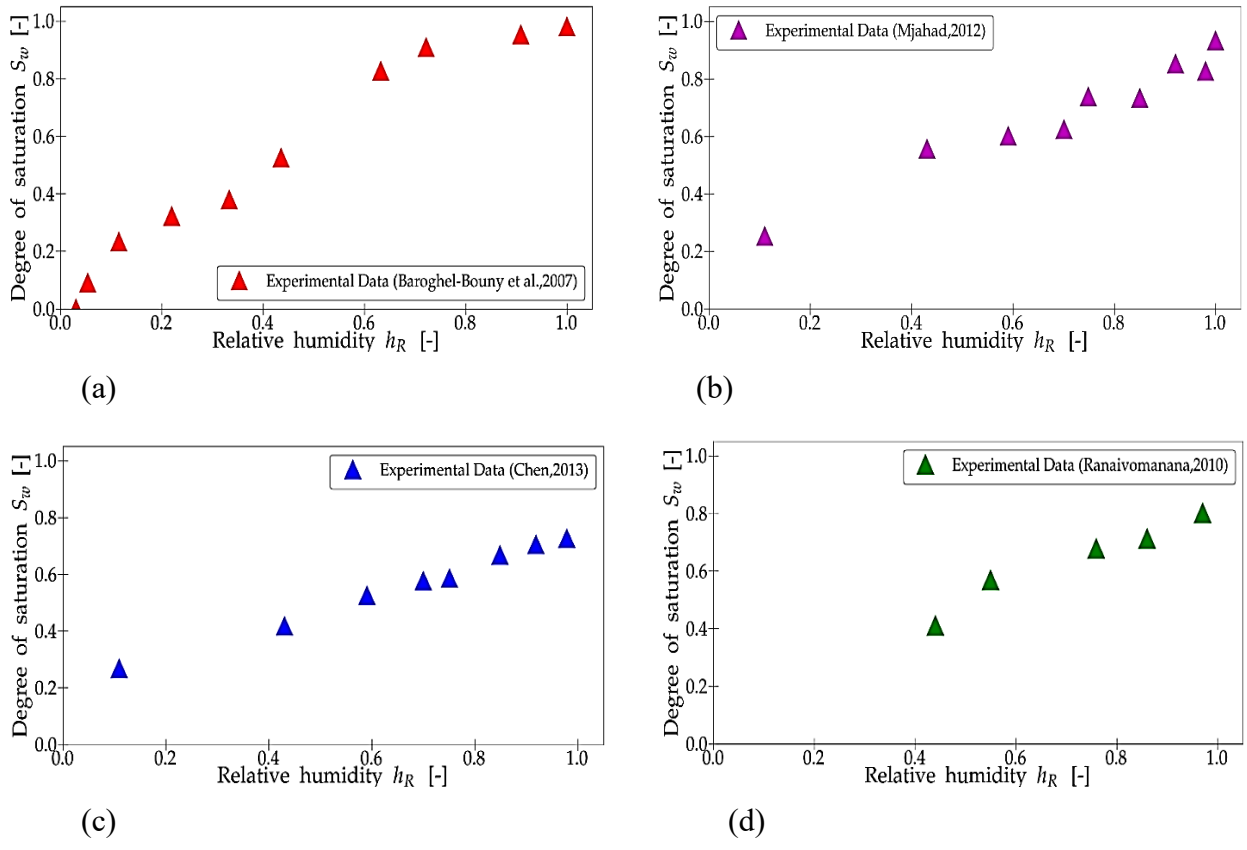

Fig. 2-34 – Desorption isotherms of a high-performance concrete studied in: (a) Baroghel-Bouny et al. (2007) – (b) Mjahad (2012) – (c) Chen (2013) – (d) Ranaivomanana (2010)

Fig. 2-34 shows the desorption isotherms obtained by Baroghel-Bouny et al. (2007), Mjahad (2012), Chen (2013) and Ranaivomanana (2010). For all these drying tests, a high-performance concrete of type CEMI was used. The authors placed their samples in desiccators where the relative humidity was adjusted via saline solutions. The moisture content of the samples was determined by weighing them. The temperature in those tests was set to an ambient temperature variating between

T=20°C for the tests of Chen (2013) and Ranaivomanana (2010) and T =23±0.1℃ for Baroghel-Bouny et al. (2007) and Mjahad (2012).

Desorption tests of Baroghel-Bouny et al. (2007) were carried out over a wide range of relative humidity from 3% to 100%. In these tests:

- The authors choose a dry state of the samples for a relative humidity value of 3%.
- The maximum degree of saturation (for h_R=100%) is not exactly equal to 1. It is not clear from the paper which saturated reference condition is taken, but it does not seem to correspond to the mass value obtained for a sample submitted to h_R=100% but to a sample saturated under water.

The desorption tests of Mjahad (2012) and Chen (2013) start with samples matured under water for a period of 6 months. It can be noted that experimental uncertainties affected the shape of the curve of the experimental data of Mjahad (2012) at high relative humidities. In the tests of Mjahad (2012) and Chen (2013):

- The mass of the dry sample is determined from a dried sample at 60°C for Mjahad (2012) and a dried sample at 105°C for Chen (2013).
- The maximum degree of saturation (for h_R=100%) is not equal to 1. The saturated reference state does not correspond to the value of the sample submitted to 100% but to a sample saturated under water.

Finally, in the tests of Ranaivomanana (2010):

- The dry sample mass is determined from a dried sample at 105°C.
- The maximum degree of saturation (for $h_R \approx$100%) is not equal to 1. The saturated reference state does not therefore correspond to the mass value obtained when the sample is exposed to a relative humidity of 100%.

It is noticeable that the above described desorption tests differ in the reference values of the dry and the saturated mass. For the dry state, we have several possibilities:

- h_R=3% at the test temperature Baroghel-Bouny (2007).
- 60°C (without a provided relative humidity measured in the oven Chen (2013), Mjahad (2012)
- 105°C (without a provided relative humidity measured in the oven Ranaivomanana (2010)

For the saturated state, there are two possibilities:

- Sample saturated under water ((Baroghel-Bouny, 2007; Chen, 2013; Mjahad, 2012; Ranaivomanana, 2010))
- $h_R \approx$100% (as could be found in other experimental data sets found in literature such as Brue et al. (2017) and Poyet (2016)).

2.3.2. Numerical calibration with the Van Genuchten (1980) model and proposition of a modified Van Genuchten model

In this section, the experimental data sets of Baroghel-Bouny et al., (2007), Mjahad (2012) , Chen (2013), Ranaivomanana, 2010 are calibrated with the classical Van Genuchten (1980) model (found in *Code_Aster*). This model is developed and mainly used in *Code_Aster*. We remind that the equation of this model is given by equation (2-23).

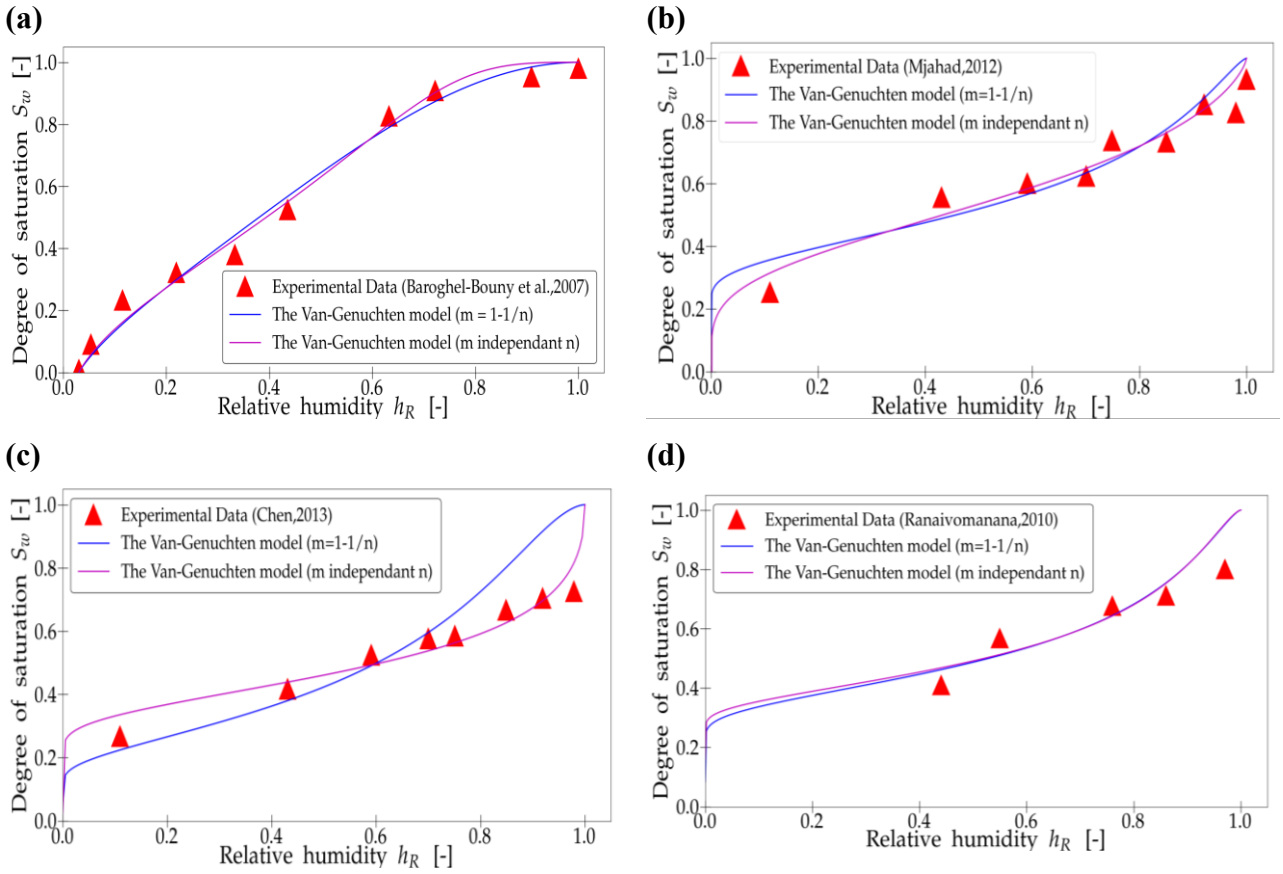

Fig. 2-35 – Numerical calibration with the Van Genuchten model for the experimental desorption isotherms of (a) (Baroghel-Bouny et al., 2007) (b)(Mjahad,2012) (c) (Chen,2013) (d) (Ranaivomanana, 2010)

Fig. 2-35 tests the numerical calibration with a Van Genuchten (1980) model for two cases:

- the case where the parameter m= 1- 1/n as given in Van Genuchten (1980)
- the case where the parameters m and n are considered to be independent as proposed by Van Genuchten and Nielsen (1985) (see section 2.1.6).

As could be seen, the independency between the two parameters could in some cases induce some flexibility in the model calibration (Fig. 2-35-c). However, in both tested cases, the main insufficiency of this model stands in the relative humidities near 100%. As a matter of fact, when $h_R \rightarrow 100\%$, the Van Genuchten model is found inconsistent with experimental observations. as noted in equation (2-23), the Van Genuchten (1980) model imposes, at a relative humidity $h_R \rightarrow 100\%$, a degree of saturation $S_w = 1$.

The constraint near 100% of relative humidity is clearly the cause of this inconsistency. Indeed, experimentally the mass of the sample soaked in water (when all the pores are saturated with water) is greater than that obtained at a relative humidity near 100% (where the macropores are not all saturated).

It is therefore necessary that in the retained water retention model (expressed as a function of the degree of saturation in *Code_Aster*) a maximum saturation degree less than 1 appear for a relative humidity of 100%. Following what has been said, it is proposed to calibrate the experimental data (section 2.3.1) with the Van Genuchten model after modifying its general form. So it will allow the degree of saturation S_{100} when $h_R \rightarrow 100\%$ to be lower than 1. In a similar way to equation (2-23), we propose to define the effective saturation S_e as:

$$S_e = \frac{S_w - S_r}{S_{100} - S_r} = (1 + (-c\ln(h_R))^{n})^{-m} \quad (2\text{-}37)$$

In this new form, the model imposes:

- $S_w = S_r$ and $S_e = 0$ when $h_R \to 0\%$
- $S_w = S_{100}$ and $S_e = 1$ when $h_R \to 100\%$

In Fig. 2-36 and Fig. 2-37, the new modified model while taking m = 1-1/n is tested to calibrate the previously introduced experimental desorption isotherms. The modified model is also compared with the classical model (without S_{100}).

It should be noted that the Van Genuchten equation is numerically difficult to manage for $h_R \to 0\%$ where the model imposes an infinite value for the saturation degree. Hence the difficulty is to calibrate and determine the S_r parameter (for $h_R \to 0\%$). We then chose to calibrate this new modified model with a parameter S_3 (for a relative humidity h_R=3% considered as reference state by Baroghel-Bouny (2007)). Equation (2-38) is then used for the calibration. The link between S_r and S_3 in the latter equation is done via with equation (2-37) (by taking h_R=3% and S_w= S_3). For the experimental data of Baroghel-Bouny (2007), S_3 in equation (2-38) is fixed to zero.

$$S_e = \frac{S_w - S_3}{S_{100} - S_3} = (1 + (-c * \ln(h_R))^{n})^{-m} \quad (2\text{-}38)$$

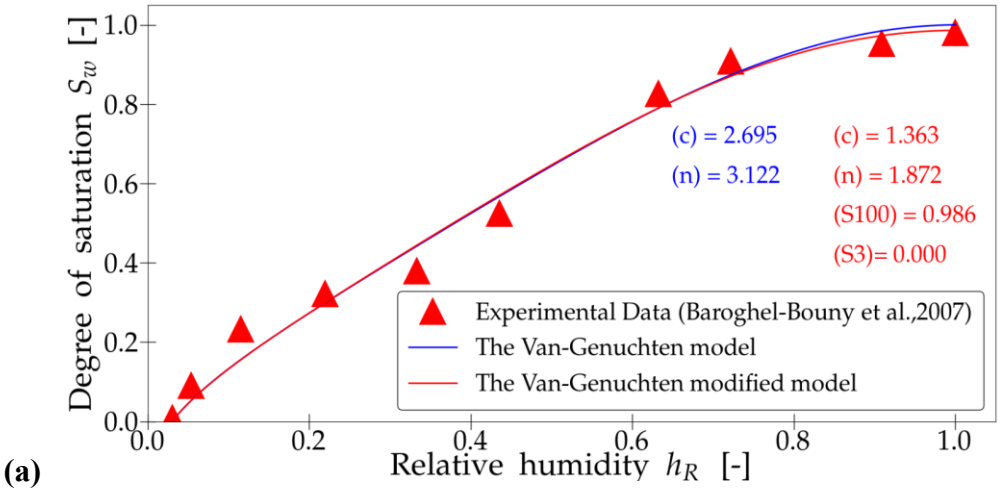

(a)

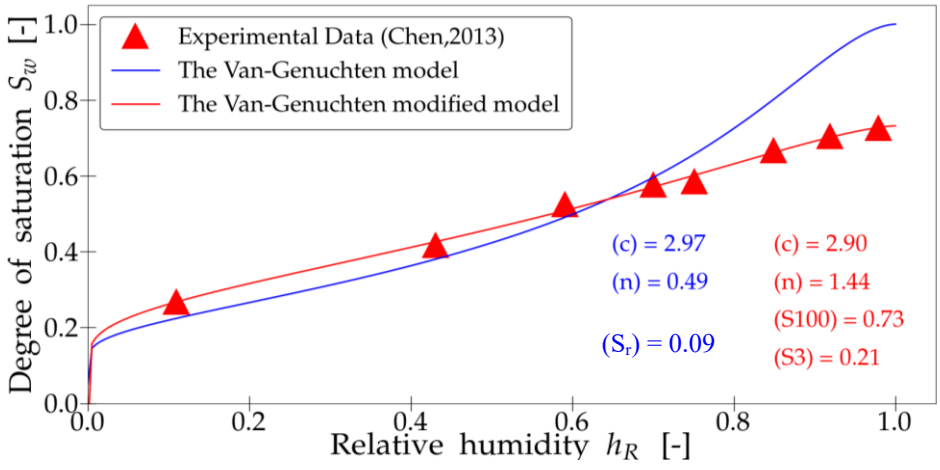

(b)

Fig. 2-36 – Calibration of the classical model of Van – Genuchten vs the modified model for the experimental data of (a) Baroghel-Bouny et al. (2007) (b) Chen (2013)

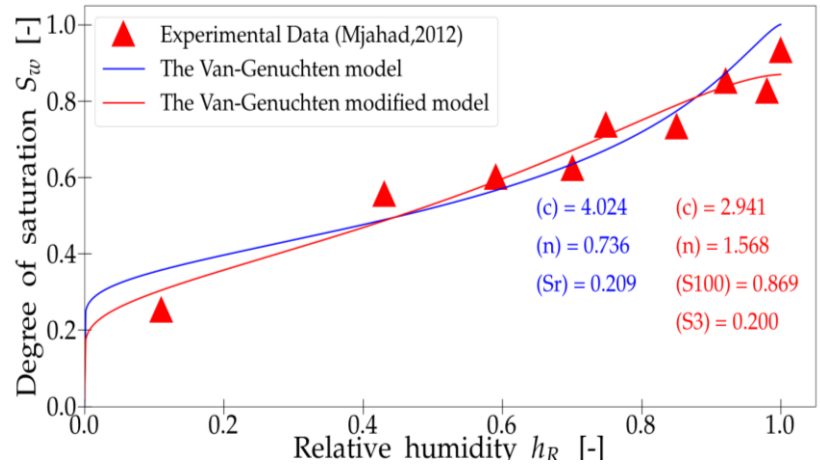

(a)

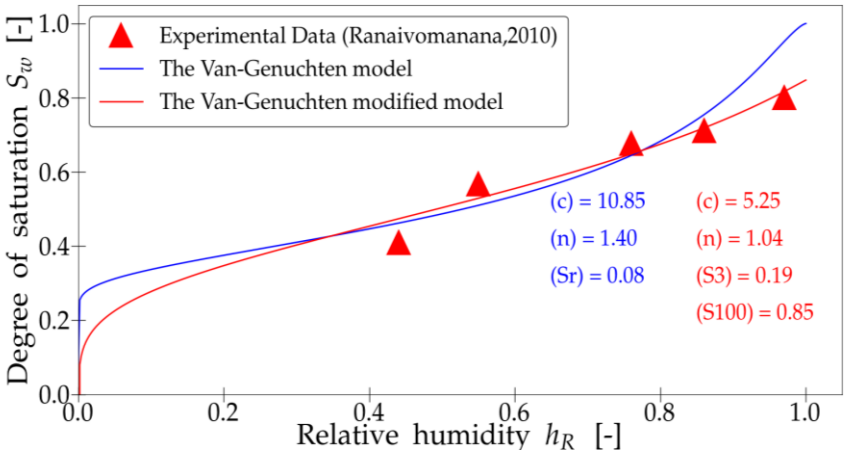

(b)

Fig. 2-37 – Calibration of the classical model of Van Genuchten vs the modified model for the experimental data of (a) Mjahad (2012), (b) Ranaivomanana (2010)

We could eventually conclude that the modified model is able to represent all the tested experimental data successfully. Starting from this point, we can then consider that the modified Van Genuchten model is a 4 parameters model (taking m=1-1/n): n, c, S_{100}, S_3. In the tested cases (presenting a limited number of experimental points), the modified Van Genuchten model with 4 parameters is sufficient hence there is no need to consider an independent m in addition to n.

The parameters of the calibration of the Van Genuchten modified model, for each of the previously tested experimental data, are shown in Table 2-6:

	c	***n***	***S_3***	***S_{100}***
Baroghel-Bouny et al. (2007)	1.363	1.87	0.00	0.98
Chen (2013)	2.90	1.44	0.21	0.73
Mjahad (2012)	2.94	1.56	0.20	0.87
Ranaivomanana (2010)	5.25	1.04	0.19	0.85

Table 2-6– Calibrated parameters of the modified Van Genuchten model

2.3.3. Numerical calibration of the F44Adj concrete SSS desorption isotherms with the modified Van Genuchten model

The experimental desorption isotherms of the F44Adj concrete obtained with the SSS method (section 2.2 - Fig. 2-26, Fig. 2-28) are calibrated in this section with the modified Van Genuchten model (equation (2-37)).

In Fig. 2-38 are calibrated the experimental desorption isotherms obtained with the SSS method for the scenario 1 of insufficient saturation of the 7x7x28 sample (from Fig. 2-26). In Fig. 2-39, are calibrated the experimental desorption isotherms obtained with the SSS for the scenario 2 of micro-cracks formation in the 7x7x1 and 7x7x3 samples (from Fig. 2-28). For the calibration done in this section, the used experimental points are the average values obtained while testing the 7x7x1cm and 7x7x3 cm samples, while noting that the standard-deviation between those two values is very small. Despite the fact that the experimental point near 98% of relative humidity (for T=20°C) represent a sorption state rather than a desorption state (section 2.2.2.4), it was chosen however to use this point for the fitting. Nevertheless, it should be kept in mind that the point corresponding to a desorption state near 98% of relative humidity could be possibly in reality bigger than that corresponding to the sorption state.

It is important to note that, due to the long needed duration to reach equilibrium for all fixed relative humidities (see section 2.2.2.3), the corresponding experimental desorption isotherms of the F44Adj concrete were completed with desorption experimental points from the literature (Baroghel-Bouny et al., 1999)(Brue et al., 2017) obtained for similar tested concretes.

On another hand, as indicated in section 2.1.6, we will consider based on the observations done by Poyet (2016), that the parameter n (equation (2-37)) will have the same value for a given material regardless of the tested temperatures (in our case 20°C and 50°C). This is an additional constraint that we will be considering while fitting both desorption isotherms at 20°C and 50°C. The fitted parameters of the model are indicated in each figure (Fig. 2-38 and In Fig. 2-39) and for each study case (T=20°C and T=50°C).

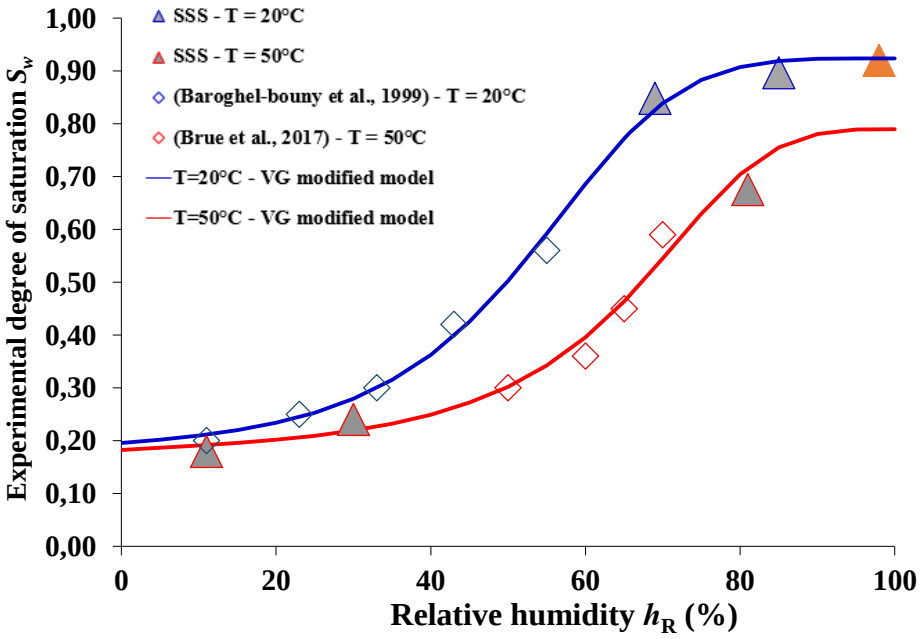

T	20°C	50°C
c	1.791	2.897
n	3.759	3.759
S_{100}	0.924	0.79
S_r	0.195	0.182

Fig. 2-38 – Calibrated SSS desorption isotherm of the F44Adj concrete with a modified Van Genuchten model at the temperatures of 20°C and 50°C for the considered scenario of insufficient saturation

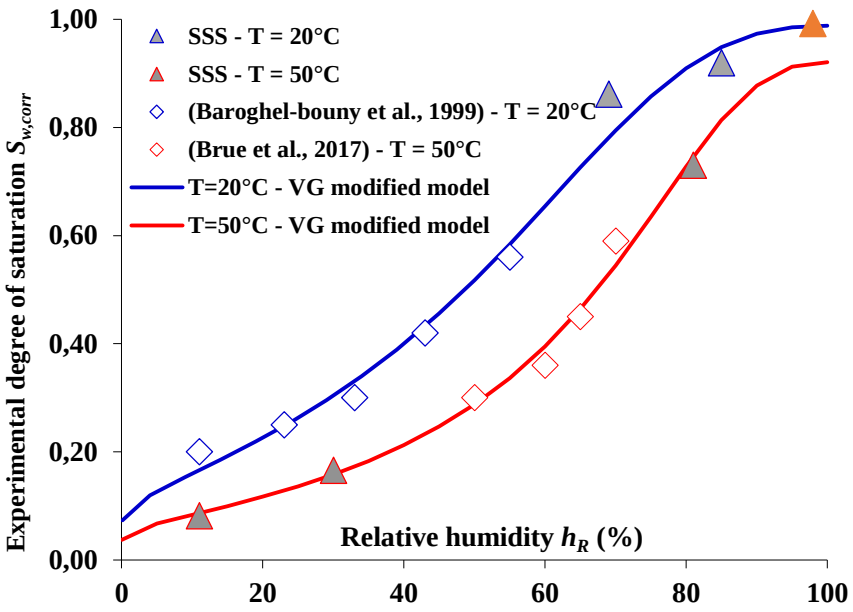

T	20°C	50°C
c	2.073	3.42
n	2.353	2.353
S_{100}	0.988	0.93
S_r	0.05	0.03

Fig. 2-39 - Calibrated SSS desorption isotherm of the F44Adj concrete with a modified Van-Genuchten model at the temperatures of 20°C and 50°C for the considered scenario of micro-cracks formation

The calibration of the experimental desorption curves in terms of the capillary pressure with the calibrated parameters (S_r, S_{100}, n, P_r) are shown in Appendix 2.

2.3.4. Numerical calibration of the F44Adj concrete DVS desorption isotherms with the modified Van Genuchten model

The experimental desorption isotherms of the F44Adj concrete obtained with the DVS method (section 2.2 - Fig. 2-33) are calibrated in this section with the modified Van Genuchten model (equation (2-37)). Fig. 2-40 and Fig. 2-41 present the calibration of the experimental desorption isotherm for T=20°C and T=50°C respectively. Given the large number of experimental points, the modified Van Genuchten model can appear insufficient for modelling the desorption isotherm at T=20°C. Therefore, the previously proposed modification to the Van Genuchten model can be equally done to the (Durner, 1994) model. Equation (2-24) can be modified into (2-39) under the constraint $\sum_{i=1}^{k} w_i = 1$.

$$S_e = \frac{S_w - S_r}{S_{100} - S_r} = \sum_{i=1}^{k} w_i \left(1 + \left(-c_i ln(HR)\right)^{n_i}\right)^{-m_i} \quad (2\text{-}39)$$

For the temperature of 20°C, a Durner (1994) model with k equal to 3 had to be taken in order to correctly model the whole desorption isotherm (see Fig. 2-40). In contrast, for T=50°C, a Durner (1994) model with k equal to 2 is sufficient (see Fig. 2-41). The parameters of the two modified models used in Fig. 2-40 and Fig. 2-41 are given in Table 2-7. The DVS desorption isotherms calibrated in this section correspond to the scenario 1 of insufficient saturation and drying of the 7x7x28cm sample (see section 2.2.4). The calibrations of the DVS desorption isotherms corresponding to scenario 2 are given in Appendix 3.

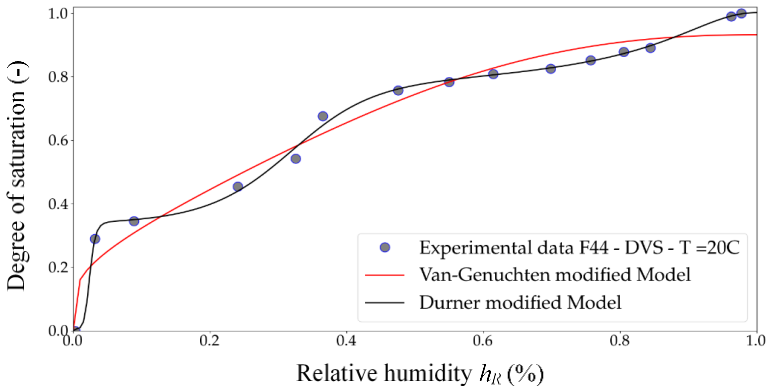

Fig. 2-40 - Calibrated DVS desorption isotherm of the F44Adj concrete with a modified Van Genuchten model and Durner (1994) model at the temperature of 20°C

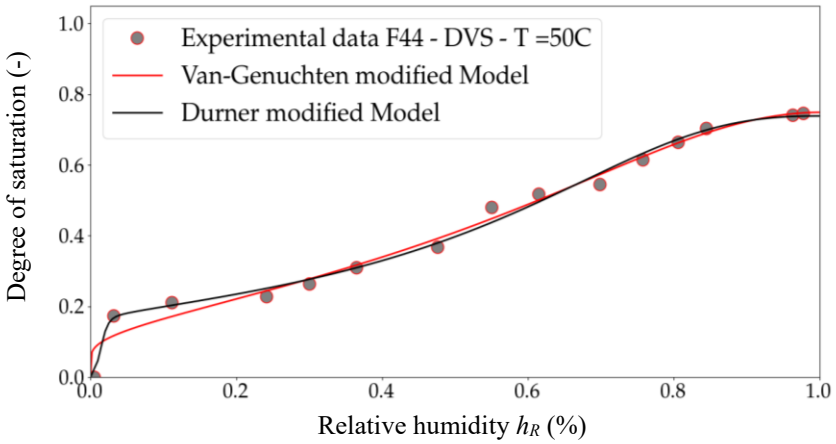

Fig. 2-41 - Calibrated DVS desorption isotherm of the F44Adj concrete with a modified Van Genuchten model and Durner (1994) model at the temperature of 50°C

The Van Genuchten modified model		
T	**20°C**	**50°C**
c	0.39	0.64
n	2.09	1.87
S_{100}	0.93	0.75
S_r	0.00	0.00

The Durner (1994) modified model		
T	**20°C**	**50°C**
S_{100}	1.00	0.74
S_r	0.00	0.00
c_1	0.91	2.44
n_1	6.57	2.32
c_2	0.27	0.24
n_2	22.85	16.41
c_3	7.87	-
n_3	2.03	-
w_1	0.41	0.813
w_2	0.33	-

Table 2-7 – Parameters of the modified Van Genuchten and Durner (1994) models

2.3.5. Conclusions

Various water retention curve models from the literature are presented in section 2.1.6, among which the Van Genuchten (1980), Durner (1994), GAB and Pickett models since they have previously made it possible to describe the desorption of cementitious materials in a fairly representative manner. A major emphasis has been given to the Van Genuchten (1980) model due its wide use in the literature.

After presenting the experimental desorption isotherm of the F44Adj high performance concrete studied in this work (section 2.2) and other experimental desorption isotherms of high performance concretes found in the literature (section 2.3.1), it turned out that the degree of saturation for a relative humidity of 100% is not necessarily equal to one: placing a sample in an environment with a relative humidity of 100% does not impose the saturation of all the pores of the material. Hence, these experimental observations showed the importance of introducing in the Van Genuchten (1980) model, in addition to a parameter S_r for the residual water saturation at 0% of relative humidity, another parameter S_{100} indicating the maximum saturation of the sample at 100% relative humidity. .

It should be noted that the modification proposed to the Van Genuchten (1980) model can be equally done to other models as for instance the Durner (1994) model (section 2.3.4 for the DVS desorption isotherms). However, this model already presents a large number of parameters to be calibrated. The interest of its use will only be remarkable if a large number of experimental points are available.

Chapter 3

Moisture transfer in concrete

List of Figures

List of Tables

The durability of a cementitious material is determined by its ability to resist transfers with the external environment. In fact, these transfers can lead to the penetration of aggressive agents or to the establishment of moisture gradients (in the case of water transfer) and hence to deformations. In the first part of this chapter (section 3.1), a literature survey focuses on the water transfer equations of porous materials and their transfer properties such as the intrinsic permeability, the relative permeability and the diffusion coefficient. In the second part, the effect of hydric boundary conditions on the drying kinetics will be examined. An experimental campaign aiming to quantify the permeability of the concrete is presented in section 3.2. This campaign includes several mass loss tests under various thermo-hydric conditions and on various material geometries. The tests provide necessary data for the fitting study done on a last section (section 3.3). This study seeks to characterize the drying kinetics by calibrating the previously introduced transfer laws on the mass loss curves of the concrete.

3.1. State of the art

3.1.1. Mass conservation equations

In what follows, the porous medium is considered to be filled with two constituents, which are water and air. Each of them can coexist in two phases: a liquid (*L*) and a gaseous phase (*G*). Thus water as a constituent can exist either in the liquid form (*w*) or in the gaseous form as vapor (*vp*). Similarly, air can exist either in liquid form as dissolved air (*da*) or in gaseous form as dry air (*dra*). Afterwards, one writes:

- Water = liquid water (*w*) + water vapor (*vp*)
- Air = dissolved air (*da*) + dry air (*dra*)
- Liquid phase (*L*) = liquid water (*w)* + dissolved air (*da*)
- Gas phase (*G*) = water vapor (*vp*) + dry air (*dra*)

The material transport equations are based on the mass conservation equations of the different elements. In equation (3-1) they are written for water and air with their different phases, with no external contribution:

$$\begin{cases} \dot{m_w} + \dot{m_{vp}} + Div\left(M_w + M_{vp}\right) = 0 \\ \dot{m_{da}} + \dot{m_{dra}} + Div\left(M_{da} + M_{dra}\right) = 0 \end{cases} \tag{3-1}$$

The mass supply and mass flows of the elements defined with respect to an initial state are written as in equation (3-2) and (3-3) respectively:

$$\begin{cases} m_w = \rho_w \emptyset S_w \\ m_{vp} = \rho_{vp} \emptyset (1 - S_w) \\ m_{da} = \rho_{da} \emptyset S_w \\ m_{dra} = \rho_{dra} \emptyset (1 - S_w) \end{cases} \tag{3-2}$$

$$\begin{cases} M_{lq} = \rho_w \, \emptyset \, S_w (v_w - v_s) \\ M_{vp} = \rho_{vp} \emptyset (1 - S_w)(v_{vp} - v_s) \\ M_{da} = \rho_{da} \emptyset S_w (v_{da} - v_s) \\ M_{dra} = \rho_{dra} \emptyset (1 - S_w)(v_{dra} - v_s) \end{cases} \tag{3-3}$$

where:

- m_i is the mass supply of the element i, ρ_i is the density of the element i, $\emptyset$ is the material's porosity and S_w is the water degree of saturation.
- $\dot{m}_i = \frac{\partial m}{\partial t}$ is the mass variation function of time of the ith element.
- M_i is the mass flow of the ith element.
- v_i the transport velocity of the different elements and v_s the speed of the solid skeleton.

3.1.2. Moisture transfer modes and laws

In this section, we cite all the transfer laws describing various modes of fluid's transfer in porous materials.

3.1.2.1. Darcy's law (1856)

Darcy's law describes a flow of fluid through a porous medium under a pressure gradient. In the context of this thesis, the Darcy law is applied to both liquid and gas. The Darcy law states that the pressure gradient and the fluid velocity are proportional, through the fluid viscosity and through another factor introduced by Darcy and called "permeability". When applying Darcy's law, the following assumptions have to be made:

- The flow and thus the filtration resistance force of the fluid is essentially the result of the viscous forces at the fluid-solid interface.
- The flow is considered to be laminar and under a steady-state.
- There are no physico-chemical interactions between the material and the fluid.
- The pore saturation is done with one single fluid at a time.
- Inertial forces are neglected.

The last hypothesis is usually accepted for most porous media but should always be verified. In fluid mechanics, the Reynolds number is an indicator of the importance of inertia (Mjahad, 2012). This dimensionless number Re being equal to the ratio of the inertial forces and those due to viscosity, it is written as:

$$Re = \frac{\rho_j v_j l}{\eta_j} \tag{3-4}$$

where l is the characteristic length which for a porous medium can be chosen as the average pore diameter and η_j is the dynamic viscosity of the fluid (liquid or gas). When the Reynolds number is less than 2000, the flow is considered to be laminar. When the Reynolds number is less than 1, the flow is considered inertially low. The limit for flows with negligible inertia depends on the flow characteristics and pores size. The validity of Darcy's law is then questioned for porous media with a large porosimetric distribution: a Forchheimer-type transfer law is then required (Daian, 2013).

Darcy's law for the filtration of any fluid phase (liquid or gas) can be written according to equation (3-5):

$$\frac{M_j}{\rho_j} = v_j = -\frac{K_{eff}(S_w)}{\eta_j} \cdot \nabla(P_j) + \rho_j F_m \tag{3-5}$$

where:

- M_j is the mass flow of the jth phase, ρ_j its mass density and v_j its transfer velocity (for j= L ,G)
- K_{eff} is the effective permeability of the material
- P_j is the pressure of the liquid or gas (j= L ,G)
- F_m is the mass gravity force

In equation (3-5), the hydraulic conductivity λ_j^H is defined as:

$$\lambda_j^H(S_w) = \frac{K_{eff}(S_w)}{\eta_j} = \frac{K_{rj}(S_w)\, K_j}{\eta_j} \tag{3-6}$$

K_{eff} is the effective permeability of the material. This permeability is the material permeability specified for each saturation state. It can be written as a product (see equation (3-6)) of a permeability in a fluid saturated state called the 'intrinsic' permeability K_j and a relative permeability K_{rj} with a value between 0 and 1. The saturation state of the material is an important factor in determining the effective permeability. Indeed:

- In partially saturated systems, the effective permeability of the gas will be lower than the permeability in the dry state (intrinsic permeability). In liquid saturated pore networks, the accessibility of the pore volume to the gas is prevented, so the effective gas permeability becomes zero.
- On the contrary, when the liquid phase is continuous, the passage of water through the pores is easier, so the effective permeability to liquid will increase during wetting. It will pass from zero at the dry state and become equal to the 'intrinsic' permeability when the pores are water saturated.

It is concluded that saturation impacts the effective permeability of porous materials: Abbas et al. (1999) have experimentally studied the influence of liquid water saturation on the variation of the effective gas permeability of ordinary concrete (Fig. 3-1). The authors were able to confirm that, as the concrete becomes saturated, the continuous phase of liquid water in the pores prevents the circulation of gas and thus gas permeability progressively decreases.

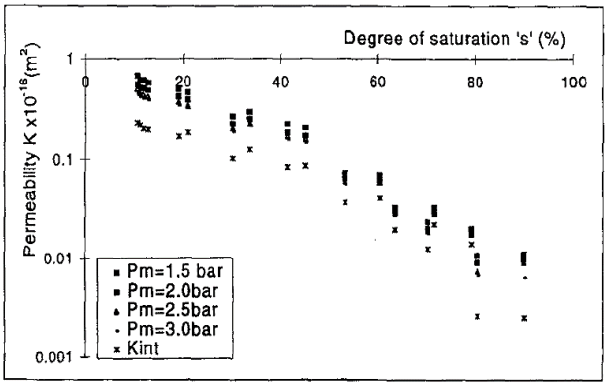

Fig. 3-1 – Evolution of the effective permeability to gas function of the water degree of saturation (Abbas et al., 1999)

As indicated by its name, the 'intrinsic' permeability (K_G or K_L) is supposed to be a material characteristic. However, this permeability of concrete is not always 'intrinsic' as it depends on the fluid used for measuring it. This notion will be discussed furtherly in section 3.1.3.2.

As for the relative gas permeability K_{rg}, it is then the ratio between the effective gas permeability K_{eff} and the gas permeability K_G ($K_{rg} = K_{eff}/K_G$). K_{rg}varies respectively between 0 and 1 depending on whether the material is saturated or dry. The relative water permeability K_{rl} ($= K_{eff}/K_L$) takes a value of 1 if the material is saturated and 0 if it is dry (see Fig. 3-2). Additional information about the relative permeabilities and the 'intrinsic' permeability will be given in section 3.1.3.2.

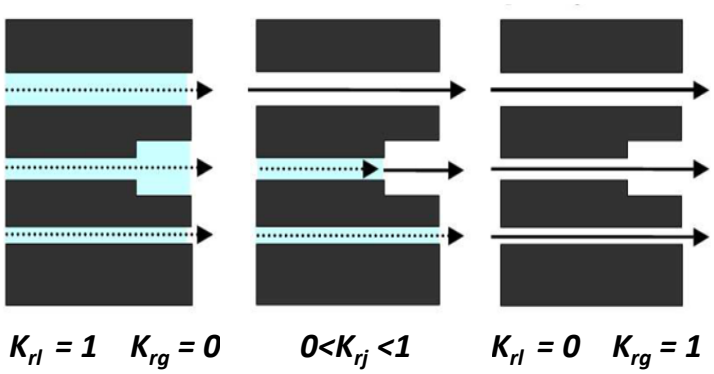

Fig. 3-2 – Evolution of the relative permeability between the saturated and dry state (Chen, 2013)

On another hand, the properties of water that might impact the transfer phenomenon (see equation (3-5)) are its density and dynamic viscosity. As the temperature T increases, water expands, which implies a decrease in its density ρ_L. Chhun (2017) cites a relationship proposed by Raznjevic (1970) and frequently used in the literature:

$$\rho_L = 314.4 + 685.6\left(1 - \left(\frac{T-273.15}{374.14}\right)^{\frac{1}{0.55}}\right)^{0.55} \quad (3\text{-}7)$$

The dynamic viscosity of water is also a temperature-dependent parameter. Bary et al. (2012) and Thomas (1995) used respectively the relationships proposed by Pezzani (1992) and given by equations (3-8) and (3-9). Chhun (2017) compared these two relationships with the experimental results of Reid (1987) and showed that both relationships are reliable and describe well experimental results from Reid (1987) (Fig. 3-3).

$$\eta_L = 2.414\ 10^5 exp\left(\frac{570.58058}{T + 133.15}\right) \quad (3\text{-}8)$$

$$\eta_L = 0.6612(T - 229)^{-1.562} \quad (3\text{-}9)$$

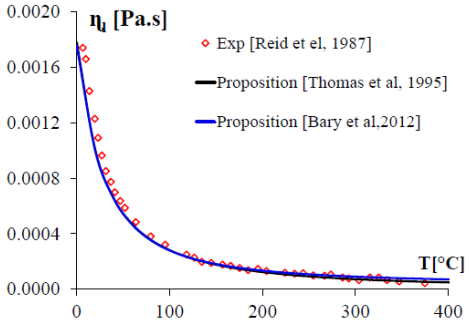

Fig. 3-3 - Variation of the dynamic viscosity of water as a function of temperature (Chhun, 2017)

As for the gas phase, the dynamic viscosity of the gas is also a parameter that varies with temperature. In his study, Chhun (2017) used a relation of Perrot (1992) given by equation (3-10):

$$\eta_G = 3.85\text{x}10^{-8}\ \text{T} \quad (3\text{-}10)$$

3.1.2.2. Fick's law

When a gas molecules concentration gradient exists in the porous medium even in absence of gradient of pressure, gas molecules move from areas of higher concentration to areas of lower concentration. This is called diffusion and is described by Fick's law.

For the gas phase (water vapor + dry air), the Fick's law is written in terms of molar volume concentration (mol/m^3) as:

$$g_{vp/dra} = -g_{dra/vp} = -D_{vp}\,\nabla n_{vp} \tag{3-11}$$

with:

- $g_{vp/dra}$: molar flux density (mol/m^2/s in SI units) of water vapor in dry air.
- $g_{dra/vp}$: molar flux density (mol/m^2/s in SI units) of dry air in water vapor.
- D_{vp}: diffusion coefficient (m^2/s in SI units) of water vapor through dry air at the pore level.
- n_{vp}: molar volume concentration of water vapor (mol/m^3 in SI units) present in the pores, defined as: $n_{vp} = \rho_{vp} \cdot M_{vp}^{mol}$ with ρ_{vp}: the density of the water vapor (kg/m^3 in SI units) and M_{vp}^{mol} its molar mass (kg/mol in SI units).

By replacing the molar concentration by the mass concentration ($\rho_{vp} = n_{vp} \cdot M_i^{mol}$), we write:

$$M_{vp} = g_{vp/dra}\, M_{vp}^{mol} = -D_{vp}\nabla\rho_{vp} = -M_{dra} \tag{3-12}$$

with M_{vp} and M_{dra} the mass flow density (kg/m^2/s in SI units) of the water vapor in dry air and of the dry air in water vapor respectively at the pore level.

For the gas phase, we speak of a Knudsen effect when the transfer takes place in a pore whose diameter d is small (approximately 10 times smaller (Ewart, 2009)) compared to the average free path l_m of the gas molecule. The latter is defined as the average distance to be traveled by a gas molecule before colliding with another molecule. The Knudsen number $Kn = l_m / d$ allows to distinguish between different transports domains when the gas mixture is formed by two components:

- The domain of effusion where the Knudsen effect takes place ($Kn >> 1$, $d << l_m$). In this case, each component of the gas phase is transported independently of the other under the effect of the collisions that will take place between the molecules and the solid walls. Gas mixture diffusion is governed by Fick's law with a modified diffusion coefficient taking these collisions into account.
- The binary diffusion domain (for a $Kn << 1$, $d >> l_m$). The gas behaves as a single phase with a unique viscosity and diffusion coefficient. Gas mixture diffusion is governed by an ordinary Fick's law.

The Knudsen effect is taken into account in the effusion domain by modifying the vapor diffusion coefficient D_{vp} as in equation (3-13):

$$D_{vp}^{eff} = D_{vp} \cdot \beta_d \tag{3-13}$$

with:

- D_{vp}^{eff}: Effective water vapor diffusion coefficient

- β_d: Knudsen's reductive factor, written as $\beta_d = \frac{1}{1+\frac{l_m}{d_m}}$ with d_m an average diameter of the porous medium
- The mean free path l_m of a gas molecule is inversely proportional to the gas pressure P_g and according to the literature at atmospheric pressure it is of the order of 100 nm.

In equation 3-13, the Knudsen effect is then taken into account by means of an effective diffusion coefficient D_{vp}^{eff} that decreases with the porous radius.

3.1.2.3. Moisture transfer modes

Baroghel-Bouny (1994) distinguishes four modes of moisture transfer that depend on the saturation level of the pores:

- When the pores are saturated (Fig. 3-4 – 1), the liquid phase is continuous: the transfer or advection is governed by the Darcy's law (section 3.1.2.1).

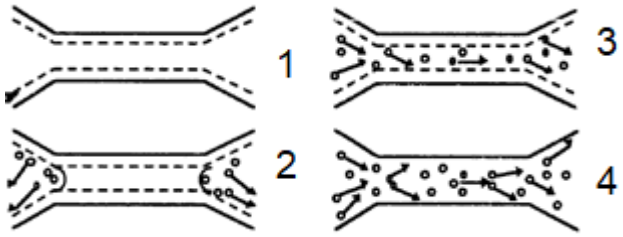

Fig. 3-4 – Moisture transfer modes - (Baroghel-Bouny, 1994)

- For intermediate saturation the liquid phase becomes discontinuous, with water films adsorbed in the form of multilayers on the internal surfaces of the pores. Water exchanges in the pores take place by successive evaporation and condensation (Fig. 3-4 – 2), so that vapor transfer in the gaseous phase is more and more important while the relative humidity is decreasing. Eventually, transport by gaseous diffusion, governed by Fick's law (section 3.1.2.2), becomes preponderant (Fig. 3-4 – 3).
- At a very low saturation, the adsorbed water is in the form of a monolayer. While gas advection could be present, when the gas pressure is equal to the atmospheric domain, the predominant transport engine is gaseous diffusion (Fig. 3-4 – 4). Gaseous transport is governed by Fick's law.

3.1.2.4. Equilibrium between liquid water and water vapor

Let us note h_w^m the specific mass enthalpy of water and h_{vp}^m that of the water vapor; s_w^m is the specific mass entropy of water while s_{vp}^m is the specific mass entropy of water vapor; g_w is the specific Gibbs free energy of water (for reversible systems: $g_w = h_w^m - Ts_w^m$ (Coussy, 2004)) and g_{vp} that of the water vapor ($g_{vp} = h_{vp}^m - Ts_{vp}^m$). The thermodynamic equilibrium of water under its different forms can allow us to write equation (3-14):

$$g_w = g_{vp} \tag{3-14}$$

According to equation (3-14), we can write equation (3-15) :

$$\left(h_{vp}^m - h_w^m\right) = T(s_{vp}^m - s_w^m) \tag{3-15}$$

The definition of the free enthalpy of Gibbs gives $dg = \frac{dP}{\rho} - sdT$ (Coussy, 2004). This relation, applied to each of the water components and combined with $dg_w = dg_{vp}$ (while considering an instantaneous phase change without dissipation (Verdier, 2001)), results in:

$$\frac{dP_{vp}}{\rho_{vp}} = \frac{dP_w}{\rho_w} + \left(h_{vp}^m - h_w^m\right)\frac{dT}{T} \tag{3-16}$$

The term $\left(h_{vp}^m - h_w^m\right)$ in equation (3-16) is what we call the enthalpy of phase change of water or also the heat of sorption (Pan et al., 1998). For the water constituent, we can write:

$$h_w^m = h_{init,w}^m + dh_w^m \tag{3-17}$$

$$h_{vp}^m = h_{init,vp}^m + dh_{vp}^m \tag{3-18}$$

with h_{init}^m the specific mass enthalpy at the initial state and dh^m the variation of enthalpy leading to the current state. The initial specific mass enthalpy of water can be written as $h_{init,w}^m = \frac{P_{w,ini}}{\rho_w}$ with $P_{w,ini}$ the liquid pressure at the initial state. The initial specific mass enthalpy of vapor $h_{init,vp}^m$ is taken equal to the latent heat of vaporization $L(T)$. Multiple empirical expressions for $L(T)$ can be found in Henderson-Sellers (1984) and Torquato and Stell (1982).

The mass enthalpy h^m is closely related to the notion of sorption because it translates the binding energy between the water and the porous medium (Duforestel, 2015). Since the equilibrium between water and the porous medium is described by sorption isotherms (refer to chapter 2) which are functions of both pressure and temperature, it appears therefore adequate to consider that h^m is a function of these variables (Duforestel, 2015). Hence, we can write:

$$dh_w^m = \left(\frac{\partial h^m}{\partial T}\right)\Big|_{P_w} dT + \left(\frac{\partial h^m}{\partial P_w}\right)\Big|_T \frac{dP_w}{\rho_w} \tag{3-19}$$

We define $\left(\frac{\partial h^m}{\partial T}\right)\Big|_{P_w}$ as the specific mass heat of water at a constant pressure noted as C_w^P and $\left(\frac{\partial h^m}{\partial P_w}\right)\Big|_T$ is the calorimetric coefficient of compression or isothermal latent heat of compression and can be written as $(1 - 3\alpha_w)$ with α_w the coefficient of linear expansion of water (Cornu, 1873).

As for the vapor pressure, considered as an ideal gas, it is admitted that the mass enthalpy of such a gas only depends on the temperature (thermodynamical law of Joule-Thomson). Therefore, the variation of the enthalpy of water vapor is written according to:

$$dh_{vp}^m = C_{vp}^P(\mathrm{T})\, dT \tag{3-20}$$

with $C_{vp}^P(\mathrm{T})$ the specific mass heat of water vapor at constant pressure.

3.1.3. Determination of the mass transfer parameters

The transfer parameters figuring in equations (3-5), (3-12) such as the hydraulic conductivity (the relative and 'intrinsic' permeability) and the diffusion coefficient can be determined either by experimental methods or/and by employing numerical models. These methods are detailed in the following sections.

3.1.3.1. Diffusion coefficient in concrete – experimental measurements and numerical models

We recall that Fick's law for the diffusion of water vapor in the porous medium without taking into account the Knudsen effect is written as given by equation (3-12). This relationship can be expressed in terms of water vapor pressure as in equation (3-21) (Baroghel-Bouny, 2007):

$$M_{vp/as} = -\delta \nabla P_{vp} = -D_{vp} \frac{M_{vp}^{ol}}{R\,T} \nabla P_{vp} \tag{3-21}$$

with δ (kg.m^{-1}.s^{-1}.Pa^{-1} in SI units) called in the literature the water vapor permeability associated with a diffusion process.

According to Baroghel-Bouny (2007), the water vapor diffusion coefficient in the porous medium D_{vp} can be evaluated experimentally under unsaturated conditions of the material and at a stable flow regime (constant flow density $M_{vp/as}$), using the cup test method (Fig. 3-5) with $h_{R,1}$ and $h_{R,2}$ the ambient relative humidity in compartments 1 and 2.

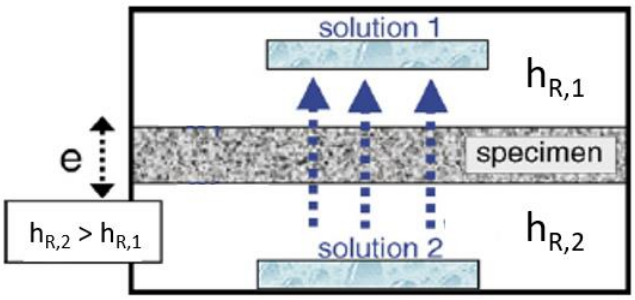

Fig. 3-5 – Cup test method (Baroghel-Bouny, 2007)

The experimental cell consists of two compartments separated by the sample of material to be tested. In each compartment the relative humidity is imposed by means of a saturated salt solution of different concentration. The temperature is constant and the total pressure is the same in both compartments (and equal to the atmospheric pressure P_{atm}). After stabilization of the sample mass, given that the thickness *e* of the sample is small enough, it can be supposed that the relative humidity gradient through the specimen is constant. This hypothesis will allow to write the diffusion coefficient D_{vp} figuring in equation (3-21) as:

$$D_{vp} = \delta \frac{RT}{M_{vp}^{ol}} = -\frac{M_{vp/as}}{grad\ P_{vp}} \frac{RT}{M_{vp}^{ol}} = -\frac{M_{vp/as}\ e}{P_{vp,sat}\,(h_{R,2}-h_{R,1})} \frac{RT}{M_{vp}^{ol}} \tag{3-22}$$

Being supplied through upper and lower openings, the salts type in compartments 1 and 2 as well as their concentrations can be changed. For each combination of relative humidity ($h_{R,1}, h_{R,2}$), the flux density through the sample can be measured (through mass measuring), thus the evolution of the vapor diffusion coefficient D_{vp} as a function of the relative humidity can be estimated.

From a numerical point of view, the water vapor diffusion coefficient D_{vp} can be considered proportional to a diffusion coefficient D_{v0} in the free air as in:

$$D_{vp} = D_{v0}\, R_M \tag{3-23}$$

where R_M is the proportionality factor that takes into account the resistance of the porous medium to gas diffusion. It depends on the porous structure and on the saturation rate of the cementitious material. Based on experimental measures found in the literature for soils, Millington (1959) proposes the following relationship for the calculation of this factor:

$$R_M = \emptyset^a (1 - S_w)^b \quad (3\text{-}24)$$

with a=4/3 and b=10/3. The coefficient D_{v0} depends on the temperature and pressure of the gas. It can be calculated from the following empirical equation (De Vries D.A, 1966) :

$$D_{v0} = 0.217 \cdot 10^{-4} \left(\frac{P_{atm}}{P_g}\right).\left(\frac{T}{T_0}\right) \quad (3\text{-}25)$$

where P_{atm} is the atmospheric pressure (101325 Pa), T_0 the reference temperature (273.15 °K equal to 0 °C).

Baroghel-Bouny (2007) conducts a cup-test on two ordinary concrete samples. The calculated experimental values of the water vapor diffusion coefficient in the concrete for an average relative humidity value are compared to those estimated using equations (3-23) to (3-25). The comparison is shown in Fig. 3-6.

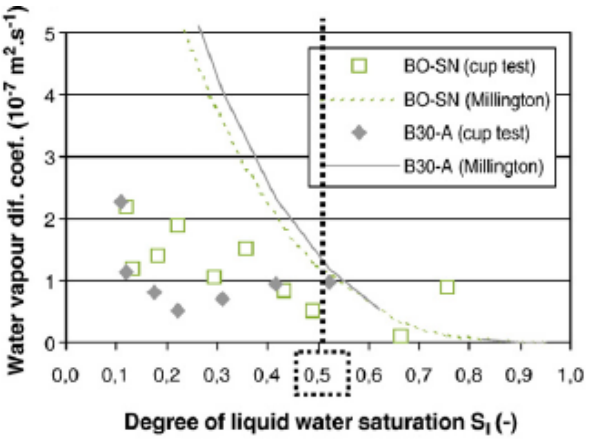

Fig. 3-6 - Comparison of the value of the vapor diffusion coefficient in concrete obtained with two methods: cup-test method and Millington (1959) method

Based on Fig. 3-6, the numerical values obtained by Millington (1959) appear to be higher than those obtained experimentally. Baroghel-Bouny (2007) explains this difference by the fact that:

- The relation (3-24) does not consider the Knudsen effect that may be present in the case of the tested concrete. To take this effect into account, some authors use equation (3-24) while modifying the values of the coefficients *a* and *b*. As an example, Thiery (2005) indicates that the equation of Millington (1959), with a=4/3 and b =10/3, was established for granular media with pore sizes larger than concrete. For this reason, Thiery (2005) proposes new values for these coefficient (a = 2.74 and b = 4.20) which ensure a better agreement with experimental results of gas diffusion in concrete (Papadakis, Vayenas, & Fardis, 1991) and which can effectively take into account the Knudsen effect in concrete pores.
- The cup-test method does not only characterize the diffusion of water vapor through the pores of the tested concrete but also the transport by advection. In fact, the vapor mass flow given in equation (3-21) cannot only be expressed under the sole influence of a vapor pressure gradient, but also under the influence of a gradient of gas pressure (see section 3.1.2.1). Duforestel (2015) has tried to quantify the relative error that could be committed when characterizing the vapor diffusion coefficient by a cup-test and hence while neglecting the advection of gas. For an ordinary concrete, a relative error of 5.3% is noted.

3.1.3.2. 'Intrinsic' permeability of concrete

Permeability is one of the most important parameters to be determined in order to solve the problem of water transfer in the material. Starting from this point, experimental methods for estimating the permeability by liquid water and gas are presented in the following section.

Measuring the water permeability involves placing a fully saturated sample in a cell and imposing a liquid injection pressure at one end. The measuring device is often referred to as a water permeameter (Fig. 3-7). The water is injected through a pump, equipped with a measuring system that measures the flow rate of water injected. The second end of the sample remains under atmospheric pressure. Under the effect of the hydraulic gradient created, the water infiltrates through the sample. Once the flow reaches steady state, so that the injected flow rate becomes constant over time, the permeability to liquid water can be determined by applying the Darcy's law as (Liu, 2011):

$$K_L = \frac{\eta_L\, Q}{A\, \nabla P} = \frac{\eta_L\, Q\, H}{A(P_{in} - P_{out})} = \frac{\eta_L\, Q\, H}{A(P_L + P_{atm} - P_{atm})} \tag{3-26}$$

where A is the sample section, η_L the liquid viscosity, H the thickness of the sample, P_{in} is the input pressure while P_{out} is the output pressure, P_L is the injection pressure of liquid water (counted in excess of the atmospheric pressure) and Q the volumetric flow rate of water infiltrated into the sample.

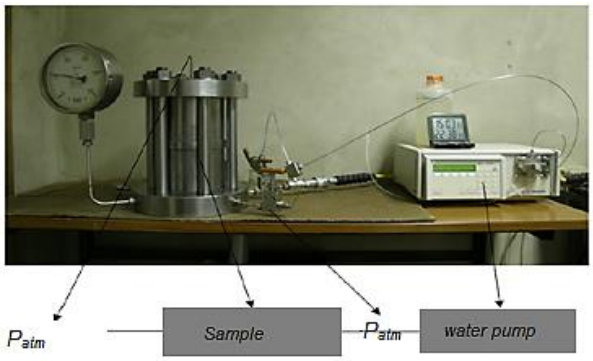

Fig. 3-7 – Measurement device of the permeability to water (Liu, 2011)

It is important to note that Darcy's law assumes that the fluid flowing through the pores is an inert fluid that does not interact with solid walls. This is not the case for water which, in cementitious materials, is a main reactor in hydration reactions. Thus the injection of water into cement can in some cases causes rehydration of anhydrous grains and significantly reduce the velocity of the molecules near the solid walls and thus reduce the measured permeability value (Coussy et al., 2001).

As for the measurements of the gas permeability of the concrete, it can also be made with a device (Fig. 3-8) named the CEMBUREAU permeameter that allows gas (Argon) to be injected into a previously dried sample, while applying mechanical containment pressure to its lateral edges (to ensure a one-dimensional flow of the gas). The gas flows from the bottom of the sample to the top, under the effect of a pressure gradient between its bottom edge (under injected pressure P_{in}) and its top edge (outlet pressure P_{out} which is usually equal to the atmospheric pressure P_{atm}). The calculation of the permeability in the stationary regime, is carried out by measuring the infiltration rate of Gas Q and is given in equation (3-27) (Chen, 2013):

$$K_A = \frac{2\, \eta_G\, Q\, P_{out}\, H}{A\, (P_{in}^2 - P_{out}^2)} \tag{3-27}$$

where η_G is the gas viscosity and the other symbols are the same as in eq (3-26).

It is important to note that the measure of the permeability may be affected by an effect of molecules collision called Klinkenberg effect (Klinkenberg, 1941). This phenomenon takes place

when the average free path of a gas molecule becomes larger than the pore radius. The smaller the size of the pores is, the greater is the possibility of gas molecules colliding. Due to these collisions between the solid walls and the gas molecules, sliding phenomena take place. The velocity at the pore walls is no longer zero. In this case of flow, not only the viscosity is the driving force behind the gas flow in the pores but also its friction with the solid walls.

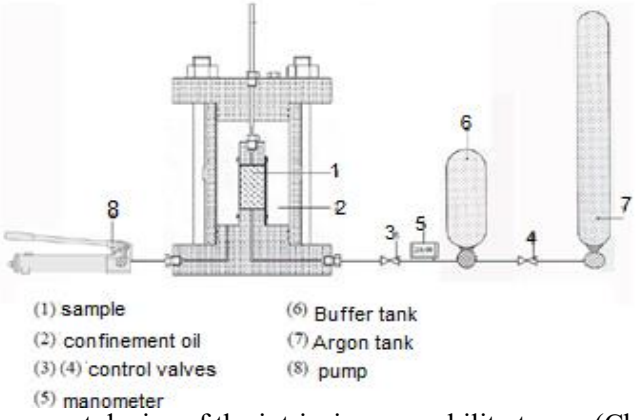

Fig. 3-8- Measurement device of the intrinsic permeability to gas (Chen, 2013)

For an imposed pressure value, the value of the apparent permeability K_A of the gas is higher than the 'intrinsic' permeability K_G, the two being linked by the relation commonly used (Lion, 2004; Villain et al., 2001) given in equation (3-28):

$$K_A = K_G\left(1 + \frac{\Gamma}{P_m}\right) \tag{3-28}$$

Γ is the Klinkenberg coefficient and P_m is the average gas pressure $P_m = \frac{P_{in}+P_{out}}{2}$. The coefficient Γ can be determined experimentally from the slope of the curve plotting K_A as a function of $(1/P_m)$ as shown in Fig. 3-9. When the average gas pressure is high, i.e when the gas phase tends to a liquid phase ($1/P_m$ tends towards zero), the apparent permeability determined experimentally is equal to the intrinsic one and the Klinkenberg effect is to be neglected. The experimental method presented above can also be used for measurements of effective permeability, by using samples with different water saturations.

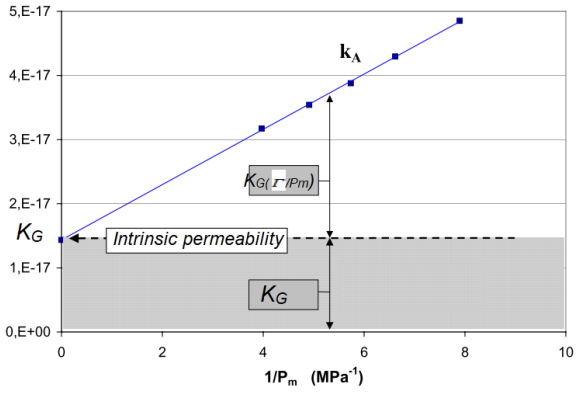

Fig. 3-9 – Experimental measurement of the apparent and 'intrinsic' permeability to gas (Picandet, 2001)

According to the definition given for the 'intrinsic' permeability in section 3.1.2.1 as the permeability of the sample in the saturated state, one should measure the same value for the sample saturated with different fluids. Hence, we should obtain $K_G = K_L$. However, according to the experimental feedbacks of Bary et al. (2012), Mjahad (2012), Thiery et al. (2007), Tsivilis et al. (2003), the value of the measured permeability by water or gas injection can differ by several orders of magnitudes, which leads to conclude that there exists no 'intrinsic' permeability for cementitious

materials. The difference may be due to different phenomena that may take place during the tests. It could be for example, slippage of gas molecules on the solid walls at low gas injection pressures or possibility of rehydration of the cement by water molecules. The result is confirmed by other authors, such as Loosveldt et al. (2002), who performed an experimental comparison (Table 3-1). This table shows an experimental comparison made by Loosveldt et al. (2002) between 'intrinsic' permeability to liquid water K_w, liquid ethanol K_e (considered as an inert fluid) and gas K_g. Experimental results from Loosveldt et al. (2002) show that the permeability of liquid water and gas can differ by several orders of magnitude: K_w is significantly lower than K_g. The ratio between 'intrinsic' permeability to liquid ethanol and gas is not as high as that between liquid water and gas, which can be explained by the fact that ethanol is an inert fluid unlike liquid water.

Sample	K_g (10^{-17} m^2)	K_e (10^{-17} m^2)	K_w (10^{-17} m^2)	K_g/K_e	K_g/K_w	K_e/K_w
1A	1.96	0.96	0.014	2.04	140	69
2A	1.52	0.85	0.054	1.79	28	16
3A	0.96	0.49	0.03	1.96	32	16
4A	1.01	0.53	0.041	1.90	25	13
1B	2.49	0.95	0.11	2.62	23	9
2B	2.56	1.02	0.035	2.51	73	29
3B	2.18	0.75	0.078	2.90	28	10
4B	2.60	1.14	0.28	2.28	9.3	4

Table 3-1- Experimental comparison of the permeabilities of cement mortars to various fluids (Loosveldt, 2012)

Thiery et al. (2007) show a significant difference between the 'intrinsic' permeability to water and gas for a high performance concrete (BH), an ordinary concrete (BO) and a cement mortar (M25): the two permeabilities differ by 5 orders of magnitude for the high performance concrete (Table 3-2). Mjahad (2012) also measures for a high performance concrete, an intrinsic water permeability of 3.9 10^{-21} m^2 compared to 5.4 10^{-18} for intrinsic gas permeability, i.e. a ratio of the order of 1000. According to the authors, the ratio between water permeability and gas permeability appears to be different. It is therefore difficult to draw conclusions as to the origin of this difference.

Bétons	E/C (-)	ϕ (-)	K_l (m^2)	K_g (m^2)
M25	0,840	0,148	2.10^{-19}	4.10^{-16}
BO	0,487	0,120	3.10^{-21}	8.10^{-17}
BH$^{(*)}$	0,267	0,082	2.10^{-22}	1.10^{-17}

Table 3-2- Intrinsic water permeability and intrinsic gas permeability of cementitious materials (results from Baroghel-Bouny (1994) and from Thiery et al. (2007)

According to what has been presented in this section, we can see that while determining experimentally the intrinsic permeability of a cementitious material, different transfer mechanisms can occur, depending on the fluid used during the experiments. As a result, the evaluated permeability might present different orders of magnitude depending on the applied experimental method and employed fluids. In contrast to direct measurement of permeability by application of a gradient of pressure, an alternative method has been used by different authors (Carette et al., 2020; Coussy et al., 2001; Reviron, 2009). This alternative method consists in determining the 'intrinsic' permeability by an inverse analysis of mass loss curves measured during the drying of the material. In some cases, with this method, other unknown transfer parameters could be also determined.

Last but not least, the 'intrinsic' permeability of cementitious materials is known to increase with the temperature (Bary et al., 2012; Drouet et al., 2015; Jooss and Reinhardt, 2002). This increase is usually explained by the strong dependence of the permeability on the morphology of the porous network together with the fact that the increase in temperature can induce a degradation in the

concrete microstructure. This degradation can either be linked to an alteration of the cement C-S-H gel (Aono et al., 2007; Brue et al., 2012) or to a coarsening of the pores structure. The latter is due to the decomposition of the ettringite that might start at a temperature as low as 50°C (Zhou and Glasser, 2001).

While using an inverse analysis (back calculation from the mass loss curves), Drouet et al. (2015) determined the permeability of a cement paste for temperatures varying between 20°C and 80°C. The transfer equations used by Drouet et al. (2015) are based solely on the transport of liquid water, without taking into account the diffusion of water vapor in the gas phase; the external relative humidity is 85%. The obtained intrinsic permeabilities for a CEMI, CEM II, CEMV are given in Fig. 3-10. Following the obtained results, Drouet et al. (2015) proposed a double exponential relation to fit the obtained values given by equation (3-29) with K_0 and T_c the fitted parameters given in Table 3-3.

$$K(T) = K_0 exp(exp\left(\frac{T - 293.15}{T_c}\right) - 1) \tag{3-29}$$

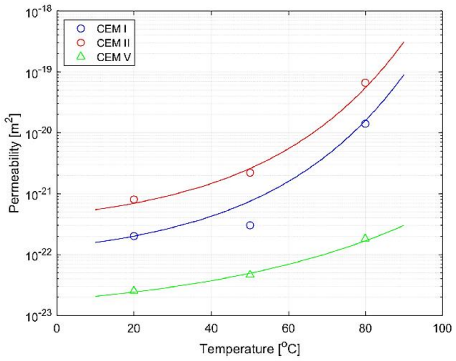

Fig. 3-10 –Intrinsic permeability of cement paste with respect to the external temperature (Drouet et al., 2015)

Parameter	CEM I	CEM II	CEM V	Unit
K_0	12.2×10^{-23}	69.1×10^{-23}	N/A	m²
T_c	35.7	35.7	N/A	K

Table 3-3 - Fitted parameters for the formula (3-30) proposed by Drouet et al. (2015)

When submitted to a high temperature (>100°C), the material can present thermal damages. Various relations present in the literature link the intrinsic permeability to the temperature by the means of damage parameters. A debrief of those relationships has been given by Davie et al. (2012). Table 3-4 presents a certain number of those relations where A_T, A_P are fitted parameters on experimental data and *D* is parameter that describes the damage state of the material.

Function of Bary et al. cited in Davie et al.(2012)	$K(T) = K_0 \cdot (10^{4D})$	Damage parameter D = [0 ; 1]
Tenchev R.T (2001)	$K(T) = K_0 \cdot \left(\frac{\phi}{\phi_0}\right)^{2/3}$	ϕ the porosity at the temperature T ϕ_0 the porosity at the ambient temperature T_0
Gawin et al . 1999)	$K(T) = K_0 \cdot \left(10^{A_T(T-T_0)}\right) \cdot \left(\frac{P_{gz}}{P_{atm}}\right)^{A_P}$	$A_T = 0.005$ $A_P = 0.368$

Table 3-4- Permeability as function of temperature, for high temperatures (Davie et al., 2012) - K_0 is the permeability of concrete when exposed to ambient conditions.

3.1.3.3. Relative permeability of concrete

The assessment of the relative permeability can be done by measuring the effective permeability at different saturation levels and then by dividing it by the value of the 'intrinsic' permeability. This has been done by Mualem (1976) who eventually proposed a model for estimating the relative permeability of porous media. In his article, Mualem (1976) defines the degree of effective saturation S_e as given in chapter 2 equation (2-22).

The work of Mualem (1976) consisted in determining the relative hydraulic conductivity K_{rl} of unsaturated soils.The equation proposed by the author is:

$$K_{rl} = (S_e)^p \cdot \left(\int_0^{S_e} \frac{1}{h(x)} \, .dx \Big/ \int_0^1 \frac{1}{h(x)} . dx \right)^q \tag{3-30}$$

with h the water column that can be related to the capillary pressure by the Jurin equation (refer to chapter 2). The values of the coefficients p and q are determined by the author while doing tests on 45 soils and deducing an optimal value for p which is 0.5 and for q which is 2.

Van Genuchten (1980) continued the work of Mualem (1976) and proposed an equation that links the degree of saturation S_e to the water column with m and n being the Van Genuchten model parameters (see equation 2-22). The inverse function $h(S_e)$ is then introduced into equation (3-30). To simplify the calculation, the condition $m = 1 - 1/n$ is imposed. The Van Genuchten (1980) work resulted in a simplified equation for the calculation of the relative hydraulic conductivity of the soil with the assumption of $m = 1 - 1/n$:

$$K_{rl} = {S_e}^p . \left(1 - \left(1 - {S_e}^{\frac{1}{m}}\right)^{\mathrm{m}}\right)^{\mathrm{q}} \tag{3-31}$$

In the above equation, $K_{rl} = 0$ when $S_e = 0$ (so that $w = w_r$) and $K_{rl} = 1$ when $S_e = 1$ (so that $w = w_s$). The relative gas permeability K_{rg} is deduced and is written in the form (Verdier, 2001):

$$K_{rg} = (1 - S_e)^p . \left(1 - {S_e}^{\frac{1}{m}}\right)^{\mathrm{q.m}} \tag{3-32}$$

Despite the fact that the model of Mualem (1976) was essentially designed for relative permeabilities in soils, it is frequently used also for cementitious materials. Indeed, Monlouis-Bonnaire et al. (2004) verify the validity of expression (3-31) for an ordinary concrete. The authors show that this relationship (with p = 0.5) does not represent well the experimental data of measured relative gas permeabilities (Fig. 3-11 - left). By setting the value of p to 5.5, the model describes experimental data better (Fig. 3-11 - right).

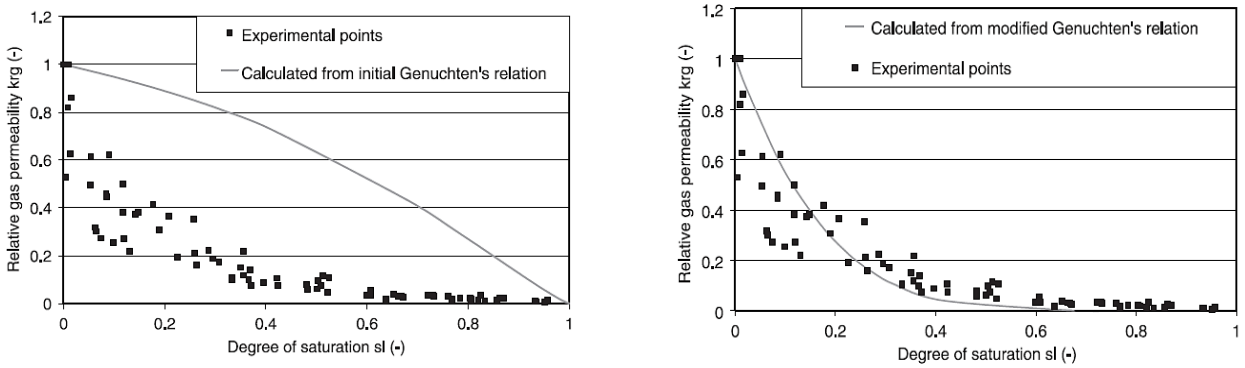

Fig. 3-11 – (left) Mualem's model with p=0.5 for an ordinary concrete – (right) Mualem's model with p=5.5 for an ordinary concrete

3.1.4. Hydric boundary conditions and mass exchange coefficient

When drying or damping a material, a water exchange between the outer surface of the material and the surrounding environment takes place. The relative humidity of the air near the surface is not the same as that of the ambient air far enough away from the specimen (Nilsson, 2002). Daian (2013) investigates the water evaporation at the surface of a plate having a constant thickness. The author notes that the drying boundary condition of the plate is affected by an air flow that occurs in a boundary layer (parietal layer) near the exposed outer surface. The boundary layer is an interface zone which is established between a body and a surrounding fluid during a relative movement between the two (see Fig. 3-12). The thickness of this boundary layer depends essentially on the ambient air properties (wind velocity, temperature), on the surface characteristics (surface roughness) and on the location on the plate (close or not to the edges).

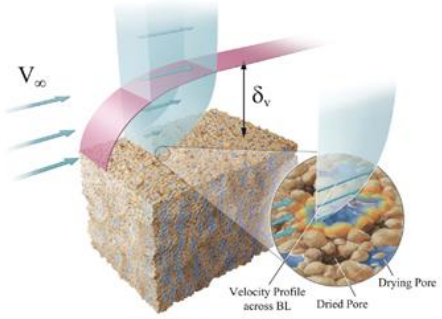

Fig. 3-12 – Boundary layer of thickness δ_v - (Shahraeeni et al., 2012)

The diffusive evaporation flux of water vapor, during the drying of a material, can be calculated from Fick's law (equation (3-12)), which is written in 1D in the direction x normal to the plate surface, as:

$$E_v = -D_{v0}\frac{d\rho_v}{dx} \approx -D_{v0}\frac{(\rho_{vs}-\rho_{va})}{\delta_v} \tag{3-33}$$

where E_v (kg/m^2/s in SI units) is called the evaporation flux normal to the surface, D_{v0} the air vapor diffusion through free air, ρ_{vs} the vapor density on the surface, ρ_{va} the density of the vapor in air far from the surface and δ_v is the thickness of the boundary layer.

Daian (2013) and Obeid (2001) take up this equation and write it in the form of an exchange equation (i.e. as a function of a mass exchange coefficient). The authors consider a relative humidity $h_{R,surface}$ at the external surface of the porous material and $h_{R,air}$ in the surrounding ambient air. The evaporation flux at the boundary is then written as:

$$E_v = -h_\rho\,(\rho_{vs} - \rho_{va}) \tag{3-34}$$

where h_ρ(m/s) is called the mass exchange coefficient and is equal to D_{v0}/δ_v . Equation (3-34) can also be written as in equation (3-35) where the relative humidities appear explicitly. This form was also adopted by Carette et al. (2020).

$$E_v = -h_\rho\,\rho_{vsat}(h_{R,surface} - h_{R,air}) \tag{3-35}$$

This evaporation condition was also written in Reviron (2009) as a function of the capillary pressure while using the Kelvin equation. Equation (3-35) is then written as given in equation (3-36) with h_{pc} a transfer coefficient function of the capillary pressure. However, the relationship proposed by Reviron (2009) can be debated. Indeed, define a capillary pressure $P_{c,air}$ is not quite physical given that no liquid phase is usually found in the ambient air.

$$E_v = -h_{pc}\left(P_{c,surface} - P_{c,air}\right) \tag{3-36}$$

In the purpose of estimating a value for the evaporation flow, multiple methods are proposed in the literature. One of the commonly used methods to determine the value of E_v is an empirical graph proposed in the ACI (1999) as given by Fig. 3-13. This graph allows to estimate the evaporation flow according to properties of the ambient air (temperature, wind speed, relative humidity) and the temperature at the surface of the concrete. It should be noted that the chart proposed by the ACI (1999) can only be used when the concrete is at early age (fresh state).

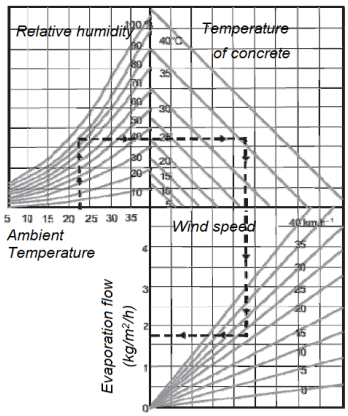

Fig. 3-13 – Estimation of the evaporation flow according to ACI (1999) – cited in Reviron (2009)

Another method is to try to estimate the thickness of the boundary layer (δ_v). While considering a hypothesis of a steady-state flow in the fluid surrounding the specimen, Blasius (1908) proposed a relation that links this thickness δ_v to the characteristic length of the sample and the square root of the Reynolds number. This leads to an equation in the form of (3-37) with C_1 an experimentally fitted constant and V_∞ the velocity of the ambient air:

$$\delta_v = \frac{C_1}{V_\infty} \tag{3-37}$$

Finally, some authors tried to estimate the mass exchange coefficient h_ρ by inverse analysis (Boukadida and Ben Nasrallah, 2002; Kaya et al., 2007). Table 3-5 resumes the values found for h_ρ by various authors. It should be noted that in some cases, authors fitted a value of the product $h_\rho\ \rho_{vsat}$ (with ρ_{vsat}= 0.0173 kg/m^3 at T=20°C (Daian, 2013)). However, as shown in Table 3-5, the values determined for this coefficient can vary by several order of magnitudes depending on the study.

Authors	$h_\rho\ \rho_{vsat}$***(kg/m²/s)***	h_ρ***(m/s)***
Ožbolt et al. (2016)	[8.00E^{-07} ; 2.00E^{-06}]	[4.62E^{-05} ; 1.16E^{-04}]
Huang et al. (2015)	1.50E^{-05}	8.67E^{-04}
Sakata (1983)	1.00E^{-03}	5.78E^{-02}
Zhang et al. (2015)	0,01	5.78E^{-01}
Tran Le (2016)	[1.7E^{-06} ; 2.6E^{-04}]	[1E^{-04} ; 1.5E^{-02}]
Boukadida et al. (2002)	1,73E^{-05}	1.00E^{-03}
Kaya et al. (2007)	1.73E^{-08}	1.00E^{-06}
Ferroukhi et al. (2016); Künzel (1995); Obeid, (2001)	1.00E^{-09}	5.78E^{-08}

Table 3-5- Order of magnitudes of the mass exchange coefficient according to the literature

Another method that permits to estimate an order of magnitude for the mass exchange coefficient is to relate it to a heat exchange coefficient, given that the latter is more studied in the literature. The phenomenon of liquid water vapor transfer can be related to the heat transfer, since the same transport mechanisms (diffusion, convection) are involved (Daian, 2013). Thereafter, to link the two exchange coefficients the following equation (3-38) was proposed by Chilton and Colburn, (1934) with the parameter *n = 2/3:*

$$h_T = h_\rho . \rho_{vp} \cdot C_{vp} \cdot (Le)^n \quad (3\text{-}38)$$

with:

- h_T: heat exchange coefficient (W/m^2.K)
- C_{vp}: calorific capacity of water vapor (J/K/kg)
- Le : Lewis' number $Le = \lambda_{vp} / (\rho_{vp} \cdot C_{vp} \cdot D_{v0})$
- n: Constant depending on the geometry and type of material and the type of air flow (proposed to be equal to 2/3 for a flat plate under a laminar flow)

This type of analogy between heat and mass transfer coefficients has been used and verified experimentally by several authors (Boukadida and Ben Nasrallah, 2002; Kaya et al., 2007): it turns out that the value of *n* is not always 2/3. The value differs according to the geometry and type of material and the type of air flow. As an example, for beds of granular particles, experiments show that *n* can take values that vary between 1.31 and 1.74 (Kaya et al., 2007). By applying equation (3-38) and considering a heat exchange coefficient of 10 W/m^2.K (Lee et al., 2008) for a temperature of 20°C, h_ρ varies between 8.5E^{-03} m/s and 9E^{-03} m/s (for *n* between 2/3 and 1.74). For a temperature of 50°C, while considering the same heat exchange coefficient, this leads to a coefficient h_ρ varying between 9E^{-03} m/s and 1E^{-02} m/s.

Expressing the evaporation flux as a function of a mass exchange coefficient can be very useful. However, the values determined for this coefficient can vary by several order of magnitudes depending on the study (Carette et al., 2020; Soleilhet, 2018). Therefore, a more accurate method for determining this coefficient might be needed.

3.1.5. Conclusions

This part of the chapter consisted in stating the various transfer laws found in the literature and that can describe the drying of a porous material. These laws included most importantly Darcy's and Fick's laws. To be correctly applied, the latter laws require the knowledge of some transfer parameters. These parameters can refer to properties of the fluid transported such as its density and viscosity. They could also refer to the properties of the material in which the transfer is occurring. Those parameters include the diffusion coefficient and the intrinsic permeability.

In section 3.1.3, experimental methods for determining both the diffusion coefficient and intrinsic permeability were introduced. It was shown that the intrinsic permeability is not exactly 'intrinsic' as proposed by its definition. In fact, such property is supposed to depend only on the materials properties. However, it was shown, based on experimental observations, that this permeability depended also on the fluid that was used to measure it. Finally, some models for the diffusion coefficient and relative permeability were also proposed by various authors in the literature.

In a final part of this section, the mass exchange boundary condition that could be considered for a transfer problem was introduced. This condition consists in evaluating an evaporation flow at the surface of the drying sample. Different methods for assessing this flow were given.

3.2. Mass loss and water permeability experiments on concrete F44Adj

The aim of the tests presented in this section is to characterize the transport phenomena occurring during the drying of the F44Adj concrete. To that purpose, the determination of the transfer parameters is required. In this section, we present two experimental procedures that were used for this objective. The first one is a drying test, carried out in the civil engineering laboratory of EDF R&D, MMC department, for the F44Adj concrete and that resulted in mass loss curves. The latter will be used in an inverse analysis (section 3.3) to determine the concrete transfer parameters. The second experimental test aims to measure the water permeability of the F44Adj concrete at room temperature of 20°C. This test was executed in the LaM^{cube} laboratory of Lille's university.

3.2.1. Mass loss experiments

Material composition and sample fabrication

3.2.1.1. The samples used for the mass loss experiments are part of the 30 samples fabricated for the whole experimental campaign (refer to section 2.2.1). The composition and the conditioning of those samples is also given in section 2.2.1. At the start of the tests, all samples were removed from the autogenous storage area after being kept there for 28 days. As a matter of fact, the time between the fabrication of the C1PG^{SP} package and the storage phase varies from one to a few months for the shell and less than a week for the cap, it was therefore decided to choose an intermediate time (28 days) between those two durations. The period of 28 days is considered representative for a relatively mature concrete. The samples were tested under two thermo-hydric conditions: the first one corresponds to the storage phase of the concrete packages (T=50°C, h_R = 30%); the second one corresponds to common ambient conditions (T=20°C, h_R = 50%) for comparison purposes.

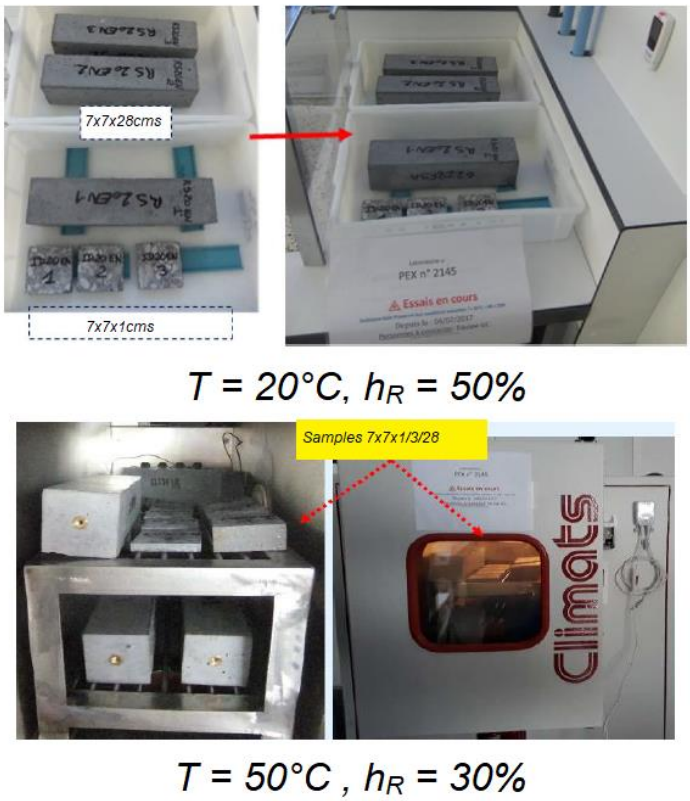

Fig. 3-14 – Tested samples at (T=20°C, h_R = 50%) and (T=50°C, h_R = 30%)

For each external condition, various sizes of samples were chosen to be tested (see in Fig. 3-14):

- For (T=20°C, h_R = 50%), three samples of 7x7x28cm were tested (named RS20-EN (1) to (3)). Additionally, a fourth sample was used to fabricate three small samples of 7x7x1cm (named ID20-EN(1) to (3)). The samples were put into a regulated room.
- For conditions (T=50°C, h_R = 30%) realized in a climatic chamber, three samples of 7x7x28cm were tested (named RS50-EN(1) to (3)). A fourth sample was used to fabricate four small samples of 7x7x1cm (named ID50-EN (1) to (4)) and three samples of 7x7x3cm (named ID50-ENb (1) to (3)).

As described in section 2.2.2.1, the thicknesses of the samples (1 cm or 3 cm) were chosen to obtain moisture equilibrium in a reasonable duration. Moreover, having different geometries to be tested allows us to have a better idea of the evolution of the transfer kinetics with respect to the samples size. The fabrication of the 7x7x1cm and 7x7x3cm samples was done mainly using a circular saw blade except for one sample (IDEN50-4) that was fabricated using a wire saw. This will allow to compare between two cutting methods and their effect on the drying of the sample.

The samples are dried from all sides. Indeed, the test devices were designed to allow a free circulation of air around the samples. On the bottomside, the specimens are supported by a grid made of round iron bars in the climatic chamber (test at 50°C) and are placed on spacers in a room under an ambient atmosphere.

Finally, the samples RS20-EN (1) to (3) and RS50-EN (1) to (3) are also used for measuring lengths variations (results in chapter 4). It should be noted that, during those measurements, experimental difficulties were encountered, causing a wrongful evolution of the lengths variations of the sample RS20-EN (1). Therefore, in section 4.3.2.1, we present only the results obtained on the samples RS20-EN (2) to (3) and RS50-EN (1) to (3).

3.2.1.2. Mass loss curves and measurement of the imposed thermo-hydric conditions

First, all samples were weighed before launching the tests. During drying, the samples are weighed daily at the beginning; after approximately 100 days the weighing is spaced since the mass evolution is slower. The mass weighing is done manually. The balance is located in the same room as the climatic chamber and the samples put at 20°C. This geographical proximity provides good measuring conditions, i.e. very short duration between the moment when the sample is taken out of the climatic chamber, weighed, and put back into the climatic chamber, which limits the disturbance of the state of the material.

The relative mass loss curves for both tested conditions and for all tested geometries are given in Fig. 3-15 (for the condition (T=20°C, h_R = 50%)) and Fig. 3-16 (for the condition (T=50°C, h_R = 30%)). A relative mass loss $\Delta m/m_{ini}$ is chosen to be represented to compare the different geometries. The temperature and relative humidity were monitored during the entire test. Several sensors were used to measure the thermo-hydric conditions in the climatic chamber and in the room. The sensors are automatic thermo-hygrometers or Rotronic sensors linked to an acquisition system. The range of uncertainty of the sensors is of ($\pm$1.6°C) for the temperature and ($\pm$8.4%) for the relative humidity. The measured thermo-hydric conditions are also given in Fig. 3-15 and Fig. 3-16.

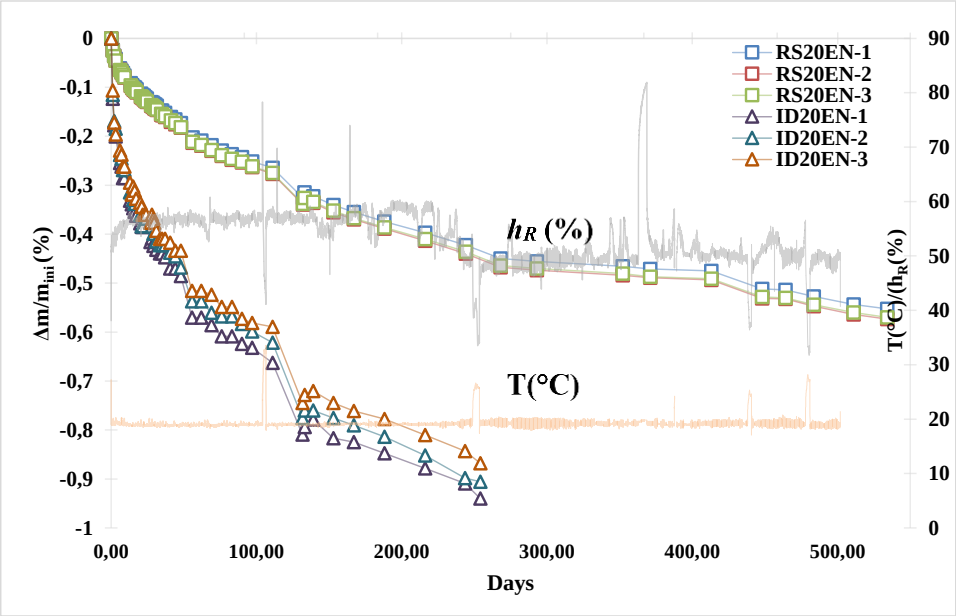

Fig. 3-15 – Relative mass loss curves and measurements of thermos-hydric conditions for samples exposed to (T=20°C, h_R = 50%)

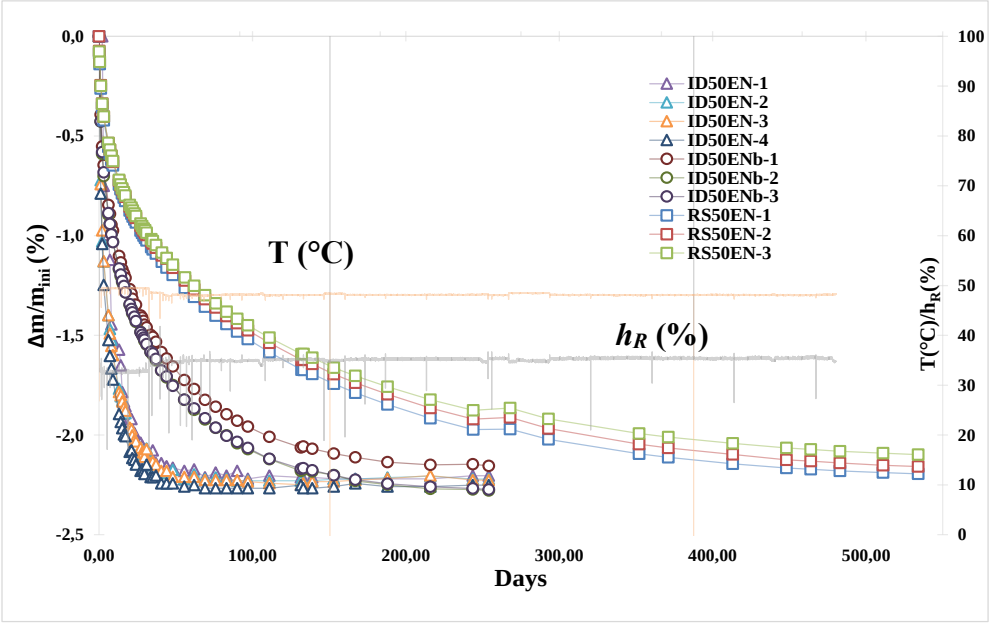

Fig. 3-16 - Relative mass loss curves and measurementss of thermos-hydric conditions for samples in the climatic chamber exposed to (T=50°C, h_R = 30%)

We can observe that the temperature and relative humidity measurements inside the climatic chamber (Fig. 3-16) vary around the target values, with a temperature of 50°C (with variations lower than 0.5°C) and relative humidity of 35%(±5%). These variations are due to several factors: first of all, the position of the sensor because the thermo-hydric conditions may be different depending on the position in the climatic chamber; secondly, the accuracy of the sensors. For temperatures, the variations remain limited and within the range of uncertainty of the sensors. For the relative humidity, the variations are greater, but are still contained within the uncertainty range of the sensors. Concerning the temperature and relative humidity of the room where the samples under ambient conditions are placed (Fig. 3-15), a relatively good temperature stability can be observed around 20°C. Larger fluctuations are observed for the relative humidity. It should be remembered that the air conditioning system imposes a relative humidity of 50% ± 10%. In the same figure, we can observe conditioning failures that took place around the 100th day and the 400th day.

Regarding the relative mass loss curves shown in Fig. 3-15 and Fig. 3-16, we could see that the curves of each family of specimens of the same size are fairly well grouped. This means that the dispersion of the measurements is fairly limited in this drying test. These observations show the consistency and reproducibility of the results. On another hand, the impact of a higher temperature and lower relative humidity on the drying amplitude is clearly observed. In fact, for a given geometry, for instance the 7x7x1cm samples, the relative mass loss after 254 days is significantly greater at 50°C/ h_R =30% ($\Delta m/m_{ini}$ = 2.3%) than that at 20°C/h_R=50% ($\Delta m/m_{ini}$ = 0.9%).

For the purpose of precisely detecting the thermo-hydric equilibrium, an equilibrium criterion (given in equation (3-39)) was used:

$$\frac{\Delta m(t)}{\Delta t}/m_{ini} \leq \varepsilon_{crit} \tag{3-39}$$

This formula allows a quantification of the equilibrium state reached for a curve of mass loss and to decide if the test can be stopped. Standard NF EN ISO 1257 (2013) proposed a criterion of equilibrium value of 10^{-3}%/day, criterion that was satisfied for all tested samples. However, as it could be seen in Fig. 3-15, this adopted equilibrium criterion was not sufficient for the samples of 20°C. The samples needed more time to reach equilibrium.

For the samples tested at T=50°C/ h_R =30%, the final equilibrium is reached for all the samples tested in the regulated climatic chambers. The relative mass loss at the end of the test at T=50°C/ h_R =30% is identical for all sizes of the tested samples. The tests lasted 254 days for the 7x7x1cm and 7x7x3cm samples and 534 days for the 7x7x28 cm samples.Finally, Fig. 3-16 allows to compare the mass evolution of the sample cut with a wire saw (ID50EN-4) with respect to the other 1 cm thick samples cut with a circular saw blade (ID50EN-(1) to(3)). Indeed, cutting with a wire saw is more precise and takes longer to perform (a few hours) than cutting with a circular saw (in the order of one minute). Fig. 3-16 shows that the cutting method does not induce any visible effect on the mass loss of the samples.

3.2.1.3. Porosity, densities and initial saturation assessment

In this section the porosities and densities are presented for all tested samples. We aim to recall that the porosity of each sample is calculated using equation (2-27). The dry mass of a sample is measured after drying it in an oven at 105 °C; its saturated mass corresponds to the mass measured after saturating the dry specimen under water (more details are given in sections 2.2.2.3 and 2.2.2.4). In Table 3- 6, the average porosities and densities of each geometry are compared to the porosity and densities of a 7x7x28 cm sample that was kept under autogenous conditions for 530 days.

Condition	***Sample***	ρ_{ini} ***(kg/m³)***	ρ_{sat} ***(kg/m³)***	$\Delta\rho_{ini-sat}$ ***(%)***	ρ_{dry} ***(kg/m³)***	$\Delta\rho_{ini-dry}$ ***(%)***	***Ø (%)***	$S_{w,ini}$
T = 20°C	7x7x28	2495	2497	0.08	2419	-3.05	7.72	0.97
h_R = 50%	7x7x1	2424	2442	0.75	2353	-2.95	9.20	0.79
T = 50°C	7x7x28	2536	2550	0.53	2462	-2.93	8.53	0.85
h_R = 30%	7x7x3	2431	2447	0.66	2358	-2.97	9.03	0.82
	7x7x1	2424	2443	0.78	2352	-2.99	9.33	0.79
Autogenous	7x7x28	2503	2509	0.24	2432	-2.8	7.50	0.92

Table 3- 6- Comparison of the porosities and densities of the tested samples

$\Delta\boldsymbol{\rho_{init-sat}}$ is the relative variation between the initial and saturated density of the sample and is calculated as follows: $\Delta\boldsymbol{\rho_{init-sat}} = \left(\frac{\rho_{sat}-\rho_{ini}}{\rho_{ini}}\right)$. $\Delta\boldsymbol{\rho_{init-dry}}$ is the relative variation between the initial and dry density of the sample and is calculated as follows: $\Delta\boldsymbol{\rho_{init-dry}} = \left(\frac{\rho_{dry}-\rho_{ini}}{\rho_{ini}}\right)$. The initial degree of saturation $S_{w,ini}$ is calculated as in equation (2-5).

For the same applied thermo-hydric condition between different geometries, the following differences are noted from Table 3- 6:

- For both tested conditions, the measured porosity of the 7x7x28cm samples is smaller than those of the 7x7x1 cm samples. For (T= 20°C, h_R = 50%), the relative difference between porosities is of 19%. For the condition (T= 50°C, h_R = 30%), the relative difference between the porosities of the 7x7x28cm and 7x7x1cm samples is of 9.3%. On another hand, the initial degrees of saturation $S_{w,ini}$ of the 7x7x28cm samples are larger than those of the 7x7x1cm samples. For (T= 20°C, h_R = 50%), the relative difference between the initial degrees of saturation of the different geometries is 22%. For the condition (T= 50°C, h_R = 30%), this relative difference between the initial degrees is of 7.6%.
- For a given condition (i.e. (T= 20°C, h_R = 50%) or (T= 50°C, h_R = 30%)), when the size of the sample increases, the relative difference $\Delta\rho_{ini-sat}$(%) and the porosity decrease.

Furthermore, it is important to observe that for samples of a given dimension submitted to different conditions, the porosities and initial degrees of saturation are not the same. For instance, for the 7x7x28cm samples submitted to an autogenous condition and to (T= 20°C, h_R = 50%), (T= 50°C, h_R = 30%), the porosity was 7.5%, 7.7% and 8.53% respectively. In the same spirit, the initial degree of saturation of those 3 samples was different, as it was equal to 0.92, 0.97 and 0.85, respectively.

The previous observations can be explained by either of the two proposed scenarios in section 2.2.2.6: scenario 1 of a possibility of an insufficient saturation of the larger samples (i.e., samples with dimensions of 7x7x28cm and 7x7x3 cm), and scenario 2 of a possible formation of micro-cracks in the small 7x7x1cm and 7x7x3 cm due to their process of fabrication. As a matter of fact, as shown in section 2.2.2.6, if a micro-crack is formed in the 7x7x1cm and 7x7x3cm samples, this will lead to an increase of their measured saturated masses and volumes. Therefore, it will lead to an increase in the measured porosities and a decrease of the initial degree of saturation (since the saturated mass intervenes in the calculation of those parameters). On another hand, if the 7x7x28cm and 7x7x3cm samples were not fully saturated, this would lead to an underestimation of their measured saturated mass and eventually to an underestimation of their measured porosities and an overestimation of the measured degree of saturation.

3.2.1.4.

A correction of the porosities and saturation degree is therefore required and is described in the following section.

Correction of porosities, densities, and evolution of the degree of saturation

For the correction methodology of the samples porosities, densities and degree of saturation at every instant *t* of the test, one can refer to section 2.2.2.6.

First, we consider the scenario 1 of an insufficient saturation of the 7x7x28cm and 7x7x3cm samples. We suppose then that only the 7x7x1cm samples have been fully saturated and dried. Therefore, for each tested condition (T= 20°C, h_R = 50%) and (T= 50°C, h_R = 30%), the saturated density of the 7x7x28cm samples and 7x7x3cm will be corrected as follows: $\rho_{sat,corr} = \rho_{ini,7x7x28} + x(\%)\ \rho_{ini,7x7x28}$.

The value of x is given by $\Delta\rho_{ini-sat}$ *(%)* in Table 3-7. It corresponds to the relative amount of water gained by the 7x7x1cm samples while being saturated. For the condition (T= 20°C, h_R = 50%), $x = 0.75\%$ and, for (T= 50°C, h_R = 30%), $x = 0.78\%$. Once the saturated densities are corrected, the porosity can be calculated as given in equation (2-28). The corrected porosities and densities are given in Table 3-7.

Condition	*Sample*	ρ_{ini}*(kg/m³)*	ρ_{sat} *(kg/m³)*	$\rho_{sat,corr}$*(kg/m³)*	ρ_{dry}*(kg/m³)*	∅*(%)*
T = 20°C h_R = 50%	7x7x28	2495	2497	2514	2419	9.50
T = 50°C	7x7x28	2536	2550	2556	2462	9.40
h_R = 30%	7x7x3	2431	2447	2450	2358	9.20

Table 3-7 - Corrected saturated densities and porosities of the tested samples. The correction applied is the one corresponding to the so-called 'scenario 1'.

For the calculation of the corrected degree of saturation at each measurement time, according to equation (2-29) in chapter 2, we write equation (3-40):

$$S_{w,corr}(t) = \frac{\rho(t) - \rho_{dry}}{\rho_{sat,corr} - \rho_{dry}} \tag{3-40}$$

This equation is applied for each tested geometry under the different thermo-hydric conditions applied during experimental tests. For every sample, the density $\rho(t)$ is calculated as follows: $\rho(t) = \rho_{ini} + \Delta\rho(t) = \rho_{ini} + \frac{\Delta m(t)}{V_0}$ with V_0 the volume of each tested sample and $\Delta m(t)$ the measured total mass loss during the test (from Fig. 3-15 and Fig. 3-16). The above corrections will lead to the curves Fig. 3-17, showing the evolution of the saturation degree in time. By applying this correction, we obtain the same initial saturation degree for all samples, equal to approximately 0.8 (see Fig. 3-17).

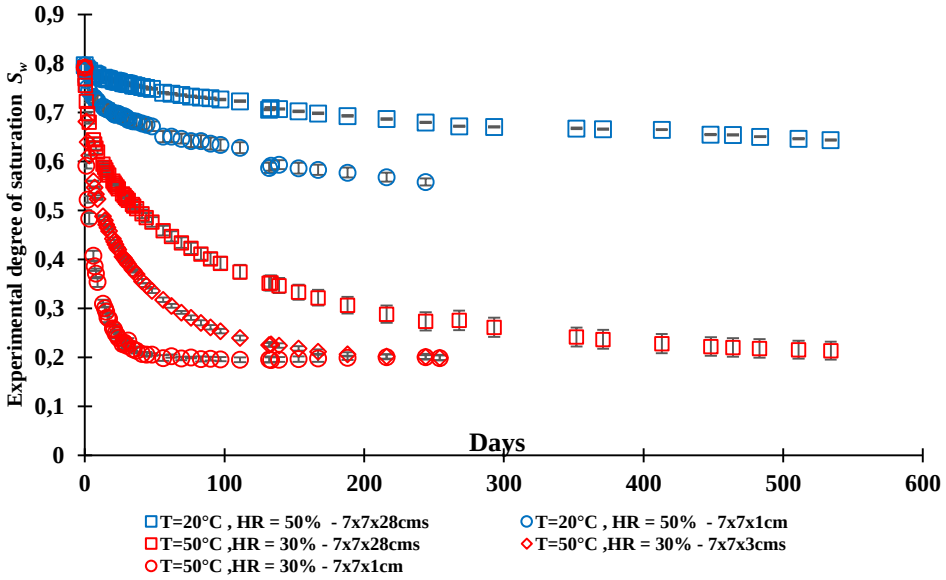

Fig. 3-17 – Experimental saturation degree evolution, when considering the case of scenario 1, in which the saturation of the 7x7x28cm and 7x7x3cm samples was insufficient.

The scenario 2 consists in assuming the formation of micro-cracks in the 7x7x1cm and 7x7x3cm samples due to their fabrication process. It should be noted that, according to this scenario, measurements (porosity, saturated density, dry density) performed on the 7x7x28cm sample kept in autogenous conditions are considered the most reliable among all samples; the reason for this choice

is due to the fact that this sample has been submitted neither to a fabrication process nor to drying. The corrected degree of saturation will be calculated according to equation (3-41), where $\rho_{dry,endo}$ and $\rho_{sat,endo}$ are respectively the dry density and saturated density of the 7x7x28cm sample kept in autogenous conditions and $\rho_{corr}(t)$ the corrected density at time t:

$$S_{w,corr}(t) = \frac{\rho_{corr}(t) - \rho_{dry,endo}}{\rho_{sat,endo} - \rho_{dry,endo}} \quad (3\text{-}41)$$

In equation (3-41), the corrected density is calculated as: $\rho_{corr}(t) = \rho_{ini,endo} + \Delta\rho(t) = \rho_{ini,endo} + \frac{\Delta m(t)}{V_0}$ where V_0 is the volume of the small samples if no micro-cracks have occurred. The latter volume can be estimated from equation (2-35) with m_{ini} the initial mass of the 7x7xcm or 7x7x3cm samples. The resulting saturation degree is given in Fig. 3-18. By applying this correction, we obtain the same initial saturation degree for all samples, equal to approximately 0.92.

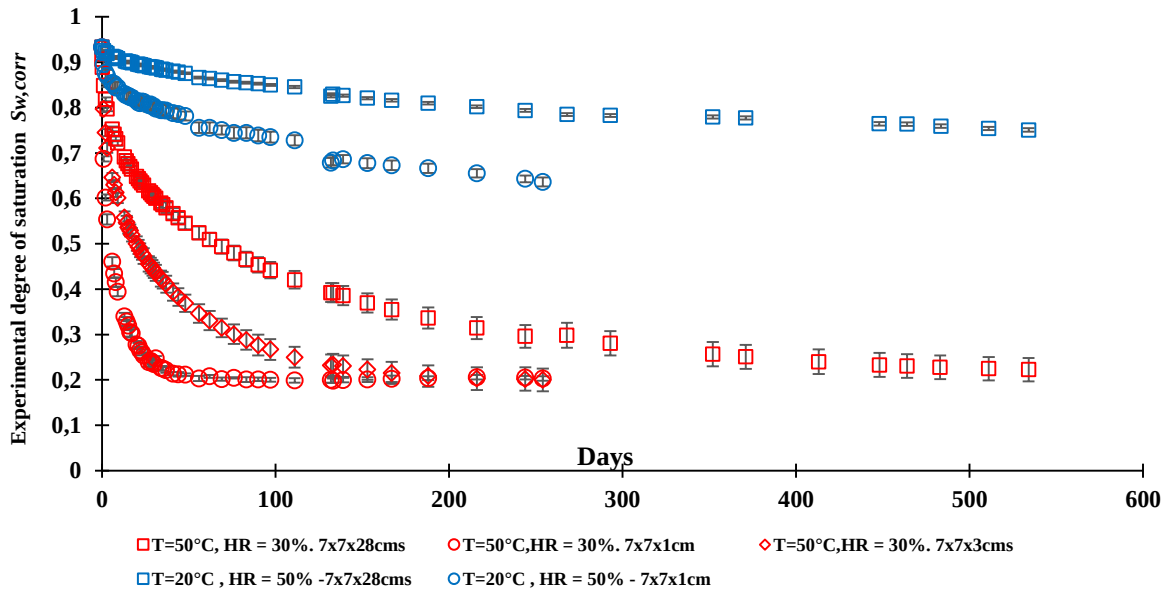

Fig. 3-18- Experimental saturation degree evolution function of time in the case of scenario 2, in which micro-cracks are assumed to have formed in the 7x7x1cm and 7x7x3cm samples.

3.2.1.5. Comparison of the mass loss experiments and the desorption experiments results

Let us remind that, in chapter 2, the desorption curves $S_w(P_c)$ of the F44Adj concrete were given. For each temperature, different curves were presented (see chapter 2 – Fig. 2-33, Fig. 2-38, Fig. 2-39 – See Appendix – Fig.A-1) according to two measuring techniques (SSS and DVS) and two correction scenarios (see section 2.2.2.6).

In this section, we aim to study the consistency, in terms of the saturation degree, between the experimental data obtained from the desorption isotherm (section 2.2) and those obtained from the mass loss or drying experiments (section 3.2). To help in this reasoning, Table 3-8 presents the saturation degree at the beginning and end of the drying experiments (from Fig. 3-17 and Fig. 3-18) for each sample and each considered scenario. On another hand, we remind in Fig. 3-19 the desorption isotherms obtained with the SSS and DVS methods, for each of the correction scenarios: the scenario 1 of insufficient saturation of bigger samples in Fig. 3-19 (a),(c) and the scenario 2 of micro-cracks formation in the small samples in Fig. 3-19 (b),(d).

		Scenario 1 - insufficient saturation		Scenario 2 - micro cracks formation	
Condition	***Sample***	$S_{w,ini}$	$S_{w,end}$	$S_{w,ini}$	$S_{w,end}$
T = 20°C	7x7x28	0.79	0.64	0.92	0.75
h_R = 50%	7x7x1	0.79	0.56	0.92	0.66
T = 50°C	7x7x28	0.79	0.21	0.92	0.22
h_R = 30%	7x7x3	0.79	0.19	0.92	0.20
	7x7x1	0.79	0.19	0.92	0.2

Table 3-8 - Initial degree $S_{w,ini}$ and final degree $S_{w,end}$ of saturation of the tested samples, for the 2 scenarios used for correction.

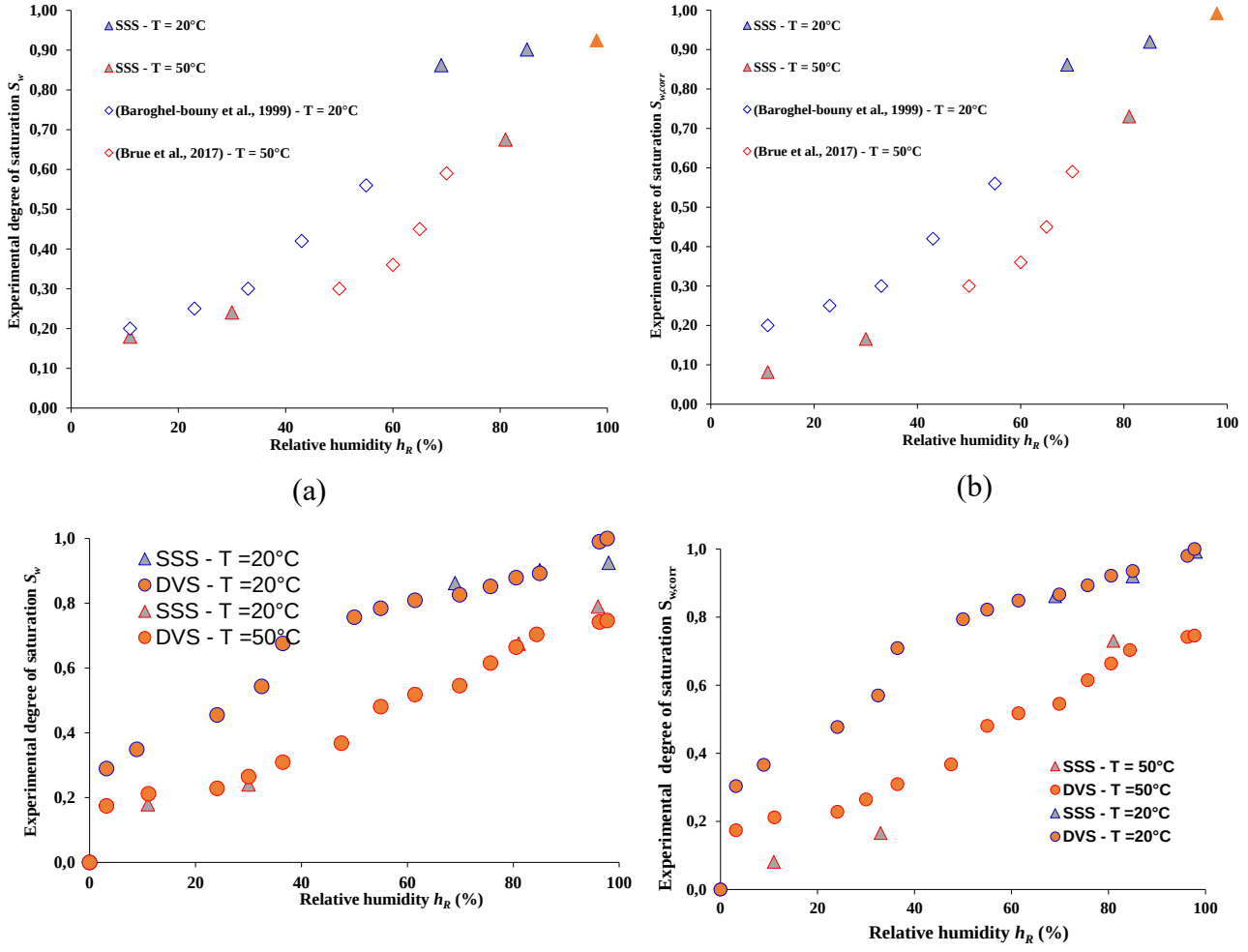

Fig. 3-19 – F44Adj Experimental desorption isotherms for scenario 1 of insufficient saturation of the larger samples obtained with (a) SSS (c) DVS, and for scenario 2 of micro-cracks formation obtained with (b) SSS (d) DVS

First, after a close comparison between Table 3-8 and Fig. 3-19, we can observe that the experimental desorption isotherms obtained with the DVS method (Fig. 3-19-c and Fig. 3-19-d) are not in accordance with the mass loss test measurements, for both considered scenarios. As a matter of fact, after applying the correction, for a temperature of 20°C, the initial saturation degree (shown in Table 3-8) is $S_{w,ini}$ = 0.79 for the scenario 1 and $S_{w,ini}$ = 0.92 for the scenario 2. Looking at Fig. 3-19-c and Fig. 3-19-d, we observe that the initial autogenous state of these samples will correspond to

a relative humidity of 60% approximately. However, this value of relative humidity is not in accordance with previous observations (done in 2.2.2.3), where it was noted that the initial autogenous state will correspond to a relative humidity of 85% for the temperature of 20°C, since by placing the specimens at this relative humidity there were no mass loss or gain. This inconsistency leads us to conclude that the DVS obtained data are not reliable in this experimental campaign. This could be due to the fact that the DVS isotherm is done on concrete powder contrary to the mass loss tests done on concrete samples that might be more representative of the concrete structure.

A second remark regards the SSS experimental desorption isotherms shown in (Fig. 3-19 - a and Fig. 3-19 - b). We note that, if scenario 1 is considered, the initial saturation degree $S_{w,ini}$ = 0.79 (Table 3-8) will present a relative humidity of approximately 65% according to Fig. 3-19 – a. Again, this is not in accordance with the observation done in section 2.2.2.3 that shows that the initial autogenous state at 20°C corresponds to 85% of relative humidity. This inconsistency leads us to exclude the scenario 1 of insufficient saturation.

It is important to note that the latter inconsistencies found between the drying test and desorption test can be due to the material variability. As a matter of fact, a different set of samples was tested for each of those two experiments. Moreover, the geometry of the tested concrete samples differed for the SSS and mass loss experiments (for which massive samples were used) and for the DVS experiments (for which powders were used).

As a conclusion, for all computations in the present and in the following chapters, we choose to work with the desorption isotherms obtained with the SSS method while considering the scenario 2 of micro-crack formation in the 7x7x1cm and 7x7x3cm samples (Fig. 3-19 – b). Indeed, for this scenario, the experimental data obtained with the drying tests appear to be in accordance with the experimental SSS desorption isotherm.

3.2.2. Experiment to measure water permeability

For the purpose of having an approximate order of magnitude of the permeability of the F44Adj concrete, water permeability tests are carried out in the LaM^{cube} laboratory of Lille's university. The three samples (6588F1, 6588F2, 6588F3) received by the LaM^{cube} laboratory are cored and cut into 7 cylinder specimens of 65mm diameter and 60mm height, named (6588F1-(1)(2), 6588F2-(1)(2)(3),6588F3-(1)(2)). Surface grinding is used to give an optimal parallelism of the surfaces. The specimens are then placed under a vacuum bell and saturated.

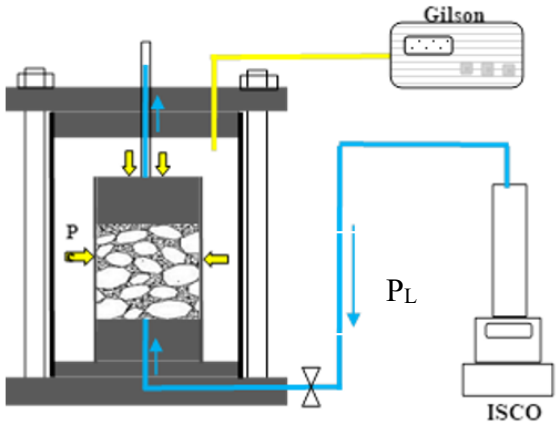

Fig. 3-20 – Measurement device used for the permeability to water

The tests are carried out under a permanent flow regime in a hydrostatic triaxial cell put into an air-conditioned room at 22°C. The water injection device will be provided by a high-precision "ISCO" pump (0.0001ml) with continuous monitoring of the injected volume by a "LabView" system (Fig. 3-

20). A confinement pressure P = 3MPa was applied to the sample during the test. The water is pumped at a constant pressure of P_L=1.5MPa from one end of the sample to the other end, which is under an atmospheric pressure. The water flow circulating through the sample can be regularly measured.

Equation (3-26) can be applied and the water permeability can be calculated. This test was executed on the 7 concrete specimens. The obtained raw values and average values for each sample are given in Table 3-9. The values obtained ranged between 3.54 10^{-21} m^2 and 8.17 10^{-21} m^2. An average value on all samples of 5.66 10^{-21} $m^2 \pm 1.77\ 10^{-21}$ m^2 can be noted.

Specimen	*K_L (m^2)*	*K_L- average (m^2)*	*Standard deviation (m^2)*
6588F1-1	4.08 10^{-21}	6.13 10^{-21}	2.89 10^{-21}
6588F1-2	8.1710^{-21}		
6588F2-1	5.51 10^{-21}	5.62 10^{-21}	2.13 10^{-21}
6588F2-2	3.5 10^{-21}		
6588F2-3	7.80 10^{-21}		
6588F3-1	5.78 10^{-21}	5.30 10^{-21}	6.86 10^{-22}
6588F3-2	4,81 10^{-21}		

Table 3-9– Experimental liquid water permeability of the F44Adj concrete

3.2.3. Conclusions

This section introduced experimental tests that were used to better characterize the hydric transfer in the F44Adj concrete. These tests included, in a first part (section 3.2.1), a drying test of the concrete done under two environmental conditions (i.e. (T=20°C, h_R = 50%) and (T=50°C, h_R = 30%)) and for various geometries of samples. The tests resulted in mass loss curves that could describe the drying kinetic of the concrete. Following the obtained results, important differences were noted in terms of the measured densities, porosities and degrees of saturations of the concrete samples. This led to some corrections of the results according to the so-called scenarios 1 and 2 (described in chapter 2 – section 2.2.2.6). On another hand, the corrected results in term of saturation degree were compared to the desorption tests results obtained with the DVS and SSS methods (chapter 2 – section 2.2). The comparison showed inconsistencies in some cases (especially when the DVS isotherms were considered). This allowed to select the most accurate desorption isotherm (namely the SSS desorption isotherms measured with the salt solution) and the most appropriated correction scenario (namely scenario 2 of micro-crack formation in the small samples). The selected experimental curves (mass loss curves, desorption isotherms) will be used in section 3.3.2 to calibrate the drying kinetic of the F44Adj concrete.

The second part of this section 3.2.2 described an experimental test done in the LaM^{cube} laboratory of Lille's university for measuring a water permeability of the F44Adj concrete. These tests led to an approximate value of 5.6 10^{-21} m^2 for the permeability of the concrete to water.

3.3. Modelling of drying experiments on F44Adj concrete

In this section, we aim to model the drying kinetic of the F44Adj concrete to describe the mass loss curves introduced in section 3.2.1 and use the thermo-hydric-mechanical (THM) model of the finite element code *Code_Aster*.

At first, a general introduction of the THM model is given in section 3.3.1. Section 3.3.2 details the calibration simulations that are executed. In the latter section, the transfer input parameters of the model, the calibration method and the transfer parameters to be fitted are given. A conclusion on the obtained results is given in section 3.3.3.

3.3.1. THM model

The THM model implemented in *Code_Aster* and used in this study is based on the transfer laws found in the literature and introduced in section 3.1.

Once reformulated, the expression of the mass flows given in equations (3-5), (3-12) are introduced in the mass conservation equations (3-1) altogether with equation (3-2). Hence, there will be for each of the water and air constituents a relationship which relates the first derivative $\dot{S_w}$ of the degree of saturation to the pressures of the liquid, water vapor and gas, noted P_L, P_{vp}, P_G, respectively. Since P_{vp} and P_L are not independent (section 3.1.2.4) the system unknowns can be reduced to two pressures (P_L, P_G) or equivalently (P_C, P_G) with $P_C = P_G - P_L$. In the THM model of *Code_Aster*, the two unknown pressures are chosen to be the capillary pressure P_C and gas pressure P_G.

For the purpose of linking the degree of saturation S_w to the capillary pressure P_C or the pressures P_L of the liquid and P_G of the gas, one can use a water retention relation (for instance the Van Genuchten's modified model - refer to chapter 2). The boundary conditions that can be considered in this model are introduced in section 3.3.1.1. Moreover, a modification of the relative permeability expression found in the THM model is proposed in section 3.3.1.2.

3.3.1.1. Boundary conditions

The boundary conditions to be considered in the THM model are of two types: either a Dirichlet condition or a mixed boundary condition. The Dirichlet condition consists in imposing a capillary pressure, corresponding to the thermo-hydric external condition, by means of the Kelvins equation (see equation 2-9).

As for the mixed boundary condition, a new mass exchange condition was implemented in *Code_Aster*. The mass exchange condition is usually written as in equations (3-34) and (3-35), i.e. as a function of the water vapor density or of the relative humidity. However, in the considered model the mass exchange flow is written as a function of the capillary pressure. By noting $P_{C,surface}$ the capillary pressure at the solid surface, equation (3-35) can be written as in equation (3-42):

$$E_v = h_\rho \, \rho_{vs}(T) \left(e^{-\frac{M \cdot P_{C,surface}}{\rho \, .R.T}} - h_{R,air} \right) \tag{3-42}$$

3.3.1.2. Reformulation of the relative permeability function

The relative permeability found in the THM model is as proposed by Mualem (1976). Accordingly, the expression of the relative permeabilities to gas and liquid are expressed by equations (3-31) and (3-32) and with the effective saturation S_e given in equation (2-22).

However, in the current framework a modification of the expression of effective saturation was proposed in chapter 2 as given in equation (3-43):

$$S_e = \frac{w - w_r}{w_{100} - w_r} = \frac{S_w - S_r}{S_{100} - S_r} \tag{3-43}$$

where S_{100} and w_{100} are respectively the saturation and the water content for 100% relative humidity.

Subsequently, to ensure consistency of the expressions, it is important to repeat the same computational steps performed by Mualem (1976) and Van Genuchten (1980) to arrive at an expression of K_{rl} as a function of the modified effective saturation S_e. To this purpose, we start from equation (3-30) by introducing the water content w_{100} at h_R=100%, which is different from the water content w_s at complete saturation of the sample. The expression obtained is:

$$K_{rl} = \left(\frac{w-w_r}{w_{100}-w_r}\right)^{p} \left[\int_{w=w_r}^{\frac{w-w_r}{w_{100}-w_r}\cdot(w_{100}-w_r)} \frac{1}{h(x)}\, dx \Big/ \int_{w=w_r}^{w_s-w_r} \frac{1}{h(x)}\, dx\right]^{q} \tag{3-44}$$

The term $\frac{w-w_r}{w_{100}-w_r}$ in equation (3-44) corresponds to the new definition of the effective saturation S_e given by equation (3-43).Thus we obtain:

$$K_{rl} = \left(S_e \frac{w_{100}-w_r}{w_s-w_r}\right)^{p} \left[\int_{w=w_r}^{S_e\cdot(w_{100}-w_r)} \frac{1}{h(x)}\, dx \Big/ \int_{w=w_r}^{w_s-w_r} \frac{1}{h(x)}\, dx\right]^{q} \tag{3-45}$$

and

$$K_{rl} = \left(S_e \frac{w_{100}-w_r}{w_s-w_r}\right)^{p} \left[\int_{0}^{S_e\cdot\frac{w_{100}-w_r}{w_s-w_r}} \frac{1}{h(x)}\, dx \Big/ \int_{0}^{1} \frac{1}{h(x)}\, dx\right]^{q} \tag{3-46}$$

Using the same approach as Van Genuchten (1980) to solve the previous integrals leads to a final expression of K_{rl} given in (3-47) or equivalently in equation (3-48) :

$$K_{rl} = \left(S_e \frac{w_{100}-w_r}{w_s-w_r}\right)^{p} \left(1 - \left(1 - \left(S_e \frac{w_{100}-w_r}{w_s-w_r}\right)^{\frac{1}{m}}\right)^{\mathrm{m}}\right)^{2} \tag{3-47}$$

$$K_{rl} = \left(S_e \frac{S_{100}-S_r}{1-S_r}\right)^{p} \cdot \left(1 - \left(1 - \left(S_e \frac{S_{100}-S_r}{1-S_r}\right)^{\frac{1}{m}}\right)^{\mathrm{m}}\right)^{2} \tag{3-48}$$

In the previous expression, we note that:

- when $S_w = S_r$, we have $S_e = 0$ and K_{rl}=0.
- when $S_w = S_{100}$, K_{rl} is not necessarily equal 1. However, if $S_w = S_{100} = 1$, then K_{rl}=1.

Similarly, K_{rg} is written as in equation (3-49) as:

$$K_{rg} = \left(1 - S_e \frac{S_{100}-S_r}{1-S_r}\right)^{p} \left(1 - \left(S_e \frac{S_{100}-S_r}{1-S_r}\right)^{\frac{1}{m}}\right)^{2.\mathrm{m}} \tag{3-49}$$

3.3.2. Simulation of drying kinetic of F44Adj concrete

In this section, the THM model (section 3.3.1) with the saturation evolution curves shown in section 3.2.1.4 will be used to calibrate the transfer parameters defining the F44Adj drying kinetic.

We remind that the correction scenario 2 was retained for all further simulations (see section 3.2.1.5). Hence, the experimental saturation curves to be calibrated are given in Fig. 3-18. The used

calibration method is given in section 3.3.2.1. The external thermo-hydric conditions and the model input parameters are given in section 3.3.2.2.

The transfer parameters to be calibrated are more precisely: the 'intrinsic' permeability and the mass exchange coefficient h_ρ if a mixed boundary condition is needed (section 3.3.2.4). For the relative permeability, as a first approach, the value of the parameter *p* (in equations (3-47) and (3-48)) will be fixed to 0.5 (Mualem, 1976). However, section 3.3.2.5 studies the impact of the value of this parameter and hence of the relative permeability on the drying kinetic. The diffusion coefficient is taken as a first approach as given by Millington (1959) in equations (3-23) and (3-24). Its impact on the drying kinetic is studied in section 3.3.2.6.

3.3.2.1. Method of calibration

For each of the tested conditions of (T=20°C, $h_R = 50\%$) and (T=50°C, $h_R = 30\%$), we look for a set of parameters able to model simultaneously the drying kinetic of all the tested geometries. We remind that, for (T=20°C, $h_R = 50\%$), two geometries of 7x7x1cm and 7x7x28cm are tested, whereas, for (T=50°C, $h_R = 30\%$), three geometries of 7x7x1cm, 7x7x3 cm and 7x7x28cm are tested.

The optimization consists in minimizing the error function given in equation (3-50):

$$J(c) = \sum_n (Err_{L2}(F_n^{exp}, F_n^{calc}))^2 \tag{3-50}$$

where *n* is the number of experimental curves (or the number of geometries tested at a certain thermo-hygrometric condition). For instance for T=20°C, $n = 2$ and for T=50°C, $n = 3$; F_n^{exp} are the experimental curves and F_n^{calc} are the curves simulated with the THM model. Err_{L2} is the relative standard square error given in equation (3-51) with v_{exp}^i the experimental vector of values and v_{calc}^i the numerical vector of values for each geometry.

$$Err_{L2} = \sqrt{\sum \left(v_{exp}^i - v_{calc}^i\right)^2 / \sum (v_{exp}^i)^2} \tag{3-51}$$

The minimization of equation (3-51) is performed by using the Levenberg-Marquardt algorithm. Since the calibration of the parameters requires an iterative procedure of optimization, a large number of computations are required. Therefore, numerical simulations are done at first on axisymmetric geometries which are equivalent to those of the 3D ones in terms of drying kinetics. The equivalent geometries will be introduced in section 3.3.2.2. Finally, once the optimal values for the transfer parameters are calibrated, a 3D calculation is run to verify the accuracy of the solution and shown in section 3.3.2.7.

3.3.2.2. External thermo-hydric conditions and input parameters of model

The external thermo-hydric conditions to be considered correspond to a moving average over 5 days of the temperature and relative humidity curves shown in Fig. 3-15 and Fig. 3-16. These conditions are imposed on all the exposed faces of the simulated samples.

The transfer parameters to be inputted in *Code_Aster* in order to perform simulations are given in Table 3-10 according to the considered imposed temperature.

Variable	*T=20°C*	*T=50°C*	*Reference*
Viscosity η_L of liquid water (Pa.s)	1.E-03	5.E-04	See section 3.1.2.1 – Equation (3-9)
Viscosity η_G of gas (Pa.s)	1.13E-05	1.24E-05	See section 3.1.2.1 – Equation (3-10)
Saturated vapor pressure $P_{vp,sat}$ of water (Pa)	2295	11632	Rankine's formula: $P_{vp,sat} = P_{atm}\, exp\left(13.7 - \frac{5120}{T}\right)$
Mass density ρ_L of liquid water (kg/m^3)	998	900	See section 3.1.2.1 – Equation (3-7)
Molar density of water M_w^{mol} (kg/mol)	0.018	0.018	(Coker, 2007)
Density ρ_{vsat} of saturated vapor (kg/m^3)	0.0173	0.0831	(J.F. Daian, 2013)
Diffusion coefficient D_{v0} of air (m^2/s)	2.33 10^{-5}	2.6 10^{-5}	See section 3.1.3.1 - Equation (3-25)
Porosity	7.5%	7.5%	Experimental data of the 7x7x28cm sample put in autogenous conditions – Table 3- 6
Initial saturation	0.92	0.92	Experimental data – Table 3- 6
Initial density of the concrete	2503	2503	Experimental data of the 7x7x28cm sample in autogenous conditions – Table 3- 6
Van Genuchten's parameters (S_r, S_{100}, n, c)	(0.05, 0.988,2.353,2.073)	(0.03,0.93,2.353,3.42)	See chapter 2 – Fig .2-39

Table 3-10- Model input transfer parameters function of the considered temperature

3.3.2.3. Equivalent axisymmetric meshing

The 3D calculation of the (7x7x28cm; 7x7x3cm; 7x7x1cm) samples can be done equivalently on the 1/8 of their geometries as schematized in Fig. 3-21.

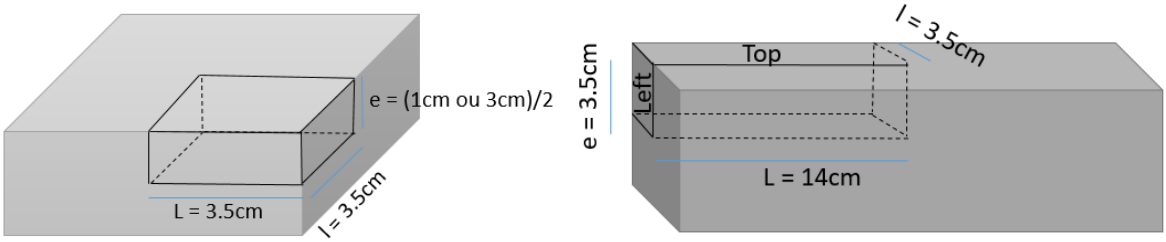

Fig. 3-21 – Representation of one eighth of the 3D geometry of the: (left) 7x7x1cm and 7x7x3 cm samples - (right) 7x7x28cm sample

However, since a large number of computations is needed in order to calibrate the transfer parameters (i.e. permeability and mass exchange coefficient), the calculation on a 3D mesh is time expensive given the large number of degrees of freedom (DOF). Therefore, we need a simplified model with fewer DOF. The followed approach corresponds to modelling the samples through a hypothesis of axial symmetry, so that the initial 3D problem becomes a 2D one. In practice, this comes back to look for a cylindrical sample having the same time evolution of the mass loss (or of the saturation degree) as the 3D sample.

For the small samples (7x7x1cm or 7x7x3cm), the 2D equivalent axisymmetric geometry is constructed by considering the same height (h=1cm or h=3cm) and the same volume for both the 2D and 3D geometry. This will lead to an equivalent cylinder with a radius of r = 3.94 cm. Another possibility is to consider a constant exposed surface and volume between the 2D and 3D geometry, with the height h and the radius r as unknowns. For the 7x7x1cm sample, the latter hypothesis leads to a possible 2D geometry with (r = 4.02 cm; h = 0.96cm) which is considered very close to the (r = 3.94 cm; h = 1cm) previously calculated. For the 7x7x3 cm sample, this hypothesis leads to (r = 4.23 cm; h = 2.61cm).

For the 7x7x28 cm sample, while considering the same exposed surface and volume between the 2D and 3D geometries, we obtain two couples of possible solutions (r = 9.78 cm; h = 4.56 cm) and (r = 3.38 cm; h = 38.04cm). The geometry (r = 3.38 cm; h = 38.04cm) is chosen for further computations.

To make sure that each of the previously estimated geometries led eventually to an evolution of the degree of saturation identical to that of a 3D geometry, computations with similar material properties and transfer parameters were done on the 2D/3D geometries. The results are then compared. The computations were done for two considered types of boundary condition:

- A Dirichlet boundary condition where a condition of (T=20°C, h_R = 50%) is directly imposed on the borders of the tested sample exchanging with the neighboring environment.
- A mixed boundary condition with a mass exchange flux considered between the sample and the neighboring environment (a random value of $h_\rho = 5.10^{-6}$m/s is considered).

The comparison between the obtained evolution of the saturation degree for 2D and 3D models is shown in Fig. 3-22: (a) for the 7x7x1cm sample, (b) for the 7x7x3cm sample, (c) for the 7x7x28cm sample.

As can be seen in Fig. 3-22, for a considered geometry and fixed boundary condition, the differences between computations on the 2D axisymmetric geometry and the 3D one are small enough (maximum relative error of 0.014) to consider the 2D axisymmetric geometries representative of the 3D geometries.

Therefore, in the next sections, the calibration of the transfer parameters will be done on axisymmetric geometries with the meshes given in Fig. 3-23. The 7x7x1cm mesh contained 9526 elements, the 7x7x3cm contained 8800 elements and the 7x7x28cm presented 9720 elements. The meshing was refined closer to the exposed edges.

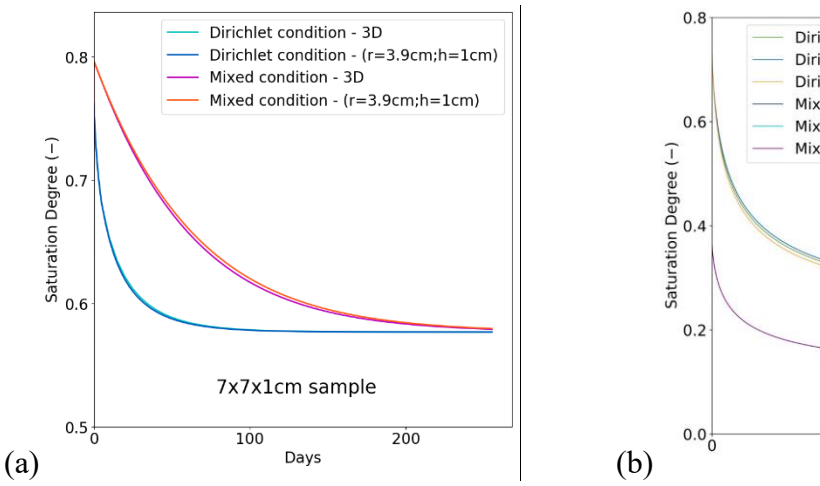

(a)

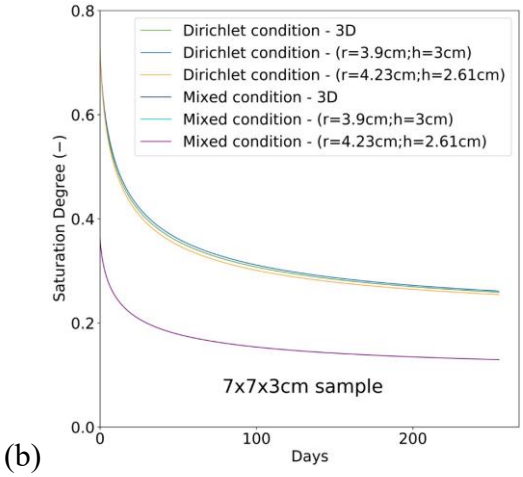

(b)

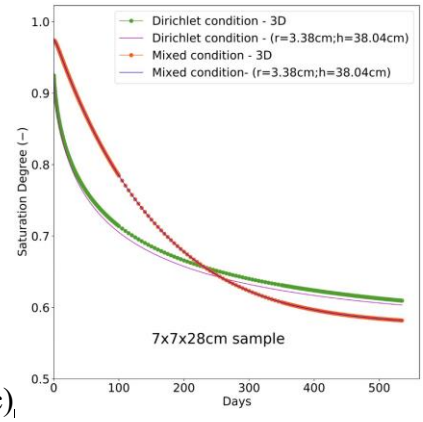

(c)

Fig. 3-22 – Comparison between computations on 2D axisymmetric geometries and 3D geometries of (a) 7x7x1cm sample (b) 7x7x3cm sample (c)7x7x28cm sample

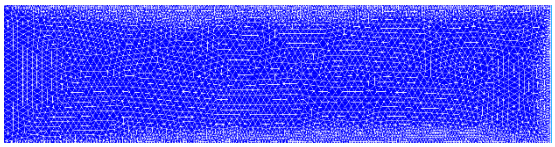

(a) r = 3.9cm - h=1cm

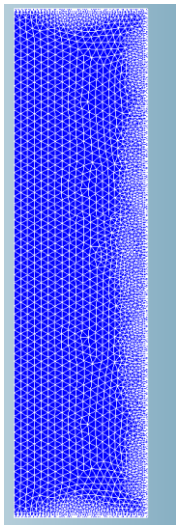

(b) r = 3.38cm - h=38.04cm

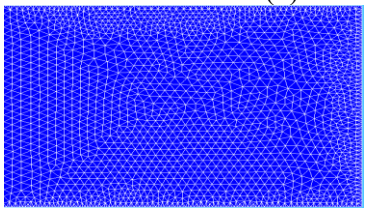

(c) r = 3.9cm - h=3cm

Fig. 3-23 – 2D axisymmetric meshes used for computations done on (a) 7x7x1cm samples (b) 7x7x28cms amples(c) 7x7x3cm samples

3.3.2.4. Impact of transfer boundary conditions on drying kinetic

In this section, we show several simulations that allow us to select a proper transfer boundary condition (a Dirichlet condition or a mixed condition) and to calibrate the transfer model parameters, i.e. the 'intrinsic' permeability and the transfer coefficient when required. In this case study, the relative permeability is taken as in equations (3-47), (3-48) with the parameter $p = 0.5$ as proposed initially by Mualem (1976).

Dirichlet boundary condition:

As a first approach, a Dirichlet boundary condition is tested to simulate the drying kinetics of the F44Adj concrete. We calibrate separately parameters for the two experimental thermo-hydric conditions (T=20°C, $h_R \approx 50\%$) and (T=50°C, $h_R \approx 30\%$).

For the external condition of (T=20°C, $h_R \approx 50\%$), the fitted value of the permeability is of 4.10^{-24} m^2. The simulated curves against the experimental values are shown in Fig. 3-24. We should remind that the sudden evolution observed at 100 days corresponds to a conditioning failure in the test room (see section 3.2.1.2).

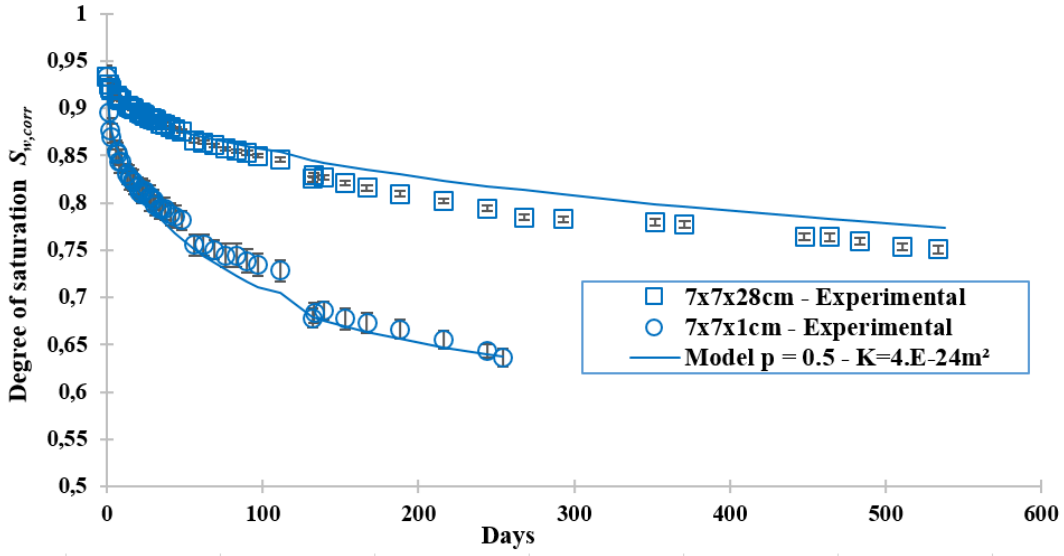

Fig. 3-24 – Calibration of the drying kinetics of two geometries tested at (T=20°C, $h_R \approx 50\%$) with a Dirichlet boundary condition

Based on the experimental data, one can observe that for both geometries, hydric equilibrium has not been reached yet: the degree of saturation when the test was stopped (i.e. $S_{w,end} = 0.64$ and $S_{w,end}$ 0.75 respectively for the 7x7x1cm and 7x7x28cm samples) is larger than the equilibrium degree of saturation given by the desorption isotherm for (T=20°C, $h_R \approx 50\%$), which is equal to 0.54.

Moreover, we tend to see that the model fits in a satisfactory way the drying kinetic of the 7x7x1cm sample, while it slightly underestimates that of the 7x7x28cm samples. This could mean that the permeability of the 7x7x28cm samples might be larger than the fitted value of 4.10^{-24} m^2, which corresponds to the 7x7x1cm samples. This can be explained by the fact that the 7x7x28cm samples, when fabricated inside metallic molds, presented three lateral faces that were in direct contact with the molds internal faces. This might have induced a boundary effect (Ollivier and Torrenti, 2008): the assembly of aggregates near the molded faces was hindered. Therefore, on those faces, the space between the aggregates might have increased and the cement paste fraction also increased. Given that the cement paste is usually more porous than the aggregates, the porosity at the three lateral faces of the 7x7x28cm will be greater than the porosity measured inside the sample. This greater porosity at the exchanging faces of the 7x7x28cm samples might lead to an acceleration of its

experimental drying kinetic. This boundary effect might have been eliminated for the 7x7x1cm samples that were submitted to a sawing process on all their lateral faces.

For the external condition of (T=50°C, $h_R \approx 30\%$), the fitted value of the permeability is of $4.5 \cdot 10^{-22}$ m^2. The simulated and experimental curves are shown in Fig. 3-25. The data show that the 7x7x1cm samples have nearly reached equilibrium after 150 days. In fact, according to the considered desorption isotherm, the model is tending to an equilibrium saturation degree of 0.18 corresponding to an external relative humidity of approximately 34% (see Fig. 3-16). This equilibrated value is slightly different from that observed experimentally in Fig. 3-25 for the 7x7x1cm and 7x7x3cm samples where a 0.2 approximate value for the saturation degree is noted. This might be due to material differences, since the desorption isotherms (refer to chapter 2) were executed on samples different from those tested in the mass loss experiments (section 3.2.1).

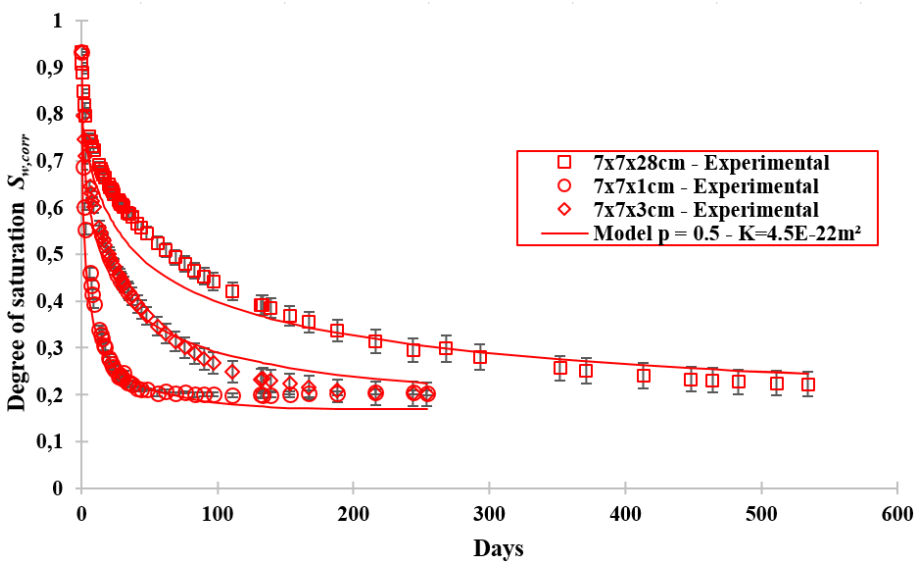

Fig. 3-25 - Calibration of the drying kinetics of three geometries tested at (T=50°C, $h_R \approx 30\%$) with a Dirichlet boundary condition.

The above results show that a Dirichlet boundary condition might be sufficient for calibrating the drying kinetic of each of the tested external conditions separately. However, it should be noted that the calibrated permeability for the (T=20°C, $h_R = 50\%$) condition is different than that obtained for (T=50°C, $h_R = 30\%$). Moreover, a value of 4.10^{-24}m^2 for the intrinsic permeability of the concrete might appear relatively small. Therefore, as a first approach, it could be questioned whether a mixed boundary condition with a mass exchange coefficient could be more accurate to model the drying kinetic of the F44Adj concrete.

Mixed boundary condition:

In this section, the impact of imposing a mixed boundary condition (equation (3-42)) at the external faces of the samples will be studied. In this study, the exchange coefficient h_ρ is a parameter to be fitted on the experimental data together with the 'intrinsic' permeability. Again, we analyze separately the two experimental thermo-hydric conditions (T=20°C, $h_R \approx 50\%$), (T=50°C, $h_R \approx 30\%$). To simplify the calibration of the optimal parameters, the optimization algorithm is applied for one parameter at a time, fixing first the 'intrinsic' permeability and then fitting the parameter h_ρ. This choice will also allow us to study more precisely the impact of the coefficient h_ρ on the transport phenomena.

For the condition (T=20°C, $h_R \approx 50\%$), it was previously shown that a Dirichlet condition with an intrinsic permeability of 4.10^{-24}m^2 gives a relatively satisfactory solution. Since the introduction of the exchange condition will slow the drying kinetics, higher permeability values should be used;

we chose the permeability in a range going from $4.10^{-24}m^2$ to $1.10^{-18}m^2$. For each tested value of permeability, the optimal curve is presented in Fig. 3-26 in terms of relative mass loss versus the square root of time. Such a representation is known for the description and detection of a diffusion-like transport mode (Carette et al., 2020; Daian, 2013; Soleilhet, 2018). In fact, early in the experiment, if the drying of the samples surface is controlled by a diffusion phenomenon, a linear behavior for the mass loss versus the square root of time will be observed.

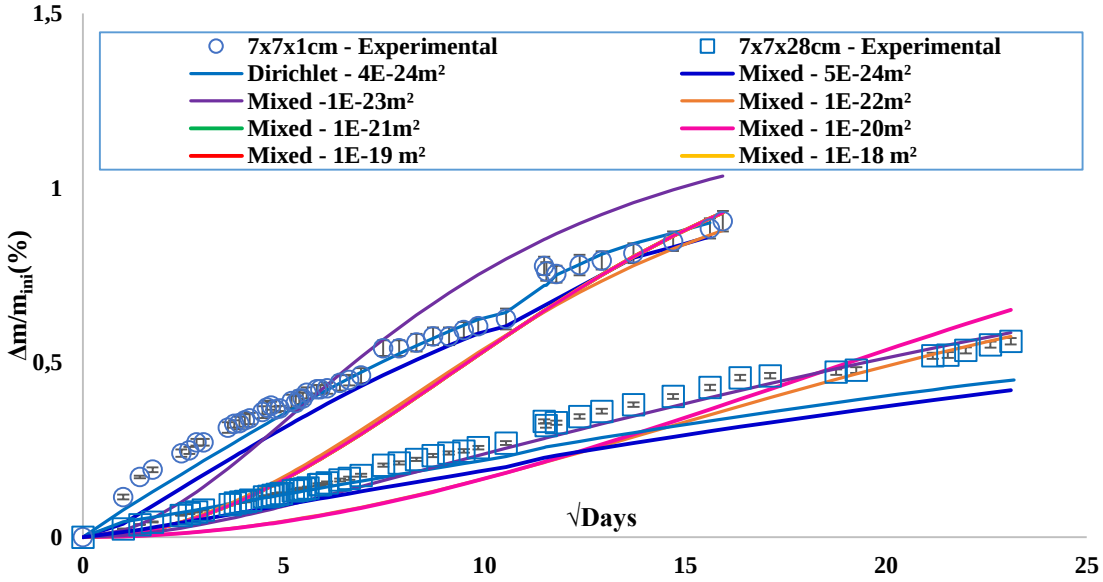

Fig. 3-26 –Impact of a mixed boundary condition for (T=20°C, $h_R = 50\%$) - Relative mass loss versus the square root of time

It can be observed in Fig. 3-26 that accounting for a mixed boundary condition has a major impact on the shape of the curve. This is clearly observed between the beginning and 100 days of the test: when a mixed boundary condition was taken into account, the curve presented a parabolic shape rather than a linear shape (as observed with a Dirichlet condition). The account for a mass exchange coefficient has clearly slowed down the transport phenomena inside the material and gave more importance to evaporation phenomena happening at the exposed surfaces.

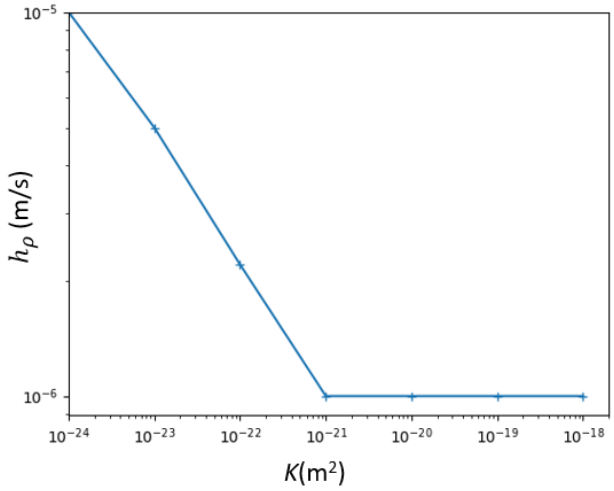

Fig. 3-27– Calibrated values of the mass exchange coefficient h_ρ

The fitted values of the mass exchange coefficient h_ρ obtained for each fixed value of permeability are given in Fig. 3-27.

The results displayed in Fig. 3-26 and Fig. 3-27 show that, when the considered 'intrinsic' permeability take values between 10^{-21} m^2 and 10^{-18} m^2, the model simulates identical drying kinetics

(Fig. 3-26). Moreover, identical values for the mass exchange coefficient are fitted (h_ρ=1.10^{-6} m/s) regardless of the fixed value of the permeability. When the permeability become smaller (for example 10^{-22} m^2) the drying kinetic begin to change and higher values of the parameter h_ρ are fitted according to the permeability value. It appears that a comparison between the value of the mass exchange coefficient and the material permeability permits to distinguish different transfer modes:

- When the permeability ranged between 10^{-21} m^2 and 10^{-18} m^2, a value of 10^{-6} m/s for the mass exchange coefficient was fitted. In this range, the drying phenomenon was controlled by the evaporation at the surface. Therefore, it is the value of the mass exchange coefficient h_ρ that controls the drying kinetic regardless of the material transfer properties, and in particular regardless of its permeability. This explains why the same value of h_ρ was calibrated each time in this range of permeability. At the same time, the material is able to rapidly release the water from its inside to its surface due to the big permeability of the material. Therefore, in this range, regardless of the value of permeability, at each instant the saturation inside the material is homogeneous throughout the sample.
- When the permeability of the material was fixed to 10^{-22} m^2 and 10^{-23} m^2, the permeability of the material began to play a role in the transport phenomena. In this range, both the permeability of the material and the mass exchange coefficient control the drying kinetic.
- Finally, when the permeability is fixed to 4.10^{-24} m^2, a value of 10^{-5} m/s was fitted for the mass exchange coefficient. For this case, since the evaporation at the surface became very significant, it is no longer the evaporation that controls the drying kinetics. It is rather the permeability value that limits the amount of water reaching the surface.

To conclude, Fig. 3-26 shows that, for the tested condition (T=20°C, h_R = 50%), a Dirichlet condition is the optimal boundary condition since it allows to describe efficiently the drying kinetic of the F44Adj concrete.

An identical calibration procedure was followed for the condition of (T=50°C, h_R = 30%) (Fig. 3-28). Again it is shown that a mixed boundary condition worsens the shape of the evolution curve at short times, leading to a misrepresentation of the drying kinetic of the concrete.

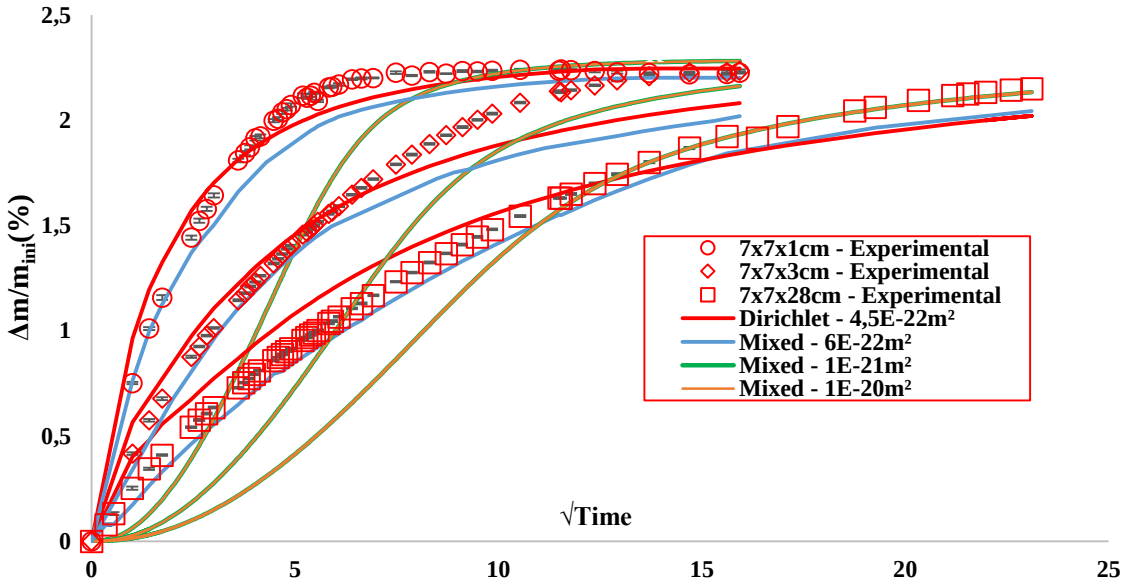

Fig. 3-28 - Impact of a mixed boundary condition for (T=50°C, h_R = 30%) - Relative mass versus the square root of time

The fitted values for h_ρ for the both tested condition and for each fixed value of permeability are given in Table 3-11.

	K= 1.10^{-20} m^2	K= 1.10^{-21} m^2	K= 1.10^{-22} m^2	K= 1.10^{-23} m^2	K= 5.10^{-24} m^2
T=20°C	1.10^{-6} m/s	1.10^{-6} m/s	2.2 10^{-6} m/s	5. 10^{-6} m/s	1.10^{-5} m/s
T=50°C	1.8 10^{-6} m/s	1.8 10^{-6} m/s	9.2 10^{-6} m/s	-	-

Table 3-11 – Fitted values of h_ρ

From what has been presented in this section, it can be concluded that a model accounting for a Dirichlet boundary condition is able to correctly describe the drying kinetic for both tested conditions. For all further computations, a Dirichlet boundary condition will be considered.

3.3.2.5. Impact of relative permeability on kinetic of drying

The evolution of the relative permeabilities K_{rl} and K_{rg} (given in equations (3-48)(3-49)) as a function of the saturation degree S_w is represented in Fig. 3-29, for two values of the parameter p (refer to section 3.1.3.3): 0.5 as given by Mualem (1976) and 5.5 as given by Monlouis-Bonnaire et al. (2004). As shown in Fig. 3-29, the evolution of the gas and liquid relative permeability differ significantly whether the parameter p in equations (3-47) and (3-48) was taken equal to 0.5 (Mualem, 1976) or equal to 5.5 (Monlouis-Bonnaire et al., 2004). Therefore, in this section, the impact of this parameter on the drying kinetic of the F44Adj concrete is studied.

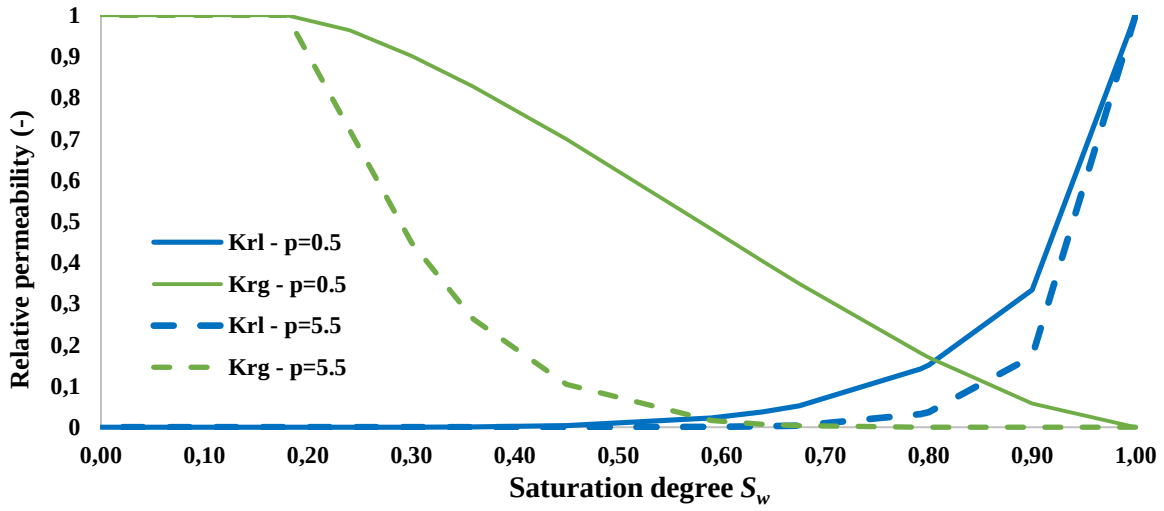

Fig. 3-29 – Variation of the relative permeability of liquid and gas as a function of the saturation degree

For the condition (T=20°C, $h_R \approx 50\%$), the simultaneous calibration of the intrinsic permeability is done for the two tested geometries and with $p = 5.5$. The obtained saturation evolution curve is shown in Fig. 3-30 and is compared to the numerical curve obtained calibrating the intrinsic permeability with $p = 0.5$ (Fig. 3-24). As a result, the fitted value of the intrinsic permeability when $p = 5.5$ is 2.3 10^{-23} m^2 and is larger than the fitted value of 4.10^{-24} m^2 when p was taken 0.5. This is related to the decrease in the relative permeability when $p = 5.5$ (see Fig. 3-29). Therefore, in order to recapture the experimental drying kinetic, the value of the intrinsic permeability had to increase when $p = 5.5$.

In Fig. 3-30 – (a), apart from the increase of the fitted value of 'intrinsic' permeability when $p = 5.5$, a change of the drying kinetic at the beginning and end of tests is also observed. As a matter of fact, for the 7x7x28cm samples, compared the drying kinetic when p is taken equal to 0.5 the drying kinetic is generally slowed down when $p = 5.5$. In contrast, for the 7x7x1cm samples, this kinetic for p=5.5 is slowed down at the beginning of the test compared to the observed kinetic when p=0.5. After 100 days, the drying kinetic for p=5.5 is then slowly accelerated compared to when p was taken equal to 0.5. To better understand this change, it can be important to draw the evolution of

the effective permeability to liquid water ($K_{eff} = K_{rl}K_L$) with respect to the degree of saturation. This evolution is also given in Fig. 3-30-b.

For the 7x7x28cm samples, the degree of saturation decreases from 0.92 to 0.75 during the test (Fig. 3-30 – (a)). In this range of saturation, the effective permeability K_{eff} for p = 5.5 is bigger than that for p = 0.5 (Fig. 3-30 – (b)). Therefore, when p = 5.5, the whole drying kinetic will be accelerated compared to the drying kinetic for p=0.5. For the 7x7x1cm samples, when the degree of saturation is between 0.92 and 0.7, the effective permeability for p = 5.5 is bigger than that for p = 0.5 (Fig. 3-30 – (b)). In this range of saturation, the drying kinetic for p=5.5 is hence accelerated compared to the drying kinetic when p=0.5 (Fig. 3-30 – (a)). In contrast, when the saturation varies between 0.7 and 0.64, the effective permeabilities for p = 0.5 and p = 5.5 become very small with values relatively smaller for p = 5.5 than for p= 0.5 (Fig. 3-30 – (b)). This could explain the slower drying kinetic in this range when p is taken of *5.5* compared to when p=0.5 (Fig. 3-30 – (a)).

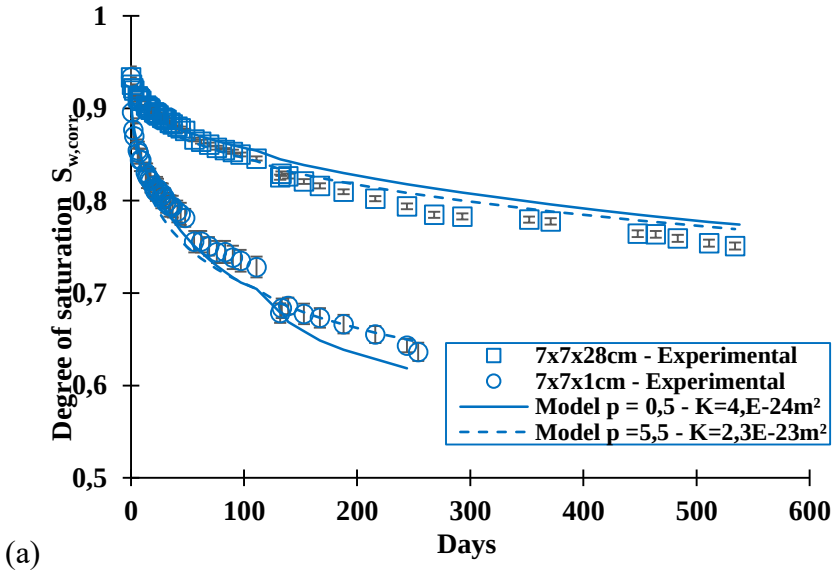

(a)

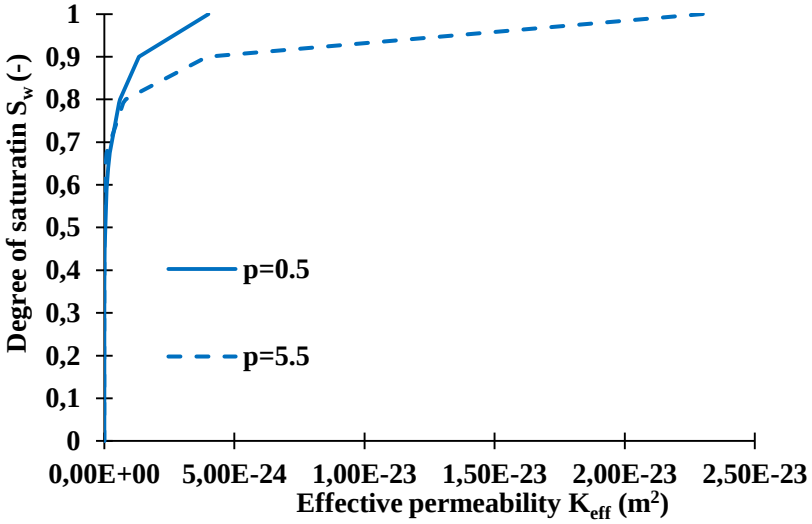

(b)

Fig. 3-30 – (T=20°C, $h_R \approx 50\%$) (a) Calibration of the drying kinetics of two geometries with different values of the relative permeability (b) the effective permeability for different values of the relative permeability

For the condition (T=50°C, $h_R \approx 30\%$), the simultaneous calibration is also done for the three tested geometries with p = 5.5. The obtained solution is compared to that obtained for a value of p = 0.5 (see Fig. 3-31). It could be observed that, for p = 5.5, the model is unable to correctly capture

the drying kinetic of the tested samples. The optimal noted value for the intrinsic permeability is $1.10^{-21}m^2$ when p = 5.5 and is larger than the value 4.5 $10^{-22}m^2$ when p = 0.5.

Looking at the curves at 50°C in Fig. 3-31, one could question if repeating the calibration with a relative permeability as given in Monlouis-Bonnaire et al. (2004) while introducing a mass exchange coefficient (as done in section 3.3.2.4) could impact the shape of the curve. However, given that for T=20°C, the modification of the relative permeability (Fig. 3-30 – (a)) does not impact the results, the reasoning made before to exclude the use of a mass exchange coefficient still stands.

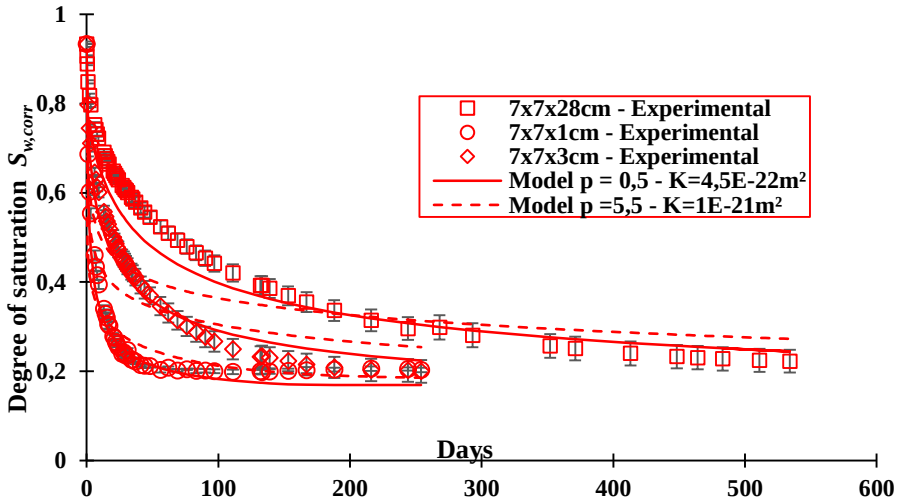

Fig. 3-31 - Calibration of the drying kinetics of two geometries at (T=50°C, $h_R \approx 30\%$) with different values of the relative permeability

From what has been presented in this section, it can be concluded that a model accounting for a relative permeability as given in Monlouis-Bonnaire et al. (2004), with p=5.5, is able to correctly calibrate the drying kinetic for (T=20°C, $h_R \approx 50\%$). However, for (T=50°C, $h_R \approx 30\%$), the latter model fails to show a good calibration.

3.3.2.6. Impact of diffusion on kinetic of drying

In this section, the impact of diffusion on the kinetic of drying. In order to test the sensibility of the results to the coefficient D_{v0} of equation (3-23), this parameter is taken equal to 1 rather than to 2.33 10^{-5} m^2/s at T=20°C and 2.6 10^{-5} m^2/s at T=50°C (see Table 3-10). This would mean multiplying the diffusion coefficient D_{vp} in equation (3-23) by a factor of approximately 10^5. This calibration test was done for both relative permeability functions given by Mualem (1976) and by Monlouis-Bonnaire et al. (2004).

For a temperature of T=20°C, the increase of the diffusion coefficient showed no impact on the results (see Appendix 4). For T=50°C, the results are shown in Fig. 3-32 for the relative permeability function of Mualem (1976) with p= 0.5 and in Fig. 3-33 for the relative permeability function of Monlouis-Bonnaire et al. (2004) with p=5.5. When p= 0.5 (Fig. 3-32), the increase in the diffusion coefficient shows a very small impact on the drying kinetics of the 7x7x1cm samples. However, this impact can be considered negligible regarding the important increment factor considered for the diffusion coefficient. When p= 5.5 (Fig. 3-33), the increase in the diffusion coefficient shows no impact on the drying kinetic.

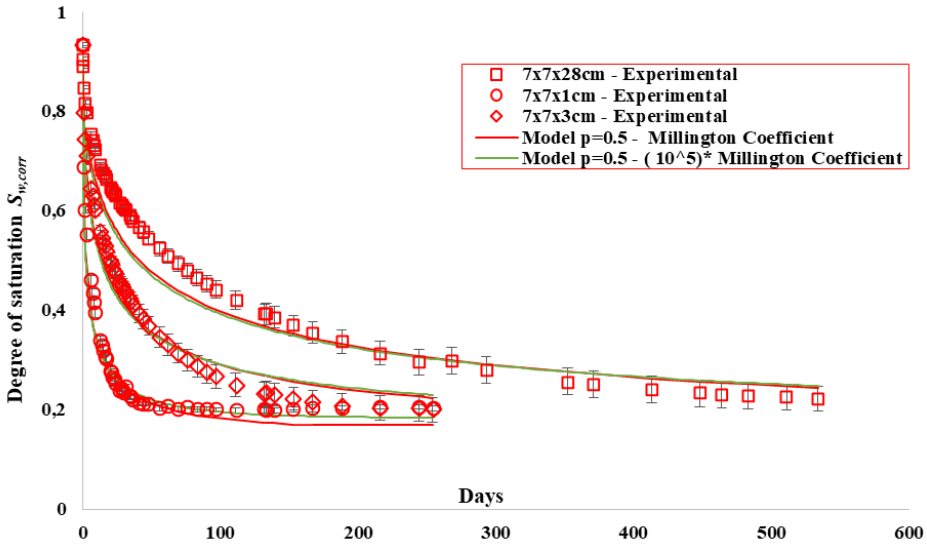

Fig. 3-32 - Role played by the diffusion on the drying kinetic at T=50°C for a relative permeability given by Mualem (1976)

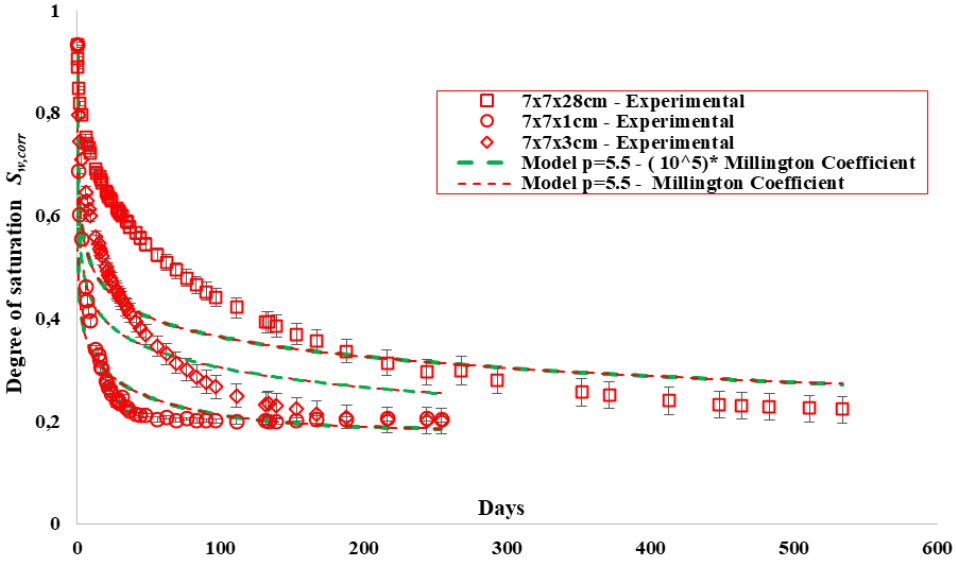

Fig. 3-33- Role played by the diffusion on the drying kinetic at T=50°C for a relative permeability given by Monlouis-Bonnaire et al. (2004)

Therefore, from what has been presented in this section, it could be concluded that the diffusion phenomenon plays a negligible role in the transfer phenomenon of the studied F44Adj concrete, for the tested external conditions.

3.3.2.7. Optimal calibrated transfer parameters and final verifications

The previous simulations showed that the drying kinetic of the F44Adj concrete can be optimally described by a Dirichlet condition and a relative permeability as given by Mualem (1976). It is important to note that the fitted permeability differed according to external thermos-hydric condition: for a (T=20°C, h_R = 50%) an optimal permeability of 4.10^{-24} m^2 was found, while for (T=50°C, h_R = 30%) an optimal permeability of 4.510^{-22} m^2 was found.

A final observation can be done regarding the tested samples at T=50°C, especially the 7x7x28cm samples (Fig. 3-25): the experimental drying kinetic at the beginning of the test is slower than that simulated by the model. This could be linked to the experimental measurement procedure. As a matter of fact, the mass of the samples was measured outside the climatic chamber in which

(T=50°C, h_R =30%) was imposed. Hence, during the measurement, the samples were submitted to ambient conditions (temperature lower than 50°C, relative humidity higher than 30%) and hence the experimental drying kinetic might have been slowed.

It is important to note that in the previous simulations, the gas pressure of the samples was kept constant and equal to the atmospheric pressure on all the samples faces subjected to drying. The gas pressure inside the tested samples is free to vary. However, it is important to verify that no gas over pressure will occur during the drying of the samples. This verification was done for both tested temperatures T=20°C and T=50°C. For each tested sample, the evolution profile of the gas pressure at a horizontal plan passing through the middle of each geometry is presented in Fig. 3-34 and Fig. 3-35. Fig. 3-34 and Fig. 3-35 shows that for a temperature of 50°C, the gas pressure inside the material presents in general larger values (maximum 1.095 atm) than those found at a temperature of 20°C (maximum 1.006 atm). Those values indicate the existence of a small overpressure.

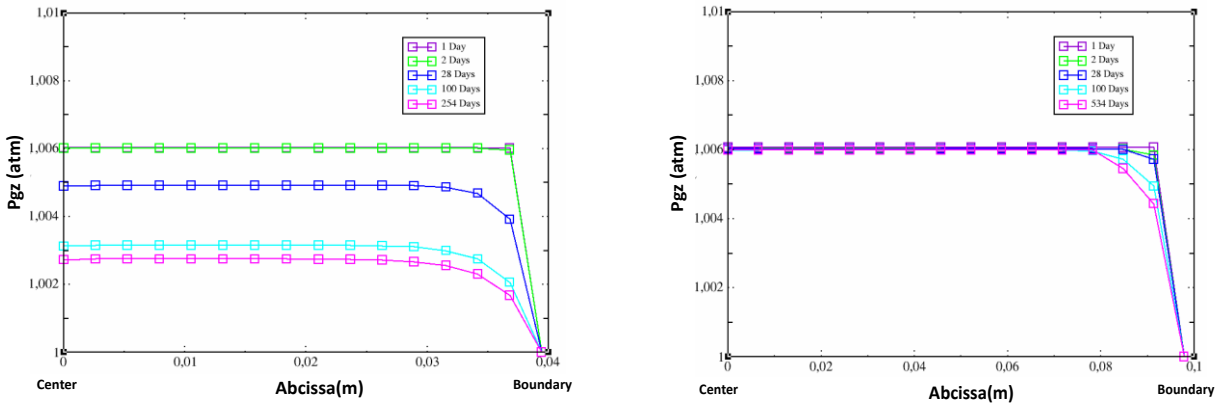

Fig. 3-34 – T=20°C Gas pressure evolution profile on a horizontal middle plan of the: 7x7x1cm sample (left) - 7x7x28cm sample (right)

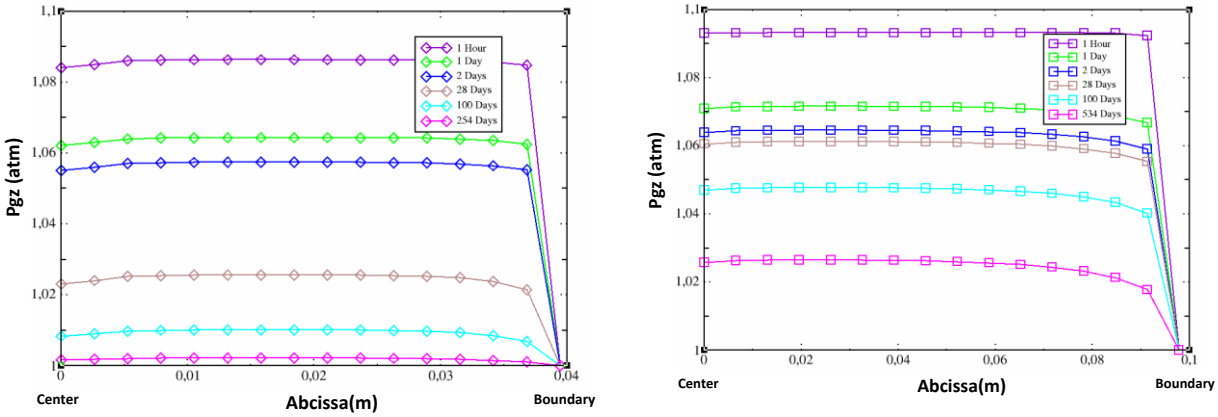

Fig. 3-35 - T=50°C Gas pressure evolution profile on a horizontal middle plan of the: 7x7x1cm sample (left) - 7x7x28cm sample (right)

On another hand, it is also important to verify the validity of using a Darcy's law for the drying of the F44Adj concrete. For that purpose, we refer to section 3.1.2.1 and more specifically to equation (3-4). The Reynolds number for the water transport in the F44Adj concrete is estimated. For (T=20°C, h_R = 50%): the values of ρ_L and η_L are taken from Table 3-10. The value of the liquid velocity v_L is calculated from the maximum liquid flow M_L simulated by the model and divided by ρ_L. This led to a value of $v_L = 3.10^{-12}$ m/s. Finally, the value of l is defined as the average diameter found in the F44Adj concrete. This value is approximately of 4 nm (given in chapter 4). Therefore, the calculated Reynolds number is 1.10^{-14}, which is very small with respect to 1. This verifies that the liquid flow in

the F44Adj concrete is of low inertia and Darcy's law can be applied. For (T=50°C, h_R = 30%), the same verification was done and led to a $v_L = 3\,.10^{-12}$m/s and $Re = 3.10^{-14}$. Therefore, additionally for this tested condition, Darcy's law is considered to be valid.

Finally, the optimal set of transfer parameters and conditions found with a calibration on axisymmetric geometries were also tested on the 3D geometries. The corresponding 1/8th of each 3D geometry mesh are presented in Fig. 3-36. The obtained results (given in Appendix 5) verify the accuracy of the found solutions.

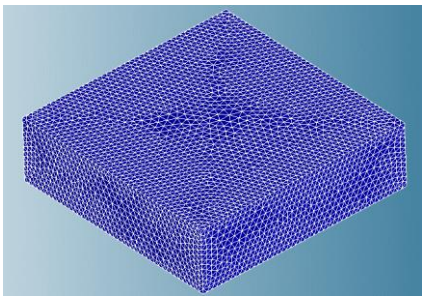

(a) 7x7x1cm

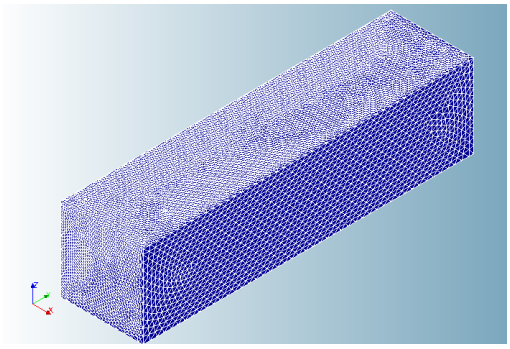

(b) 7x7x28cm

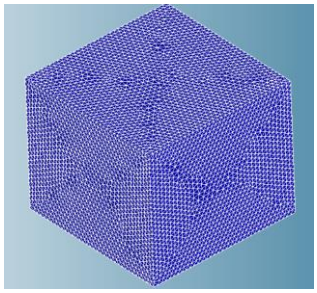

(c) 7x7x3cm

Fig. 3-36 – 1/8th of the 3D geometries used for computations done on (a) 7x7x1cm samples (b) 7x7x28cm samples (c) 7x7x3cm samples

3.3.3. Conclusions

In this section, we aim to model efficiently the drying kinetic of the F44Adj concrete. Therefore, the mass loss curves resulting from the drying tests (section 3.2.1) were used in an inverse analysis in order to determine the best set of transfer parameters for the F44Adj concrete. In this section, we first summarized the THM model (section 3.3.1) implemented in *Code_Aster* and used for this analysis. Some modifications to the model already available in *Code_Aster* were proposed and newly implemented in the code, including a new expression for the relative permeability and an implementation of an exchange boundary condition.

In the second part (section 3.3.2), multiple simulations were run for each experimental condition (T=20°C, h_R = 50%) and (T=50°C, h_R = 30%) and for the different tested geometries. The simulations allowed us to study the impact of a mixed boundary condition, the impact of the relative permeability and of diffusion on the drying of the concrete and finally to calibrate the model transfer parameters.

We found that a Dirichlet boundary condition is the optimal boundary condition for simulating the drying kinetic of this concrete. Furthermore, it was shown that how the relative permeability depends on saturation impacts the drying kinetic of the concrete significantly. While comparing two relative permeability functions given by Mualem (1976) and Monlouis-Bonnaire et al. (2004), it was shown that the function given by Mualem (1976) and that is commonly adopted in the literature described more efficiently the drying kinetic of the F44Adj concrete for both conditions (T=20°C, h_R = 50%) and (T=50°C, h_R = 30%). Finally, the impact of the diffusion phenomena was also studied

and it was observed that these phenomena play a minor role in the transport occurring in the F44Adj concrete. Some final verifications were done in section 3.3.2.7. These verifications showed that no noticeable gas overpressure is observed and that Darcy's law is indeed applicable for this case study.

All the presented simulations let us conclude that the drying kinetic of the concrete at (T=20°C, h_R = 50%) is described optimally when the relative permeability function is that of Mualem (1976) and the intrinsic permeability is 4.10^{-24} m^2. The drying kinetic at (T=50°C, h_R = 30%) is optimally described when the relative permeability function is that of Mualem (1976) and the intrinsic permeability is $4.5.10^{-22}$ m^2.

Chapter 4

Drying shrinkage modelling

List of Figures

List of Tables

Concrete is known to be subjected to delayed deformations. Regardless of their nature, these delayed deformations can induce, if they are restricted, cracks inside the material. These cracks might impact the durability and the mechanical strength of the concrete. Therefore, it is of a major importance to be able to estimate and foresee those deformations.

Delayed deformations can be separated into two main categories: shrinkage strains which occur without any external mechanical loading and creep strains which result from the application of a mechanical loading. Another classification of those strains can be done according to their interaction with the external environment. As a matter of fact, drying shrinkage and drying creep strains occur when the water inside the concrete can be released to the external surroundings. In contrast, autogenous shrinkage and basic creep occur even when no water transfer is expected to take place with the outside environment.

In this chapter, we discuss exclusively the shrinkage phenomena. These include in particular the autogenous and drying shrinkage. The mechanisms responsible for shrinkage in concrete are introduced at first in a bibliographic study (section 4.1) along with various numerical models known for estimating the drying shrinkage strains. A second part of the chapter (section 4.2) consists in introducing a new poromechanical model for the drying shrinkage considering capillary and adsorption effects. This model is validated on several porous materials: cement pastes, concrete and Vycor glass. Finally, the latter model once implemented in *Code_Aster* is used to model drying shrinkage experiments on the F44Adj concrete (section 4.4).

4.1. State of the art

4.1.1. Autogenous shrinkage

By terminology, the autogenous shrinkage of a cementitious material includes the chemical shrinkage and the self-desiccation shrinkage. The chemical shrinkage normally occurs during the hydration of the cement paste and before its setting, whereas the self-desiccation begins after the setting of the cement paste (Hilaire, 2015).

The chemical shrinkage is also known as ‘Le Chatelier’ contraction (Le Chatelier, 1900). It is due to the fact that the volume of the hydrated products such as the C-S-H, CH (see chapter 2 – section 2.1.1) is less than the volume of the anhydrous elements and of the water that resulted in their production. Although the ‘Le Chatelier’ contraction occurs mainly before the setting of the paste, it has been shown by Tazawa and Miyazawa (1995) that this contraction may continue to increase during the whole hydration phase. After complete hydration, the contraction is about 10% of the initial volume of the paste (Baroghel-Bouny, 1994).

Once the paste has set, the liquid water that has not been consumed by the hydration will be in equilibrium with a gas phase in the pores. This will induce a meniscus formation in the pores (see section 2.1.3). This surface tension at the solid surface will put the material locally in tension. To compensate this tension, the solid matrix will contract. This corresponds to the self-desiccation shrinkage (Brue et al., 2012).

On another hand, it is important to note that, in some cases, a swelling of the cement paste might appear at the early age. This swelling is mainly due to a swelling of the portlandite and the ettringite products (see section 2.1.1). In fact, during hydration, when the latter crystals have not enough space to grow, this will create additional porosity and the occurrence of a swelling (Baroghel-Bouny, 1994).

4.1.1.1. Factors influencing autogenous shrinkage

In addition to the high influence of the hydration degree of the material, other factors might influence the amplitude of the autogenous shrinkage. One of those is the formulation of the cement paste and more specifically the water/cement ratio. Notably, Baroghel-Bouny et al. (2017) measured the autogenous shrinkage on cement pastes that differed in their water/cement ratio (Fig. 4-1).

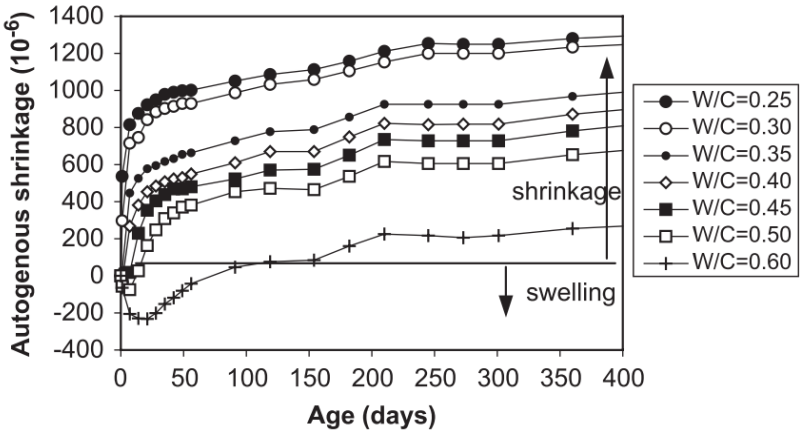

Fig. 4-1 – Autogenous shrinkage measurements on cement pastes with different water/cement ratios (Baroghel-bouny et al., 2017)

The authors showed that, when the ratio of water to cement decreases, the autogenous shrinkage strains increase. Indeed, when this ratio is low, the hydrated material will present a porous network with a small water quantity. Therefore, the capillary tensions will be more important and the autogenous shrinkage is thus higher. On another hand, it has been said that for concretes with a high water/cement ratio (higher than 0.4-0.45), the autogenous shrinkage has low mechanical effect on the structure (Jensen and Hansen, 2001). In this case, those strains are small with respect to thermal shrinkage due to temperature variations for massive structures or with respect to desiccation shrinkage for thinner structures (Hilaire, 2015). Another parameter that can influence the autogenous shrinkage is the nature of the cement and its granulometry. As a matter of fact, it is shown that a finer cement will develop a greater autogenous shrinkage (Koenders and Van Breugel, 1997; Tazawa and Miyazawa, 1995)

Moreover, the effect of temperature on the autogenous shrinkage during an isothermal drying of cementitious materials, especially at early age, has been studied by many authors (Baroghel-Bouny et al., 2017; Lura et al., 2001; Mounanga, 2003; Soliman and Nehdi, 2011). All these studies indicate that an increase in temperature results in an acceleration of the autogenous shrinkage kinetics, especially at the initial phase when the 'Le Chatelier' contraction is predominant. For instance, for an ultra-high performance concrete (see Fig. 4-2 –left), Soliman and Nehdi (2011) showed that, when the temperature increased from 20°C to 40°C during the first 24h, the autogenous shrinkage was accelerated. Regarding the effect on the amplitude of the autogenous shrinkage, it is generally difficult to generalize the conclusions obtained in the literature. Going back to the tests done by Soliman and Nehdi (2011), it is seen (Fig. 4-2 –left) that when the temperature increases, the amplitude of the autogenous shrinkage increases. However, in their works, Lura et al. (2001) showed that the influence of temperature on the amplitude of autogenous shrinkage is not systematic (Fig. 4-2 - right). While carrying out autogenous shrinkage tests on concrete at various temperatures (10, 20, 30 and 40°C), Lura et al. (2001) observed that, for a temperature of 10°C and 40°C, the amplitude of the autogenous shrinkage after 144 hours becomes smaller than that at 20°C and 30°C. To conclude, it has been stated by Mounanga (2003) that the comparison of the autogenous deformations at different temperatures is not always conclusive. The difference in the strain rate is majorly impacted by the moment of initialization of these deformations. In fact, it is necessary to be sure that the shrinkage curves at

different temperatures start at the same degree of hydration. These initialization times are often unspecified and depend on the study.

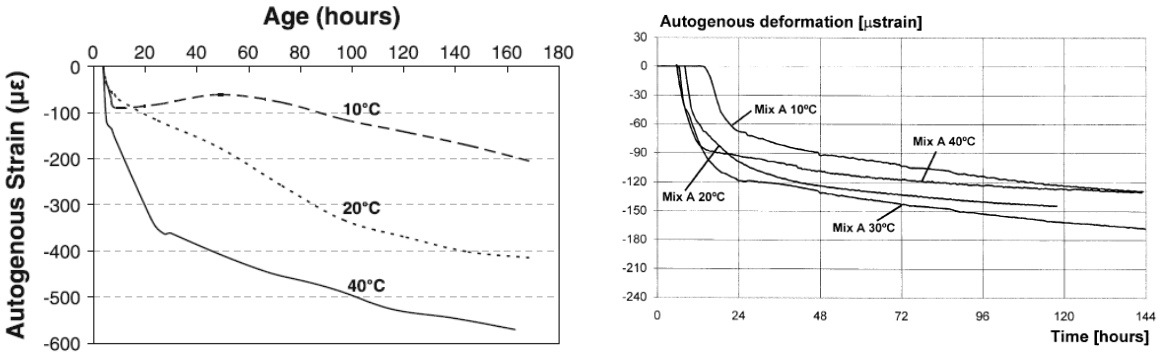

Fig. 4-2 – The influence of temperature on the autogenous shrinkage for (left): an ultra-high-performance concrete studied by Soliman and Nehdi (2011) – (right): an ordinary concrete studied by Lura et al. (2001)

4.1.2. Drying shrinkage

In concrete, the drying shrinkage strain, also called the desiccation shrinkage strain, is the deformation caused by the drying of the material due to the hydric transfer with the surrounding environment.

The decomposition of shrinkage strains into autogenous and drying contributions is conventional (Hilaire, 2015). This decomposition of strains is acceptable if the hydration process no longer develops significantly. This is generally the case when the age of material is more than 28 days (Briffaut, 2010). Hence, the drying shrinkage strains are the strains measured for a sample in contact with the surrounding environment minus the autogenous shrinkage strain.

The different mechanisms explaining the drying shrinkage are basically: the capillary pressure effect, the surface adsorption effect and the disjoining pressure (Kovler and Zhutovsky, 2006). The latter mechanisms will be studied in details in section 4.1.3. These mechanisms are also at the source of the autogenous shrinkage. Section 4.1.2.1 will introduce the parameters that can influence the amplitude of the drying shrinkage while section 4.1.2.2 addresses the effects induced by the drying shrinkage.

4.1.2.1. Mechanical effects of drying shrinkage

Drying shrinkage is the main cause of the stresses induced within the material when the corresponding strains are restrained. Those restraints are present at different scales going from a micro scale to a macro scale.

At the scale of cement paste, only the cement paste shrinks. In contrast, the aggregates undergo no significant dimensional variation due to water loss. Thus, the differential deformation between the cement paste and the aggregates can result in self-stresses inside the material and lead to a micro-cracking of the cement matrix (Baroghel-Bouny, 1994). On another hand, at the micro-scale the cement paste is a heterogeneous system consisting of C-S-H, portlandite, non-hydrated cement... (see chapter 2 – section 2.1.1). This heterogeneity can also induce differential deformations between the constituents. For instance, C-S-H, which is known to be highly porous, will undergo a significant volume decrease due to drying, whereas the portlandite undergoes generally no volume decrease (Soleilhet, 2018).

At a larger scale, given that the drying of cementitious materials is a relatively slow phenomenon, the drying state of the material can differ between its core and its exchanging surface. As a matter of fact, the exchanging surface tends to dry more significantly than the center of the

sample and hence to contract more. This will generate surface tensile stresses and compressive stresses in the core. When the surface tensile stress reaches the tensile strength of the material, a surface micro-crack appears. At the end of the drying, the core tends to contract. This can induce tensile stresses in the core and compressive stresses at the surface (Benboudjema, 2004; Hilaire, 2015) when the tensile stresses attain the tensile strength of the restrained material, through-cracks will appear.

From what has been presented, it can be concluded that the drying of cementitious materials can have a significant "structural" effect. In a general way, the appearance of the micro-cracking or macro-cracking can lead to change of mechanical and transfer properties of the material.

It is important to note that, without precautions to reduce cracking, the measurement of drying shrinkage strains will include simultaneously a structural effect superimposed with effects resulting from physico-chemical driving mechanisms (see section 4.1.4). The structural effect can be reduced by choosing small specimens (a few millimeters for a cement paste) and/or by drying the material in small decreasing successive steps of relative humidity (Di Bella et al., 2017; Benboudjema, 2004).

4.1.2.2. Factors influencing drying shrinkage

Several factors can impact the amplitude and the kinetics of the drying shrinkage. For instance, the fraction of the cement paste and the water/cement ratio are important factors related to the cement paste. As a matter of fact, it has been observed experimentally that the greater the fraction of the cement paste is, the more important the amplitude of the desiccation shrinkage strains (see Fig. 4-3 - left). Moreover, when the water/cement ratio increases, the latter amplitude will also increase (see Fig. 4-3 - right). This is due to a higher porosity in the case of a higher water/cement ratio for a cement paste which results in a bigger capillary pressure.

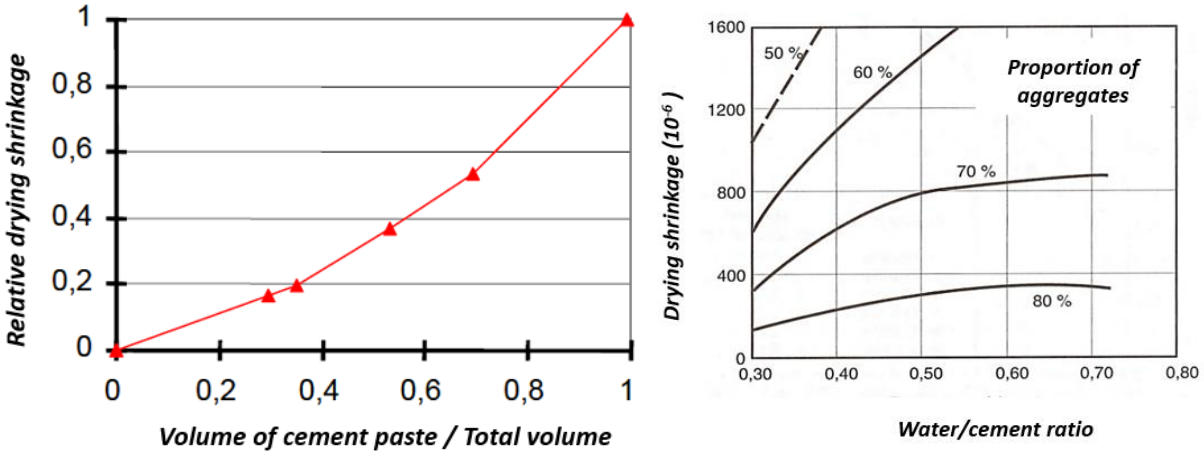

Fig. 4-3 – (left) Relative drying shrinkage strains vs the fraction of cement paste (Benboudjema, 2004) – (right) Drying shrinkage strains vs water/cement ratio (Odman,1968) cited by Hubert and Giraud (2004)

The influence of aggregates on the drying shrinkage is also highlighted in Fig. 4-3 – right: for a fixed water/cement ratio, aggregates generally reduce shrinkage. Indeed, the higher the aggregate volume fraction is, the lower the shrinkage will be. On another hand, it was also observed that the nature of the aggregate may slightly influence the drying shrinkage strains: the greater the stiffness of the aggregate is, the lower the shrinkage will be.

Finally, it is important to acknowledge the "scale" effect: when the size of the tested sample increases, a decrease in the amplitude of the desiccation shrinkage strains can be observed (Fig. 4-4). It is probable that this observation is due to the surface cracking (see section 4.1.3.1). Indeed, the greater the thickness of the sample is, the greater the crack is (Benboudjema, 2004). Moreover, the "scale" effect is responsible for a heterogeneous distribution of the drying shrinkage strains through

the sample (Ayano and Wittmann, 2002). Hence, it is important to note precisely the location of the instruments measuring displacements when performing an experimental drying shrinkage test.

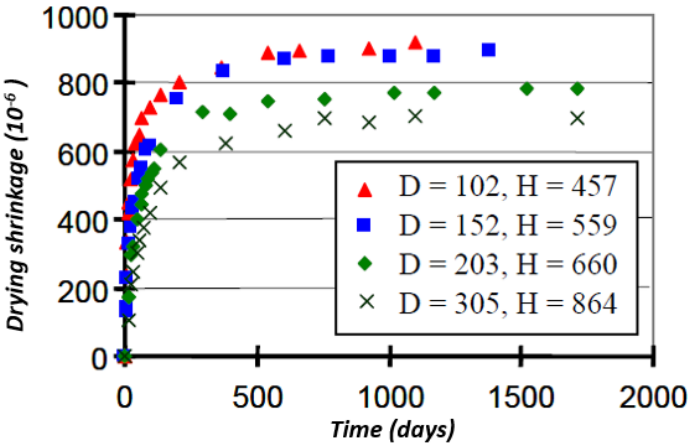

Fig. 4-4 – Influence of the size sample on the drying shrinkage strains
((Hansen & Mattock, 1966) cited in Benboudjema (2004))

4.1.3. Mechanisms for self-desiccation and desiccation shrinkage: capillary pressure, surface adsorption and disjoining pressure

Given that both self-desiccation and drying shrinkage are similarly linked to a process of water loss, the mechanisms explaining both types of shrinkage can be common. Indeed, the works presented in the literature agree that shrinkage is the result of three main mechanisms: the capillary pressure, the disjoining pressure and the surface adsorption (Baroghel-Bouny , 1994; Ferraris, 1986; Kovler and Zhutovsky, 2006).

4.1.3.1. The capillary pressure mechanism

This mechanism is detailed in chapter 2 – section 2.1.3. It is linked to the appearance, during desiccation, of a pressure difference at the interface between the liquid and the gas phase. As a matter of fact, the liquid pressure decreases when the relative humidity inside the pores decreases due to drying. The physical law describing the thermodynamical equilibrium between the liquid phase and gas phase is Kelvin's law (see chapter 2- equation 2.9).

This pressure difference (i.e. capillary pressure) can lead to the appearance of menisci at the liquid-gas interface, to which a surface stress is associated. The mechanical law describing the mechanical equilibrium between the two phases and the role played by the interface is the Laplace's law (see chapter 2 - equation 2.6). The surface tension and the depression of the liquid phase can then cause a contraction of the solid matrix and hence a shrinkage of the material.

4.1.3.2. The disjoining pressure mechanism

The disjoining pressure P_d develops in areas where water adsorption is hindered, i.e. where the distance between the solid surfaces is of the same order of magnitude as the thickness of a layer of freely adsorbed water (Brue, 2011; Mounanga, 2003) (Fig. 4-5). Disjoining pressure is a combination of Van der Waals interaction forces with electro-chemical interaction forces (Hilaire, 2015). Disjoining pressure is equal to the difference between the mechanical pressure of the fluid and its thermodynamic pressure (Coussy, 2010).The disjoining pressure expression is a function of the relative humidity.Therefore it is said that a variation of the relative humidity can cause a variation of the disjoining pressure inside the pores and hence a shrinkage or swelling of the solid matrix.

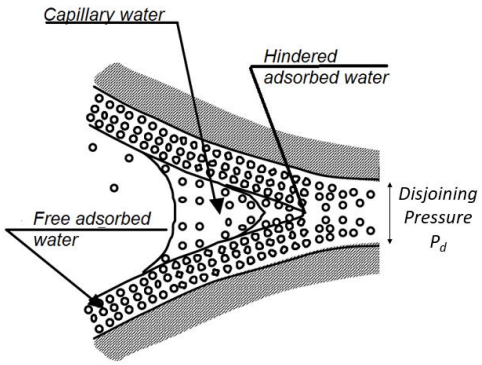

Fig. 4-5 – Disjoining pressure in hindered water areas – adapted from Brue (2011)

The theoretical aspect of disjoining pressure has been studied in detail by Churaev and Derjaguin (1985). However, how disjoining pressure is related to dimensional variations is an object of controversy (Kovler and Zhutovsky, 2006). Some researchers suppose that the disjoining pressure is responsible for the volume changes at high relative humidity (Wittmann, 1973)(Setzer, 1996), some consider that it is operative on the whole range of relative humidity (Powers, 1968) and some reject the impact of this mechanism on dimensional variations (Feldman and Sereda, 1968; Rahman and Grasley, 2017)

4.1.3.3. The surface adsorption mechanism

Going back to Gibbs's work (see chapter 2.1.3 – Fig 2-4), between two considered phases α (gas or liquid phase) and β (the solid surface of the unsaturated or saturated pores), there exists a transition zone or interface region (Fig. 4-6 -a) in which the composition is not homogeneous and does not correspond to those of α and β (Maugis, 1980). Gibbs (1928) proposed to define an ideal system with an interface **Σ** located in the transition zone and to assume that the composition of the neighboring phases remains homogeneous until reaching this surface (Fig. 4-6 - b).

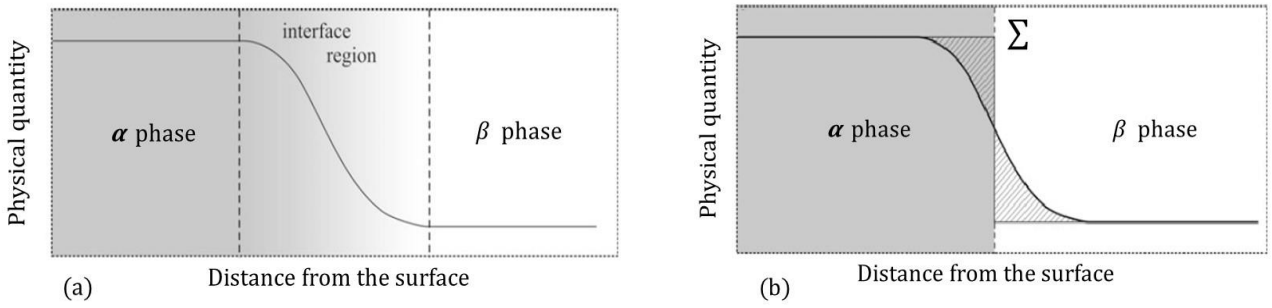

Fig. 4-6 The system with the interface region (b) The Gibbs system for the interface, adapted from Gyozo and Cesar (2012)

In this Gibbs's system, it is assumed that the total number N of moles of a given constituent (water or air) in the ideal system is equal to (see equation (4-1)):

$$N = N_\alpha + N_\beta + N_{ex} \tag{4-1}$$

where N_α and N_β are the number of moles of the constituent found in the phases α and β ; N_{ex} is the number of moles of the constituent in excess placed on the interface so that the total number of moles in the initial system and the ideal system is the same.

The surface energy γ of an interface is defined as the energy needed to create a new surface of area (by adding new moles to the surface or by cleavage) with no deformation of the surface (Kramer and Weissmüller, 2007).

When the relative humidity decreases, a fraction of the pores are emptied from their liquid water but an adsorbed film of water (with a thickness that can reach several molecules) is deposed at their solid surface. The adsorption can modify the surface energy γ of the solid/liquid interface, according to Gibbs's isotherm (equation (4-2) - (Gibbs, 1928)):

$$A_{S/L}.d\gamma = -N^{ex}d\mu \tag{4-2}$$

where μ is the chemical potential, $A_{S/L}$ the surface area of the solid/liquid interface and N^{ex} is the number of excess water molecules at the solid surface. In this relation, we can define a density of excess moles at the interface per unit surface noted as $\Gamma = N^{ex}/A_{S/L}$.

Many authors consider that the variation of the surface energy γ to which those pore walls are submitted is mainly responsible for the shrinkage of the porous material when the relative humidity becomes smaller than 40%-50% (i.e. when the fraction of unsaturated pores becomes important). This effect was regularly acknowledged in the literature (Lura et al., 2003; Setzer et al., 2006; Wittmann, 2008).

4.1.3.4. Discussion of the shrinkage mechanisms

Despite numerous studies on the driving mechanisms of shrinkage, no agreement has yet been reached on the physical origin of drying shrinkage. However, it can be said that no single mechanism can explain the shrinkage over the whole range of relative humidity.

The capillary pressure mechanism is frequently made responsible for shrinkage. However, authors like Beltzung and Wittmann (2005) or Wittmann (2008) consider that this mechanism reaches its limit for small pores (orders of the nm). This is due to the fact that, in nanometer-sized pores, we cannot consider that there is a meniscus separating the liquid and gas continuum phases. However, it was shown by Rahman and Grasley (2017) that the validity of the Kelvin's law (equation (2-9)) describing the capillary pressure mechanism, does not require the presence of a meniscus. As a matter of fact, this equation can be derived by means of a Gibbs-Duhem-type state equation between a gas phase and a liquid phase regardless of the liquid phase's form (capillary or adsorbed). Hence, Rahman and Grasley (2017) indicated that the use of Kelvin's law neither requires nor implies the presence of a meniscus.

On another hand, it is agreed that, when the water inside the pores is mostly under an adsorbed form, it is therefore the surface adsorption mechanism that is responsible for shrinkage. Hansen (1987) tried considering this adsorption mechanism as responsible for shrinkage on the whole range of relative humidity. However, the author showed that referring only to this mechanism underestimated the drying shrinkage, especially at high relative humidity.

4.1.4. Models found in the literature for shrinkage

In the literature, a variety of models exist that describe the autogenous and desiccation shrinkage in a porous material. These models can be separated between phenomenological, empirical models (Bangham et al., 1934; Granger, 1995) and models based on poromechanical approaches (Coussy et al., 2003; Dangla and Pereira, 2014; Gray and Schrefler, 2001; Sellier and Buffo-Lacarrière, 2009; Vandamme et al., 2010a). Both types of models will be introduced in the current section.

4.1.4.1. Phenomenological and empirical models

Based on experimental works in the literature, Bažant and Yunping (1994) showed that there exists a linear relation between the variation of the desiccation shrinkage strains ε and the variation of the relative humidity: $\Delta\varepsilon = k_d\,\Delta h_R$ where k_d is a hydric compressibility coefficient. Granger

(1995), Torrenti and Granger (1997), Benboudjema (2001b) used a linear relation between the desiccation shrinkage strains and the water content w in the material: $\Delta\varepsilon = k_w\,\Delta w$ where k_w is a proportionality coefficient deduced from the drying shrinkage strains vs mass loss curve. More recently, Sellier and Buffo-Lacarrière (2009) used an approach based on the previous works of Torrenti and Granger (1997) but considered the hydraulic pore pressure proportional to the mass loss by the means of a fitting parameter K^w.

Concerning shrinkage strains induced by surface adsorption effects, many authors refer to the works of Bangham (1931) that link the strains to the change of the surface energy γ. The empirical relation given in Bangham et al. (1934) is written as:

$$\Delta\varepsilon = \lambda_B\,\Delta\gamma \tag{4-3}$$

with λ_B a proportionality factor that depends on the material properties. $\Delta\gamma$ can be written according to equation (4-2), with $d\mu = RT\ln(h_R)$, as a function of the relative humidity: $\Delta\gamma = \int_{h_{R,0}}^{h_R} RT\Gamma \mathrm{d}\ln(h_R)$. Equation (4-3) was at first elaborated by Bangham for charcoal materials but has later been proven valid for modelling the drying shrinkage of other porous material such as Vycor glass (Hiller, 1964; Bentz et al., 1998) and cementitious materials (Koenders and Van Breugel, 1997).

It is important to distinguish between the so-called surface energy γ (also known as the surface tension) and σ_s the surface stress. This distinction has been previously discussed in the literature (Gor and Bernstein, 2016; Kramer and Weissmüller, 2007; Schulman et al., 2018; Vandamme et al., 2010b). While γ is the energy needed to create a new surface of area at a constant structure, σ_s is the force that opposes an elastic strain of the surface, changing the intermolecular distance at a constant number of moles at the surface. Like Kramer and Weissmüller (2007), these authors emphasize the fact that, in systems in which surface effects on solid surface prevail, strains are governed by variations of surface stress rather than of surface energy. However, Bangham's equation (equation (4-3)) in which strains are linked to variations of surface energy has been recently reviewed by Gor and Bernstein (2016), who showed that, in the general case, Bangham's law is only an approximation. The authors showed that Bangham's equation is verified for small strains and small adsorbed molecules with non-specific interactions, in which case the variations $\Delta\gamma$ of the surface energy are approximately equal to the variations $\Delta\sigma_s$ of the surface stress.

Finally, regarding the autogenous shrinkage, Aili et al. (2018) proposed a logarithmic relation describing the evolution in time of the autogenous strains. This relation is:

$$\varepsilon_a = \alpha_a \ln\left(\frac{t}{\tau_0}\right) + \beta_a \tag{4-4}$$

where ε_a is the autogenous strain, t is the age of concrete, τ_0=1 day is a reference time, α_a and β_a are fitting parameters and correspond respectively to the slope and the y-intercept of the autogenous shrinkage versus the age t. This relation was deduced from various experimental observations done on cementitious materials, including cement paste and concrete: an example is given in Fig. 4-7. In their work, Aili et al. (2018) presented values of α_a for a large number of experimental data. For high-performance concretes, the fitting parameter α_a varies between 15 µm/m and 31 µm/m.

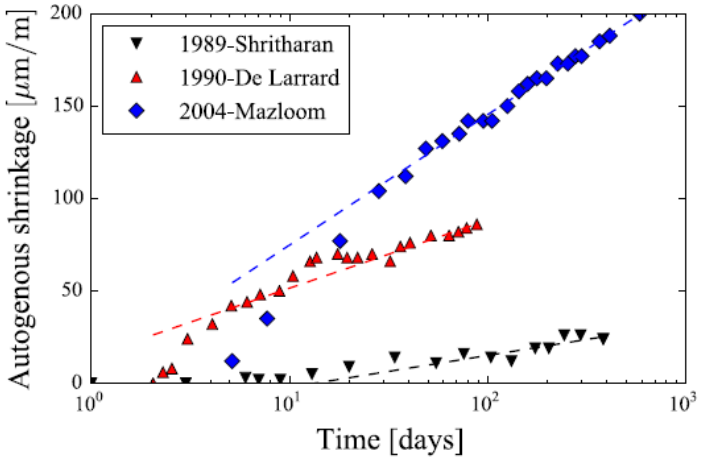

Fig. 4-7 – Fitting with a logarithmic relation of the autogenous shrinkage of concretes studied by Shitharan (1989), De Larrard (1990), Mazloom (2004) cited by Aili et al. (2018)

4.1.4.2. Poromechanical models

The constitutive behavior of a porous material subjected to a variation of pore pressure has been widely investigated by poromechanical approaches. Those approaches relate the origin of shrinkage either to the capillary pressure or to surface adsorption.

Approaches based on the capillary pressure:

In the 1920s, Terzaghi introduced the notion of effective stress σ' in a porous body, i.e. the difference between the total stress σ applied on the considered body and the hydraulic stress σ_f. Posteriorly, the works of Biot (1941) and Biot and Willis (1957) initiated the poroelasticity approach for isotropic elastic saturated porous bodies. In the absence of external stresses, the latter approach relates the corresponding volumetric strains ε to the pore pressure (equation (4-5)):

$$\varepsilon = \left(\frac{b}{K_b}\right) P^* \tag{4-5}$$

where P^* is the pore pressure, b is called Biot coefficient, and K_b is the elastic bulk modulus of the porous material. Based on thermodynamical considerations, it can be shown that $b = 1 - K_b/K_s$ for a porous body with a homogeneous solid skeleton, being K_s the elastic bulk modulus of the solid skeleton.

For a partially saturated porous body with two or more fluids occupying the pores, the works of Terzaghi and Biot were extended afterwards by Bishop and Blight (1963). In this approach, the pore pressure was written as a weighted average sum of the fluid pressures with a weighting coefficient χ. For instance, if we consider a porous body with a liquid phase (of a pressure P_l) and a gas phase (of a pressure P_g), P^* will be written as:

$$P^* = \chi P_l + (1 - \chi) P_g \tag{4-6}$$

where χ is known as the Bishop parameter. This parameter depends essentially on the saturation of the porous body: $\chi = 1$ if the porous body is fully saturated and $\chi = 0$ if the body is completely dried. It was replaced in the works of Lewis and Schrefler (1987), Hassanizadeh and Gray (1980), Hutter et al. (1999), by the water degree of saturation S_w. This postulation was expansively examined by Gawin et al. (2006), Gawin et al. (2006) and Pereira et al. (2010).

By accepting this notion $\chi = S_w$ the volumetric strains can be assessed from equation (4-7):

$$\varepsilon = \left(\frac{b}{K_b}\right) P^* = -\left(\frac{b}{K_b}\right)(S_w P_c) \quad (4\text{-}7)$$

in which the reference state from which strains are calculated is a state in which the pore space is saturated with a fluid at atmospheric pressure and in which the pressure of the gas is assumed to remain equal to the atmospheric pressure.

This equation is known as the Biot-Bishop model. An extension of this model was established by Coussy et al. (2003) who substituted the average pore pressure with an equivalent pore pressure π that also takes into account the contribution of the interfaces energy, noted as U. In the approach of Coussy et al. (2003), the Helmholtz[1] free energy (per unit volume) F_{sk} of the solid skeleton was subdivided into a Helmholtz free energy F_{sol} for the solid matrix and Helmholtz energy F_{int} for all the existing interfaces: solid/gas – solid/liquid – gas/liquid (see equation (4-8)):

$$F_{sk} = F_{sol} + F_{int} \quad (4\text{-}8)$$

The variation dF_{int} of the Helmholtz energy of the interfaces was taken equal to $\emptyset dU$. The term U is proposed to be calculated, as in equation (4-9), from sorption/desorption tests by considering its dependency solely on the water saturation S_w:

$$U(S_w) = \int_{S_w}^{1} P_c(S_w) dS_w \quad (4\text{-}9)$$

The evaluation of the drying shrinkage volumetric strains ε by Coussy et al. (2003) is done with:

$$\varepsilon = (b/K_b)\pi = \left(\frac{b}{K_b}\right)(P_G - S_w P_c - U) \quad (4\text{-}10)$$

In the work of Coussy et al. (2003), an Eulerian approach for the definition of the state variables was considered. This means that all variables are defined with respect to a current reference state. Dangla and Pereira (2014) rewrote this thermodynamic formulation with a Lagrangian approach (i.e. state variables defined with respect to an initial undeformed reference state).

In the approaches of Biot (1941), Coussy et al. (2003), Dangla and Pereira (2014), the capillary pressure is considered to be the driving mechanism of the drying/wetting of the partially saturated porous materials. Similar approaches based on capillary mechanisms have been also introduced by Gawin et al. (2006) and Vlahinić et al. (2009).

Finally, it is important to recall that in the previous works an effective stress concept is employed. This concept was applied for numerous studies on soils, rocks and concretes. However, it should be noted that according to Carmeliet et al. (2013) the validity of the poroelastic concept relying on a linear relation between stresses and strains can be sometimes questionable. It was shown by Carmeliet and Abeele (2004) that certain materials, like sandstones and woods, show a strong dependency of the elastic modulus on moisture content. For these kind of materials, a nonlinear poroelastic model was needed and is proposed by the authors.

Approaches based on the surface adsorption effect:

The previously cited models were compared in the works of Wyrzykowski et al. (2017) and it was shown that for a low relative humidity (lower than 40%-50%) those models fail to describe drying

[1] The Helmholtz energy of a system is defined as $F = E - TS$ with E the total energy of the system, T the temperature and S the entropy of the system

shrinkage experiments on an extended range of relative humidity. A possible explanation has been given by the authors that linked this limitation to experimental uncertainties in the assessment of the experimental water degree of saturation. On a different approach, Grasley and Leung (2011) suggest that the explanation may be more connected to the absence of a viscoelastic contribution in model. Furthermore, as we will see in section 4.2, we can consider that this limitation can also be partly due to the fact that those models neglect the energy contribution of the presence of adsorbed water or the surface adsorption effect (section 4.1.3.3).

Despite the success of the Bangham's law (equation (4-7)) in evaluating drying strains at low relative humidity range and in taking surface energy effects into account, this relation remains empirical. An extension of poromechanics to account for surface energy effects in absence of capillary effects is proposed by Vandamme et al. (2010) and Zhang (2018).

In the works of Vandamme et al. (2010), a porous system saturated with a fluid at pressure P_f is considered. The Helmholtz free energy F_{int} of the solid/fluid interface (eq. 4-8) is considered to be modified by surface fluid adsorption effect. A Helmholtz free energy (per unit volume) due to fluid adsorption is hence defined as F_{ex} and is given by:

$$F_{ex} = \gamma A_{s/f} + \mu N_{ex} \tag{4-11}$$

where γ is the surface energy of the solid/fluid interface, $A_{s/f}$ its surface area per unit volume, N_{ex} the number of fluid excess moles per unit volume and μ the chemical potential of the corresponding excess moles of fluid.

The variation dF_{ex} of the free energy of the interface can be linked to the variation $dA_{s/f}$ of the interface area and to the variation dN_{ex} of the number of excess moles. According to thermodynamics (Andrieu and Muller, 2005; Maugis, 1980; Weber et al., 1988), the surface area of an interface can be increased either by adding new moles to its surface or by straining the surface at a constant number of moles. The increment dA_{cre} of area is defined as the contribution (per unit volume) to the increment of the interface area of the process of creation of new moles and dA_{def} as the contribution (per unit volume) of the deformation of the existing interface surface area. Accordingly dF_{ex} can be written as (Andrieu and Muller, 2005):

$$dF_{ex} = \sigma_s dA_{def} + \gamma dA_{cre} + \mu dN_{ex} \tag{4-12}$$

The surface stress σ_s can be linked to the surface energy γ by the means of the Shuttleworth equation (Shuttleworth, 1950) given in equation (4-13) where ε_s is equal to $A_{def}/\ A_{s/f}$:

$$\sigma_s = \gamma + \left.\frac{\partial \gamma}{\partial \varepsilon_s}\right|_{\mu} \tag{4-13}$$

Once dF_{ex} is defined, the derivation made in Vandamme et al. (2010) led to an expression of the volumetric drying shrinkage strains as:

$$\varepsilon = \frac{b}{K_b}(P_f - P_a) \tag{4-14}$$

where P_a is a pressure related to adsorption and and is equal to $\sigma_s \left.\frac{\partial A_{s/f}}{\partial \emptyset}\right|_{\varepsilon}$.

4.1.4.3. General discussion

In materials with a wide pore size distribution (like concrete) in contact with a gas at a generic partial pressure, some (smaller) pores are filled with fluid while some other (larger) pores are not filled but have their surface covered with adsorbed fluid. Consequently, in the case of partially saturated porous solids, a proper poromechanical model for fluid-induced deformation should take into account both capillary effects and fluid adsorption effects at the surface of unsaturated pores.

Comparable attempts were earlier made in the literature Nguyen et al. (2020), Pinson et al. (2015). For instance, while treating porous materials with a unique size of pores, Balzer et al. (2017) and Gor et al. (2018) calculated the fluid-induced strains. The authors used surface-energy/stress-based models prior to the occurrence of the capillary condensation and referred to capillary-based models after the capillary condensation takes place. Moreover, while using poromechanics and molecular simulations, Kulasinski et al. (2015) and Chen et al. (2020) proposed sorption-induced deformations models.

Rahoui (2018) accounted for both capillary and fluid adsorption effects by proposing an intuitive combination of the Coussy et al. (2003) model and Bangham's law. Rahimi-Aghdam et al. (2019) proposed a thermodynamic formulation based on a Gibbs energy potential that considers both capillary and fluid adsorption effects. However, in their approach the energy contribution of the adsorbed fluid was only linked to the process of addition of new moles, whereas the contribution corresponding to the deformation of the existing interface was neglected.

4.1.5. Conclusions

In this section, a literature survey concerning shrinkage (autogenous, desiccation) is presented. For each of the latter strains, multiple factors can influence the amplitude and kinetic of strains and are detailed in sections 4.1.1 and 4.1.2. The mechanisms responsible for self-desiccation and desiccation shrinkage are presented in section 4.1.3. Those mechanisms are associated to the capillary pressure, the disjoining pressure and the surface adsorption.

Models for the drying shrinkage based on the previously introduced mechanisms and found in the literature are presented in section 4.1.4. They include phenomenological and poromechanical models. However, most of the presented models do not combine capillary/disjoining pressure and surface adsorption effects. Hence, they remain only valid either for the high range of relative humidity or for the low range of relative humidity.

A poromechanical model is required covering a large spectrum of relative humidity for some applications. Section 4.2 will present hence a new poromechanical model that accounts for capillary and adsorption effects.

4.2. A new model for drying shrinkage

In this section a new poromechanical model that takes into account both the capillary and the adsorption contributions is developed. Section 4.2.1 describes the porous system considered in this work along with the interfaces at play. The constitutive model is derived in section 4.2.1.3 and is then validated on experimental drying shrinkage strains taken from the literature in section 4.2.2.

4.2.1. Thermodynamic derivation of the model

The thermodynamic derivation in this work is established while considering isothermal transformations ($dT = 0$), under the frame of thermodynamics of continuum media. Thus the derived model in this work is valid only for systems formed by mesopores and macropores (i.e. systems with pores larger than two nanometers). The local state postulate allows us to write the thermodynamic equations for any system of volume V from those written for infinitesimal elementary volumes belonging to V (Coussy, 2004). Accordingly, the thermodynamic derivation presented in this section is considered to be written for a local elementary volume V_0. Also, all physical quantities are expressed per unit volume V_0.

The studied elementary volume is assumed to be formed by a solid matrix and a connected porous network formed by saturated pores and unsaturated pores (Fig. 4-8). This system is put into contact with a fluid at a given partial pressure. The reasoning can be applied to any fluid, but here we consider water. Some (smaller) pores may contain liquid water, while some (larger) pores may contain gas.

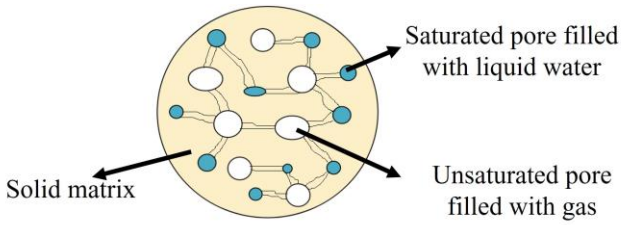

Fig. 4-8 - Schematics of the considered porous medium

We consider that the unsaturated pores have their bulk volume V_G filled with a gas phase composed of N_{vp} moles of water vapor and N_{dra} moles of dry air (as we will see later on, an additional amount of water is adsorbed on the unsaturated pores surface). For the saturated pores, we consider that their bulk volume V_L is filled with a liquid phase composed of N_{lq} moles of liquid water.

By applying Gibbs' vision to the described porous system, the interfaces **Σ** that will be brought into play are: the interface between the solid and gas phases in the unsaturated pores, the interface between solid and liquid in the saturated pores as well as that separating the liquid and gas phases (see Fig. 4-9). Regarding the excess moles to be placed on those interfaces, two assumptions are made in this work. First, at the solid surface of the saturated pores, no transition zone is to be considered (no water excess moles will be placed at the solid/liquid interface), which can be justified by relatively comparable densities of the adsorbed water and the liquid water found in those pores (Powers and Brownyard, 1947) and by an appropriate choice of the location of the Gibbs' interface. Second, at the solid/gas interface, the excess moles N_{ex} is considered to be principally composed of water (see Fig. 4-9). It can be finally noted that in the unsaturated pores, the number of water moles is $N_{ex}+ N_{vp}$, whereas the total number of water moles in the previously defined system is $N_{ex}+ N_{vp} + N_{lq}$.

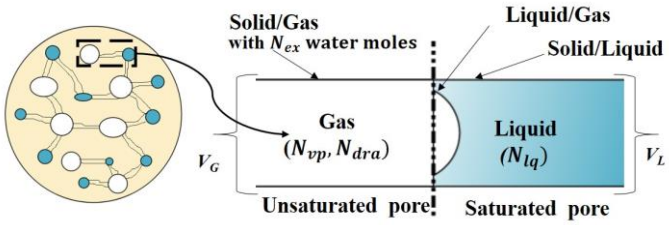

Fig. 4-9 - Schematics of the considered porous medium

4.2.1.1. Notions of Lagrangian porosity and Lagrangian saturation

When talking about a variable describing the system and evolving in time, it is important to indicate the reference state considered. In this frame, we write all equations within a Lagrangian approach. Accordingly, the Lagrangian porosity denoted by ϕ is equal to the ratio of the current pores volume V_p with respect to the initial volume V_0 (Coussy, 2004). An increment φ in the Lagrangian porosity can therefore be defined as:

$$\varphi = \phi - \phi_0 \tag{4-15}$$

where ϕ_0 is the initial porosity of the system (i.e. the initial volume of pores $V_{p,0}$ divided by V_0). Moreover, we define ϕ_L and ϕ_G as the Lagrangian partial porosities respectively filled with liquid and gas phase ($\phi_\alpha = \frac{V_\alpha}{V_0}$ with V_α the current volume of pores filled with the α phase). Those partial porosities verify the relation: $\phi = \phi_L + \phi_G$.

The partial porosity ϕ_α can be written as (Coussy, 2007) :

$$\phi_\alpha = S_\alpha \phi_0 + \varphi_\alpha \tag{4-16}$$

where φ_α is the change of the partial Lagrangian porosity of the phase α. The term φ_α represents the contribution of the deformation process to the partial porosity ϕ_α. The term $(S_\alpha \phi_0)$ represents the contribution of the porous invasion by a phase α to the partial porosity ϕ_α, or also the partial porosity before any deformation. S_α is the Lagrangian saturation, which can be defined as the ratio between the initial volume of pores that are currently filled by the phase α (i.e., the volume of those pores prior to any deformation noted as $V_{\alpha,0}$) divided by the initial volume of pores $V_{p,0}$. Under the frame of this work, S_L is the Lagrangian volume fraction of the saturated pores and S_G the Lagrangian volume fraction of the unsaturated pores.

This definition for Lagrangian saturation will allow us in section 4.2.1.2 to separate the contributions to the energy balance related to the invasion process and to the deformation process (see Equation (4-29)).

4.2.1.2. Constitutive equations

With the purpose of deriving the constitutive laws of poromechanics for the considered system, the energy balance of the solid matrix must be correctly written. To this end, the following procedure is adopted:

i. We write the energy balance of the considered elementary volume V_0.
ii. We subtract the energy contribution of the different 'bulk' components considered from the total energy balance of the system.
iii. We subtract the energy contribution due to the presence of excess water molecules at the solid/gas interface. The energy balance for the solid skeleton (solid matrix + solid/gas, solid/liquid and liquid/gas interfaces) is obtained.

iv. We subtract the energy contribution of the three interfaces: solid/gas (with no excess moles) – solid/liquid – liquid/gas. The energy balance of the solid matrix is obtained.

The transformations in this system are considered to be reversible: first, because they are so slow that viscous dissipations are negligible and then because the solid skeleton is considered to be elastic. Hence, let us remind that the increment in the Helmholtz free energy dF (per unit volume) for the system of interest, formed by multiple phases and undergoing reversible isothermal evolutions can be written as (Coussy, 2004):

$$\mathrm{d}F = \delta W + \sum_i \mu_i \, dN_i \tag{4-17}$$

where δW is the quantity of mechanical work exchanged with the external environment (per unit volume), μ_i is the chemical potential of the ith component and N_i its number of moles (per unit volume).

At first, by referring to equation (4-17) the mechanical work provided to this volume is $\delta W = \sigma d\varepsilon$, σ and ε are respectively the volumetric stress and volumetric strain (no deviatoric load is considered in this approach) developed in the volume V_0 of the porous system.

We recall that the number of moles by components (per unit volume) in the considered volume are: N_{lq} moles of liquid water, N_{vp} moles of water vapor, N_{dra} moles of dry air and N_{ex} excess water moles placed at the solid/gas interface. It is important to note that at thermodynamical equilibrium of the system, the water under its different phases (vapor, liquid, adsorbed) is at the same chemical potential μ_w. Accordingly, equation (4-17) will be then written as:

$$dF = \sigma d\varepsilon + \mu_w dN_{lq} + \mu_w dN_{vp} + \mu_{dra} \, dN_{dra} + \mu_w dN_{ex} \tag{4-18}$$

As a second step, we subtract from equation (4-18) the increments dF_i of the Helmholtz free energy (per unit volume) of each of the 'bulk' components. The latter can be written by analogy to equation (4-17) while considering that the corresponding mechanical work δW is purely hydrostatic and equal to $-P_i \, d\phi_i$, with P_i being the pressure and ϕ_i the Lagrangian volume fraction occupied by the i^{th} component. The increments dF_i are then written as:

$$\mathrm{d}F_{lq} = -P_{lq} \, d\phi_L + \mu_w \, dN_{lq} \tag{4-19}$$

$$\mathrm{d}F_{vp} = -P_{vp} \, d\phi_G + \mu_w \, dN_{vp} \tag{4-20}$$

$$\mathrm{d}F_{dra} = -P_{dra} \, d\phi_G + \mu_{dra} \, dN_{dra} \tag{4-21}$$

In equations (4-19) to (4-21), the water vapor and the dry air occupy the same volume fraction ϕ_G of unsaturated pores while the liquid water occupies the volume fraction ϕ_L of saturated pores. Equations (4-19) to (4-21) are subtracted from equation (4-18) while considering that the gas is perfect and the mixture ideal. So the gas pressure P_G is equal to the sum of the vapor water pressure and the dry air pressure $P_G = P_{vp} + P_{dra}$. Thus we obtain:

$$dF - dF_{lq} - dF_{vp} - dF_{dra} = \sigma d\varepsilon + P_L d\phi_L + P_G d\phi_G \; + \mu_w dN_{ex} \tag{4-22}$$

As a third step, we aim to subtract from the energy balance in equation (4-22), the increment of the free energy (per unit volume) due only to the presence of adsorbed water at the solid/gas interface. This energy is noted as F_{ads} and can be expressed as:

$$F_{ads} = F_{ex} - F_{S/G} \tag{4-23}$$

The free energy F_{ads} is defined as the difference between that F_{ex} of the solid/gas interface when the excess water molecules are adsorbed at its surface and that $F_{S/G}$ of the same interface when no adsorption occurs.

In the purpose of correctly writing each of those energies, let us begin by defining the surface area of the considered solid/gas interface. As indicated in equation (4-12), the variation of this surface area $A_{S/G}$ could be linked to two processes:

- The straining of the considered interface at a constant number of moles. This contribution (per unit volume) is noted as A_{def}.
- The addition of new moles at the considered interface. This contribution (per unit volume) A_{cre} will be written for what follows as a product of $A_0\omega_G$ where A_0 is the total surface area of the pores (per unit volume) at the un-deformed state and ω_G a new variable that defines the Lagrangian surface fraction of the unsaturated pores in the porous body.

This previous consideration leads us to write $A_{S/G}$ as:

$$A_{S/G} = A_0\omega_G + A_{def} \tag{4-24}$$

The previous expression of $A_{S/G}$ is indeed analogous to the expression of ϕ_α given in equation (4-16). Once the different contributions to the increment of $A_{S/G}$ are identified, by referring to equation (4-11), we can write $F_{ex} = \gamma A_{S/G} + \mu_w N_{ex}$ and $F_{S/G} = \gamma_0 A_{S/G}$. In the expression of $F_{S/G}$, γ_0 is the surface energy density prior to deformation and without adsorbed molecules. According to equation (4-12), we write dF_{ex} as:

$$dF_{ex} = \gamma d(A_0\omega_G) + \sigma_s dA_{def} + \mu_w dN_{ex} \tag{4-25}$$

And by differentiating the expression of $F_{S/G}$, we write:

$$dF_{S/G} = \gamma_0 d(A_0\omega_G) + \gamma_0 dA_{def} \tag{4-26}$$

Once equation (4-23) is differentiated, dF_{ads} is then subtracted from equation (4-22). The obtained energy $F_{sk} = F - F_w - F_{ad} - F_{vp} - F_{dra} - F_{ads}$ is defined as the free energy per unit volume of the solid skeleton (i.e. the solid matrix + all three interfaces with constant surface energy densities and with no water excess moles on the solid/gas interface). dF_{sk} is then written as in (after noting $\Delta\gamma = \gamma - \gamma_0$):

$$dF_{sk} = \sigma d\varepsilon + P_L d\phi_L + P_G d\phi_G - (\sigma_s - \gamma_0) dA_{def} - \Delta\gamma d(A_0\omega_G) \tag{4-27}$$

After substitution of each of the partial porosities ϕ_L and ϕ_G by their corresponding expression given in equation (4-16) and while noting that $S_L + S_G = 1$ and $P_c = P_G - P_L$, we derive and obtain:

$$dF_{sk} = \sigma d\varepsilon + P_L d\varphi_L + P_G d\varphi_G - \phi_0 P_c dS_L - (\sigma_s - \gamma_0) dA_{def} - A_0\Delta\gamma d\omega_G \tag{4-28}$$

In the energy balance given by equation (4-28), we can clearly observe that the definition of a Lagrangian porosity and saturation has allowed the separation of the terms related to the pores invasion process (the two terms $-\phi_0 P_c dS_L$ and $-A_0\Delta\gamma d\omega_G$) from the terms related to the deformation process ($\sigma d\varepsilon, P_L d\varphi_L, P_G d\varphi_G$ and $-(\sigma_s - \gamma_0) dA_{def}$)).

If we consider that $A_{def} = A_{def}(\varepsilon, \varphi_L, \varphi_G, S_L)$, we can write:

$$dF_{sk} = (\sigma - \sigma_a) d\varepsilon + (P_L - P_L^a) d\varphi_L + (P_G - P_G^a) d\varphi_G - \phi_0 P_c dS_L - A_0\Delta\gamma d\omega_G \tag{4-29}$$

where:

$$\sigma_a = (\sigma_s - \gamma_0) \left.\frac{\partial A_{def}}{\partial \varepsilon}\right|_{\varphi_L, \varphi_G, S_L} \tag{4-30}$$

$$P_L^a = (\sigma_s - \gamma_0) \left.\frac{\partial A_{def}}{\partial \varphi_L}\right|_{\varepsilon, \varphi_G, S_L} \tag{4-31}$$

$$P_G^a = (\sigma_s - \gamma_0)\frac{\partial A_{def}}{\partial \varphi_G}\Big|_{\varepsilon,\varphi_L,S_L} \tag{4-32}$$

In equation (4-29), the term $(\sigma_s - \gamma_0)\frac{\partial A_{def}}{\partial S_L}\Big|_{\varepsilon,\varphi_L,\varphi_G}$ was neglected because it is considered to be very small with respect to the term $(\phi_0 P_c)$. In fact, the variation of A_{def} with respect to the Lagrangian degree of saturation is negligible compared to the variation of A_{def} with $\varepsilon, \varphi_G, \varphi_L$ (i.e. A_{def} is a contribution to the increment of the interface surface area primarily linked to the deformation process)

As a fourth step, by considering that constant surface energies are accounted for in the energy of the solid skeleton F_{sk}, the approach used in Dangla and Pereira (2014) can be used and F_{sk} can be subdivided as in equation (4-33):

$$F_{sk} = F_{sol}(\varepsilon, \varphi_L, \varphi_G, S_L) + F_{int}(\varphi_L, \varphi_G, S_L) \tag{4-33}$$

F_{sol} is the free energy (per unit volume) stored in the solid matrix and F_{int} the free energy (per unit volume) stored at the interfaces. In equation (4-33), F_{int} is not a function of the porous material strains; in fact, it depends on them only indirectly through the pores volumes and the saturation. According to Dangla and Pereira (2014), we can write:

$$F_{int}(\varphi_L + \lambda\phi_0 S_L, \varphi_G + \lambda\phi_0 S_G, S_L) = \left(1 + \frac{2}{3}\lambda\right) F_{int} \qquad \forall \lambda \ll 1 \tag{4-34}$$

Equation *(*4-34) indicates that from the current state, at a constant degree of saturation, any isotropic homothetic variation of the pore dimension by a factor (1+$\lambda/3$) will induce a volume variation of $(1+\lambda)$ and a surface variation of $(1+2\lambda/3)$ (with $\phi_0 S_\alpha$ the initial volume of the considered pore in the undeformed state). This statement is valid regardless of the shape of the pores (see Appendix 6). The differentiation of equation (4-34) with respect to λ leads to:

$$\phi_0 S_L \frac{\partial F_{int}}{\partial \varphi_L}\Big|_{\varphi_G,S_L} + \phi_0 S_G \frac{\partial F_{int}}{\partial \varphi_G}\Big|_{\varphi_l,S_L} = \frac{2}{3} F_{int} \tag{4-35}$$

We perform a first-order expansion of F_{int} with respect to φ_L and φ_G and write equation (4-36):

$$F_{int} = \frac{2}{3} U_L(S_L)\varphi_L + \frac{2}{3} U_G(S_L)\varphi_G + \phi_0 U(S_L) \tag{4-36}$$

with $U(S_L)$ being the energy of the interfaces before any deformation process, per unit volume of porous solid. $U_L(S_L)$ and $U_G(S_L)$ are interfaces energies respectively associated with liquid and gas phases. By combining equations (4-35) and (4-36), we identify U_L and U_G as two functions that verify the following relation: $U = S_L U_L + S_G U_G$.

By equating the expression given in *(*4-29) with the derivative of equation (4-33), and knowing that $\partial F_{sol}/\partial S_L$ is negligible compared to $\partial F_{int}/\partial S_L$ and that the terms $\frac{2}{3}\varphi_L dU_L(S_L)$ and $\frac{2}{3}\varphi_G dU_G(S_L)$ are considered to be very small (assumption of small deformations and porosities), we obtain:

$$\frac{\partial Fint}{\partial S_L} = \phi_0 \frac{dU(S_L)}{dS_L} = -\phi_0 P_c - A_0 \Delta\gamma \frac{d\omega_G}{dS_L} \tag{4-37}$$

After integration of equation (4-37) from a reference saturated state (considered for a relative humidity of 100%), we write:

$$U(S_L) = -\int_{S_{100}}^{S_L} P_c(S_L)\, dS_L - A_0/\phi_0 \int_{\omega_{100}}^{\omega_G} \Delta\gamma\, d\omega_G \tag{4-38}$$

In equation (4-38), the volume fraction of saturated pores for a relative humidity of 100% is considered to be equal to S_{100} ($S_{100} \leq 1$) and the surface fraction of unsaturated pores is equal to ω_{100} ($\omega_{100} \geq 0$). In fact, based on experimental observations of sorption tests found in the literature (Baroghel-Bouny et al., 1999; Chen, 2013; Mjahad, 2012), when a porous material is exposed to an atmosphere with a relative humidity approaching 100%, the pores (especially the large ones) are not necessarily fully saturated (see chapter 2)

As a final step, we write the free energy (per unit volume) of the solid matrix as in equation (4-39):

$$(dF_{sol})_{S_L} = (\sigma - \sigma_a)d\varepsilon + \left(P_L - P_L^a - \frac{2}{3}U_L\right)d\varphi_L + \left(P_G - P_G^a - \frac{2}{3}U_G\right)d\varphi_G \quad (4\text{-}39)$$

where $(dF_{sol})_{S_L}$ means that the differentiation is performed at constant liquid saturation S_L.

In equation (4-39), we define $\pi_L = \left(P_L - P_L^a - \frac{2}{3}U_L\right)$ and $\pi_G = \left(P_G - P_G^a - \frac{2}{3}U_G\right)$ as the equivalent pore pressures associated respectively to the liquid and gas phases. Equation (4-39) will be used in the following section to write the poromechanical constitutive laws.

It should be noted that the above derived approach considers the presence of a "spreading pressure" (i.e. a force acting on the solid surface of the unsaturated pores, tangential to it) (Gor et al., 2018). In their approach, Gor et al. (2018) considered that both the radius and length of their cylindrical pore could vary, differently from each other. However, according to equation (4-34) and Appendix 6, in our approach we impose the radial deformation of the cylindrical pore to be equal to its axial deformation: indeed, the radius and length vary by the same factor ($1+\lambda/3$) given that in our approach a unique thermodynamic variable φ links the different dimensions of the pore.

4.2.1.3. Constitutive laws of poromechanics and the equivalent pore pressure

Once the free energy of the solid matrix is written, we define its Legendre-Frenchel conjugate function as $F_{sol}^* = F_{sol} - \pi_L\varphi_L - \pi_G\varphi_G$ and $dF_{sol}^* = (\sigma - \sigma_a)d\varepsilon - \varphi_L d\pi_L - \varphi_G d\pi_G$. Within the frame of linear elasticity, F_{sol}^* must be a quadratic function with respect to the variables ε, π_L and π_G. Therefore F_{sol}^* is written as (Coussy, 2004):

$$F_{sol}^* = \frac{1}{2}K_b\varepsilon^2 - b_L\varepsilon\,\pi_L - b_G\varepsilon\,\pi_G - \frac{1}{2}\frac{{\pi_L}^2}{N_{LL}} - \frac{1}{2}\frac{{\pi_G}^2}{N_{GG}} - \frac{\pi_G\cdot\pi_L}{N_{LG}} \quad (4\text{-}40)$$

After comparing the expression of dF_{sol}^* with the derivative of equation (4-40), we will be able to write the following constitutive equations:

$$\sigma - \sigma^a = K_b\varepsilon - b_L\pi_L - b_G\pi_G \quad (4\text{-}41)$$

$$\varphi_L = b_L\varepsilon + \frac{\pi_L}{N_{LL}} + \frac{\pi_G}{N_{LG}} \quad (4\text{-}42)$$

$$\varphi_G = b_G\varepsilon + \frac{\pi_L}{N_{LG}} + \frac{\pi_G}{N_{GG}} \quad (4\text{-}43)$$

where K_b is the elastic bulk modulus of the porous medium; N_{LL}, N_{LG} and N_{GG} are the Biot moduli; b_L and b_G are the Biot coefficients associated respectively to the liquid and gas phases. The Biot coefficient of the porous medium is defined as $b = b_L + b_G$. When assuming that the saturated and unsaturated pores in the considered porous system undergo an iso-deformation (this hypothesis states that porous volume filled by each of the two considered fluids (liquid and gas) deforms in the same way whenever they are subjected to volumetric stresses but to no pressure and temperature variations (Coussy, 2007)), we come to find that $b_L = S_L \cdot b$ and $b_G = S_G \cdot b$. Those two relations allow us to write equation (4-41) as:

$$\sigma - \sigma^a = K_b\varepsilon - b(S_L\pi_L + S_G\pi_G) = K_b\varepsilon - b\pi \quad (4\text{-}44)$$

In the above equation, the equivalent pore pressure is defined as $\pi = (S_L\pi_L + S_G\pi_G)$. After replacing π_L and π_G by their expressions given in section 4.2.1.2, we write:

$$\pi = S_L P_L + S_G P_G - \frac{2}{3}U - (\sigma_s - \gamma_0)(S_L \frac{\partial A_{def}}{\partial \varphi_L}\Big|_{\varepsilon,\varphi_G,S_L} + S_G \frac{\partial A_{def}}{\partial \varphi_G}\Big|_{\varepsilon,\varphi_L,S_L}) \quad (4\text{-}45)$$

We consider that $\frac{\partial A_{def}}{\partial \varepsilon}\Big|_{\varphi_L,\varphi_G,S_L}$ is small compared to $\frac{\partial A_{def}}{\partial \varphi_L}\Big|_{\varepsilon,\varphi_G,S_L}$ and $\frac{\partial A_{def}}{\partial \varphi_G}\Big|_{\varepsilon,\varphi_L,S_L}$. By taking into account this assumption and by analogy with the approach adopted in Dangla and Pereira (2014):

$$A_{def}(\varphi_L + \lambda\phi_0 S_L, \varphi_G + \lambda\phi_0 S_G, S_L) = \left(1 + \tfrac{2}{3}\lambda\right) A_0\omega_G \ \forall\lambda \ll 1 \quad (4\text{-}46)$$

The derivation of equation (4-46) with respect to λ gives:

$$\frac{2}{3}A_0\omega_G = \phi_0 S_L \frac{\partial A_{def}}{\partial \varphi_L}\Big|_{\varphi_G,S_L} + \phi_0 S_G \frac{\partial A_{def}}{\partial \varphi_G}\Big|_{\varphi_L,S_L} \quad (4\text{-}47)$$

After substitution of equation *(*4-47) and *(*4-38) in the equivalent pore pressure expression given by equation (4-45), we derive:

$$\pi = S_L P_L + S_G P_G + \frac{2}{3}\int_{S_{100}}^{S_L} P_c(S_L)\, dS_L + \frac{2}{3}(A_0/\phi_0)(\int_{\omega_{100}}^{\omega_G} \Delta\gamma\, d\omega_G - (\sigma_s - \gamma_0)\omega_G) \quad (4\text{-}48)$$

The last term of equation (4-48) can be integrated by parts (with $\Delta\gamma = \gamma - \gamma_0$) and thus we write:

$$\pi = S_L P_L + S_G P_G + \frac{2}{3}\int_{S_{100}}^{S_L} P_c(S_L)\, dS_L + \frac{2}{3}(A_0/\phi_0)(\int_0^{\gamma} -\omega_G(S_L)d\gamma - (\sigma_s - \gamma)\,\omega_G(S_L)) \quad (4\text{-}49)$$

We replace the Gibbs isotherm relation (equation (4-2)) and the Shuttleworth relation (equation (4-13)) in equation (4-49). By replacing S_G with $1 - S_L$, the equivalent pore pressure π can be written as:

$$\pi = P_G - S_L\, P_C + \frac{2}{3}\int_{S_{100}}^{S_L} P_c(S_L)dS_L + \frac{2}{3}(A_0/\phi_0)\left(\int_0^{\mu} \omega_G(S_L)\,\Gamma\, d\mu - \left(\frac{\partial\gamma}{\partial\varepsilon_s}\right)\Big|_{\mu} \omega_G(S_L)\right) \quad (4\text{-}50)$$

Finally, from what has been mentioned in this section, we outline that the constitutive behavior law is given by equation (4-44) with the expression of the equivalent pore pressure given in equation (4-50). It should be noted that the assumption made earlier in this section of a negligible dependence of A_{def} with respect to the skeleton strains at constant partial Lagrangian porosities and saturation results in a zero adsorption stress in equation (4-44): $\sigma_a = (\sigma_s - \gamma_0)\frac{\partial A_{def}}{\partial \varepsilon}\Big|_{\varphi_L,\varphi_G,S_L} = 0$.

4.2.1.4. Contributions to the equivalent pore pressure π

It is important to note that in expression (4-49), each term underlines a specific contribution to the development of the equivalent pore pressure:

- The term $\boldsymbol{P_G - S_L P_C}$ (written also as $\boldsymbol{S_L P_L + S_G P_G}$) is the contribution of the average pore pressure.
- The term $\frac{2}{3}\int_{S_{100}}^{S_L} \boldsymbol{P_c(S_L)\, dS_L}$ is the contribution of the interfaces energy. Capillary effects are a consequence of all three terms: $\boldsymbol{P_G - S_L P_C + \frac{2}{3}\int_{S_{100}}^{S_L} P_c(S_L) dS_L}$.
- The term $\frac{2}{3}(\boldsymbol{A_0/\phi_0})(\int_0^{\mu} \boldsymbol{\omega_G(S_L)\, \Gamma\, d\mu})$ is the effect of fluid adsorption.
- The last term $\frac{2}{3}(\boldsymbol{A_0/\phi_0})(-\left(\frac{\partial \gamma}{\partial \varepsilon_s}\right)\Big|_{\mu} \boldsymbol{\omega_G(S_L)})$ is the Shuttleworth effect which can also be considered a part of the adsorption effect .

By referring to other poromechanical models found in literature, it could be pointed out that the model of Biot-Bishop accounts only for the average pore pressure. Moreover, the Coussy et al. (2003) model accounts only for the contribution of the average pore pressure and the interfaces energy. In contrast, the Bangham's model stands on the unique contribution of the fluid adsorption effects. On another hand, for fully saturated porous materials, the model proposed in Vandamme et al. (2010b) allows to consider the contribution of both the average pore pressure and the fluid adsorption effects. Finally, the model proposed by Rahoui (2018) allows to consider all three contributions of the average pore pressure, the interfaces energy and the fluid adsorption effects, for an unsaturated porous system. However, in the work of Rahoui (2018), the Shuttleworth effect was not taken into account.

4.2.2. Application to drying shrinkage - model validation on experimental data from literature

The poromechanical model developed in section 4.2.1 is used in this section to predict the strains induced by the drying of a porous material. Those strains can be evaluated according to equation *(*4-44). Given that, in a drying shrinkage experiment, the total stress σ is equal to zero and that the material is considered to be isotropic, the strain along one axis of the specimen ε_d is equal to (1/3) of the total volumetric strain ε and can be written as:

$$\varepsilon_d = \frac{1}{3}\varepsilon = \frac{1}{3}\frac{(b\,\pi)}{K_b} \qquad (4\text{-}51)$$

Equation (4-51) can be generalized to calculate an increment $\Delta\varepsilon_d$ with respect to any reference state as $\Delta\varepsilon_d = \frac{1}{3}\Delta\varepsilon = \frac{1}{3}\frac{(b\Delta\pi)}{K_b}$, where $\Delta\pi$ is the increment of equivalent pore pressure with respect to this same reference state.

4.2.2.1. Evaluation of the model parameters

The assessment of the equivalent pore pressure π requires the calculation of various input parameters. In this work, the input parameters are evaluated with respect to the relative humidity h_R. The approaches or techniques adopted for this calculation are indicated in the list below. It should be noted that, to use the BJH method (Barrett et al., 1951) to calculate ω_G and S_L, we assume the pores to be cylindrically shaped. The model parameters and hypotheses made about them are listed below:

- $\boldsymbol{P_G}$: the pressure of the gas phase is assumed to be constant and equal to the atmospheric pressure
- $\boldsymbol{S_L(h_R)}$: the Lagrangian saturation or volume fraction of the saturated pores at a given relative humidity is calculated with the BJH (Barrett et al., 1951) method as in section 4.2.2.4.
- $\boldsymbol{P_C(h_R)}$: the capillary pressure for a given relative humidity is calculated with the Kelvin equation (Chapter 2 – equation 2.9)
- $\boldsymbol{A_0}$: the total surface of the pores or specific surface area of the material per unit volume (m^2/m^3). A_0 is the product of the specific surface area (m^2/g) determined with the BET (Brunauer et al., 1938) method (detailed in Chapter 2 – section 2.1.5.2) or the BJH technique, by the experimental dry density ρ_{dry} (g/m^3).
- $\boldsymbol{\omega_G(h_R)}$: the surface fraction of the unsaturated pores at a given relative humidity is the ratio between the surface of the unsaturated pores at a given relative humidity obtained with the BET or BJH method with respect to the total surface of pores (i.e. the specific surface area A_0)
- $\boldsymbol{\phi_0}$: the initial porosity assessed by the processing of experimental data
- $\boldsymbol{d\mu}$: the total differential of the chemical potential of the adsorbed water in the unsaturated pores, calculated with the following equation derived from Kelvin equation: $d\mu = RTd\ln(h_R)$
- $\boldsymbol{\Gamma(h_R)}$: the number of the water excess moles per unit surface at the solid/gas interface. It is equal to $\frac{\rho_w}{M_w} t(h_R)$ where $t(h_R)$ is the thickness of the multimolecular adsorbed layer of water at the surface of the unsaturated pores. In the case of water adsorption at a solid surface, $t(h_R)$ can be evaluated by empirical relations such as Badmann et al. (1981) or Hagymassy et al. (1969). In this work, $t(h_R)$ is evaluated using the Badmann et al. (1981) relation (see section 4.2.2.3). We assume that the density of adsorbed water is that of bulk liquid water (Powers and Brownyard, 1947).
- $\left(\frac{\partial \gamma}{\partial \varepsilon_s}\right)\Big|_{\boldsymbol{\mu}}$: the Shuttleworth term. The value of this term depends highly on the morphology and the orientation of the solid surface (Weber et al., 1988). Although the Shuttleworth (1950) equation has been widely used (a review of this relation is given by Cammarata (1994)), how the surface energy γ varies with the skeleton strains is not obvious (Schulman et al., 2018). In this work, we propose to fit this term on experimental drying shrinkage strains.
- $\boldsymbol{K_b}$: the elastic bulk modulus K_b of the porous medium is considered to be constant (i.e., not to depend on the skeleton strains or on chemical potential μ). It is assessed by the processing of experimental data (see section 4.2.2.5).

4.2.2.2. Experimental results from literature for model validation

The predicted drying shrinkage strains by the new poromechanical model (section 4.2.1) are compared with experimental results given in the literature for three different porous materials:

Maruyama et al. (2018) experimental data on hardened cement paste

The hardened cement paste (noted as HCP) studied in this work is prepared with a Japanese white Portland cement with a water-to-cement mass ratio equal to 0.55. After mixing, the cement paste was poured into 3x13x300 mm^3 molds. Following 180 days of curing under lime-saturated water, the HCP samples were placed into a chamber an 11% relative humidity and equilibrated for

more than 6 years. Sorption isotherms were obtained with a volumetric sorption analyzer (using an HCP powder) at different temperatures and consisted of a humidification process followed by a drying process. In this work we refer to the desorption isotherm (in terms of water content) obtained at 20°C with a relative humidity ranging from 0.97 down to 0 (Fig. 4-10-a). As for the dry reference state, the HCP samples were placed under vacuum at a temperature of 105°C at the end of the measurement. The experimental water content is normalized with respect to this mass. The water content when the relative humidity approaches zero, as seen in (Fig. 4-10-a), is not null, due to the fact that the drying of the sample at 105°C carries away more water than exposing the sample to a zero relative humidity at 20°C.

The measurement of the drying shrinkage strains was done with a LVDT (Linear Variable Differential Transformer) for 3x13x300 mm^3 samples that were incrementally dried from h_R = 0.9 to h_R = 0.11. The values of the drying shrinkage strains vs h_R are given in (Fig. 4-10-b). The length of the sample at h_R =0.9 is considered to be the reference state. As for the porosity and the dry density of the considered HCP, no values for those parameters were given in the cited work. We referred to a porosity of a similar hardened cement paste (with a water-to-cement mass ratio of 0.5) studied by (Di Bella et al., 2017) where the dry reference state was equally taken by the authors for an oven drying at 105°C: in that case, the experimental porosity was $\phi_0 = 21\%$. As for the dry density of the HCP, an estimated value was later calculated and found to be compatible with the BJH calculation (details are shown in section 4.2.2.4).

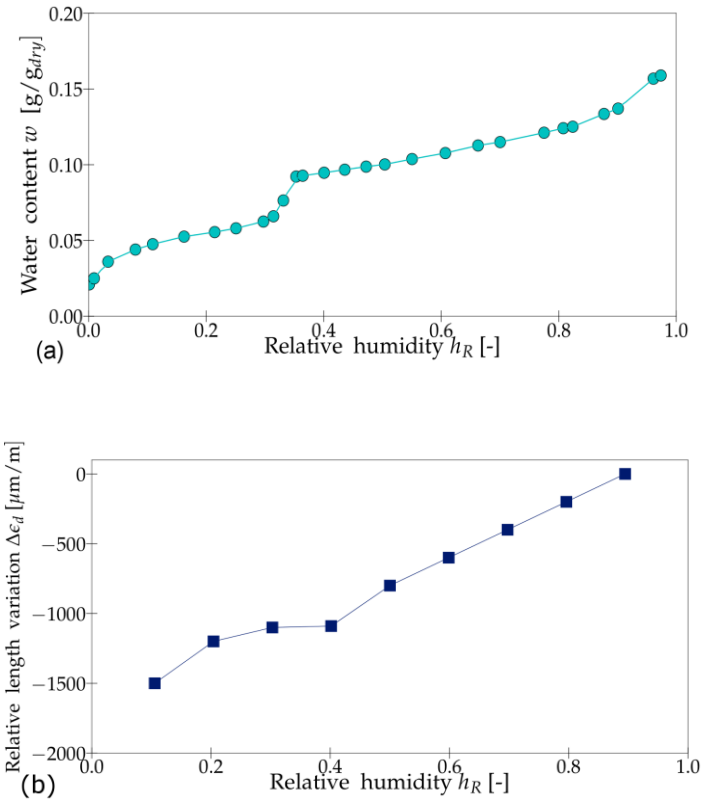

Fig. 4-10 – Data on hardened cement paste from Maruyama et al. (2018): (a) experimental water desorption isotherm – (b) experimental relative length variation

Baroghel-Bouny et al. (1999) experimental data on concrete

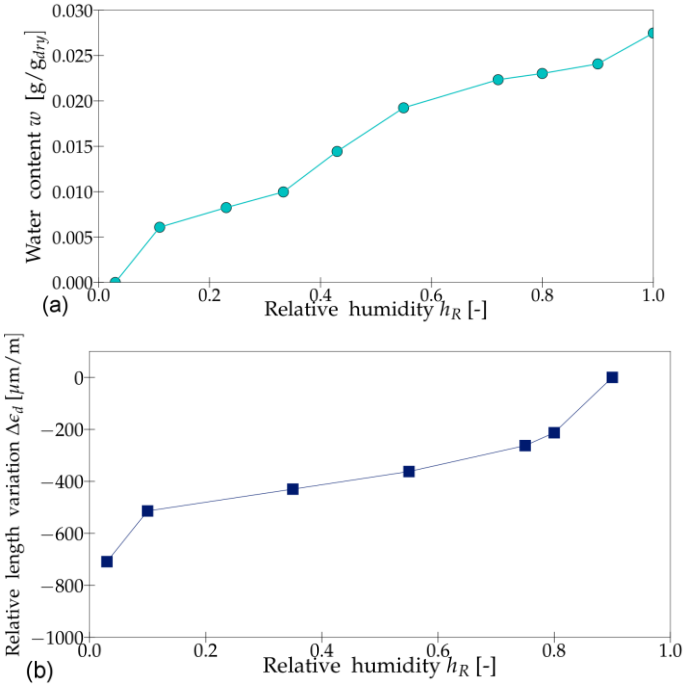

Fig. 4-11 – Data from Baroghel-Bouny et al. (1999) on concrete: (a) experimental water desorption (b) experimental relative length variation

The high-performance concrete tested by Baroghel-Bouny et al. (1999) was prepared with a normal Portland cement with a certain fraction of silica fume and of superplasticizers. The specimens were discs with a 3 mm thickness and a 90 mm diameter. At the beginning of the tests, the concrete had an age of 1 year. The sorption test consisted of a drying process followed by a re-humidification process at a temperature of T=23°C. In this work, we refer to the desorption isotherm. The relative humidity varied between 1 and 0.03. The dry reference state was chosen as the mass of the sample at h_R=0.03 and at an ambient temperature of T=23°C. By doing so, the authors wanted to avoid submitting the concrete to a drying process with conditions that differed from those of the desorption process; in fact, the risk with oven drying is that it could damage the specimen and so increase its porosity. Fig. 4-11-a displays the variation of the experimental water content with respect to h_R. This desorption isotherm can also be found in terms of the experimental degree of saturation in the work of Baroghel-Bouny et al. (1999).

The samples used for the measurement of the drying shrinkage strains were identical to the ones used for the sorption test. The diameter and length of the discs were measured with dial gauges. By considering the diameter and length at h_R= 0.904 as an initial reference state, the values of the drying shrinkage strains vs. h_R are given in (Fig. 4-11-b). The porosity of the high-performance concrete is provided and is equal to 8.2%. The dry density, given also in the referred article, is equal to 2382 kg/m^3

Amberg and McIntosh (1952) experimental data on Vycor glass

The Vycor glass cited in the work of Vlahinić et al. (2009) is a Vycor 7930 Corning glass that was originally tested by Amberg and McIntosh (1952). The desorption tests were done at a temperature of 11°C on rods of 11 cm length and 0.73 cm in diameter. The dry reference state is defined by Vlahinić et al. (2009) as the mass of the sample at h_R=0.05.The desorption isotherm is given in terms of the degree of saturation (Fig. 4-12-a). The drying shrinkage strains are given in (Fig. 4-12-b) with an initial measurement reference taken for h_R=0.99. The porosity of this material

is given by the manufacturer and is equal to 28% (Vlahinić et al., 2009a). The dry density is equal to 1450 kg/m^3.

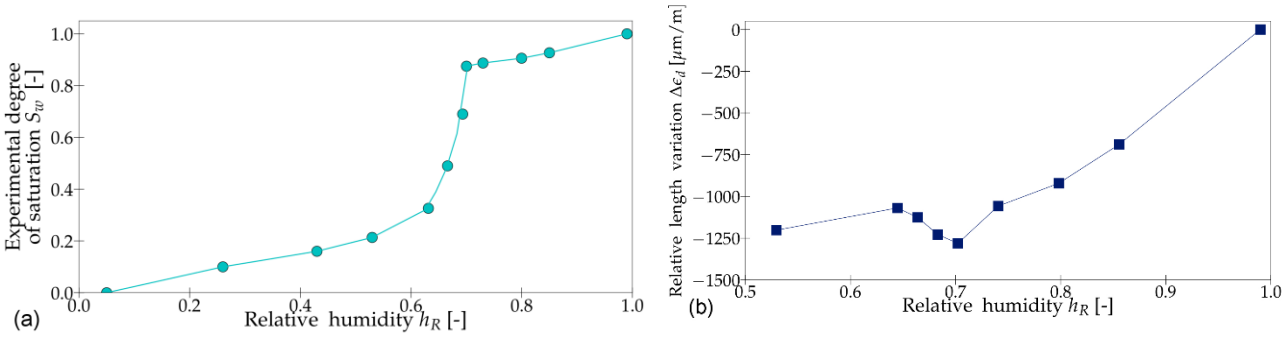

Fig. 4-12– Data on Vycor glass by Amberg and McIntosh (1952): (a) experimental water desorption isotherm – (b) experimental relative length variation

4.2.2.3. Calculation of the specific surface area and the thickness of the adsorbed water layer

The value of the specific surface area for each of the studied materials with the range of h_R where the BET theory (chapter 2 – section 2.1.5.2) is applied, is given in Table 4-1.

Experimental Data	***Range of h_R where the BET theory is applied***	***Specific surface area S_{BET}***
Maruyama et al. (2018)	0.11 – 0.30	157 m^2/g
Baroghel-Bouny et al. (1999)	0.11 – 0.33	27 m^2/g
Amberg and McIntosh (1952)	0.25 – 0.43	81 m^2/g

Table 4-1– Specific surface area of the materials calculated with the BET theory

In our experience, the value of the specific surface area calculated with the BET method depends on the number of experimental points used for the calculation. As a matter of fact, according to chapter 2- section 2.1.5.2, the surface area is calculated from a proper fit of experimental sorption points. As far as the considered experimental data are concerned, the orders of magnitude obtained for the hardened cement paste and the high-performance concrete are in agreement with the literature: for a hardened cement paste, values of specific surface area are found to vary between 100 and 200 m^2/g (Baroghel-Bouny , 2007), while for high-performance concretes values are found to be around 20 m^2/g (Chen, 2013; Baroghel-Bouny, 1994). As for the Vycor glass, the value calculated in Table 4-1. is lower than the values found in the literature. A value of 106 m^2/g obtained from water vapor isotherms is noted in (Gor and Bernstein, 2016a) and values ranging from 100 m^2/g to 173 m^2/g are given in (Bentz et al., 1998). The latter values were assessed from experimental nitrogen isotherms (with nitrogen isotherms known to provide smaller BET specific surface areas than the ones assessed from water vapor isotherms (Baroghel-Bouny, 1994)). The small specific surface area obtained in this work for the Vycor glass may be due to the limited number of experimental points that served in its computation. Indeed, only two experimental points were used in the BET calculation: the first one at h_R = 0.25 and the second one at h_R = 0.43. Therefore, for the experimental data of (Amberg and McIntosh, 1952), an alternative method for calculating the specific surface area is further proposed (see section 4.2.2.4).

Concerning the thickness t of the adsorbed layer of water, it could be determined by empirical relations as described in section 2.1.5.2. The empirical relation given by Badmann et al. (1981) is

used in this work: $t(h_R) = K_1 + K_2 \ln(-\ln(h_R))$. For each of the studied cementitious materials, we try to fit the values of K_1 and K_2 on the thickness t_{exp} of the adsorbed layer measured experimentally: $t_{exp} = V_{ads}/S_{BET}$ with V_{ads} the volume of adsorbed water assessed from the experimental water desorption isotherms. The obtained values are then compared to those given by Badmann et al. (1981) for non-porous cement raw materials : $K_1 = 0.385$ nm and $K_2 = -0.189$ nm. The comparison is shown in Fig. 4-13.

We come to find that the values fitted on each of the experimental results ($K_1 = 0.42$ nm and $K_2 = -0.15$ nm for the experimental data of Maruyama et al. (2018); $K_1 = 0.40$ nm and $K_2 = -0.21$ nm for the experimental data of Baroghel-Bouny et al. (1999)) are in the vicinity of the values given by Badmann et al. (1981). This small difference could be due to the different dry reference state taken by each of the authors while calculating the experimental water content. Nevertheless, we can admit that the Badmann et al. (1981) values are mostly respected: we use those values in what follows.

As for the experimental data of the Vycor glass, no values for K_1 and K_2 were found in the works of Badmann et al. (1981) for a similar composition. Therefore, K_1 and K_2 are fitted on the corresponding water isotherm. The values retained are: $K_1 = 0.33$ nm and $K_2 = -0.31$ nm.

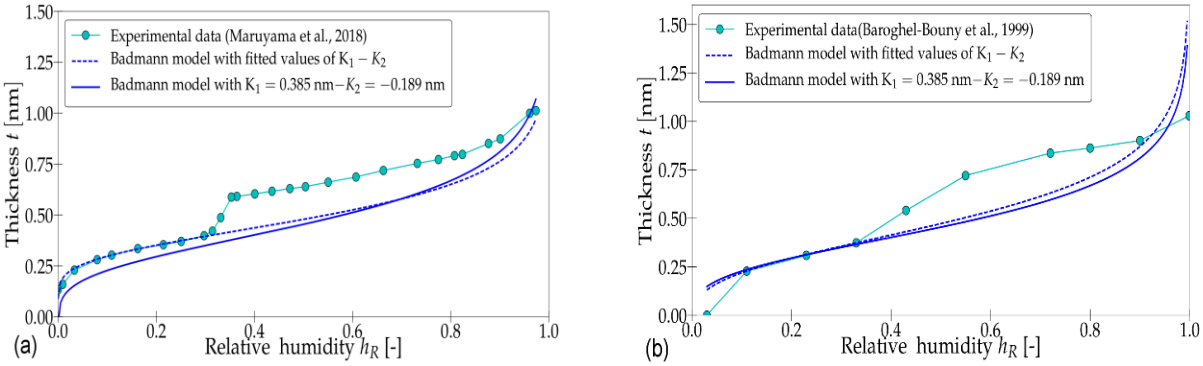

Fig. 4-13 - Experimental thickness of the adsorbed layer of water compared to the thickness given by the Badmann model: (a) experimental results of Maruyama et al. (2018) with fitted values $K_1 = 0.42$ nm and $K_2 = -0.15$ nm – (b) experimental results of Baroghel-Bouny et al (1999) with fitted values $K_1 = 0.40$ nm and $K_2 = -0.21$ nm

4.2.2.4. Results of the BJH method applied to the experimental data

The BJH method was previously detailed in Chapter 2 – section 2.1.5.2. We recall that the volume noted $\delta V_{p,n}$ and given by equation 2-18, corresponds to the class of pores that will be desaturated at a given h_R. Hence, the cumulative sum of the volumes ($\sum_i \delta V_{p,i}$) corresponds to the total volume of the unsaturated pores at a certain relative humidity h_R.

Knowing the total volume of pores per unit dry mass ($\phi_0 V_{m0}$) in the material with V_{m0} the total volume of the sample per unit of dry mass, we can now compute the volume fraction of the unsaturated pores at a certain relative humidity h_R . This volume fraction is noted as $S_G = \sum_i \delta V_{p,i} / (\phi_0 V_{m0})$) and the volume fraction of the saturated pores at the same relative humidity is $S_L = 1 - S_G$. While the experimental degree of saturation S_w indicates the total fraction of water (adsorbed water + free liquid water) found in pores at a certain relative humidity, S_L designates exclusively the fraction of the free liquid water found in the pores at this relative humidity.

On another hand, as previously noted in section 2.1.5.2, the cumulative sum of areas (noted $\sum_i \delta a_{p,i}$) corresponds to the total area of the unsaturated pores at a certain relative humidity. Knowing the total surface of pores (which is, close to a multiplying factor, equal to the specific surface area of the material), we can calculate the surface fraction of the unsaturated pores for a given relative humidity. This surface fraction is noted as ω_G and is equal to the ratio of $\sum_i \delta a_{p,i}$ with respect to the specific surface area. We recall that the total area $\sum_i \delta a_{p,i}$ calculated at the final stage of the

computation corresponds to a specific surface area S_{BJH}. This surface area can be compared to the specific surface area S_{BET} assessed with the BET method (section 4.2.2.3).

Before proceeding in the BJH computation an important point on which relies this approach must be further discussed. This point consists in identifying the initial saturation state of the pores. In fact, for calculation purposes, this method assumes that in the initial reference state, the pores are completely saturated. Therefore, according to this technique, if the initial state corresponds to a relative humidity approaching 100%, the experimentally measured degree of saturation at this state $S_w(h_R \rightarrow 100)$ must be equal to 1. However, as it can be seen in the literature, this constraint is not always experimentally verified. For cementitious materials, Baroghel-Bouny et al. (1999) noted $S_w(h_R \rightarrow 1)$ =0.8 for the high-performance concrete and $S_w(h_R \rightarrow 1)$ =0.85 for other studied hardened cement. Additionally, for high-performance concretes, Chen (2013) and Mjahad (2012) measured $S_w(h_R \rightarrow 1)$ equal to 0.8 and 0.9 respectively (see chapter 2 – section 2.3). Those experimental observations rely on the fact that submitting a porous material to a relative humidity approaching 1 may not induce a full saturation of the pores, which might only be reached by immersing the sample in liquid water.

Consequently, to be consistent with those experimental observations, for each of the cementitious materials studied in this work, the BJH calculation will start from a virtual state where the sample is considered to be fully saturated (under water) and then followed by the initial experimentally measured state (where the sample is exposed to a relative humidity approaching 1). For the latter state, we can consider that the percentage of unsaturated pores is small so that we can consider no water is adsorbed on the unsaturated pore surface (i.e. $S_L(h_R \rightarrow 1) = S_w(h_R \rightarrow 1)$). An example of the first steps of the BJH computation for the experimental data of Baroghel-Bouny et al. (1999) is given in Table 4-2.

Relative humidity	Water content	Water degree of saturat-ion	Volume of water (cm^3/g)	Desorbed water volume (cm^3/g)	Volume of unsaturat-ed pores (cm^3/g)	Area of unsaturat-ed pores (m^2/g)	Total volume of unsaturat-ed pores (cm^3/g)	Total area of unsaturated pores (m2/g)	Lagran-ian gas saturation	Lagran-gian liquid saturati-on	Lagrang-ian surface fraction
h_R	w	S_w	$V_{w,n}$	$\delta V_{w,n}$	$\delta V_{p,n}$	$\delta a_{p,n}$	$\sum_i \delta V_{p,i}$	$\sum_i \delta a_{p,i}$	S_G	S_L	ω_G
Under water	-	1.0	$\phi_0 \cdot V_{0m}$ =0.0343	0.00	0.00	0.00	0.00	0.00	0.00	1.0	0.00
$h_R \rightarrow 1$	0.0274	0.8	0.0274	0.00690	0.00690	0.00128	0.00690	0.00128	0.20	0.80	4.7 10^{-05}
0.99	0.0271	0.79	0.0271	0.00033	0.00033	0.00012	0.0072	0.00140	0.21	0.79	5.2 10^{-05}
0.98	0.0268	0.78	0.0268	0.00033	0.00034	0.00832	0.0075	0.00973	0.22	0.78	0.0004
0.97	0.0265	0.77	0.0265	0.00033	0.00034	0.01511	0.0079	0.02485	0.23	0.77	0.0009

Table 4-2– BJH computation of the experimental data of Baroghel-Bouny et al. (1999)

Concerning the experimental data of Maruyama et al. (2018), to calculate the fraction of the unsaturated/saturated pores, the total volume of pores per unit dry mass ($\phi_0 V_{m0}$) must be known. However, as indicated in section 4.2.2.2, considering that the experimental porosity of the studied HCP was not cited in the mentioned article, we chose a value of ϕ_0=21% (Di Bella et al., 2017).

On the other hand, given that sorption tests of Maruyama et al. (2018) were done using powder samples, the volume V_{m0} was not measured in this work. Therefore, according to what was mentioned earlier in this section, we can assume that for the initial experimentally measured state ($h_R = 0.97$) the experimental degree of saturation can take a value between 0.85 and 0.99. The value of 0.85 was given in Baroghel-Bouny et al. (1999) for hardened cement pastes. Therefore, for the experimental data of Maruyama et al. (2018), two calculations scenarios will be tested (named *Sc1* and *Sc2*) for the calculation of the drying shrinkage strains: for scenario *Sc1*, we consider that $S_w(h_R = 0.97) = 0.85$ and for scenario *Sc2* we consider that $S_w(h_R = 0.97) = 0.99$. For each of those scenarios, we

can calculate a volume V_{m0} (per unit of dry mass) and a dry density[2]. The calculated values for the dry densities are respectively 1120 kg/m^3 and 1320 kg/m^3 for scenarios *Sc1* and *Sc2*. Those dry densities will be used later to calculate the specific surface area A_0 per unit volume (Table 4-3).

For the experimental data of Maruyama et al. (2018), the BJH results are shown in Fig. 4-14-a and Fig. 4-14-b.

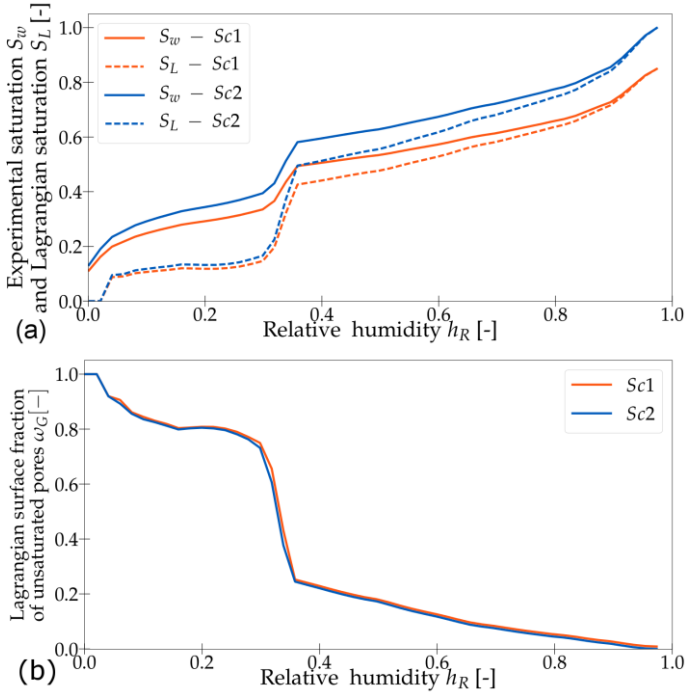

Fig. 4-14 –Variations of (a): Lagrangian liquid saturation S_L, water degree of saturation S_w and (b): Lagrangian surface fraction ω_G of unsaturated pores, for the experimental data of Maruyama et al. (2018)

For a relative humidity approximately equal to 0.35, the fraction of the saturated pores decreases sharply: the material loses a significant amount of the free liquid water. When the relative humidity h_R becomes smaller than *0.3*, a small part of the pores remains saturated (S_L ≈10%) until reaching approximately h_R=*0.03*. Below this relative humidity, all the water that remains in the pores is adsorbed water. It should be noted that in the purpose of judging the consistency of the BJH results, Rouquerol (2003) indicates that one must check that the specific surface area S_{BJH} calculated with the BJH method does not differ more than 10% from the specific surface area S_{BET} calculated with the BET method. This verification has been done with a calculated BJH surface area of 154 m^2/g compared to 157 m^2/g to that obtained with the BET method, which results in a difference of 1.9%. In Fig. 4-14-b is shown the surface fraction ω_G of the unsaturated pores as a function of the relative humidity h_R. The specific surface area used to compute ω_G is the one obtained with the BET method (Table 4-1). We should note that in this study case, the difference of 1.9% between S_{BJH} and S_{BET} is small enough not to impact significantly the evolution of ω_G, if the latter is calculated with the specific surface area S_{BJH}. For these ω_G curves, the same trends are observed as for S_L.

As for the two tested calculation scenarios *Sc1* and *Sc2*, we can note that in terms of saturation (Fig. 4-14-a) the two scenarios differ principally in the range of relative humidity where h_R >0.3. In terms of the calculated surface fraction of the unsaturated pores (Fig. 4-14-b), the difference is negligible.

[2] $S_w = V_w/(\phi_0 V_{m0})$ where the volume of water in the pores V_w (per unit of dry mass) is calculated from the experimental water content (per unit of dry mass) given by (Maruyama et al., 2018) ($V_w = w/\rho_w$). For a given value of S_w *(h_R = 0.97)*, w *(h_R = 0.97)* and ϕ_0=21%, we can calculate a volume V_{m0} (per unit of dry mass). The dry mass will be equal to $\rho_{dry} = 1/V_{m0}$

The obtained BJH results for the experimental data of Baroghel-Bouny et al. (1999) are presented in Fig. 4-15: when the relative humidity reaches a value of 0.55, S_L decreases sharply (Fig. 4-15-a) and the material loses a significant amount of liquid water from the saturated fraction of the pores. Below a relative humidity of 0.33, a small fraction of pores remains saturated (S_L ≈10%) until reaching a value of h_R=0.11 at which all pores become unsaturated. For the calculation of ω_G (shown in Fig. 4-15-b), the specific surface area used is the one calculated with the BET method (Table 4-1). The specific surface area calculated with the BJH is equal to 26.5 m^2/g, which results in a difference of 2% with respect to the 27 m^2/g calculated with the BET method.

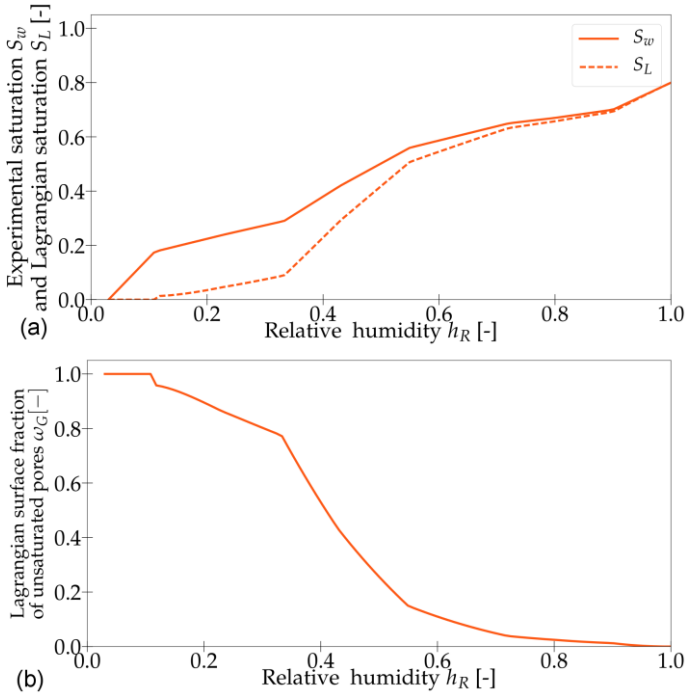

Fig. 4-15 - Variations of (a): Lagrangian liquid saturation S_L, water degree of saturation S_w and (b): Lagrangian surface fraction ω_G of unsaturated pores, for the experimental data of Baroghel-Bouny et al. (1999)

Finally, for the experimental data of Amberg and McIntosh (1952) given in Fig. 4-16, the specific surface area S_{BJH} calculated with the BJH method is 100 m^2/g. A difference of 20% with the specific surface area S_{BET} = 81 m^2/g (see Table 4-1) calculated with the BET method is noted. As previously explained, this difference could be due to an underestimation of S_{BET} linked to the limited number of experimental points used for the BET computation. Consequently, having an order of magnitude similar to specific surface areas of Vycor glasses found in the literature (see section 4.2.2.3), the specific surface area of 100 m^2/g calculated with the BJH method will be retained for processing the Amberg and McIntosh (1952) experimental data. The values of K_1 and K_2 of the Badmann formula are recalibrated while taking a specific surface of 100m^2/g. Values of 0.25nm and -0.23nm are obtained respectively for K_1 and K_2 . The results are given in Fig. 4-16: when the relative humidity h_R reaches a value of 0.59 all the pores becomes unsaturated. Below this value, water will be found only under an adsorbed form. The main difference between the results obtained for the Vycor glass and for the previously tested cement materials is that Vycor glass tends to remain saturated during the initial stages and then to release sharply all the liquid water in a very narrow range of relative humidity h_R (in this example in a range between 0.7 and 0.59). Vlahinić et al. (2009a) linked this behavior to the morphology of the Vycor glass: contrary to cementitious materials, this material shows a narrow pore size distribution, with a majority of pores in the nanometer range (Scherer, 1986). The corresponding calculated values of the Lagrangian surface fraction ω_G (=$\sum_i \delta a_{p,i}$/ S_{BJH}) of unsaturated pores is shown in Fig. 4-16-b and is compared to the calculated values of ω_G (=$\sum_i \delta a_{p,i}$/ S_{BET}).

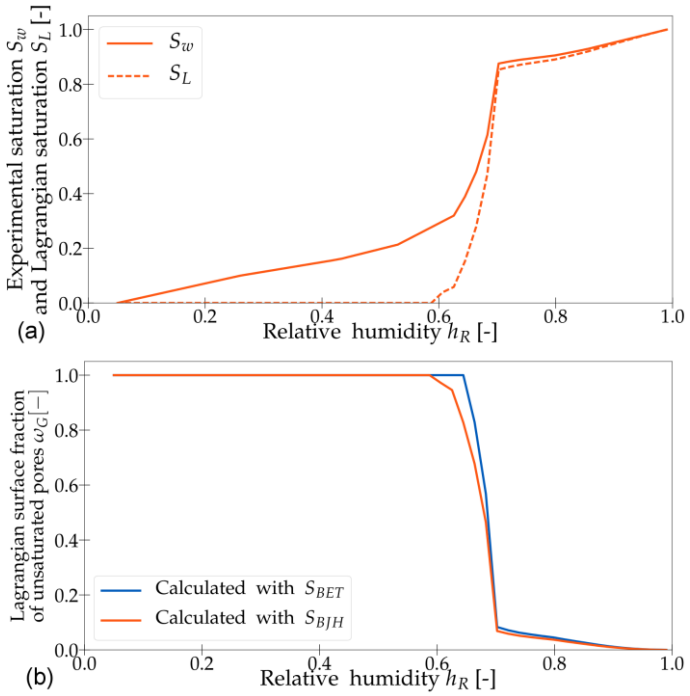

Fig. 4-16 - Variations of (a): Lagrangian liquid saturation S_L, water degree of saturation S_w and (b): Lagrangian surface fraction ω_G of unsaturated pores, for the experimental data of Amberg and McIntosh (1952)

Another important input parameter of the model is the specific surface area per unit volume A_0 (m^2/m^3): this value is calculated from the product of the previously calculated specific surface area (m^2/g) with the dry density (kg/m^3) for each of the tested materials. The calculated values are shown in Table 4-3.

Experimental Data	***Specific surface area*** (m^2/g)	***Dry density*** (kg/m^3)	A_0 (m^2/m^3)
Maruyama et al. (2018) – *Sc1*	157	1120	$1.76\ 10^{+08}$
Maruyama et al. (2018) – *Sc2*	157	1320	$2.07\ 10^{+08}$
Baroghel-Bouny et al. (1999)	27	2382	$6.43\ 10^{+07}$
Amberg and McIntosh (1952)	100	1450	$1.45\ 10^{+08}$

Table 4-3 - Calculated specific surface areas per unit volume

The previously computed quantities $S_L(h_R)$, $\omega_G(h_R)$ and A_0 will be used as input parameters for the calculation of the equivalent pore pressure and of the drying shrinkage strains. The corresponding results are shown in section 4.2.2.5.

It should be noted that in Maruyama et al. (2018), for the cement paste studied in this work (and other studied cementitious porous bodies) the sudden drop observed in the experimental water content for a relative humidity h_R near 0.35 was explained by the cavitation phenomena, that causes no liquid water to be found in the pores for a relative humidity h_R below approximately 0.35: "During adsorption or desorption, the surface tension acting on the meniscus causes negative pressure in the condensed liquid water […].When the negative pressure in the liquid water becomes too large, the liquid water becomes unstable, the nucleation of vapor bubbles must occur and suddenly a certain amount of water is released from the sample." Nonetheless, even though the previously presented BJH results (Fig. 4-14 and Fig. 4-15) showed a sharp decrease in the liquid water amount S_L for a relative humidity near 0.35, no total desaturation of the pores (i.e. $S_L \neq 0$) was observed for this value of relative humidity. Therefore, aiming at studying the impact of considering such an allegation, an alternative BJH computation method is shown in Appendix 7. This method consists on using the BJH technique until reaching a h_R near 0.35 and then to assume complete desaturation of the pores ($S_L = 0$ and $\omega_G = 1$). The impact of this method on the calculation of the drying shrinkage strains is also presented in Appendix 7.

The BJH calculation can provide an approximate value for the average radii of pores found in a studied porous material. Given that the poromechanical approach developed in this work is only valid for porous materials presenting macro and meso pores, the BJH calculation could therefore indicate approximately when micropores (if present) start to get emptied and hence under which relative humidity the developed model could lose its validity. According to the BJH results, micropores (with an average pore size < 2 nm) could be found for relative humidities smaller than approximately 20% for the studied HCP and high performance concrete and smaller than 25% for the Vycor glass. Therefore, it is important to note that while the stresses and strains are calculated (in section 4.2.2.5) for ranges of relative humidities down to 3%, the calculated values for relative humidities smaller than 20%-25% could be considered only as approximate values.

4.2.2.5. Model results – equivalent pore pressure and drying shrinkage strains

In order to compute the drying shrinkage strains, by referring to equation (4-51), two important parameters are needed: the Biot coefficient b and the elastic bulk modulus K_b of the porous medium. Due to the uncertainties in the value of the Biot coefficient, this parameter is not fixed but chosen to vary within a range, whereas the value of K_b is fixed. Results in terms of drying shrinkage strains are then given and discussed based on the defined range, by testing both the upper and the lower bound of b.

In the article of Maruyama et al. (2018), no values were provided for the two parameters K_b and b. Therefore, to be consistent with the previously assumed porosity of the studied HCP, we refer again to the work of Di Bella et al. (2017), which provide for K_b the value of 14.8 GPa. As for the elastic bulk modulus K_s of the solid skeleton, Di Bella et al. (2017) refer to the works of Grasley et al. (2007) and Hashin and Shtrikman (1963) and indicate a range of variation for this parameter: $38\ \text{GPa} \leq K_s \leq 55\ \text{GPa}$. Making use of the classical relation $b = 1 - K_b/K_s$, the given range of variation of K_s together with the adopted value of K_b leads to a range of variation of the Biot coefficient b: $0.61 \leq b \leq 0.73$.

In the same way, in the article of Baroghel-Bouny et al. (1999), the values of K_b and b for the studied concrete were not provided. We refer then to the work of Brue et al. (2017) where for a similar high-performance concrete the authors note: $K_b = 30.8$ GPa and $b = 0.55$. We consider a range of variation of the Biot coefficient for the high-performance concrete between 0.55 and 0.7.

Finally concerning the studied Vycor glass, in the works of Vlahinić et al. (2009), a value of $K_b = 7.2$ GPa is given based on the works of Scherer (1986). K_s is indicated in the range $19\ \text{GPa} \leq K_s \leq 23.6\ \text{GPa}$ based on the works of Amberg and McIntosh (1952). This range of K_s, for the given value of K_b, leads to a range of variation of Biot coefficient b between 0.62 and 0.7.

In what follows, results are given for each set of experimental data first in terms of drying shrinkage strains and then of the equivalent pore pressure. As for the equivalent pore pressure, the contribution of each term is also shown, with the following notation:

- Contribution of the average pore pressure effect ($P_G - S_L P_C$) also written as ($S_G P_G + S_L P_L$) in dark blue.
- Contribution of the interfaces energy effect ($\frac{2}{3}\int_{S_{100}}^{S_L} P_c(S_L)\, dS_L$) in orange.
- Contribution of the fluid adsorption effect ($\frac{2}{3}(A_0/\phi_0)(\int_0^{\mu} \omega_G\, \Gamma\, d\mu$)) in light blue.
- Contribution of the Shuttleworth effect ($\frac{2}{3}(A_0/\phi_0)(-\left(\frac{\partial \gamma}{\partial \varepsilon_s}\right)\Big|_{\mu} \omega_G)$)) in yellow.
- Equivalent pore pressure π in green.

Together with the equivalent pore pressure and individual contributions, the Lagrangian saturation S_L (dashed magenta curve) and the Lagrangian surface fraction of unsaturated pores ω_G (dashed blue curve) are also presented to associate them to the various contributions.

First, we discuss the results obtained with the experimental data of Maruyama et al. (2018) while taking scenario *Sc1* into account (Fig. 4-17).

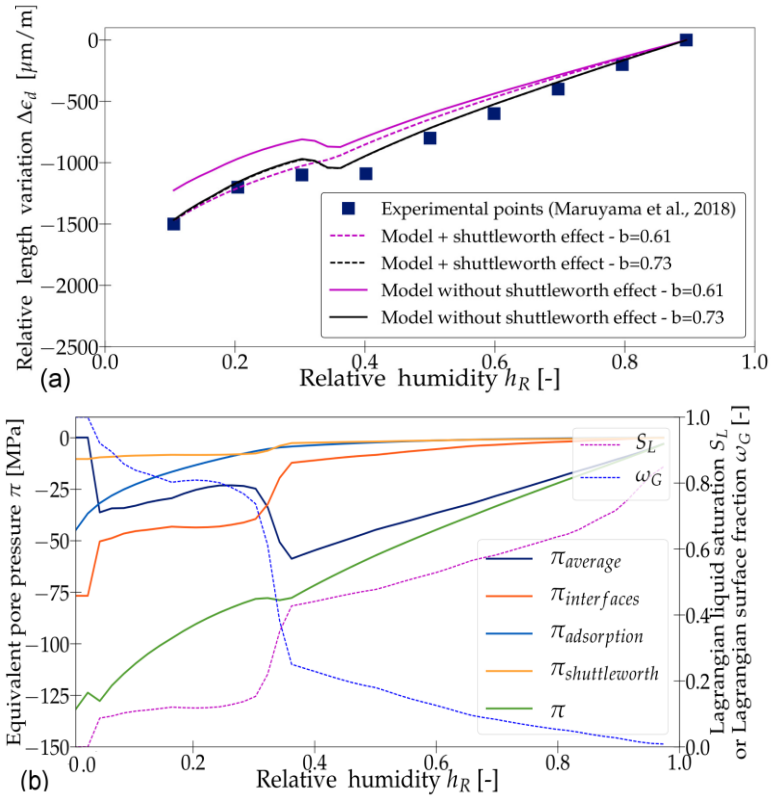

Fig. 4-17 – Results for the experimental data of Maruyama et al. (2018) with the calculation scenario *Sc1*: (a) Calculated relative length variations with $\frac{\partial\gamma}{\partial\varepsilon_s}$ = 3.96 10^{-2} (N/m) when b=0.61 and 7.29 10^{-3} (N/m) when b=0.73 (b) Contributions to the equivalent pore pressure

The calculated drying shrinkage strains compared to the experimental ones are given in Fig. 4-17-a. In solid lines, we represent the obtained model results for both tested values of Biot coefficient b while neglecting the Shuttleworth effect (i.e. by setting the term $\left(\frac{\partial\gamma}{\partial\varepsilon_s}\right)\Big|_{\mu}$ in expression (4-49) equal to zero). In dashed lines, we represent the results obtained for both tested values of Biot coefficient b while fitting the Shuttleworth term on the drying shrinkage experimental points. The obtained values for this term are 3.96 10^{-2} N/m when b=0.61 and 7.29 10^{-3} N/m when b=0.73. It is important to note that when b=0.73, the term $\frac{\partial\gamma}{\partial\varepsilon_s}$ is of a small order of magnitude compared to that of surface energies found in the literature (for instance, for a water-air interface at ambient temperature, γ_{GL} =73.10^{-03} N/m (Coussy, 2010)). As for the obtained results, when b is taken equal to 0.61, fitting the Shuttleworth term allows to better model the drying shrinkage strains. In contrast, when b is taken equal to 0.73, fitting this parameter has no impact on the modelling results, which are quite satisfactory. Due to the lack of information necessary to identify an exact value for the Shuttleworth term, both tested solutions shown in Fig. 4-17-a (considering zero fit parameter or fitting the Shuttleworth term) can be retained.

The equivalent pore pressure π with the different contributions are displayed in Fig. 4-17-b. The Shuttleworth contribution shown in this figure corresponds to a fit of the Shuttleworth term while taking an average value for the Biot coefficient (b=0.67). At first sight, it could be noticed that in the high relative humidity range (h_R>*0.35*), the average pore pressure contributes most importantly in the development of the equivalent pore pressure, whereas in the low relative humidity range (h_R<*0.35*) interfaces energy and adsorption effects contribute primarily.

We can also observe that the average pore pressure and the interfaces energy contributions are correlated to the liquid saturation S_L. In fact, when during desorption, the material loses sharply a significant amount of capillary water (S_L drops sharply near h_R =*0.35*), the contribution of the interfaces energy increases in a similar way and the contribution of the average pore pressure decreases accordingly. In the range 0.03<h_R<*0.35,* the amount of liquid water in the pores becomes very small and varies very slightly, and similarly the interfaces energy effect and the average pore pressure effect in this range of relative humidity vary, but only slightly. When the relative humidity reaches 0.03, the material loses all the remaining liquid water and the liquid saturation S_L becomes equal to 0. At this stage, the contribution of the average pore pressure drops to zero whereas the contribution of the interfaces energy increases sharply to reach a plateau.

In regards to the contribution of the adsorption effect, the latter is controlled by two important parameters: the parameter ω_G and the parameter Γ which is directly linked to the thickness t of the adsorbed layer of water. The fact that the thickness t decreases with a decreasing relative humidity h_R on the whole range of relative humidity leads to a continuous increase of the adsorption stresses σ_s with a decreasing relative humidity. Concerning the Shuttleworth effect, the corresponding contribution to the equivalent pore pressure (Fig. 4-17-b) is considered to be small compared to those of the other effects, and that over the whole range of relative humidity. Finally, it may be concluded that, for this studied case, the proposed model appears to give satisfactory results (especially when b is near 0.73) even when the Shuttleworth effect is neglected. A small improvement of the strains results can be provided when a Shuttleworth parameter is fitted on experimental results.

The same evaluation has been done for the calculation scenario *Sc2* of the experimental data of Maruyama et al. (2018). The corresponding calculated drying shrinkage strains are shown in Fig. 4-18. Similar to the previous considered scenario, the same conclusion could be drawn. The results given by the proposed model while assuming a negligible Shuttleworth effect appear to be quite satisfactory. Taking into account a fit parameter can lead to a small improvement of the results. On another hand, it can be deduced that taking into account a calculation scenario *Sc1* (with an experimental degree of saturation S_w *(h_R = 0.97) = 0.85)* or a calculation scenario *Sc2* (with an experimental degree of saturation $S_w(h_R = 0.97) = 0.99$) for the studied experimental data of Maruyama et al. (2018) shows a small impact on the modelling results.

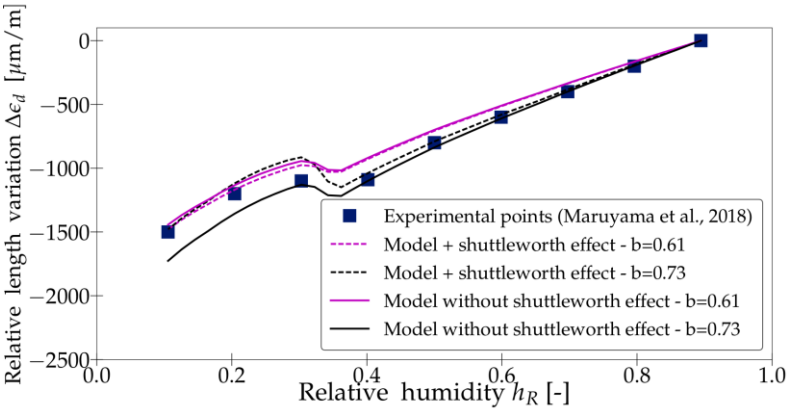

Fig. 4-18 - Calculated relative length variation for the experimental data of Maruyama et al. (2018) with the calculation scenario *Sc2* with $\frac{\partial\gamma}{\partial\varepsilon_s}$ = 4.95 10^{-3} N/m when b=0.61 and -2.8 10^{-02} N/m when b=0.73

On another hand, the analysis done with the experimental data of Baroghel-Bouny et al. (1999) leads to the results shown in Fig. 4-19.

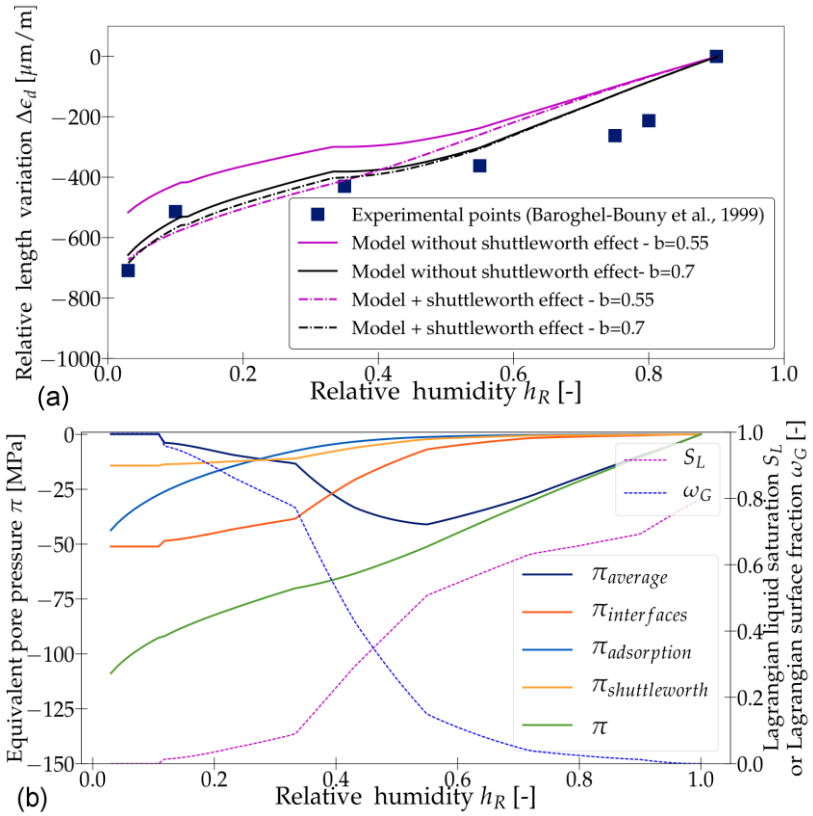

Fig. 4-19 – Results for the experimental data of Baroghel-Bouny et al. (1999): (a) Calculated relative length variation with $\left(\frac{\partial\gamma}{\partial\varepsilon_s}\right)\Big|_{\mu}$ = 4.97 10-2 N/m for b=0.55 and 6.88 10-3 N/m for b=0.7- (b) Contributions to the equivalent pore pressure

Regarding the contributions to the equivalent pore pressure (see Fig. 4-19-b), the same comments done previously with the experimental data of Maruyama et al. (2018) apply, while noting an important contribution of the average pore pressure for relative humidities larger than approximately 0.5 in this case. When the remaining amount of liquid water in the pores becomes small, the adsorption effects and the interfaces energy effect are the primordial contributions to the increase of the equivalent pore pressure. Regarding the Shuttleworth effect (that corresponds to a fit of the Shuttleworth term for an average value of $b = 0.62$), equally in this case, its contribution to the equivalent pore pressure is considered to be small with respect to other effects contributions. The previously drawn conclusions can be made: the model gives satisfactory results when neglecting the Shuttleworth effect (especially when we take a Biot coefficient of 0.7). Taking into account a parameter to fit the Shuttleworth effect can slightly refine the modelling results.

Finally, we point out that during the drying of cementitious materials, the creation of micro-cracks remains a possibility. However, micro-cracks can be avoided when the drying process is slow enough: a step by step drying is done by Maruyama et al. (2018) and Baroghel-Bouny et al. (1999). Moreover, we believe that even though stresses and pressures (of 100 MPa) calculated by the model might appear of considerable impact on the appearance of micro-cracks; those pressures created at the scale of the microstructure should not be interpreted as macro stresses leading to micro-cracks when then tension threshold of cementitious materials is exceeded. We believe that those micro stresses could be submitted to some kind of microstructural relaxation before acting on the macro scale.

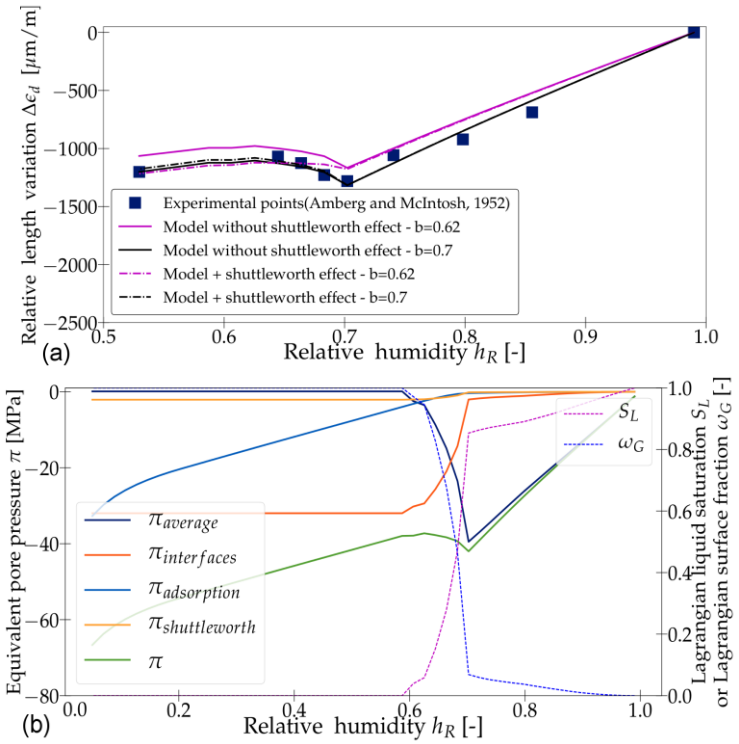

Fig. 4-20 – Results for the experimental data of Amberg and McIntosh (1952): (a) Calculated relative length variation with $\left(\frac{\partial\gamma}{\partial\varepsilon_s}\right)\Big|_{\mu}$ = 1.51 10^{-2} N/m for b=0.62 and -2.19 10^{-3} N/m for b=0.7- (b) Contributions to the equivalent pore pressure

Last but not least, beyond the estimation of correct values for the Biot coefficient and the Shuttleworth parameter, it is shown in all previous results that the proposed model is able to correctly evaluate drying shrinkage strains on the whole range of relative humidity. Moreover, the proposed model is capable of capturing the remarkable plateau in drying shrinkage strains observed at intermediate relative humidity. This plateau represents a transition in the relative contribution to the increase of the equivalent pore pressure, from the average pore pressure effects (in the high h_R range) to the interfaces energy and the adsorption effects (in the low h_R range).

Finally, we point out that during the drying of cementitious materials, the creation of micro-cracks remains a possibility. However, micro cracks can be avoided when the drying process is slow enough: a step by step drying is done by Maruyama et al. (2018) and Baroghel-Bouny et al. (1999). Moreover, we believe that even though stresses and pressures (of 100 MPa) calculated by the model might appear of considerable impact on the appearance of micro-cracks; those pressures created at the scale of the microstructure should not be interpreted as macro stresses leading to micro cracks when then tension threshold of cementitious materials is exceeded. We believe that those micro stresses could be submitted to some kind of microstructural relaxation before acting on the macro scale.

4.2.2.6. Comparison of the proposed model with the Biot-Bishop and the Coussy et al. (2003) models

In this section, we aim to compare the newly proposed poromechanical with a classical Biot-Bishop model (equation (4-5)) and the Coussy et al. (2003) model (equation (4-7)) in their ability to predict drying shrinkage strains. Comparisons are done while neglecting the Shuttleworth effect, i.e. by considering $\left(\frac{\partial \gamma}{\partial \varepsilon_s}\right)\Big|_{\mu} = 0$. In such case, our model comes back to the model of Rahoui (2008). Both the upper and lower bounds of the Biot coefficient were tested for each set of experimental data. The results (see Fig. 4-21) show a good estimation of the drying shrinkage strains by the three models in the higher range of relative humidity.

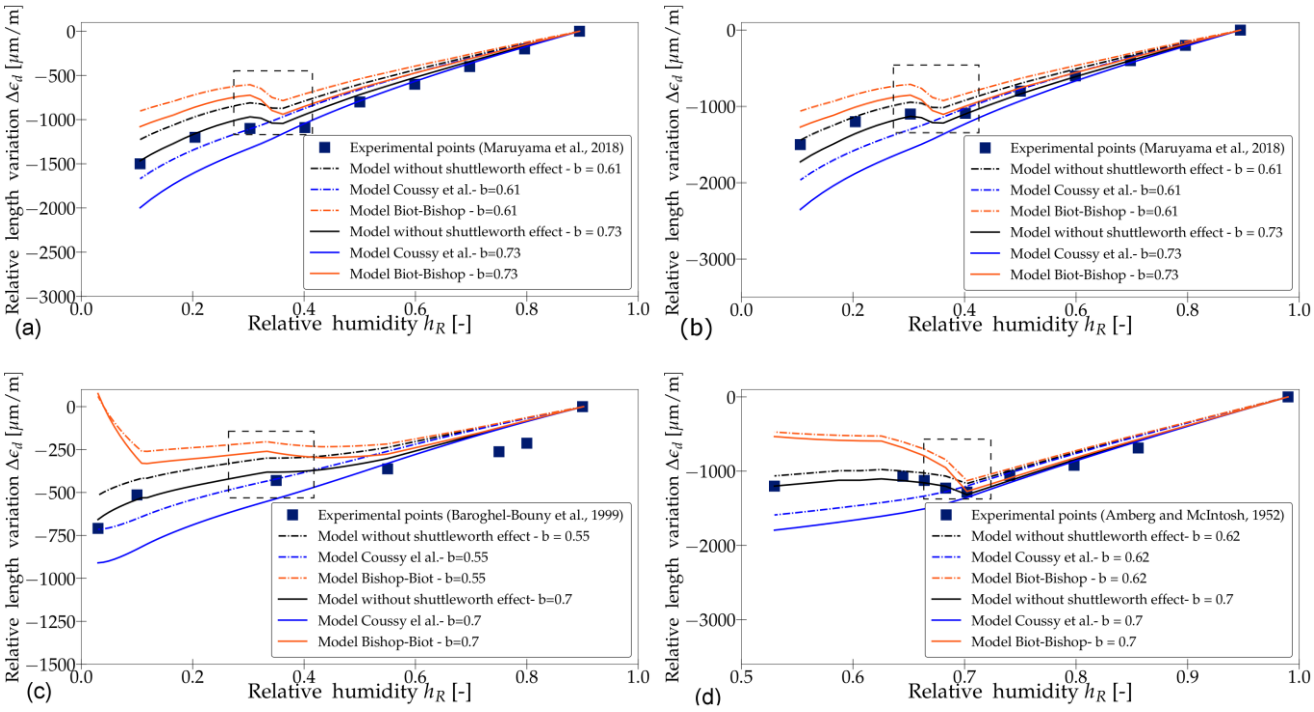

Fig. 4-21- Comparison of the new model with the Biot-Bishop and the Coussy et al. (2003) models for the experimental data of: (a) Maruyama et al. (2018) with the calculation scenario *Sc1*– (b) Maruyama et al. (2018) with the calculation scenario *Sc2*– (c) Baroghel-Bouny et al. (2018)- (d) Amberg and McIntosh (1952)

In this range, the average pore pressure is the main contributor to the equivalent pore pressure. This range corresponds more precisely to relative humidities larger than approximately 0.4 for the cementitious material studied in Maruyama et al. (2018) and Baroghel-Bouny et al. (1999) and then approximately 0.7 for those of Amberg and McIntosh (1952).

Nevertheless, in the low range of relative humidity, the Biot-Bishop model shows less satisfactory results. In fact, this model is strongly impacted by the experimental method adopted to measure the experimental degree of saturation S_w. More specifically, it is affected by the choice of the dry reference state (Di Bella et al., 2017). Indeed, as it can be seen in Fig. 4-21-c and Fig. 4-21-d, this model can even predict a swelling of the material instead of a shrinkage. On another hand, regarding the Coussy et al. (2003) model, it is observed that the latter can lead to an over-estimation of the drying shrinkage strains in the low range of relative humidity. Moreover, it should be pointed out that this model predicts an approximately constant slope over the whole range of h_R. The latter observation has been previously made in the works of Di Bella et al. (2017) and Wyrzykowski et al. (2017). In contrast to the previous models, the proposed model provides a better estimation of the drying shrinkage strains especially when the Biot coefficient is near 0.7. In addition, this model

permits to clearly capture the transition (pointed out with the dashed frames of Fig. 4-21) at which contributions to the effective pore pressure stem mostly from the average pore pressure on one hand, and mostly from the fluid adsorption and interfaces energy effects on the other hand.

4.2.3. Discussion of the new poromechanical approach

In this section, the macroscopic poromechanical approach for unsaturated bodies has been revisited and extended to the low relative humidity ranges to model the drying processes. By adopting a proper thermodynamical derivation, we derived a new model that allows to account for different contributions in the development of the effective stresses such as the average pore pressure contribution, the interfaces energy contribution, the fluid adsorption and the Shuttleworth effect contributions. Regarding the input parameters, this model requires essentially the use of two commonly known techniques for the identification of features of the pores structures: the BET theory (Brunauer et al., 1938) and the BJH technique (Barrett et al., 1951). In the current framework, the BJH technique was used because of its consistency with the developed poromechanical approach.

The poromechanical model has been tested and validated on experimental results (water desorption curves and drying shrinkage strains curves) found in the literature. Different porous materials are studied, such as an ordinary cement paste from the works of Maruyama et al. (2018), a high-performance concrete tested by Baroghel-Bouny et al. (1999) and a Vycor glass tested by Amberg and McIntosh (1952).

By applying the newly developed model to the mentioned experimental data, we have shown that the average pore pressure is the main contributor to the strains/stresses development in the higher relative humidity range (i.e., for relative humidities larger than approximately 0.4 for cementitious materials and than 0.7 for Vycor Glass). In the low relative humidity range, both interfaces energy effects and fluid adsorption effects play an important role. Regarding the Shuttleworth effect (which captures the variation of the surface energy with respect to the skeleton strains), due to the fact that the magnitude of the effect cannot be assessed in an evident way a priori, we proposed to fit the parameter that governs its magnitude (i.e. the term $\left(\frac{\partial \gamma}{\partial \varepsilon_s}\right)\Big|_{\mu}$) on experimental data drying shrinkage strains. We came to realize that the contribution of the Shuttleworth effect to the development of the equivalent pore pressure is negligible when compared to the contribution of the other effects.

As for the estimated drying shrinkage strains, for the experimental data on which we validated our model, exact values of the Biot coefficient were not provided. Hence, we considered a range for this parameter, based on literature works. Both the upper and the lower bounds of this range have been tested, for all studied materials. For the materials considered, even when neglecting the Shuttleworth term, our model can give a good estimation of the drying shrinkage strains when the Biot coefficient is equal to 0.7. It should be noted that this approach does not take into account the long-term viscous deformations. However, those deformations could be approximately accounted for by the adjustment of the Biot coefficient.

Finally, the drying shrinkage strains estimated with the proposed model when the Shuttleworth effect is neglected have been compared to those obtained with the Biot-Bishop and the Coussy et al. (2003) models. The three of them gave good results in the higher range of relative humidity. However, in contrast to the last two models, we showed that the proposed model is not only capable of successfully evaluating drying shrinkage strains for low relative humidity but more specifically it is able to predict a noticeable plateau in the evolution of the drying shrinkage strains, which also appears in the considered experimental data sets. In our model, this plateau represents the transition between a contribution to the effective pore pressure stemming mostly from the average pore pressure (at high relative humidity) and stemming mostly from interfaces energy and adsorption of fluid (at low relative humidity).

4.2.4. Model implementation in *Code_Aster*

For further calculations, the Coussy et al. (2003) poromechanical model implemented in *Code_Aster* is modified according to the model proposed in section 4.2.1.

In *Code_Aster,* the calculation of stresses is done in an incremental form as in equation (4-52) where $\boldsymbol{\sigma}$, $\boldsymbol{\sigma}'$ and $\boldsymbol{P_f}$ are respectively the total stresses tensor, the effective stresses tensor and the pore pressure (or hydraulic pressure) tensor:

$$d\boldsymbol{\sigma} = d\boldsymbol{\sigma}' + d\boldsymbol{P_f} \tag{4-52}$$

According to the model of Coussy et al.(2003), $\boldsymbol{dP_f}$ is taken equal to $-\boldsymbol{B}.d\pi$ where in the isotropic case the tensor $\boldsymbol{B} = b.\boldsymbol{I}$ with b the Biot coefficient and $\boldsymbol{I}$ the identity tensor. $d\pi$ is the increment of the equivalent pore pressure and is written as in equation (4-53):

$$d\pi = dP_G - S_w dP_c \tag{4-53}$$

We recall that the new expression of the equivalent pressure π, according to the model introduced in section 4.2.1, is given by equation *(*4-50). This equation is implemented in *Code_Aster*, in an incremental form:

$$\begin{aligned} d\pi = dP_G - S_L dP_C - \frac{1}{3}P_c(S_L)dS_L \\ + \frac{2}{3}(A_0/\phi_0)\left(\left(\omega_G(S_L)\,dt(h_R) + t(h_R)d\omega_G(S_L)\right).(-dP_c) - \left(\left(\frac{\partial\gamma}{\partial\varepsilon_s}\right)\Big|_\mu d\omega_G(S_L)\right)\right) \end{aligned} \tag{4-54}$$

Therefore, we can say that the modification of this model according to the new proposed approach consisted basically on the following points:

- Allowing the user to provide the material new input parameters ($S_L(h_R)$; $\omega_G(h_R)$; $t(h_R)$; A_0 ; $\left(\frac{\partial\gamma}{\partial\varepsilon_s}\right)\Big|_\mu$)
- Modifying the increment of the equivalent pore pressure expression as given by equation (4-54).

The new keywords in *Code_Aster,* used to make use of the new model and model parameters are given in Appendix 8.

4.2.4.1. A proposed modification of the relative permeability expression

Once the new poromechanical model is implemented in the THM model of *Code_Aster*, we propose to modify the relative permeabilities expressions according to those given in Chapter 3 – equations (3-32) and (3-33).

The modification consists in considering that relative permeabilities K_{rl} and K_{rg} are linked to the amount of liquid water S_L instead of the total amount of water S_w. We recall that S_w accounts for all the water, under liquid and adsorbed forms, found inside the pores of the material. The degree S_w of saturation is determined experimentally by weight measurements (see Chapter 2 – equation (2-5)). The degree S_L of saturation corresponds only to the liquid water fraction and is calculated as shown in section 4.2.2.4.

More specifically, the modified version of the equations (3-31) and (3-32) used to express K_{rl} and K_{rg} are:

$$K_{rl} = {S_L}^p\left(1 - \left(1 - {S_L}^{\frac{1}{m}}\right)^m\right)^2 \tag{4-55}$$

$$K_{rg} = (1 - S_L)^p \left(1 - S_L^{\frac{1}{m}}\right)^{2.m} \quad (4\text{-}56)$$

In equation (4-55), $K_{rl} = 0$ when $S_L = 0$ i.e. when all liquid water is released and $K_{rl} = 1$ when $S_L = 1$ i.e. if the concrete is fully saturated.

This modification allows to consider that the transport of liquid water inside the porous is not interfered by the transport of the adsorbed water. A comparison of numerical calibrations of the saturation degree time evolution curves, when K_{rl} and K_{rg} are linked to S_L versus when K_{rl} and K_{rg} are linked to S_w, is shown in Appendix 9. This comparison was done for both tested conditions (T=20°C, h_R=50%) and (T=50°C, h_R=30%). At T=20°C, the calibration obtained by considering that K_{rl} and K_{rg} depend on S_L is almost the same as the one obtained in Chapter 3 by considering that K_{rl} and K_{rg} depend on S_w. At T=50°C, when considering that K_{rl} and K_{rg} depend on S_L, the numerical calibration is not satisfactory, in contrast to the calibration obtained in Chapter 3 by considering that that K_{rl} and K_{rg} depend on S_w. Therefore, it is admitted that parametric study done in Chapter 3 – section 3.3 remains valid: K_{rl} and K_{rg} are linked to S_w and the permeabilities are as determined in section 3.3.2.

4.3. Drying and autogenous shrinkage experiments on F44Adj concrete

The aim of the tests presented in this section is to characterize the drying and autogenous shrinkage of the F44Adj concrete. The tests consist of shrinkage measurements executed mostly in the civil engineering laboratory of EDF R&D, MMC department but also in the Materials and Buildings Durability Laboratory (LMDC) in Toulouse.

Section 4.3.1 will recall the fabrication and conservation conditions of the tested samples in both laboratories. The obtained results are given in section 4.3.2: they include measurements under drying conditions and under autogenous ones.

4.3.1. Samples fabrication, conservation conditioning and experimental procedures

In this section, the samples tested in the MMC laboratory and the LMDC laboratory will be described (section 4.3.1.1 and 4.3.2.2 respectively). The conservation conditioning and experimental procedures are also noted. A summary of the tested samples and conditions is given in Table 4-4.

	T=20°C		***T=50°C***	
	Drying at h_R = 50%	***Autogenous***	***Drying at h_R = 50%***	***Autogenous***
EDF R&D Laboratory - MMC	RS20-EN-2 RS20-EN-3	RE20-EN-1 RE20-EN-1 RE20-EN-3	RS50-EN-1 RS50-EN-2 RS50-EN-3	-
LMDC	-	-	-	REJ-50-28-1 REJ-50-28-2

Table 4-4 – Summary of the tested F44Adj concrete samples for shrinkage

4.3.1.1. Tests performed at the laboratory of EDF R&D, MMC department

The samples used for the mass loss tests (see chapter 3 – section 3.2.1.1) were also used for length measurements. We recall that the measurements are done under two tested external thermo-hydric conditions:

- For (T=20°C, h_R = 50%), two samples of 7x7x28cm were tested (named RS20-EN (2) and (3)).
- For (T=50°C, h_R = 30%) realized in a climatic chamber, three samples of 7x7x28cm were tested (named RS50-EN (1) to (3)).

The samples were removed from the autogenous storage area after being kept there for 28 days. On another hand, two other samples (named RE20 - EN (2) and (3)), kept in autogenous conditions, were used for autogenous shrinkage measurements. Those measurements were only done under a temperature of 20°C.

From a material point of view, it should be noted that the molds used to cast the concrete samples allow the insertion of bolts on the two 7x7cm opposite sides of the samples. These bolts are introduced in order to measure the samples dimensional evolution while using a refractometer (see Fig. 4-22). This measurement is carried out using an Invar rod which is used as a fixed length reference, according to the principle illustrated in Fig. 4-22. The measurement of the length of this reference is always performed just before the measurement of each sample. Once this step is done, the sample is placed between the ball probes of the refractometer to measure its length. The

measurements are repeated so to obtain the evolution in time of the relative length. The measurement procedure is defined in the standard NF P18-427 (1996).

It is important to note that for the samples placed under (T=50°C, h_R = 30%), an important attention was required to preserve the conditioning of the samples. Measurements are taken on one sample at a time, so that the door of the climatic chamber is only open while the sample is being taken out, the other samples remaining under test conditions.

We recall that several sensors were used to measure the thermo-hydric conditions in the climatic chamber and in the room (see section 3.2.1.2 – Fig. 3-15 and Fig. 3-16).

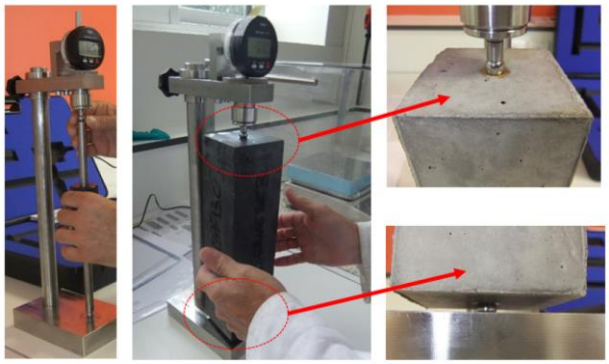

Fig. 4-22 – Measurements done with the refractometer

4.3.1.2. Tests performed at the LMDC laboratory

The tests samples were fabricated in TEGG laboratory of EDF (situated in Aix-en-Provence). The samples were received after 30 days at LMDC. During the transport, the samples were conserved in sealed containers to ensure an autogenous condition. Once received by the LMDC, 3 layers of adhesive aluminum were applied to the samples in order to maintain the autogenous condition of the specimens extracted from the containers, while preparing the tests.

Afterwards, the autogenous shrinkage is measured at a temperature of 50°C, which was applied by using a climatic chamber, in which temperature and relative humidity were measured. Similarly to the tests performed at the MMC laboratory, the samples were tested at an age of 28 days.

The measurement method adopted for these tests is based on the use of strain gauges (Vishay brand) with an automatic monitoring system. It should be noted that for those measurements, two 7x7x28cm samples (with no bolts) are used with two gauges placed on the two opposite molded sides. Gauges were placed after creating small windows in the aluminum protection sheet to host them, then adding an anti-desiccation protection product over them (see Fig. 4-23).

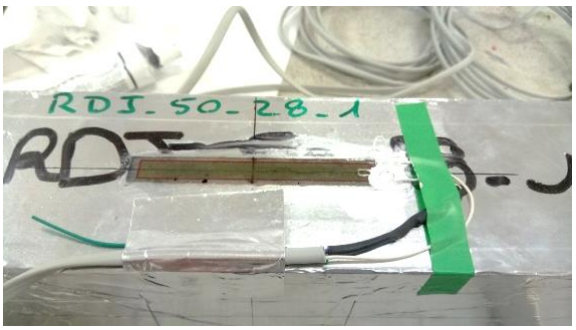

Fig. 4-23 – Deformation gauge placed on a sample used for drying shrinkage measurement

4.3.2. Experimental shrinkage strains

Following a common protocol, the relative lengths measured under drying conditions are considered as the sum of two shrinkage components: the autogenous shrinkage and the so-called drying shrinkage. In the following section, the relative length variations $\Delta\varepsilon_{d+a}(= \Delta L/L_i$ with L the axial length of the sample) are measured under drying conditions, while $\Delta\varepsilon_a$ are obtained under autogenous conditions. Both are presented in this section. While aiming to reach an equilibrated deformation state, the tests done at the MMC laboratory were done for 534 days and then stopped. At the time of submission of the thesis, the tests done in the LMDC are still ongoing: results for the first 328 days are presented.

4.3.2.1. Relative length variation in autogenous sealed conditions

In this section, we present the evolution of the relative length variation under an autogenous condition obtained by the EDF R&D laboratory under a temperature of 20°C (Fig. 4-24 – (a)) and by the LMDC laboratory under a temperature of 50°C Fig. 4-24 - (b)). The time t=0 in Fig. 4-24 corresponds to an age of 28 days of the concrete. Measurements at the EDF laboratory were taken on three samples. The average mass loss for these samples during the test is approximately 0.05% after 300 days. As shown in Fig. 4-24, in both tests no important temperature variation was noted.

It should be noted that the number of measurements at T=20°C remains limited over time. Therefore, for further calculation purposes, we propose to fit the experimental autogenous strains according to equation (4-4) given by Aili et al. (2018). The fitting curve of the experimental measurements at T=20°C, along with a comparison with the strains at T=50°C is given in Fig. 4-25. The fitting parameter α_a (in equation (4-4)) is of 40.46 µm/m and 36.1 µm/m respectively for T=20°C and T=50°C.

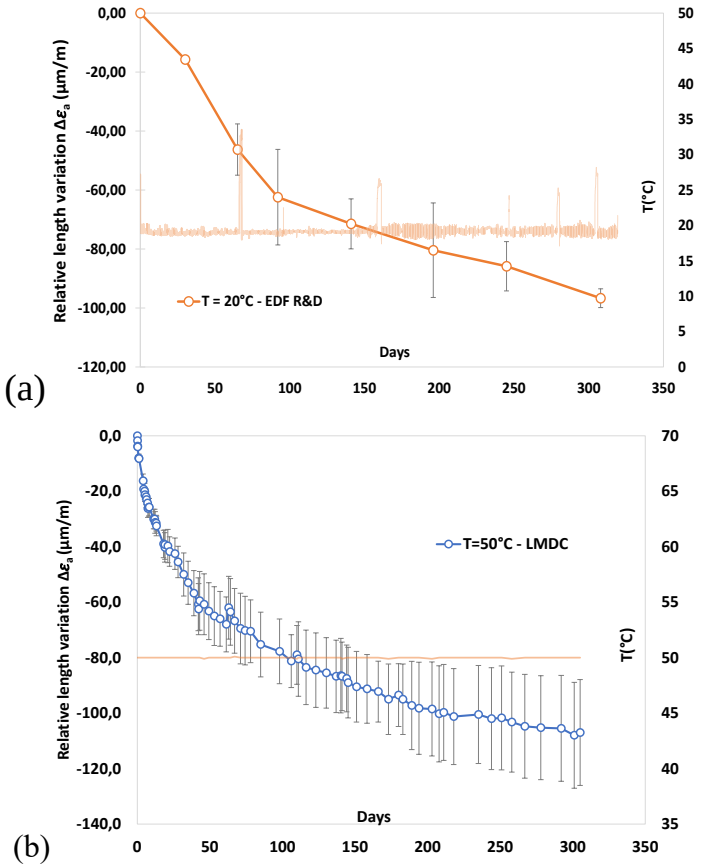

Fig. 4-24 - Relative length variation in autogenous conditions (a) at T=20°C, performed in the EDF laboratory and (b) at T=50°C performed in the LMDC laboratory

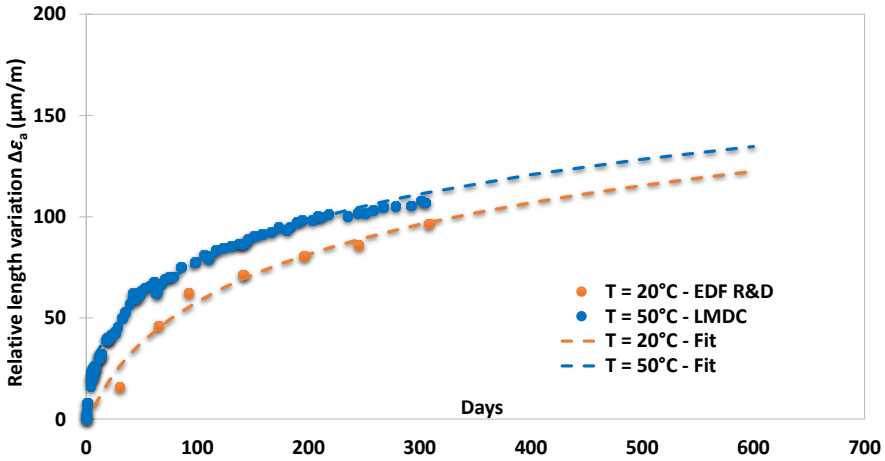

Fig. 4-25 – Fitting of the relative length variation in an autogenous conditions

4.3.2.2. Relative length variations upon drying

Relative length measurements under drying conditions were done in the MMC Laboratory. For each tested thermo-hydric condition, measurements are done on two or three different samples (Fig. 4-26). The evolution of the measured strains over time is shown in Fig. 4-26. The temperature and relative humidity measurements in the test room and climatic chamber are shown in Fig. 3-15 and Fig. 3-16.

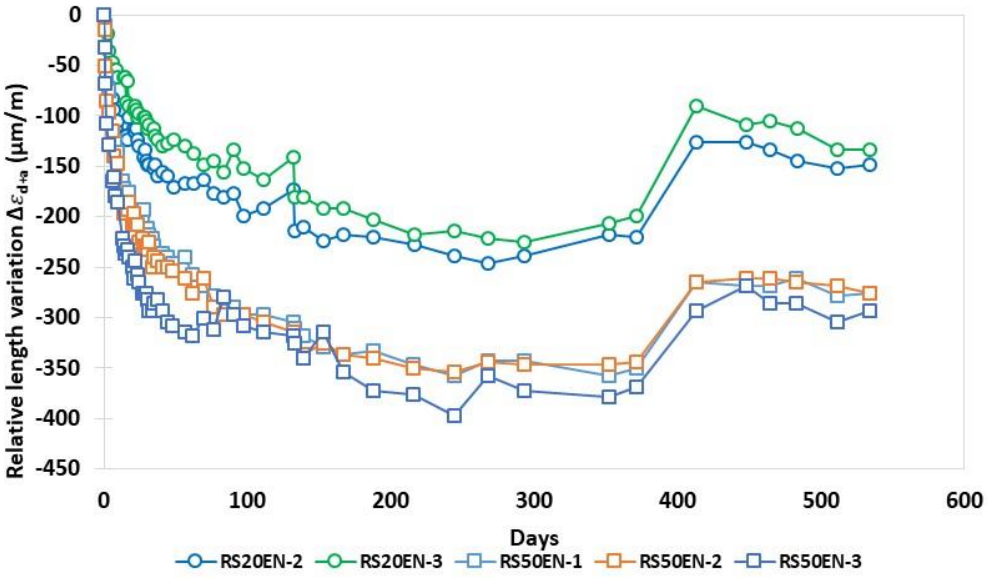

Fig. 4-26 – Relative length variation under drying conditions at (T=20°C, h_R = 50%) and (T=50°C, h_R = 30%), performed in the EDF R&D - MMC laboratory

It should be first brought into mind that tests done in the MMC laboratory were carried out for a total duration of 534 days. However, after 268 days of test, the measurements showed a questionable evolution: an increase of strains between 268 and 400 days. This evolution is linked to a deterioration of the invar rod used as a reference for the refractometer, observed after the end of the test. Therefore, for further calculations, we only consider the time evolution of the strains during the first 268 days of tests. For the purpose of verifying that the measurements during those 268 days are not impacted by the invar rod defect, the test under the condition (T=50°C, h_R = 30%) was repeated on three new different samples while using a new intact invar rod. The test lasted 100 days. The results showed a similar strain evolution as the one already obtained and showed in Fig. 4-26. This confirms that the evolution of the strains over time shown in Fig. 4-26 is correct.

Fig. 4-26 shows that when temperature increases, total shrinkage strains increase. For each of the tested condition of (T=20°C, h_R = 50%) and (T=50°C, h_R =30%), the measurements done on the various samples appear to be relatively close. For further calculations, an average of those measurements is considered

4.3.3. Conclusions

This section presented experimental tests done in the EDF R&D – MMC laboratory and the LMDC laboratories. The tests consisted in measuring relative length variations of samples submitted either to autogenous conditions (under a temperature of 20°C and 50°C) or to drying conditions (T=20°C, h_R = 50%) and (T=50°C, h_R = 30%). Two measurements methods were used, as shown in section 4.3.1. The EDF R&D laboratory used a refractometer while the LMDC laboratory used strain gauges.

The obtained results are shown in section 4.3.2. The relative length variations under a drying condition evolved in a suspicious manner after 300 days. This observation was linked to a deterioration of the invar calibration rod that led to a reduction of its length. However, the results obtained during the first 268 days are assumed to be valid. This was verified by repeating the experimental test for 100 days and obtaining similar strains evolutions.

Relative length variations of the samples were also measured in autogenous conditions at temperatures of 20°C and 50°C. The magnitude of autogenous shrinkage appears to increase with temperature.

4.4. Comparison of numerical results from the model with drying shrinkage measurements for F44Adj concrete

Until now, at EDF, the mechanical behavior of the F44Adj concrete shell was a model based on the poromechanical works of Coussy (2003), implemented in the THM module of *Code_Aster*. Nevertheless, as already pointed out in section 4.1.5 and in section 4.2, the Coussy (2003) approach fails to describe the evolution of drying shrinkage strains for a relative humidity lower than 40% - 50%. Therefore, given that the concrete F44Adj could be submitted during its storage phase to a relative humidity of 30% (see chapter 1), the new poromechanical model derived in section 4.2.1 will be tested for describing its mechanical behavior upon drying.

The determination of the new model parameters (such as the BJH curves $S_L(h_R)$ and $\omega_G(h_R)$) is introduced in section 4.4.1.The comparison between the model drying shrinkage strains and the F44Adj experimental drying shrinkage strains (section 4.3.2) is done in section 4.4.2. This comparison is done on the transient strains, rather than on the strains at equilibrium, because the corresponding experimental tests (in section 4.3.2) did not reach equilibrium.

4.4.1. Inputs to poromechanical model

We showed in section 4.2 that the poromechanical model requires input parameters determined experimentally from the desorption isotherm by means of the BET theory and the BJH technique. The corresponding desorption isotherms of the F44Adj concrete are given in Fig 3-19 – b for the temperature of 20°C and 50°C. The BET method as described in chapter 2 – section 2.1.5.2, was applied to each of the experimental desorption isotherms at T=20°C and T=50°C. The specific surface area S_{BET} obtained at the temperature of 20°C is of 23 m^2/g. For the temperature of 50°C, the corresponding surface area is of 15 m^2/g. Poyet (2016) showed a similar evolution of the assessed surface area with the BET method: for an ordinary concrete at T= 30°C the specific surface area is of 40 m^2/g, while at T=80°C this surface area becomes 13 m^2/g. The author linked this observation to a possible increase in the pore size of concrete when subjected to high temperature, which is due to the dissolution of ettringite and alteration of the C-S-H structure (Drouet et al., 2015). Concerning the thickness t of the adsorbed layer of water, the empirical relation given by Badmann et al. (1981) is used like in section 2.1.5.2: $t(h_R) = K_1 + K_2 \ln(-\ln(h_R))$. At each temperature, we try to fit the values of K_1 and K_2 on the thickness t_{exp} of the adsorbed layer measured experimentally: $t_{exp} = V_{ads}/S_{BET}$ with V_{ads} the volume of adsorbed water assessed from the experimental water desorption isotherms. The fitted curves are shown in Fig. 4-27.

The fitted curves in Fig. 4-27 are compared with the curve given by Badmann et al. (1981) for non-porous cement raw materials and tested at an ambient temperature: $K_1 = 0.385$ nm and $K_2 = -0.189$ nm. Fig. 4-27-left shows that the fitted values at T=20°C, $K_1 = 0.43$ nm and $K_2 = -0.2$ nm are quite close to those given by Badmann et al. (1981). However, at T=50°C (see Fig. 4-27– right), the thickness of the adsorbed water layer appears to be smaller than that obtained by Badmann et al. (1981) and hence the fitted values are $K_1 = 0.38$ nm and $K_2 = -0.26$ nm.

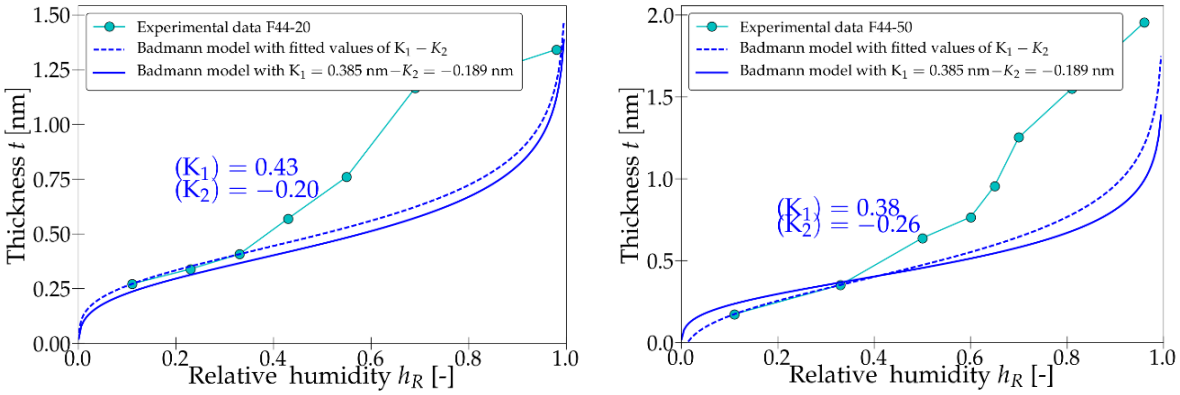

Fig. 4-27 – Thickness of the adsorbed water layer at a temperature of (left) T=20°C and (right) T=50°C

The BJH calculation is performed as described in section 4.2.2.4. For the BJH computation, the fitted curves with the Van Genuchten modified model as given by Fig. 2-1 are used. The BJH calculation at T=20°C gave a specific surface area S_{BJH} = 25 m^2/g, which differs by 8.6% from the specific surface obtained with the BET, S_{BET} = 23 m^2/g. This difference, which is smaller than 10%, allows us to validate the BJH results (Rouquerol, 2003), as explained in section 2.1.5.2.

However, this difference of 8.6% is not negligible and can somehow induce an inconsistency in the BJH results: if $\omega_G(h_R)$ is calculated by using the BET specific surface area, $\omega_G(h_R)$ becomes equal to 1 at a relative humidity bigger than the one at which $S_L(h_R)$ becomes equal to 0. Therefore, for what follows, while calculating $\omega_G(h_R)$, we propose to consider the BJH specific surface area. For more consistency, the values of the parameters K_1 and K_2 are re-calibrated while using the BJH specific surface area, i.e $t_{exp} = V_{ads}/S_{BJH}$. The BJH calculation is also repeated while taking into account the new calibrated values of K_1 and K_2 ; a new specific surface area $S_{BJH,1}$ is calculated and is compared to the specific area S_{BJH} previously assessed. If the difference between S_{BJH} and $S_{BJH,1}$ remains not negligible, the re-calibration of K_1 and K_2 and the BJH calculation are iterationaly repeated until obtaining a near-zero difference. For this case, after two iterations, we arrived at K_1= 0.36nm and K_2=-0.16nm and a specific surface area of 27 m^2/g.

At T = 50°C, the specific surface area obtained with the BJH method is S_{BJH} = 16.5 m^2/g, which differs by 9% relatively to S_{BET} = 15 m^2/g. According to the iteration procedure cited in the previous section, while considering the BJH specific surface area for the calculation of $\omega_G(h_R)$, we re-calibrate accordingly the values of K_1 and K_2. After two iterations, a negligible difference between S_{BJH} and $S_{BJH,1}$ is obtained for $K_1 = 0.3$ nm and $K_2 = -0.19$ nm and a specific surface area of 21 m^2/g.

The obtained evolutions $S_L(h_R)$ and $\omega_G(h_R)$, for both tested temperatures, are shown respectively in Fig. 4-28(a) and (b). Fig. 4-28 (a) shows that the concrete F44Adj loses all its liquid water for a relative humidity of 27% at T=20°C and for a relative humidity of 30% at T=50°C.

The evolution of the equivalent pore pressure versus relative humidity, calculated with equation (4-50), is given for both tested temperatures in Fig. 4-29 and Fig. 4-30.

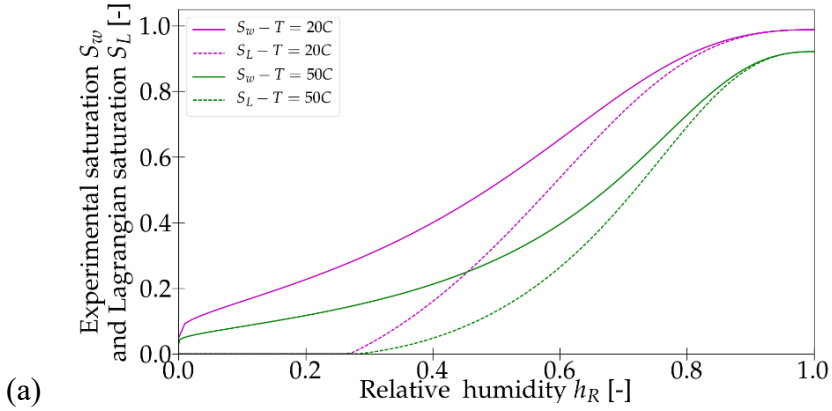

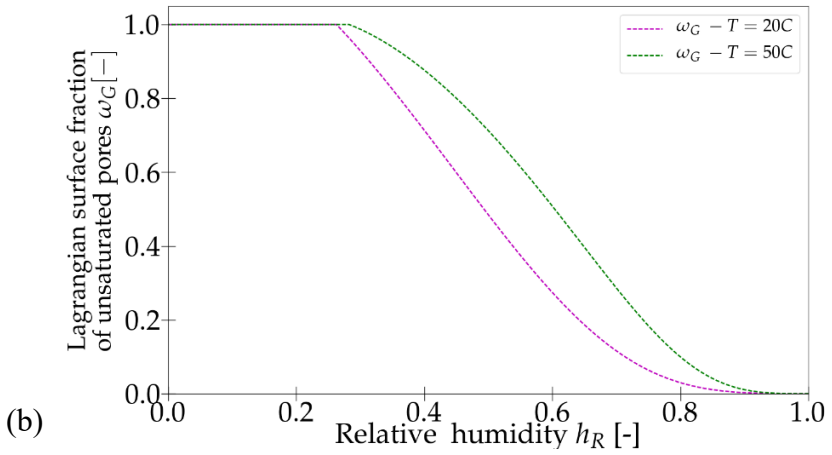

Fig. 4-28 – (a) $S_L(h_R)$ evolution curve and (b) $\omega_G(h_R)$ evolution curve

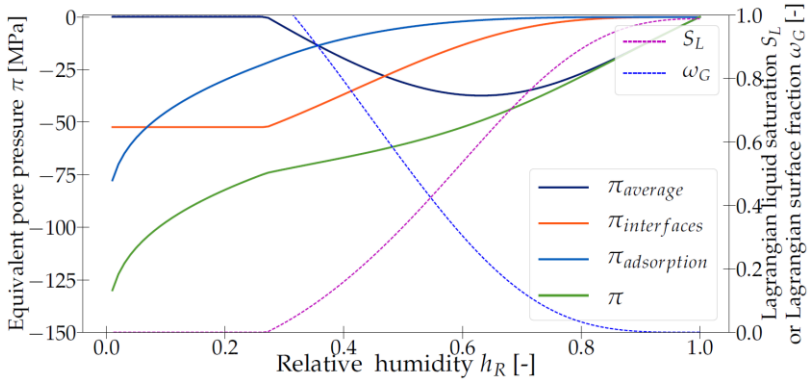

Fig. 4-29 – Contributions to the equivalent pore pressure for T= 20°C

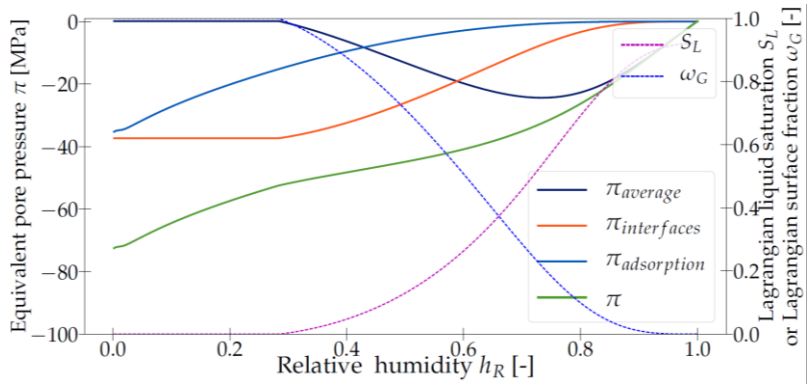

Fig. 4-30– Contributions to the equivalent pore pressure for T= 50°C

Table 4-5 presents parameters used for the determination of the F44Adj shrinkage strains with the new poromechanical model (section 4.2). The elastic Young's modulus of the concrete is determined experimentally by a static compression test executed at internal laboratories of EDF and is equal to 44 GPa. The elastic bulk modulus K_b of the F44Adj concrete was assessed from its corresponding elastic Young's modulus, while considering a Poisson's ratio of 0.2. According to the conclusion made in section 4.2.3, the Shuttleworth parameter was taken equal to zero. Regarding the Biot coefficient, it will be fitted on the experimental evolution of drying shrinkage strains (shown in section 4.3).

Parameter	***Values***
$S_L(h_R)$	Curve in Fig. 4-28 – (a) for T=20°C and T=50°C
$\omega_G(h_R)$	Curve in Fig. 4-28 – (b) for T=20°C and T=50°C
$t(h_R)$	$= 0.36\ln(-\ln(h_R)) - 0.36$ for T=20°C $= 0.3\ln(-\ln(h_R)) - 0.19$ for T=50°C
ρ_{dry}	2432 (kg/m^3) – see Chapter 3 – Table 3-6
A_0	6.56 10^7 (m^2/m^3) for T =20°C 5.11 10^7(m^2/m^3) for T=50°C
$\emptyset_0$	0.075 - see Chapter 3 – Table 3-6
K_b	24.44 GPa
b	0.42 for T=50°C - 1 for T=20°C / See section 4.4.2

Table 4-5–Input parameters to the poromechanical model for the F44Adj concrete

4.4.2. Comparison of numerical results in *Code_Aster* with the experimental results

In what follows, we model the experimental drying tests carried on the F44Adj concrete and described in section 4.3. The numerical simulation is performed on a 3D model representing 1/8th of the 7x7x28cm tested sample as shown in Fig. 4-31. As a matter of fact, all the samples faces are submitted to a same 'Dirichlet' drying condition. Moreover, the 'down', 'right' and 'front' faces represent symmetric planes of the sample. For the purpose of reducing the simulation time, three faces (the exposed faces: 'top', 'left', 'back') of the latter mesh are finely meshed while the remaining three faces are coarsely meshed.

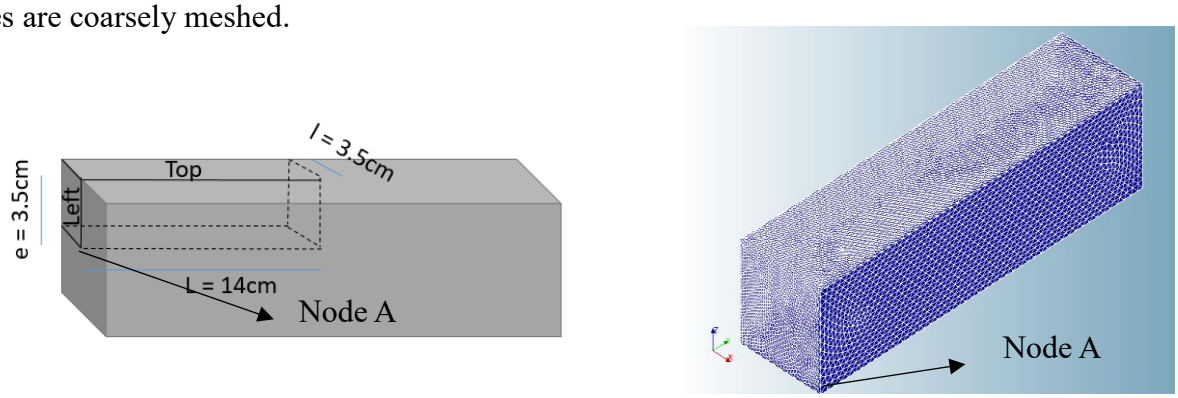

Fig. 4-31 – The 3D sample

The input parameters of the new poromechanical model are given in Table 4-5. For each tested condition (T=20°C, h_R = 50%) and (T=50°C, h_R = 30%), we aim to fit the Biot coefficient of the model in order to correctly replicate the experimental evolution of the drying shrinkage strains shown in section 4.3.2. The transfer parameters of the model are those defined in Chapter 3 – Table 3-10 and a permeability determined by inverse analysis: of 4.10^{-24} m^2 for T= 20°C and 4.5 10^{-22} m^2 for T= 50°C.

We recall that the model introduced in section 4.2.1 was validated on experimental data that correspond to mature cementitious material: a 1-year-old concrete studied by Baroghel-Bouny et al. (1999) and a 6-years-old cement paste studied by Maruyama et al. (2018). At such age, the variation of the autogenous shrinkage strains is considered to be negligible. Therefore, the model developed and implemented in *Code_Aster* is considered to account only for drying shrinkage strains.

The experimental shrinkage strains of the F44Adj concrete, shown in Fig. 4-26, correspond to the sum of drying and autogenous shrinkage strains. Therefore, for further comparisons with the numerical model drying shrinkage results, we subtract from the experimental strains obtained under drying conditions the experimental autogenous shrinkage strains:

- For (T=20°C, h_R = 50%), the fitted autogenous strains shown in Fig. 4-25 are subtracted from the average of the strains measured for RS20EN-2 and RS20EN-3 shown in Fig. 4-26.
- For (T=50°C, h_R = 30%), the measured autogenous strains shown in Fig. 4-24-b are subtracted from the average of the measured strain of all three tested samples, shown in Fig. 4-26.

Once the experimental drying shrinkage displacements are assessed, they are compared with twice the longitudinal displacement (displacement along the axis of the sample) at the Node A shown in Fig. 4-31. This node corresponds to the displacement measuring point of the tested sample, i.e. to where the refractometer was placed (see Fig. 4-31).

The comparison for (T=20°C, h_R = 50%) and (T=50°C, h_R = 30%) is shown in Fig. 4-32. For (T=20°C, h_R = 50%), Fig. 4-32-a shows that a value for the Biot coefficient $b = 1$ is the optimal value to fit the evolution of the displacements over time. However, this fit shows that the model underestimates the displacements during the first 100 days. For (T=50°C, h_R = 30%), Fig. 4-32-a shows that a value of 0.42 for the Biot coefficient allows to describe optimally the drying shrinkage displacements of the F44Adj concrete. It could be seen that the model is able to correctly describe the amplitude and the kinetic of the drying shrinkage strains of this concrete for the tested condition of (T=50°C, h_R = 30%).

We start by discussing the numerical results for the condition (T=50°C, h_R = 30%) and shown in Fig. 4-32-a and Fig. 4-32-b. In Fig. 4-32-a, it could be visualized that the model describes correctly the kinetic and values of the drying shrinkage of the F44Adj concrete. An optimal value of 0.42 for the Biot coefficient is noted. This value of $b = 0.42$ is smaller than the value of 0.7 determined in section 4.2.2 for a high-performance concrete studied at T= 20°C on small-sized samples (Baroghel-Bouny et al., 1999). However, the drying of the quite large size of samples (7x7x28cm) of F44Adj might have induced some surface micro-cracking (refer to section 4.1.2.2). As a consequence, the experimental measured strains or displacements (Fig. 4-32-a) might have been underestimated by this "scale" effect. This strain reduction can somehow explain the small fitted value for the Biot coefficient.

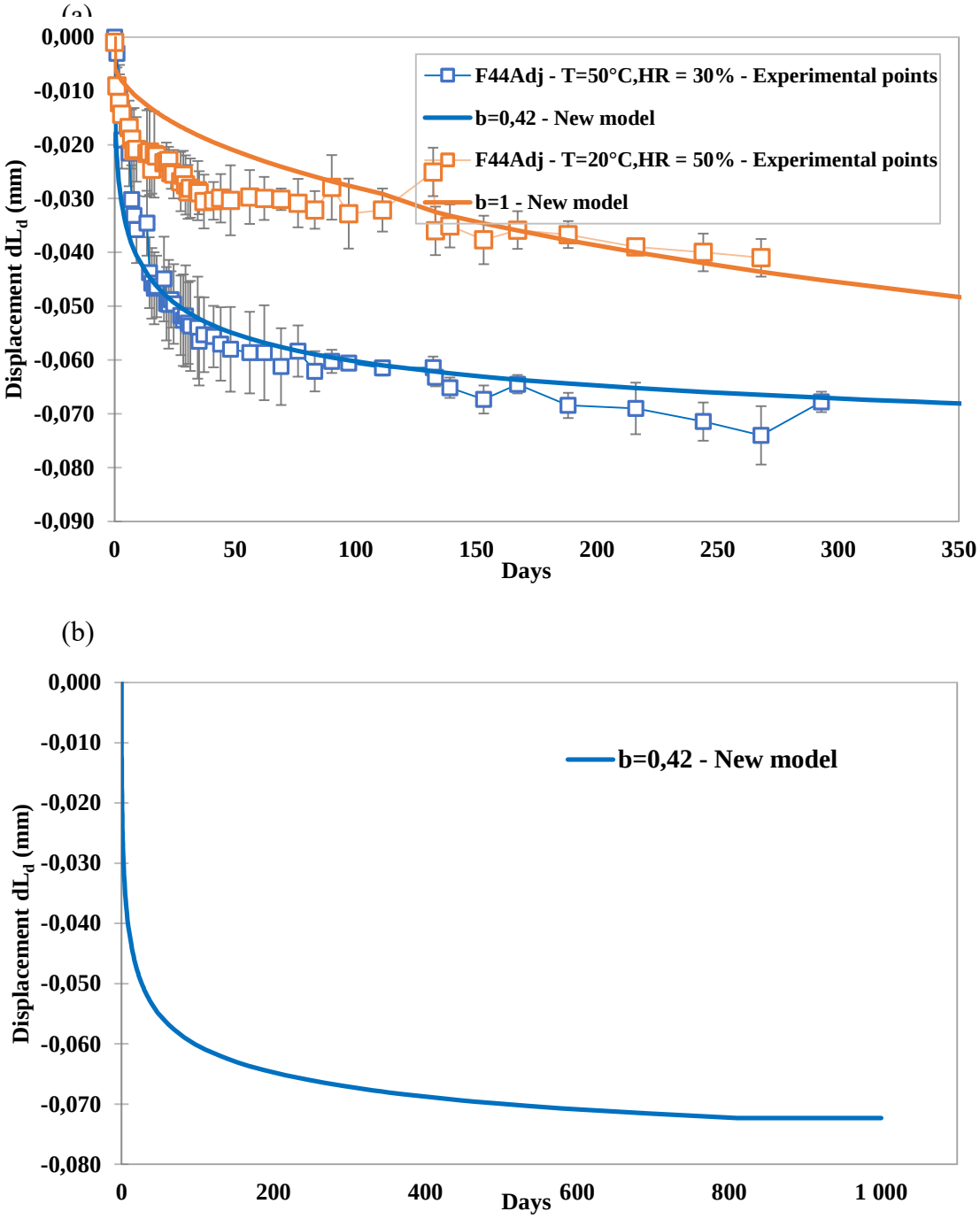

Fig. 4-32 - (a) Model numerical displacements vs experimental displacements for (T=20°C, h_R = 50%) and (T=50°C, h_R = 30%) (b) Model numerical displacements after 1000 days at (T=50°C, h_R = 30%)

The drying shrinkage at T=50°C reaches equilibrium after 1000 days (see Fig. 4-32-b). As a matter of fact after 1000 days, the displacement reached is 0.072 mm (which corresponds to a strain of 257 µm/m). According to Fig. 4-30, for a relative humidity of 30% and a temperature of 50°C, the equivalent pore pressure to be reached at equilibrium is 44.8 MPa. For a Biot coefficient of 0.42 and an elastic bulk modulus K_b = 24.44 GPa (see Table 4-5), this equivalent pore pressure corresponds to a strain at equilibrium equal to 257 µm/m. This observation verifies that, after 1000 days, equilibrium was indeed reached.

For the tested condition (T=20°C, h_R = 50%), the numerical and experimental results in Fig. 4-32-a indicate that the sample after 350 days is still far from being equilibrated hydrically. To discuss the magnitude of the Biot coefficient fitted for this condition (i.e. $b = 1$), it might be helpful to refer to the high-performance concrete tested in section 4.2.2, on which our new poromechanical model was validated. We recall that this concrete, presenting a water-to-cement ratio of 0.26, was tested by Baroghel-Bouny et al. (1999) at an age of 1 year and under an ambient temperature. Compared to that concrete, the F44Adj concrete, which presents a larger water-to-cement ratio of 0.35, is expected to develop larger drying shrinkage strains (refer to Fig. 4-3). Therefore, one can expect a larger fitted Biot coefficient for the F44Adj concrete (we found $b = 1$) than for the concrete studied in section 4.2.2 (for which we found $b = 0.73$). However, a value for the Biot coefficient of $b = 1$ can be found relatively big compared to the values commonly found in the litterature for cementitious materials. For instance, Ghabezloo (2010) indicated values of the Biot coefficient ranging between $b = 0.55$ and $b = 0.8$ for cement pastes with water-to-cement ratios ranging between 0.4 and 0.65.

The high value of the Biot coefficient $b=1$, fitted in this case study, can be linked to additional strains developing in the F44Adj concrete. Those strains correspond to creep strains that appear under the effect of shrinkage tension stresses. The development of creep strains is known to be strongly dependent on the concrete age (Benboudjema, 2004). Therefore, those strains might be of a good importance in the case of a 28-days-old concrete such as the F44Adj concrete. In the same spirit, it is observed in Fig. 4-32-a that the model underestimates slightly the drying shrinkage strains before 100 days for the tested temperature of 20°C. This observation can be linked to a wrongful representation of the creep strains at early age. As a matter of fact, the creep strains are known to develop with a higher kinetic during the early age of loading and to slow down asymptomatically with time (Parrott, 1974).

Lastly, the difference between the values obtained for the Biot coefficient at T=20°C (b = 1) and T=50°C (b = 0.42) should be addressed. Since creep strains are known to increase with temperature (Bažant et al., 2004), the fitted Biot coefficient (which includes creep strains in an effective manner) is expected to increase with the temperature. This trend is not observed in this study case. However, it should be pointed out that the experimental uncertainties encountered in the whole experimental campaign make it difficult to conclude on the observed results. Moreover, the equivalent pore pressures calculated with the model are strongly impacted by the concrete water retention curve (as shown in section 4.2.2). Therefore, given that for the F44Adj concrete the water retention curve was partially determined from literature experimental data (see chapter 2 – section 2.3.3), the fitted Biot coefficients and numerical curves in this study remain an approximation. The correct values should be re-determined once we have the complete water retention curves of the F44Adj concrete.

4.4.3. Conclusions

This section consisted in modelling the mechanical drying shrinkage of the F44Adj concrete. Such modelling has been done using a new poromechanical model (developed in section 4.2) that is able to satisfactorily describe drying shrinkage strains in a porous material, on the whole range of relative humidity. The model was implemented in *Code_Aster* (see section 4.2.4) and used for comparison with experimental data on the F44Adj concrete in this section.

The model input parameters are in majority obtained from experimental data on the F44Adj concrete, namely the water retention curve analyzed with the BJH method (section 4.4.1). The displacements obtained numerically with the model were compared to shrinkage displacements data measured on the corresponding concrete (shown in section 4.3).

In a general way, section 4.4.2 shows that the model is able to describe the evolution of the drying shrinkage strains reasonably well, while considering only one fitting parameter: the Biot

coefficient. In the case of the condition (T=20°C, h_R = 50%), a Biot coefficient of 1 might be needed. The model shows an underestimation of shrinkage strains at T=20°C during the first 100 days. This under-estimation might be due to an occurrence of experimental creep strains when the concrete is young. However, such a statement needs to be taken with caution because of the number of experimental uncertainties encountered during the whole experimental campaign on the F44Adj concrete. Indeed, uncertainties were observed while determining different input parameters of the model: the lack of experimental points for the water retention curve, the possible occurrence of micro-cracking in samples used for modelling the drying kinetic of the concrete and hence determining its permeability. Therefore, any further conclusion regarding the applicabilty of the model must be done once all needed experimental input parameters are available.

As for the temperature of (T=50°C, h_R =30%), the model with a Biot coefficient of 0.42 appears to describe satisfactorily the drying shrinkage of concrete during the whole duration of the test. Consequently, this model will be used in Chapter 5, to describe the drying of the $C1PG^{SP}$ concrete package submitted to an external condition of (T=50°C, h_R =30%).

Chapter 5

Industrial application to a concrete nuclear waste package

List of Figures

List of Tables

The work described in the previous chapters consisted in studying the drying behavior of a high-performance concrete: the F44Adj concrete. This concrete, as described in chapter 1, constitutes the shell of the C1PG^{SP} nuclear waste packages. When stored at the ICEDA facility, the packages may be submitted to a low relative humidity (conservative value of 30% estimated by EDF) and a relatively high ambient temperature (conservative value of 50°C). It is therefore important to study the impact of the drying under those conditions on the mechanical integrity of the concrete shell. This is the main objective of this chapter.

We will begin by presenting the C1PG^{SP} package, its concept and its material composition (section 5.1). The calculation methodology as well as the adopted mesh of the package and the considered mechanical loadings used in the numerical simulations are presented in section 5.2. Finally, numerical results in terms of saturation, strains and stresses are presented in section 5.3. Previous studies of the drying behavior of the package have been performed while using a model based on the works of Coussy et al. (2013). The corresponding results are compared with those obtained with the new model in section 5.3.

5.1. C1PG^{SP} package and its material properties

As mentioned in Chapter 1, the C1PG^{SP} package is composed of a shell (or container) made of non-prestressed F44Adj high-performance reinforced concrete with steel reinforcements, a steel basket and a F44Adj concrete cap. The retained wastes are deposited in the steel basket and embedded in a "2421Fbis" cementitious grout (EDF notation). This basket is then placed in the F44Adj concrete shell. The volume between the basket and the shell is again filled with 2421Fbis grout. A flat and thin ferrule, belonging to the shell, separates the latter from the grout. Finally, the basket is closed by a cap made by the concrete F44Adj. A transversal section on the cylindrical package is shown in Fig. 5-1.

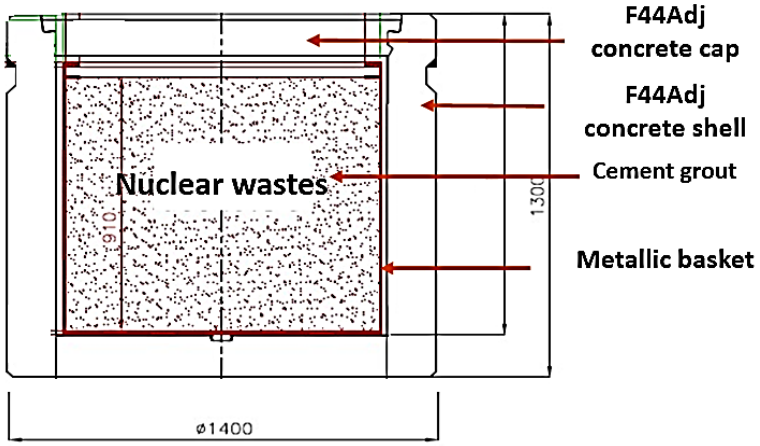

Fig. 5-1– Transversal section of the C1PG^{SP} package. Indicated dimensions are in mm.

The thermo-hydro-mechanical properties of the concrete are assessed in the previous chapters (Chap 2 to Chap 4) for a temperature of 50°C. These parameters are recalled in Table 5-1. They include: the water retention curves of the F44Adj concrete calibrated with a Van Genuchten modified model in section 2.3.3 and the permeability determined with inverse analysis in Chapter 3 – Section 3.3.2.

Parameters	*Values*	Reference
Young's modulus *E* (GPa)	44	Experimental value measured at internal laboratories of EDF
Poisson's ratio ν	0.2	Standard values for concrete
Initial porosity $\emptyset_0$	7.5%	See Chap 3 – Table 6
Biot coefficient	0.6	See Section 5.2.1
Initial mass density ρ_{ini} (kg/m3)	2503	See Chap 3 – Table 6
Initial saturation degree S_{ini}	0.92	See Chap 3 – Table 6
Initial capillary pressure $P_{c,ini}$ (MPa)	7.6	Calculated with the Van Genuchten relation $S(P_C)$ (Equation A-1)
Van Genuchten parameters (S_{100}, S_r, n, P_r)	(0.93,0.03,2.353,43.23)	See Chap 2 – Fig 2.39
Intrinsic permeability *K*(m^2)	$4.5\ 10^{-22}$	See Chap 3 - Section 3.3.2
New model required parameters (S_L, ω_G, A_0, t)	See Chap 4 – Table 4-5 for values at T=50°C	

Table 5-1- Hydro-mechanical properties of the F44concrete shell

Regarding the 2421Fbis cementitious grout and the steel basket, their properties are given in Table 5-2. These properties were determined from experimental studies performed outside the framework of the thesis.

Parameters	*Values – 2421Fbis grout*	*Values – Steel basket*
Young's modulus *E* (GPa)	15	210
Poisson's ratio ν	0.2	0.3
Biot coefficient b	0.8	-
Initial porosity $\emptyset_0$	49.5%	-
Initial mass density ρ_{ini} (kg/m^3)	1737	8500
Initial saturation degree S_{ini}	0.94	-
Initial capillary pressure $P_{c,ini}$ (MPa)	9.14	-
Intrinsic permeability *K* (m^2)	$4.\ 10^{-15}$	-
Van Genuchten parameters (S_{100}, S_r, n, P_r)	(1.0 , 0.0 , 2.0 , 25.0)	-

Table 5-2- Properties of cementitious grout and steel basket

5.2. Description of the simulation of drying of the concrete shell

5.2.1. Calculation methodology

We recall that the poromechanical drying behavior laws found in the THM model implemented in *Code_Aster*, were initially based on the works of Coussy et al. (2003). Nevertheless, it has been

shown in Chapter 4 that this poromechanical model is insufficient for describing the drying shrinkage of porous materials for low relative humidities. As a consequence, a new poromechanical model able to describe more correctly the drying shrinkage of this concrete on a whole range of relative humidity is developed and presented in Chapter 4. Once validated on experimental data from literature for various porous materials, this model has been implemented in the THM module of *Code_Aster* (Chap. 4 – Section 4.2.4).

It is important to recall that, during the lifetime of the concrete, autogenous shrinkage strains are expected to play a non-negligible role (see Chapter 4 – section 4.3.2.2), especially at a young age (28 days). Therefore, accounting for such shrinkage in this work is of notable importance. However, the chemical interactions occurring during autogenous shrinkage are not currently taken into account in the THM model. Therefore, it is proposed to account for both autogenous and drying shrinkage in our modelling, by proposing an adapted fit of the Biot coefficient. This fit is done on experimental shrinkage (autogenous and drying) displacements of the F44Adj. The fit is shown in Appendix 10. A value of 0.6 is obtained for the apparent Biot coefficient and will be used for this study.

5.2.2. Meshing and boundary conditions of the package

Numerical simulations carried out previously at EDF on the concrete shell were done while taking into account the effect of the reinforcement, which is initially designed to remain intact when submitted to a vertical force during handling. These calculations showed that taking into account the reinforcement on the model had a negligible impact on the results.

In the present study, we use an axisymmetric geometry to model the cylindrical package. Fig. 5-2 shows the mesh used with the cement grout in red, the concrete shell in green and the plug in yellow. The metal parts consisting of the basket and the ferrule are also shown. These parts are modelled as non-porous elastic materials.

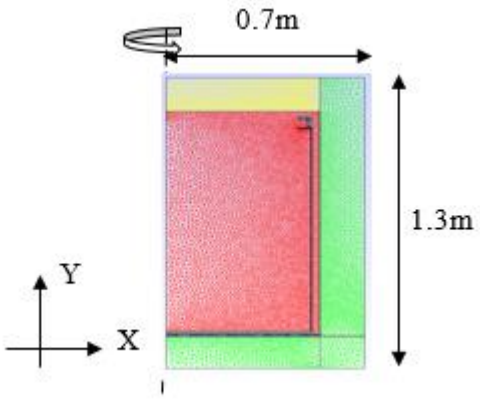

Fig. 5-2 – Axisymmetric mesh of the modeled package
- cement grout in red, concrete shell in green and concrete cap in yellow

Total stresses and displacements are initially considered to be zero across the entire domain. The initial temperature in the shell is considered to be 25°C. In this simulation, we account for the heat production of the nuclear wastes. Therefore, the temperature inside the cementitious grout is fixed to 61°C due to the presence of the nuclear wastes. This temperature is maintained during the whole simulation time.

Moreover, we block the displacement in the X direction of all nodes on the Y symmetry axis due to axial symmetry. The package rests upon ground which in previous studies was modeled as a set of springs corresponding to a soft soil. These studies showed that when we consider this kinematic boundary condition, we obtain similar results to that when we consider blocking the displacement in

the Y direction at the lower right corner. The latter boundary condition was selected for this study (see Fig. 5-3). Finally, all the other boundaries of the package are considered to be unconstrained.

A relative humidity h_R of 30% and temperature of 50°C are imposed as a Dirichlet condition at the top and right edges of the package. We recall (refer to chapter 1) that these conditions are considered to be representative in a conservative way of the storage condition at ICEDA because in this study case they are considered to be applied permanently over time whereas in reality these conditions would only be met temporarily over the few hottest periods. Moreover, compared to the real conditions at the Cigéo disposal, these conditions (T=50°C, $h_R = 30$) are also considered more penalizing since the ambient conditions in the Cigéo disposal cells should be generally maintained (according to Andra) at a temperature of 50°C and a relative humidity around 40%-60% except in the case of the most exothermic cells where the relative humidity can reach 30% to 40%.

This thermo-hydric condition is translated into a capillary pressure by means of the Kelvin's law (Chap 2 – Equation 2.9). Additionally, a gas pressure of 1 atm is imposed at these boundaries (see Fig. 5-3).

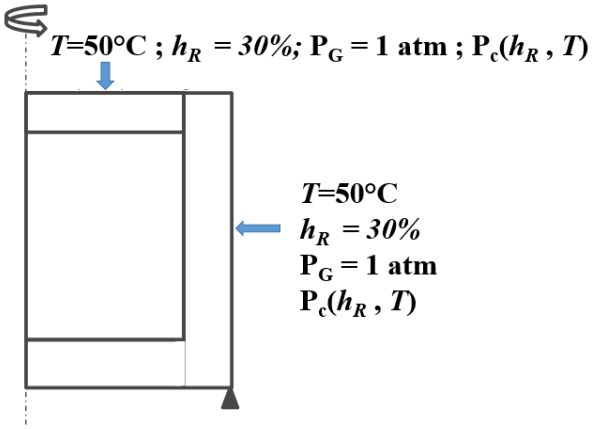

Fig. 5-3 – Thermo-hydric boundary conditions

5.3. Numerical results and discussion

The simulation of the C1PG^{SP} drying is executed for a duration of 150 years. It corresponds approximatively to the total exploitation duration of storage and reversible disposal of the packages (see chapter 1). The corresponding results in terms of saturation, strains and stresses are presented in the following sections.

5.3.1. Degree of saturation in the concrete shell and cap

In this section, we present the evolution of the saturation degree inside the concrete shell and cap (Fig. 5-4), as predicted by the thermo-hydric transfer model considered in this thesis and described in Chap 3. The saturation degree is the same for the Coussy et al. (2003) model and for the new model, since the water transfer is not affected by the extension of the model to adsorption effects.

Initially, the saturation degree of the concrete is 0.92. The drying front is observed to move from the exterior surfaces of the shell and cap to the interior of the package. In a general way, the concrete cap is drying at a slower rate than the concrete shell. This is due to a water inflow from the direct contact between the concrete cap and the cementitious grout inside the metallic basket ((Fig. 5-1). Finally, after 150 years, we observe that the concrete cap is globally still saturated with a saturation degree between 0.8 and 0.92. On contrary, the saturation degree in the concrete shell is mainly small and close to the saturation degree expected to be reached at 30% of relative humidity (refer to Fig. 3-19-b – $S(30\%) = 0.17$).

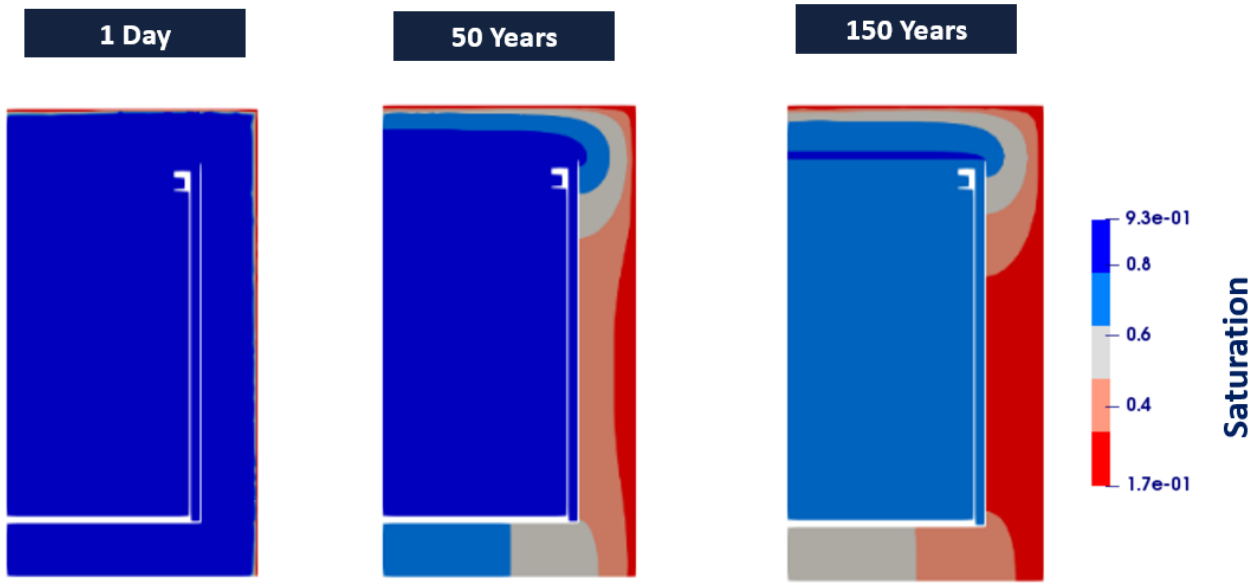

Fig. 5-4 - Evolution of the saturation degree in the concrete shell and cap.

5.3.2. Hydraulic and effective stresses in the concrete shell and cap

The difference of the calculated hydraulic stresses at 50 and 150 days between the simulation done with the Coussy et al. (2003) and the new model is shown in Fig. 5-5 and Fig. 5-6. The hydraulic stress is written as $\sigma_f = -b.\pi$ with π the equivalent pore pressure calculated as in Chapter 4 – section 4.2.3.

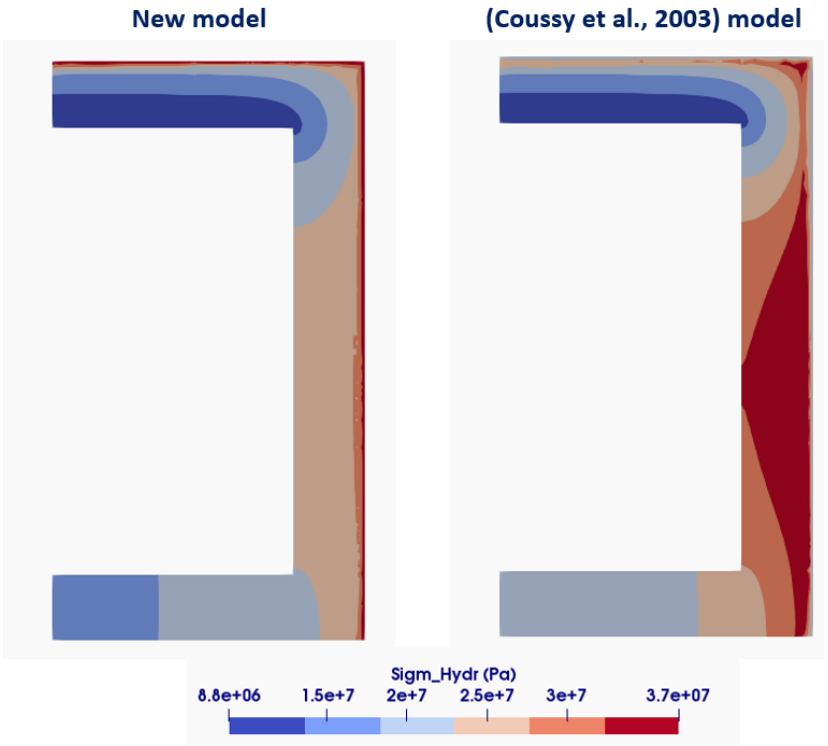

Fig. 5-5 - Hydraulic stress in the concrete shell and cap after 50 years: (left) new model (right) Coussy et al. (2003) model.

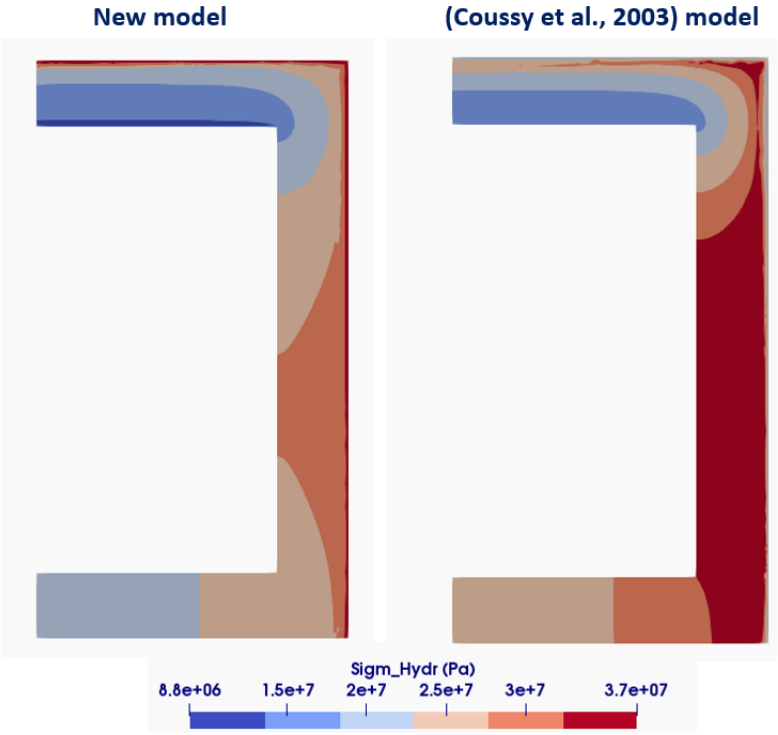

Fig. 5-6 - Hydraulic stress in the concrete shell and cap after 150 years: (left) new model (right) Coussy et al. (2003) model.

At first, by referring to Chapter 4 – Fig. 4-30, we recall that the equivalent pore pressure reached at mechanical equilibrium when the concrete is submitted to T=50°C and h_R = 30% is π = - 44.8 MPa. This value of π corresponds to a hydraulic stress $\sigma_f = -b.\pi = 27$MPa with a Biot coefficient b = 0.6. The results in Fig. 5-6 – (left) show that, after 150 days, the hydraulic stresses in the majority of the concrete shell thickness have reached a value near 27 MPa. This indicates that an equilibrated mechanical state has been reached in the concrete shell. Meanwhile, the hydraulic stress inside the concrete cap after 150 days is still ranging between 13 and 20 MPa. The concrete cap has only reached an equilibrated state near its exchanging surface. This observation is in accordance with the values of the degree of saturation (see Fig. 5-4), which show that the concrete cap has not reached its final equilibrated dried state after 150 days.

Furthermore, while comparing the values obtained with the new model with those obtained with the Coussy et al. (2003) model, we can observe (Fig. 5-6 – (right)) that the latter gives higher values of hydraulic pressure (37 MPa after 150 days) than the new model. This observation is consistent with what was explained in Chapter 4 – section 4.2, namely that the equivalent pore pressure in Coussy et al. (2003) is overestimated for low relative humidities (in this study case h_R = 30%).

In Fig. 5-7 and Fig. 5-8, the effective stresses in the concrete cap and shell after 50 and 150 years are shown and compared, depending on whether they are obtained with the new model or with the Coussy et al. (2003) model. We observe that the solid matrix is contracting, as the effective stresses shown in Fig. 5-7 and Fig. 5-8 are compressive stresses (i.e. with negative values). Moreover, by comparing the two models, we can see that the effective stresses in the concrete, when calculated with the Coussy et al. (2003) model, are bigger than those obtained with the new model.

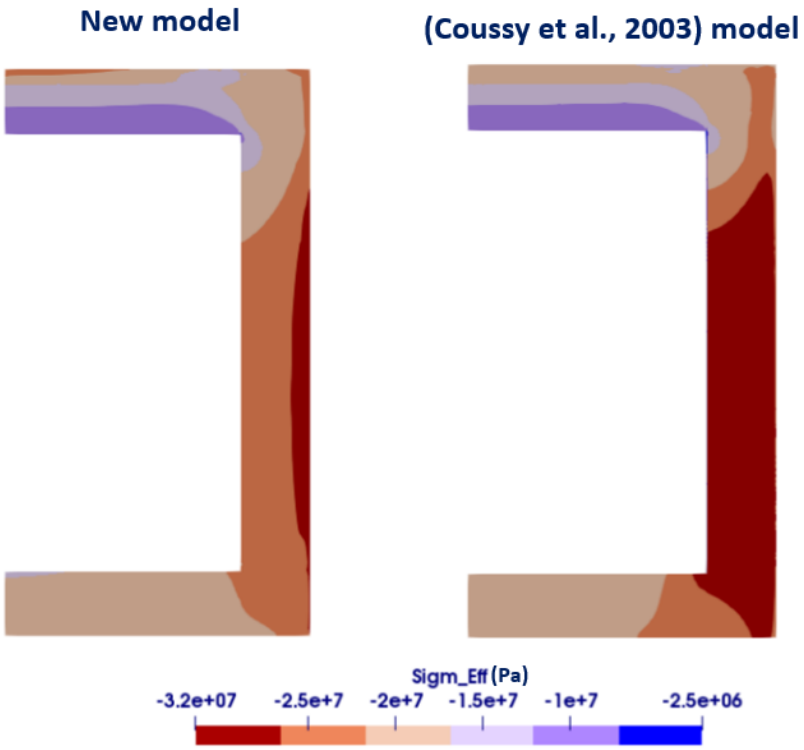

Fig. 5-7 - Effective stresses in the concrete shell and cap after 50 years: (left) new model (right) Coussy et al., (2003) model.

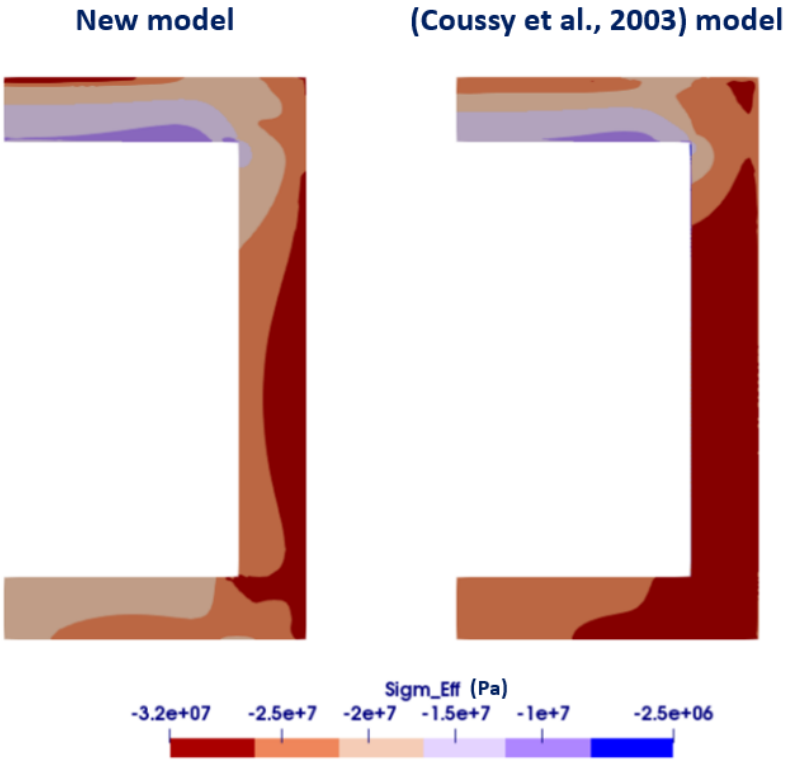

Fig. 5-8 - Effective stresses in the concrete shell and cap after 150 years: (left) new model (right) Coussy et al., (2003) model.

5.3.3. Strains in the concrete shell and cap

The strains components ε_{xx} and ε_{yy} of the concrete shell and cap after 150 years are given in Fig. 5-9 and Fig. 5-10. In each figure, a comparison between the strains obtained with the new model with those obtained with the Coussy et al. (2003) model is presented. The areas where positive strains prevail are colored in blue while areas with negative strains are colored in magenta.

It is observed in Fig. 5-9 and Fig. 5-10 that, when the concrete shell is submitted to drying, the external surface tends to contract. Aiming to shrink in the horizontal direction, the concrete shell is restrained by the presence of a metallic basket mush stiffer than the concrete (see Fig. 5-1). This will cause a maximum positive (traction) horizontal strain to appear at the right internal corner concrete shells as indicated with the arrow in Fig. 5-9. This strain is 140 $\mu m/m$ according to the new model (Fig. 5-9 – (left)) and 200 $\mu m/m$ according to the Coussy et al. (2003) model (Fig. 5-9– (right)). The traction observed at this internal corner is also linked to the appearance of a compression stress zone as seen in Fig. 5-14.

As for the concrete cap, we can observe also negative strains at its external surface (Fig. 5-10). While aiming to shrink vertically, the concrete cap is equally restrained by the rigid basket and hence a positive (traction) vertical strain appears on its internal surface. The maximum vertical strain is observed in the concrete cap and is 230 $\mu m/m$ according to the new model (Fig. 5-10 – (left)) and 250 $\mu m/m$ according to Coussy et al. (2003) model (Fig. 5-10 – (right)). It is also important to note that the vertical behavior of the concrete package in terms of strains is not symmetrical with respect to the horizontal (Fig. 5-10), given that the concrete package is not submitted to drying at its bottom.

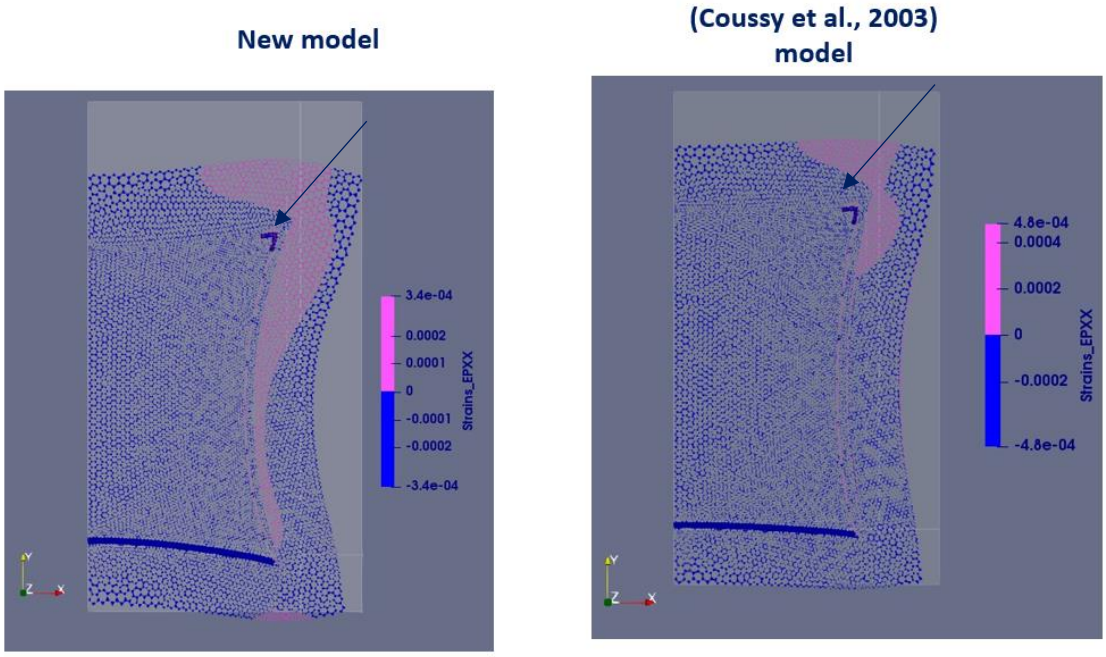

Fig. 5-9 – Strains component ε_{xx} after 150 years modelled with (left) the new model and with (right) the Coussy et al. (2003) model, plotted on the deformed shape (the gray shape is the undeformed one). On the deformed shape, displacements are magnified with a factor of 500.

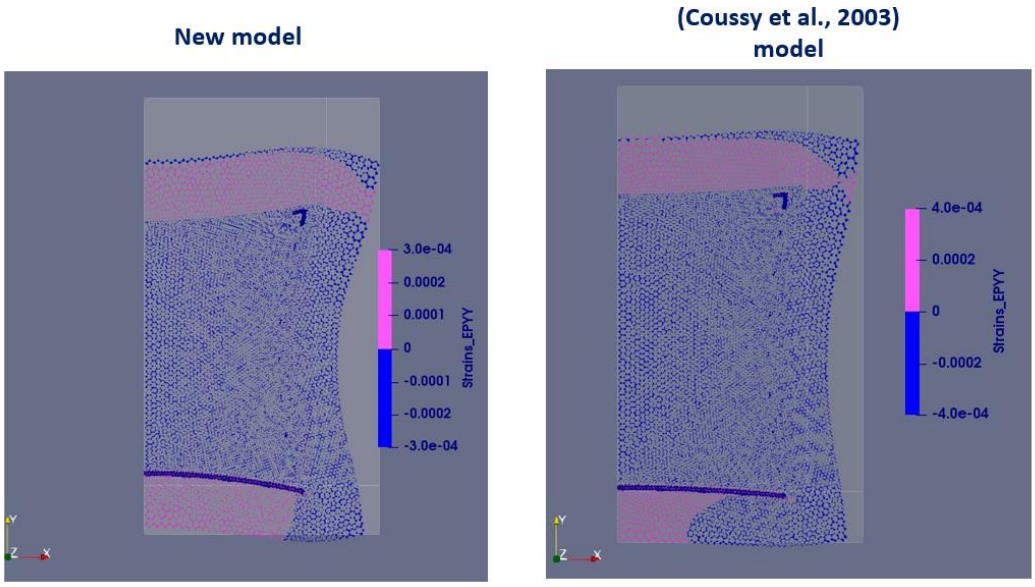

Fig. 5-10 – Vertical strains after 150 years modelled with (left) the new model (right) Coussy et al. (2003) model plotted on the deformed shape (the gray shape is the undeformed one). On the deformed shape, displacements are magnified with a factor of 500.

From what has been presented previously in this section, we can note that the Coussy et al. (2003) model is predicting larger drying (negative) strains in the concrete shell and cap than those predicted with the new model. This is majorly linked to the over-estimation of hydraulic pore pressures done with this former model (as shown in section 5.3.1).

5.3.4. Stresses in concrete shell and cap

In this section, results are given in terms of stresses (Fig. 5-11 to Fig. 5-14). Since the main risk to be studied is with respect to cracking of the concrete shell, we will consider that cracking is governed by a Rankine criterion (Collins, 1993): this means that we will consider that a crack occurs when the largest positive principal stress σ_3 exceeds the tensile strength f_t of the F44Adj concrete at any point of the shell. Also, for this criterion, we choose to refer to total stresses rather than to effective stresses, since total stresses can be directly compared to experimental measurements of tensile strength.

Due to the confidentiality of the results shown in this industrial application, the stresses are presented after being made dimensionless, i.e. we present $\sigma_3 / \sigma_{3,max}$. The scaling stress $\sigma_{3,max}$ represents the maximum value of σ_3 attained in the concrete shell over time and for the two case studies (with the Coussy et al. (2003) model and with the new model): this maximum value is obtained with the Coussy et al. (2003) model. As for the tensile strength of the concrete, it is also given in a dimensionless manner as $f_t/\sigma_{3,max}$. In this study $f_t/\sigma_{3,max}$ is approximately equal to 0.6.

For all the results shown Fig. 5-11, the dimensionless stress $\sigma_3 / \sigma_{3,max}$ ranges between a negative value and 1. The areas showing positive values will hence correspond to an area submitted to tensile stresses while the areas showing negative values are submitted to compressive stresses. The results in Fig. 5-11 to Fig. 5-14 show that in both modelling cases, maximum tensile stresses are observed at the surface of the concrete cap and shell. This can be explained by the fact that the surface of the package is usually drying at a rate faster than that of the inside of the shell and cap. Therefore, tensile stresses tend to be more significant at the surface of the package than in its inside. Furthermore, by comparing both modelling cases, it is observed that generally, when the Coussy et al. (2003) model is used for modelling the behavior of the concrete shell and cap, the areas where the concrete is in tension (areas where $\sigma_3 / \sigma_{3,max} > 0$) are wider than when the new model is used.

As for the risk of cracking, in Fig. 5-11 to Fig. 5-14 in the areas where $\sigma_3/\ \sigma_{3,max}$ are bigger than 0.6 (i.e. $f_t/\sigma_{3,max}$), a crack is expected to occur. It is seen that that, in this study, the tensile zone where cracking is expected to occur does not go through the shell and limited to a thin area close the external surface of the package. Hence, the packages are considered to conserve their mechanical integrity and retention properties during the storage and disposal phase. It could be observed that, when using the Coussy et al. (2003) model, this risk of cracking is larger than when evaluated with the new model: larger zones where $\sigma_3/\ \sigma_{3,max} > 0.6$ are observed. Those larger values of tensile stresses are due mainly to the the larger values of the hydraulic stresses (see section 5.3.2) and of the strains (see section 5.3.3) obtained with the Coussy et al. (2003) model, when compared to those obtained with the new model.

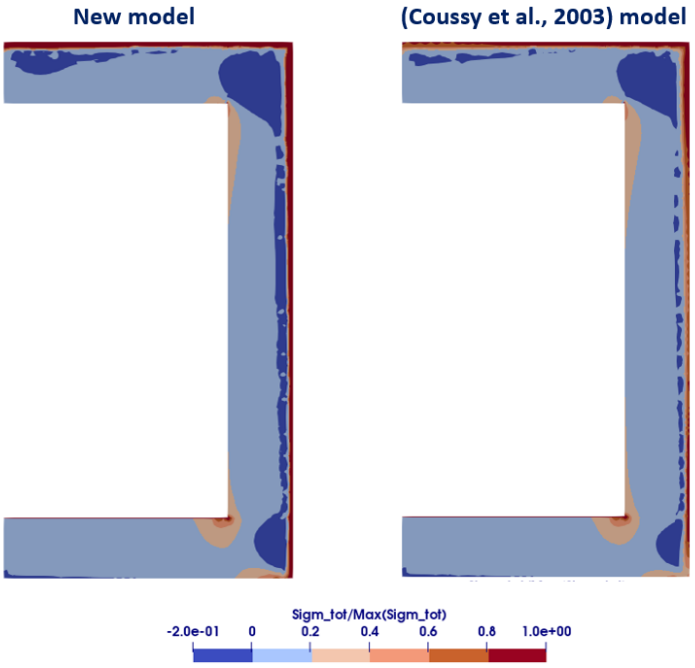

Fig. 5-11 – Dimensionless maximal principal total stress $\sigma_3/\ \sigma_{3,max}$ in the concrete shell and cap after 1 day

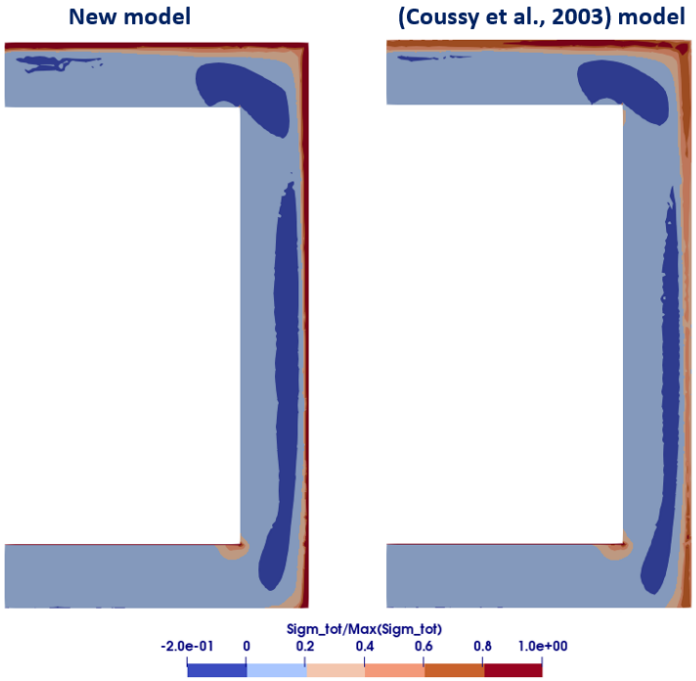

Fig. 5-12 – Dimensionless maximal principal total stress $\sigma_3/\ \sigma_{3,max}$ in the concrete shell and cap after 1 year

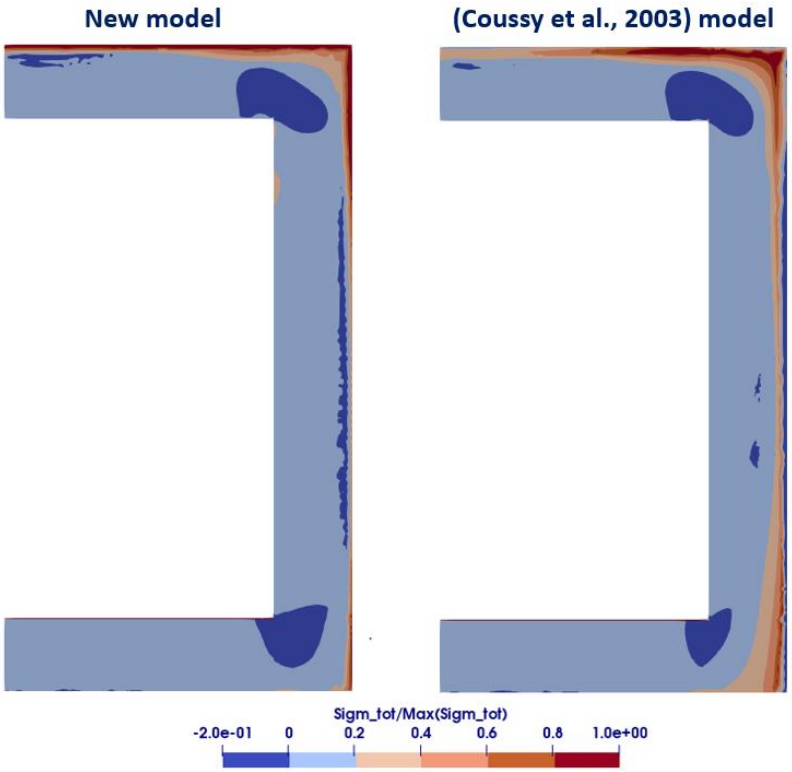

Fig. 5-13 – Dimensionless maximal principal total stress $\sigma_3/\ \sigma_{3,max}$ in the concrete shell and cap after 50 years

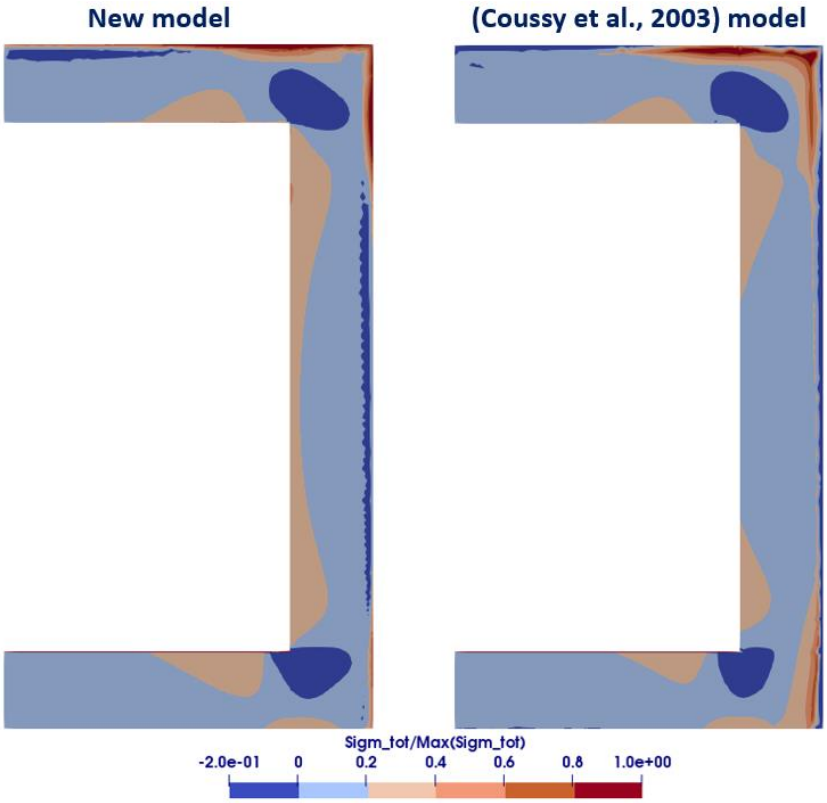

Fig. 5-14 – Dimensionless maximal principal total stress $\sigma_3/\ \sigma_{3,max}$ in the concrete shell and cap after 150 years

5.4. Conclusions

This chapter presents the thermo-hydro-mechanical modelling of a C1PG^{SP} nuclear waste subjected to environmental conditions with a relative humidity of 30% and a temperature of 50°C. The poromechanical behavior is described with the newly derived model introduced in chapter 4 and is compared to that described with a model based on the works of Coussy et al. (2003).

A description of the drying simulation is given in section 5.2 regarding the calculation methodology, the chosen mesh and boundary conditions. Section 5.3 presents and compares the numerical results (i.e. the stresses, strains and saturation degree in the concrete shell and cap) obtained with the new model to those obtained with the Coussy et al. (2003) model.

We recall that, by using the new poromechanical model, an accurate description of the drying behavior of concrete at low relative humidities is obtained. Compared to the Coussy et al. (2003) model, smaller hydraulic stresses are calculated with the new model. The hydraulic stress calculation is directly linked to the calculation of the strains. Those strains are smaller when calculated with the new model than when calculated with the Coussy et al. (2003) model. Finally, compared to the new model, the Coussy et al. (2003) model induces bigger stresses and larger tensile zones in the concrete.

Finally, the results provided in section 5.3.4 show that, by using any of the two models (i.e. the new model and the Coussy et al. (2003) model), we expect no risk of a crack propagating through the whole thickness of the F44Adj concrete shell or cap and that only a thin external layer could be subjected to cracking. This conclusion is reached for a period of 50 years of storage at ICEDA and 100 years of disposal at CIGEO.

Chapter 6

Conclusions and perspectives

The main objective of this work was to model the drying behavior of a concrete package (noted $C1PG^{SP}$) used by EDF for storage and disposal of nuclear waste. We recall that those packages will be placed in a storage facility (ICEDA) during a maximum period of 50 years and then disposed of at the deep geological disposal Cigéo. During their storage and the disposal reversibility phase, packages have to resist to a maximum temperature due to the exothermicity of the radioactive waste and a minimum relative humidity due to temperature and atmospheric conditions. To be conservative, a maximum temperature of 50°C and a minimum relative humidity of 30% are considered.

The outer shell of the package is made of a high-performance reinforced concrete: the "F44Adj" concrete (EDF notation). Previous industrial computations questioned whether the storage conditions (with its relatively high temperature and low relative humidity) can lead to significant shrinkage by desiccation and thus to stresses that could lead to the concrete cracking. Aiming at answering this question, this thesis work presents a full scientific study of the phenomena involved in the drying of the concrete of this package.

The study is organized in four chapters (Chapters 2 - 3 - 4 -5). Chapters 2-4 examine and review the different aspects of the drying of concrete: description of water equilibrium in pores (Chapter 2), of drying kinetic of concrete (Chapter 3) and the hygro-mechanical coupling leading to an estimation of drying strains in Chapter 4. Chapter 4 is also devoted to proposing a new poromechanical model valid on a large range of relative humidity. This proposition constitutes the most innovative contribution of this thesis. The subjects studied in Chapters 2-4 finally permitted to model the drying behavior of the CIPG considered packages (Chapter 5) and so to refine the computations performed previously at EDF R&D.

Chapters 2 to 4 are organized in three parts: the first consists in a revue of the main results available in the literature, the second consists in experimental tests done in various laboratories and the third is based on modelling and numerical simulations carried out in this thesis. The conclusions drawn from each chapter along with perspectives are summarized in the current chapter and furtherly discussed.

6.1. Conclusions regarding experiments

In the framework of this thesis, an experimental campaign was carried out in various laboratories (internal and external to EDF). The tests aimed to provide us with material properties and to validate the poromechanical model we developed.

Chapter 2 presented experimental water retention tests performed at the EDF-MMC Laboratory. Those tests aimed to characterize the retention properties of the concrete. Two different experimental methods were tested to impose the relative humidity: a method based on the use of salt saturated solutions (SSS) and another method based on the use of a dynamic vapor sorption (DVS) apparatus.

The SSS method consists in exposing concrete samples to temperatures of 20°C and 50°C and to various relative humidities. For every tested temperature and relative humidity, the test was supposed to last until reaching equilibrium (at which state the mass of the sample remain constant over time). Given that the drying kinetics is a relatively slow process for concrete, only few samples of concrete are equilibrated after 2 years. Therefore, in 2 years, the assessment of the full experimental SSS desorption isotherm for the F44Adj concrete was not possible. We hence proposed to complete this desorption isotherm with data points from the literature for another high-performance concrete.

During the SSS tests, we noted some inconsistencies in the saturated densities measured on small (7x7x1cm and 7x7x3cm) specimens undergoing drying and a larger specimen (7x7x28cm) conserved in sealed autogenous conditions and serving as a reference. In both cases, samples were resaturated after approximately two years of tests in order to measure the saturated mass. In order to interpretate the results, we had to make hypotheses and formulate scenarios which may explain the

inconsistencies. We finally selected two possible scenarios, allowing us to correct the results and so the desorption isotherms.

According to the first scenario, the larger (7x7x28cm) reference specimen was not completely resaturated, the specimen did not remain long enough in water to effectively saturate all the concrete pores.The second scenario related the inconsistencies to the presence of micro-cracks in the smaller samples (7x7x1cm and 7x7x3cm), formed during drying or during fabrication; in fact, small specimens were obtained by sawing 7x7x28cm prisms. In both proposed scenarios, we corrected the desorption isotherms accordingly.

Chapter 2 also presents the DVS method, which consists in measuring the desorption isotherm of a material ground to a powder and is known to be faster than the SSS method. As a matter of fact, under a fixed relative humidity, a powder reaches equilibrium in a relatively very short duration (when compared to a bulk sample). Hence, we assessed the complete desorption isotherm of the studied concrete. However, it was shown that this desorption isotherm differed from the one obtained with the SSS method. This behavior was observed also in previous literature works (Poyet et al., 2016), who related it to the fact that the concrete powder may not be representative of the material since the total volume is smaller than an RVE.

Chapter 3 presented experimental drying tests performed at the EDF-MMC Laboratory that aimed at a better characterization of the drying kinetic of the F44Adj concrete. Those tests consisted in drying various geometries of concrete samples (7x7x1cm, 7x7x3cm, 7x7x28cm) under two environmental conditions (i.e. ($T = 20°C$, $h_R = 50\%$) and ($T = 50°C$, $h_R = 30\%$)) and provided mass loss curves. The tests lasted 250 days for the 7x7x1cm and 7x7x3cm samples and 530 days for the 7x7x28cm sample. It was observed that the latter durations were not sufficient for the 7x7x28cm samples to reach equilibrium at a temperature of 20°C, as their mass still evolved at this time. The saturated masses of the different geometries samples were measured after the end of the drying experiments. We noted equally important differences between those measurements. Again, we explained those inconsistencies with the same two scenarios mentioned previously. Corresponding corrections of the results (i.e. of the evolution of the saturation degree over time) were also proposed.

A final verification was done, when we compared the corrected initial degree of saturation obtained from the water retention tests (Chapter 2) with those obtained from the drying tests (Chapter 3). The comparison showed inconsistencies in some cases. This comparison made it possible for us to select the most accurate desorption isotherm (namely the SSS desorption isotherms) and the most appropriated correction scenario (namely scenario 2, which relies on the potential formation of micro-cracks in the 7x7x1cm and 7x7x3cm samples).

From what has been presented previously, one can eventually question the optimal experimental procedure to adopt in order to obtain an accurate value of the saturated mass, when performing a test that requires drying of samples. Ideally, specimens should be first casted in their final shape, then saturated from the beginning before being dried. In our case, we chose to start from the autogenous state to reproduce the initial state of the package shell. However, another possibility would be to begin the desorption test from the saturated state. Concerning the fabrication process, it would be theoretically best to dry larger specimens, but that would lead to very long duration of tests which laboratories usually avoid due to related costs.

Furthermore, the observation regarding the DVS test led us to question whether this test is appropriate for concrete samples. As a matter of fact, in comparison with a cement paste sample, a concrete sample presents more heterogeneities (aggregates), which makes it difficult to grind the concrete into a powder that is representative. Hence, for future concrete desorption tests, if no time constraint is imposed, an SSS desorption test can be found more appropriate than a DVS paste.

On a second part of chapter 3, a water permeability measuring test done at LAM^{cube} laboratory of Lille's university is presented. This test was done under an ambient temperature, on 7 samples with a 65mm diameter and a 60mm height. The measured permeability of the concrete to water was 5.66 10^{-21} m^2$\pm$1.77 10^{-21}m^2. In this test, the measured value of permeability should be considered as an approximate value, given that water permeability measurements are known to be highly impacted by the degree of hydration of concrete.

Chapter 4 described measurements of drying and autogenous shrinkage performed at the EDF R&D – MMC laboratory and at the LMDC laboratory. The tests consisted in measuring relative length variations of samples submitted either to autogenous conditions (at a temperature of 20°C and 50°C) or to drying conditions (i.e. ($T = 20°C$,$h_R = 50\%$) or ($T = 50°C$,$h_R = 30\%$)). The drying shrinkage tests done at the MMC laboratory were carried out for a total duration of 530 days, with the aim of reaching equilibrium. However, the results showed suspicious evolutions after 268 days. These evolutions were due to a defect in the measurement material: an invar rod used for the calibration of the refractometer setup had been deteriorated. Nevertheless, the shrinkage strains measured up to 268 days were assumed to be valid. This validity was verified by repeating the drying shrinkage experiments, which yielded in repeatable results. Regarding the autogenous shrinkage tests, the tests at a temperature of 20°C were performed at the EDF-MMC laboratory, while the tests at 50°C were performed at the LMDC laboratory. We observed an increase of autogenous shrinkage with temperature. At 20°C, the number of data points was relatively small. Therefore, it was proposed to fit the autogenous experimental curves according to the modelling works of Aili et al. (2018).

The observations done regarding the drying shrinkage tests in Chapter 4 lead us to consider performing shrinkage experiments with various measurement techniques: refractometer, strains gauges and displacement sensors. Such redundancy might help overcoming difficulties encountered while using only one of those techniques. This consideration has already been envisioned under the current framework. However, additional experimental difficulties regarding the use and calibration of strain gauges and sensors under a temperature of 50°C are to be controlled.

6.2. Conclusions regarding modelling and numerical simulations

Drying of concrete is the main phenomenon studied in this work. Aspects related to transfers during drying and to drying-induced deformations were carefully explored in chapters 2 to 4, respectively, which allowed us to accurately model the drying behavior of the concrete package in chapter 5.

At first, since the water retention curve is an input that is important for a variety of poromechanical models (e.g. Coussy (2003), Vlahinić et al. (2009)), we studied in detail how to describe it. After introducing various experimental methods to obtain a sorption/desorption isotherm, chapter 2 mainly aimed to find an appropriate model of the retention (i.e. a mathematical expression describing the desorption isotherm) of a high-performance concrete. Different models were already used in the literature and were detailed in section 2.1.6. A particular attention was given to the Van Genuchten (1980) model, which is frequently applied in the literature for soils and cementitious materials and which relies on three parameters.

It was shown in chapter 2, while testing the Van Genuchten (1980) model and fitting it on desorption isotherms of high-performance concretes, that a modification in its mathematical expression was required. This modification is particularly needed in the range of relative humidity near 100%. As a matter of fact, in its expression, this model imposes a saturation degree which tends toward 1 when the relative humidity tends toward 100%, this constraint was not always consistent with experimental observations: indeed, these observations showed that a sample put in contact with air at a relative humidity of 100% is not always able to become fully saturated. Therefore, the saturation degree near a relative humidity of 100% is not always equal to 1. To alleviate this inconsistency, we proposed an additional fit parameter S_{100} to the Van Genuchten (1980) model. This parameter represents the maximum saturation degree reached by the sample in contact with water vapor. Finally, it was shown that, after this modification, the Van Genuchten (1980) model was able to accurately describe water retention curves on the whole range of relative humidity.

Chapter 3 focuses on the moisture transfer in concrete, with the aim of accurately describing the drying kinetic. The modelling was done with a THM model (implemented in *Code_Aster)* based on water transfer equations like Darcy's law and Fick's law. Transfer parameters found in those equations, such as the intrinsic permeability, the relative permeabilities and the diffusion coefficient, can be determined experimentally, as presented in section 3.1.3. In this work, those parameters were determined by performing an inverse analysis of the mass loss over time of concrete samples dried at two different conditions namely ($T = 20$°C, h_R = 50%) and ($T = 50$°C, h_R = 30%).

Before performing this inverse analysis, two aspects were deemed important to study: the first one was linked to the choice of a boundary condition (Dirichlet or mixed condition) and the second one was linked to the expression of the relative permeability. Concerning the boundary condition, a detailed bibliographic study was performed and resulted in the implementation of a new boundary condition in *Code_Aster*. Based on literature works, this condition was written in the form of a moisture exchange equation that contained a mass exchange coefficient to be determined. A specific study of the impact of this coefficient on the drying kinetic was performed in this work. This study showed that the small permeability of the concrete led to a fit value of the mass exchange coefficient that is high enough to consider that the surface exchange is important. This finding allowed us to choose a Dirichlet condition as the most appropriate boundary condition for our study case.

Regarding the relative permeability, a numerical expression introduced by Mualem (1976) and linked to the works of Van Genuchten (1980) was used. This expression was reformulated according to the modification made previously (i.e., in chapter 2, when we introduced the maximal saturation

S_{100} of a sample in contact with water vapor) for the Van Genuchten (1980) model. The impact of the relative permeability on the drying kinetic was also studied. It allowed to verify the accuracy of the values of the relative permeability parameters $p = 0.5$ and $q = 2$ found in the Mualem (1976) expression. Finally, concerning the calibration of the intrinsic permeability, it was found that this parameter took different values according to the temperature considered: we fitted an intrinsic permeability of 4.10^{-24}m^2 at $T = 20$°C and $4.5\ 10^{-22}$m^2 at $T = 50$°C. The findings in Chapter 3 raise questions regarding the possibility of finding an 'intrinsic' permeability for concrete that would be independent of the temperature to which the concrete is exposed and can be thus the manifestation of shortcomings of the transfer models used in this study. The fulfilment of those shortcomings should constitute further perspectives of this work

Finally, a major attention was given to the development of a poromechanical model that allows to describe the drying shrinkage of a porous material over a wide range of relative humidity. As a matter of fact, the poromechanical model implemented in *Code_Aster* and used nowadays at EDF to describe this drying behaviour of the concrete shell is based on the work of Coussy et al. (2003). However, literature works reviewed in chapter 4 pointed out the insufficiency of this model in describing drying shrinkage strains at low relative humidities (i.e., at relative humidities lower to 50%). Moreover, other attempts were also made by various authors (e.g. Beltzung and Wittmann (2005), Rougelot et al. (2009)) to describe the drying shrinkage based on the effect of capillary pressure and disjoining pressure. Nevertheless, those models neglected the effect of water adsorbed on the pores surface and hence were shown insufficient to describe the drying shrinkage at low relative humidity (Wyrzykowski et al., 2017).

Therefore, in this work, a poromechanical model that accounts for both capillary and water adsorption effects is proposed (section 4.2). This model was derived using a thermodynamical approach based on the Helmholtz energy balance. As a result of the derivation, the energy of the porous material solid matrix was linked to contributions of capillary pressure, interfaces and fluid adsorption effects. An energy derivation made it possible to write new expressions for the constitutive laws and equivalent pore pressure. An application of this new model to the drying shrinkage of porous materials was proposed in section 4.2.2. As input parameters, this model requires essentially sorption isotherms analyzed with the BET theory (Brunauer et al., 1938) and the BJH technique (Barrett et al., 1951) and poroelastic properties such as the Biot coefficient. Another input parameter (linked to the Shuttleworth effect) is fitted on experimental drying shrinkage strains. This model was tested and validated with experimental data for various porous materials for which data were available in the literature, namely a hardened ordinary cement paste (Maruyama et al., 2018), a high-performance concrete (Baroghel-Bouny et al., 1999) and a Vycor glass (Amberg and McIntosh, 1952). The results show a satisfactory evaluation of the drying shrinkage strains for all three tested materials, with the possibility of considering only one fitting parameter, namely the Biot coefficient that presented a fit value of approximately 0.7. It should be noted that this new approach does not take into account the long-term viscous deformations, as the solid skeleton is considered elastic. Compared to other poromechanical models found in the literature such as the classical Biot-Bishop (Biot, 1941) model or the Coussy et al. (2003) model, this model appears to be capable of displaying the transition at a certain relative humidity between the capillary pressure effects and the surface adsorption effect, which manifests itself by a plateau in the drying shrinkage strains curve at this value of relative humidity.

This poromechanical model was implemented in *Code_Aster* and its accuracy in assessing the drying shrinkage strains of the F44Adj concrete is then tested. This assessment was performed by comparing numerical results with experimental drying shrinkage strains of the F44Adj concrete. In a general way, the model was able to describe the evolution of the drying shrinkage strains while considering one fitting parameter: the Biot coefficient. In the case of the condition ($T = 20$°C, $h_R = 50\%$), a Biot coefficient of b=1 was needed. This value is larger than the expected value of $b = 0.7$

fitted previously on the experimental data of Baroghel-Bouny et al.(1999) and is different from common values found for a Biot coefficient in the litterature. This may be explained by the fact that the latter coefficient in the case of the F44Adj concrete may have accounted for additional creep strains developing in the F44Adj concrete under the hydraulic pressures and hence should have been named differently from a "Biot coefficient". Given that the development of creep strains is known to be strongly dependent on the concrete, those strains are of a good importance in the case of a 28-days-old concrete as the F44Adj concrete. Therefore, the value of the "Biot coefficient" in this case might be larger than the expected value. Regarding the condition ($T = 50$°C,$h_R = 30\%$), the model with a Biot coefficient of b=0.42 appeared to describe satisfactorily the drying shrinkage of concrete during the whole duration of the test.

Following the work presented in this thesis, two important points require further exmamination. At first, the dependency of the concrete permeability on the surrounding temperatures (especially for moderate temperatures T<100°C) must be inspected more carefully. Apart from the works of Drouet el al. (2015), this aspect is not frequently studied in the litterature. Therefore, the difference between the two permeabilities of the F44Adj concrete fitted at each temperature must be examined more thouroughly. Moreover, the difference between the values of the Biot coefficient fitted at T=20°C and T=50°C must be addressed. As a matter of fact, if the latter coefficient is accounting for viscous creep strains, it would be expected that its value increase respectively with the temperature. This is not the case in our study.

However, we should recall the number of experimental difficulties encountered during the experimental campaign (refer to section 6.1), such as lack of data points for the water retention curve, potential appearance of micro-cracks on samples used for modelling the drying kinetic of the concrete and hence determining its permeability. Those difficulties induced uncertainties regarding the various input parameters of the model. Therefore, any further conclusion regarding the consistency of the model must be done once all needed experimental input parameters are available.

Chapter 5 presented a simulation of the drying behavior of the concrete package C1PG^{SP} while using the new poromechanical model. This simulation used all hydro-mechanical parameters already introduced in chapter 2, 3 and 4. The results of the simulation, in terms of stresses and strains, were compared to those obtained with a Coussy et al. (2003) model. The computation with the Coussy et al. (2003) model led to larger hydraulic pore pressures, strains and stresses than those obtained with the new model. Finally, the results show that, by using any of the two models (i.e. the new model and the Coussy et al. (2003) model), we expect no risk of a crack propagating through the whole thickness of the F44Adj concrete shell or cap and that only a thin external layer could be subjected to cracking.

6.3. Perspectives

The work presented in this thesis describes thoroughly the hydro-mechanical phenomena involved in the drying of concrete. Some work remains to be done in order to describe the behavior of concrete more generally. Those works can be presented simultaneously as scientific and industrial perspectives.

An important aspect that needs to be explored is the viscous behavior of concrete: this aspect is not considered in the developed poro-elastic approach described in this thesis. Viscous strains might have a role not only for the interpretation of creep tests but also to model shrinkage, since delayed strains may develop under the hydraulic pressures. Moreover, an important aspect of creep must be more thoroughly explored. This aspect is linked to the "Pickett effect" (Pickett, 1942): when the specimen dries simultaneously with the application of load (total creep test), the creep deformation of concrete is more important than that measured on a loaded and pre-dried specimen. This observation must be accounted for in further creep modelling attempts. For a better investigation of the role of viscous strains in the shrinkage and creep of concrete upon drying, basic and drying creep experiments were foreseen and performed on the concrete F44Adj at the LMDC laboratory. The corresponding results must be further analyzed.

Furthermore, more importance must be given to the behavior of concrete at early age. As a matter of fact, the considered THM model does not consider the chemical reactions linked to the hydration of concrete. In this study, the autogenous shrinkage was accounted for by a proper fit of the Biot coefficient. However, a proper incorporation of this shrinkage aspect in the THM model must be foreseen. For that purpose, additional autogenous shrinkage tests on the F44Adj concrete might be required.

Additionally, the effect of temperature on the variation of the BJH input parameters (adsorbed water thickness, specific surface area) of the poromechanical model must be explored more carefully. This could allow us in the future to assess more easily the drying shrinkage of a porous material at a temperature different from the ambient one. Moreover, the effect of temperature on the permeability of concrete and on the Biot coefficient need to be investigated more deeply.

Another important point to be studied is the modelling of non-isothermal conditions. A reflection has been initiated on this subject and must be carried on. This reflection includes the effect of temperature on water retention isotherms and hence on water equilibrium in pores. This study will allow us to complete a non-isothermal simulation of the concrete package behavior.

Finally, a global validation of the F44Adj concrete behavior model (including creep and shrinkage strains) is also envisioned, based on a ring test (ASTM C - 1581, 2013). In this test, a freshly mixed concrete is compacted in a circular mold around an instrumented steel ring on which strain gauges are placed; then the concrete specimen is exposed to an external drying ambient. A metallic rigid ring restrains the concrete deformations, so that the sample is under tension due to the restrained shrinkage. Hence, creep and shrinkage strains happen at the same time, so that results can be used to validate a drying model including delayed strains. This ring test will be performed in the internal laboratories of EDF, for the condition T=50°C and h_R = 30%.

REFERENCES

A

Abbas, A., Carcasses, M., and Ollivier, J.-P. (1999). Gas permeability of concrete in relation to its degree of saturation. Mater. Struct. *32*, 3–8.

Aili, A., Vandamme, M., Torrenti, J-M., and Masson, B. (2018). Is long-term autogenous shrinkage a creep phenomenon induced by capillary effects due to self-desiccation? Cem. Concr. Res. *108*, 186–200.

Alfaro Soto, M.A., and Chang, H.K. (2015). Behaviour of LNAPL in soils with multimodal pore-size distribution. From Fundam. to Appl. Geotech. 2284–2291.

Aligizaki, K. (2006). Pore structure of cement-based materials : testing, interpretation and requirements (Taylor & Francis).

Amberg, C., and McIntosh, R. (1952). A study of adsorption hysteresis by means of length changes of a rod of porous glass. Can. J. Chem. *30*, 1012–1032.

Anderson, R. (1946). J. Am. Chem. Soc. Sot. 68.

Andra. (2020). *www.andra.fr*. Récupéré sur agence nationale de la gestion des déchets radioactifs:

Andrieu, S., and Müller, P. (2005). Les surfaces solides: concepts et méthodes.

Aono, Y., Matsushita, F., Shibata, S., and Hama, Y. (2007). Nano-structural changes of C-S-H in hardened cement paste during Drying at 50°C. J. Adv. Concr. Technol. *5*, 313–323.

ASTM C - 1581 (2013). Standard test method for determining age at cracking and induced tensile stress. 1–7.

Ayano, T., and Wittmann, F.H. (2002). Drying, moisture distribution, and shrinkage of cement-based materials. Mater. Struct. Constr. *34*, 134–140.

B

Badmann, R., Stockhausen, N., and Setzer, M.J. (1981). The statistical thickness and the chemical potential of adsorbed water films. J. Colloid Interface Sci. *82*, 534–542.

Balzer, C., Waag, A.M., Gehret, S., Reichenauer, G., Putz, F., Hüsing, N., Paris, O., Bernstein, N., Gor, G.Y., and Neimark, A. V. (2017). Adsorption-induced deformation of hierarchically structured mesoporous silica - effect of pore-level anisotropy. Langmuir *33*, 5592–5602.

Bangham, D.H. (1931). The swelling of charcoal. Proc. R. Soc. London, Ser. A *130*, 81–89.

Bangham, D.H., Fakhoury, N., and Mohamed, a. F. (1934). The swelling of charcoal. Part iii. Experiments with the lower alcohols. Proc. R. Soc. A Math. Phys. Eng. Sci. *147*, 152–175.

Baroghel-bouny, V., Mounanga, P., Khelidj, A., and Loukili, A. (2017). Autogenous deformations of cement pastes : Part II . W / C effects , micro-macro correlations , and threshold values To cite this version : HAL Id : hal-01005282

Baroghel-Bouny, V. (1994). Caractérisation microstructurale et hydrique des pâtes de ciment et des bétons ordinaires e at es hautes performances.

Baroghel-Bouny, V. (2007). Water vapour sorption experiments on hardened cementitious materials. Part II: Essential tool for assessment of transport properties and for durability prediction. Cem. Concr. Res. *Volume 37*, 438–454.

Baroghel-Bouny, V., Mainguy, M., Lassabatere, T., and Coussy, O. (1999). Characterization and identification of equilibrium and transfer moisture properties for ordinary and high-performance cementitious materials. Cem. Concr. Res.

Barrett E., Joyner L., and Halenda P. (1951). The determination of pore volume and area distributions in porous substances. I. Computations from Nitrogen Isotherms. *1896*.

Bary, B., De Morais, M.V.G., Poyet, S., and Durand, S. (2012). Simulations of the thermo-hydro-mechanical behaviour of an annular reinforced concrete structure heated up to 200°C. Eng. Struct.

Bažant, Z.P., and Yunping, X.I. (1994). Drying creep of concrete: constitutive model and new experiments separating its mechanisms. Mater. Struct. *27*, 3–14.

Bažant, Z.P., Cusatis, G., and Cedolin, L. (2004). Temperature effect on concrete creep modeled by microprestress- solidification theory. J. Eng. Mech. *130*, 691–699.

Beltzung, F., and Wittmann, F.H. (2005). Role of disjoining pressure in cement based materials. Cem. Concr. Res. *35*, 2364–2370.

Benboudjema, F. (2004). Modélisation des déformations différées du béton sous sollicitations biaxiales. Application aux enceintes de confinement de batiments reacteurs des centrales nucléaires.

Bentz, D.P., Garboczi, E.J., and Quenard, D.A. (1998). Modelling drying shrinkage in reconstructed porous materials: Application to porous Vycor glass. Model. Simul. Mater. Sci. Eng. *6*, 211–236.

Biot, M.A. (1941). General theory of three-dimensional consolidation. J. Appl. Phys. *12*, 155–164.

Biot, M.A., and Willis, D.G. (1957). The elastic coefficients of the theory of consolidation. J. Appl. Mech 594–601.

Bishop, A.W., and Blight, G.E. (1963). Some aspects of effective stress in saturated and partly saturated soils. Géotechnique *13*, 177–197.

Boer, J.D. (1953). The Dynamical Character of Adsorption. Clarendon, Oxford,.

Boukadida, N., and Ben Nasrallah, S. (2002). Effect of the varaiability of heat and mass transfer coefficients on convective and convective-radiative drying of porous media. *Volume Dry*.

Van Breugel, K. (2001). Numerical modelling of volume changes at early ages - Potential, pitfalls and challenges. Mater. Struct. Constr. *34*, 293–301.

Briffaut, M. (2010). Étude De La Fissuration Au Jeune Âge Des Structures Massives En Béton: Influence De La Vitesse De Refroidissement, Des Reprises De Bétonnage Et Des Armatures. p202.

Brooks, R.H., and Corey, A.T. (1964). Hydraulic properties of porous media, Hydrology papers, Colorado State University

Brue, F. (2011). Rôle de la température et de la composition sur le couplage thermo-hydro-mécanique des bétons.Ecole centrale de Lille, HAL Id : tel- 00578753.

Brue, F., Davy, C.A., Skoczylas, F., Burlion, N., and Bourbon, X. (2012). Effect of

temperature on the water retention properties of two high performance concretes. Cem. Concr. Res. *42*, 384–396.

Brue, F.N.G., Davy, C.A., Burlion, N., Skoczylas, F., and Bourbon, X. (2017). Five year drying of high performance concretes: Effect of temperature and cement-type on shrinkage. Cem. Concr. Res. *99*, 70–85.

Brunauer, S., Emmett, P.H., and Teller, E. (1938). Adsorption of gases in multimolecular layers. J. Am. Chem. Soc. *60*, 309–319.

Brunauer, S., Skalny, J., and Bodor, E.E. (1969). Adsorption on nonporous solids. J. Colloid Interface Sci. *30*, 546–552.

C

Cammarata, R.C. (1994). Surface and interface stress effects in thin films. Prog. Surf. Sci. *46*, 1–38.

Carette, J., Soleilhet, F., Benboudjema, F., Ma, X., Nahas, G., Abahri, K., Darquennes, A., and Bennacer, R. (2020). Identifying the mechanisms of concrete drying: An experimental-numerical approach. Constr. Build. Mater. *230*, 117001.

Carlier, J-P., and Burlion, N. (2010). Experimental and numerical study of the fracture and self-healing of cementitious materials, Transport in Porous Media.

Carmeliet, J., and Abeele, K. Van Den (2004). Poromechanical approach describing the moisture influence on the non-linear quasi-static and dynamic behaviour of porous building materials. *37*, 271–280.

Carmeliet, J., Derome, D., and Guyer, R.A. (2013). Nonlinear poro-elastic model for unsaturated porous solids. *80*, 1–10.

Chen, W. (2013). Etude expérimentale de la perméabilité du béton sous conditions thermiques et hydriques variables. Ecole Centrale de Lille, HAL Id : tel- 00778621.

Chen, M., Coasne, B., Derome, D., and Carmeliet, J. (2020). Coupling of sorption and deformation in soft nanoporous polymers: Molecular simulation and poromechanics. J. Mech. Phys. Solids *137*, 103830.

Chen, W., Liu, J., Brue, F., Skoczylas, F., Davy, C.A., Bourbon, X., and Talandier, J. (2012). Water retention and gas relative permeability of two industrial concretes. Cem. Concr. Res. *42*, 1001–1013.

Chhun, P. (2017). Modélisation du comportement thermo-hydro-chemo-mécanique des enceintes de confinement nucléaire en béton armé-précontraint.Université de Toulouse.

Chilton, T.H., and Colburn, A.P. (1934). Mass transfer (Absorption) Coefficients. Ind. Eng. Chem. Res. *26*, 1183–1187.

Churaev, N.., and Derjaguin, B.. (1985). Inclusion of structural forces in the theory of stability of colloids and films. J. Colloid Interface Sci. *103*, 542–553.

Coker, A.K. (2007). Physical properties of liquids and gases. Ludwig's Appl. Process Des. Chem. Petrochemical Plants 103–132.

Collins, Jack A. (1993). Maximum normal stress theory (Rankine's theory). Failure of materials in mechanical design : analysis, prediction, prevention (2nd ed.). New York: Wiley. 142–143.

Cornu, A. (1873). Relations entre les coefficients thermiques et thermo-élastiques des corps. J.

Phys. Théorique Appliquée *2*, 41–50.

Coussy, O. (2003). The equivalent pore pressure and the swelling and shrinkage of cement-based materials. Mater. Struct. *37*, 15–20.

Coussy, O. (2004). Poromechanics, John Wiley & Sons

Coussy, O. (2007). Revisiting the constitutive equations of unsaturated porous solids using a Lagrangian saturation concept - Tel-00359952.

Coussy, O. (2010). Mechanics and physics of porous solids, John Wiley & Sons

Coussy, O., Baroghel-Bouny, V., Dangla, P., and Mainguy, M. (2001). Evaluation de la perméabilité à l'eau liquide des bétons à partir de leur perte de masse durant le séchage. Rev. Française Génie Civ. *5*, 269–284.

Coussy, O., Dangla, P., Lassabatere, T., and Baroghel-Bouny, V. (2003). The equivalent pore pressure and the swelling and shrinkage of cement-based materials. Mater. Struct. *37*, 15–20.

D

Dangla, P., and Pereira, J.-M (2014). A thermodynamic approach to effective stresses in unsaturated soils incorporating the concept of partial pore deformations.

Davie, C.T., Pearce, C.J., and Bićanić, N. (2012). Aspects of permeability in modelling of concrete exposed to high temperatures. Transp. Porous Media.

de Boer, J.H., and Lippens, B.C. (1965). Studies on pore systems in catalysts. V. The t method. J. Catal. *4*, 319–323.

De Vries D.A, K. A. (1966). On the value of diffusion coefficient of water vapour in air, Phénomènes de transport avec changement de phase dans les milieux poreux ou colloïdaux. *ed.CNRS*, pp 561-572 tiré de (Ranaivomanana, 2010).

Di Bella, C., Wyrzykowski, M., and Lura, P. (2017). Evaluation of the ultimate drying shrinkage of cement-based mortars with poroelastic models. Mater. Struct. Constr. *50*, 1–13.

Drouet, E., Poyet, S., and Torrenti, J.M. (2015). Temperature influence on water transport in hardened cement pastes. Cem. Concr. Res. *76*, 37–50.

Duforestel, T. (2015). Des transferts couplés de masse et de chaleur à la conception bioclimatique: recherches sur l'efficacité énergétique des bâtiments. Hdr 241.

Durner, W. (1994). Hydraulic conductivity estimation for soils with heterogeneus pore structure. Water resour. Res. *30*, 211;223.

E

EDF. (2020). Récupéré sur Electricité de France: https://edf.fr

Ewart, T. (2009). Etude des écoulements gazeux isothermes en microconduit : du régime hydrodynamique au proche régime moléculaire libre - HAL Id : tel-00396378 Etude des écoulements gazeux isothermes en microconduits

F

Feldman, R.F., and Sereda, P.J. (1968). A model for hydrated Portland cement paste as deduced from sorption-length change and mechanical properties. Matériaux Constr. *1*, 509–520.

Ferraris, C. (1986). Mecanisme du retrait de la pate de ciment durcie. Ecole polytechnique

fédérale de Lausanne

Ferroukhi, M.Y., Abahri, K., Belarbi, R., Limam, K., and Nouviaire, A. (2016). Experimental validation of coupled heat, air and moisture transfer modeling in multilayer building components. Heat Mass Transf. Und Stoffuebertragung *52*, 2257–2269.

G

Gallé, C. (2001). Effect of drying on cement-based materials pore structure as identified by mercury intrusion porosimetry: A comparative study between oven-, vacuum-, and freeze-drying. Cem. Concr. Res. *31*, 1467–1477.

Gawin, D., Majorana, C.E., and Schrefler, B.A. (1999). Numerical analysis of hygro-thermal behaviour and damage of concrete at high temperature. Mech. Cohesive-Frictional Mater. *4*, 37–74.

Gawin, D., Pesavento, F., and Schrefler, B.A. (2006). Hygro-thermo-chemo-mechanical modelling of concrete at early ages and beyond. Part II: Shrinkage and creep of concrete. Int. J. Numer. Methods Eng. *67*, 332–363.

Ghabezloo, S. (2010). Association of macroscopic laboratory testing and micromechanics modelling for the evaluation of the poroelastic parameters of a hardened cement paste. Cem. Concr. Res. *40*, 1197–1210.

Gibbs, J.W.A. (1928). The collected works of J. W. Gibbs

Ginette Arliguie, H. H. (2007). Grandeurs associées à la durabilité des bétons. Association Française de Génie Civil. Laboratoire Matériaux et durabilité des constructions (Toulouse).

Gor, G.Y., and Bernstein, N. (2016). Revisiting bangham's law of adsorption-induced deformation: changes of surface energy and surface stress. Phys. Chem. Chem. Phys. *18*, 9788–9798.

Gor, G.Y., Huber, P., and Weissmüller, J. (2018). Elastocapillarity in nanopores : Sorption strain from the actions of surface tension and surface stress. *086002*, 1–17.

Granger, L. (1995). Comportement différé du béton dans les enceintes de centralesnucléaires. Analyse et modélisation. Thèse de doctorat de l'ENPC.

Grasley, Z.C., and Leung, C.K. (2011). Desiccation shrinkage of cementitious materials as an aging, poroviscoelastic response. Cem. Concr. Res. *41*, 77–89.

Grasley, Z.C., Scherer, G.W., Lange, D.A., and Valenza, J.J. (2007). Dynamic pressurization method for measuring permeability and modulus: II. cementitious materials. Mater. Struct. Constr. *40*, 711–721.

Gray, W.G., and Schrefler, B.A. (2001). Thermodynamic approach to effective stress in partially saturated porous media. Eur. J. Mech. A/Solids *20*, 521–538.

Guggenheim, E. (1966). Applications of statistical mechanics. Clarendon, Oxford,.

Gyozo, L., and Cesar, B. (2012). Laser techniques for the study of electrode processes (Springer, dordrecht, the netherlands).

H

Hagymassy, J., Brunauer, S., and Mikhail, R.S. (1969). Pore structure analysis by water vapor adsorption. J. Colloid Interface Sci. *Volume 29*, p485-491.

Halsey, G. (1948). Physical adsorption on non-uniform surfaces. J. Chem. Phys. *16*, 931–937.

Hansen, W. (1987). Drying shrinkage mechanisms in portland cement paste. J. Am. Ceram. Soc. *70*, 323–328.

Hansen, & Mattock. (1966). Influence of size and shape of member on the shrinkage and creep of concrete. Journal of the American concrete Institute.

Harkins, W.D., and Jura, G. (1944). Surfaces of Solids. XII. An Absolute Method for the Determination of the Area of a Finely Divided Crystalline Solid. J. Am. Chem. Soc. *66*, 1362–1366.

Hashin, Z., and Shtrikman, S. (1963). A variational approach to the theory of the elastic behaviour of multiphase materials. J. Mech. Phys. Solids *11*, 127–140.

Hassanizadeh, S.., and Gray, W.. (1980). General conservation equations for multi-phase systems: 3. Constitutive theory for porous media flow. Adv. Water Ressources *3*, 25–40.

Henderson-Sellers, B. (1984). A new formula for latent heat of vaporization of water as a function of temperature. Q. J. R. Meteorol. Soc. *110*, 1186–1190.

Hilaire, A. (2015). Etude des déformations différées des bétons en compression et en traction , du jeune au long terme : application aux enceintes de confinement. 263.

Hiller, K.H. (1964). Strength reduction and length changes in porous glass caused by water vapor adsorption. J. Appl. Phys. *35*, 1622–1628.

Huang, Q., Jiang, Z., Gu, X., Zhang, W., and Guo, B. (2015). Numerical simulation of moisture transport in concrete based on a pore size distribution model. Cem. Concr. Res. *67*, 31–43.

Hubert, F., and Giraud, M.A. (2004). Contribution à l ' étude du comportement mécanique des ouvrages en béton avec prise en compte des effets de la dessiccation. 1–188., universite des sciences et technologies de lille sujet :

Hutter, K., Laloui, L., and Vulliet, L. (1999). Thermodynamically based mixture models of saturated and unsaturated soils. Mech. Cohesive-Frictional Mater. *4*, 295–338.

I

IUPAC (1994). International Union of Pure and Applied Chemistry. Recommendations for the characterization of porous solids.

J

J.F. Daian (1986). Processus de condensation et de transfert d'eau dans un matériau meso et macroporeux: étude expérimentale du mortier de ciment l - HAL Id : tel- 00686400

J.F. Daian (2013). Equilibre et transferts en milieux poreux. Hal 646.

Jaffel, H. (2007). Caractérisation multi-échelles de matériaux poreux en évolution : cas du plâtre - Hamouda Jaffel - HAL Id : tel-00122888.

Jensen, O.M., and Hansen, P.F. (2001). Autogenous deformation and RH-change in perspective. Cem. Concr. Res. *31*, 1859–1865.

Johannesson, B., and Janz, M. (2002). Test of four different experimental methods to determine sorption isotherms. J. Mater. Civ. Eng. *14*, 471–477.

Jooss, M., and Reinhardt, H.W. (2002). Permeability and diffusivity of concrete as function

of temperature. Cem. Concr. Res. *32*, 1497–1504

K

Kang, W., and Chung, W.Y. (2009). Liquid water diffusivity of wood from the capillary pressure-moisture relation. J. Wood Sci.

Kaya, A., Aydin, O., and Dincer, I. (2007). Numerical modeling of forced-convection drying of cylindrical moist objects. Numer. Heat Transf. Part A Appl.

Kébré, M.B., Ouedraogo, F., Betaboalé, N., Zougmoré, F., and Cherblanc, F. (2013). Soil-water characteristic curve modeling at low water content: empirical and semi-empirical approaches. Int. J. Eng. Res. *Volume 2*, p432-437.

Koenders, E.A.B., and Van Breugel, K. (1997). Numerical modelling of autogenous shrinkage of hardening cement paste. Cem. Concr. Res. *27*, 1489–1499.

Kovler, K., and Zhutovsky, S. (2006). Overview and future trends of shrinkage research. Mater. Struct. Constr. *39*, 827–847.

Kramer, D., and Weissmüller, J. (2007). A note on surface stress and surface tension and their interrelation via Shuttleworth's equation and the Lippmann equation. Surf. Sci. *601*, 3042–3051.

Kulasinski, K., Guyer, R., Derome, D., and Carmeliet, J. (2015). Poroelastic model for adsorption-induced deformation of biopolymers obtained from molecular simulations. Phys. Rev. E - Stat. Nonlinear, Soft Matter Phys. *92*, 1–10.

Künzel, H.M. (1995). Simultaneous heat and moisture transport in building components one- and two-dimensional calculation using simple parameters. Physics (College. Park. Md). *1995*, 1–65.

L

Lafhaj, Z. (2002). Experimental study of gas and liquid permeability of a mortar. *32*, 1357–1363.

Lee, Y., Choi, M-S., Yi, S-T., and Kim, J-K. (2008). Experimental study on the convective heat transfer coefficient of early-age concrete. Cem. Concr. Compos. *Volume 31*, p60-71.

Le Chatelier, H. (1900). Sur les changements de volume qui accompagnent le durcissement des ciments. Bulletin de la Société d'Encouragement pour l'Industrie Nationale pages 54–57.

Lewis, R.W. (Roland W., and Schrefler, B.A. (1987). The finite element method in the deformation and consolidation of porous media. John Wiley and sons publication.

Lion, M. (2004). Influence de la température sur le comportement poromécanique ou hydraulique d'une roche carbonatée et d'un mortier. Etudes expérimentales.

Liu, J. (2011). Etude expérimentale de la perméabilité relative des matériaux cimentaires et simulation numérique du transfert d'eau dans le béton.

Loosveldt, H., Lafhaj, Z., and Skoczylas, F. (2002). Experimental study of gas and liquid permeability of a mortar. Cem. Concr. Res. *32*, 1357–1363.

Lura, P., Van Breugel, K., and Maruyama, I. (2001). Effect of curing temperature and type of cement on early-age shrinkage of high-performance concrete. Cem. Concr. Res. *31*, 1867–1872.

Lura, P., Jensen, O.M., and Van Breugel, K. (2003). Autogenous shrinkage in high-

performance cement paste: An evaluation of basic mechanisms. Cem. Concr. Res. *33*, 223–232.

M

Maruyama, I., Rymeš, J., Vandamme, M., and Coasne, B. (2018). Cavitation of water in hardened cement paste under short-term desorption measurements. Mater. Struct. Constr. *51*.

Maugis, D. (1980). Cahiers du groupe français de rheologie. *Volume.5*

Mcbain. J. (1935). An explanation of hysteresis in the hydration and dehydration of gels, Journal of the American Chemical Society. *Volume.57, n°4*, pp 699-700 tiré de (Mjahad, 2012).

Mehta. P. (1986). Concrete: structure, properties and materials. Prentice-Hall. Inc Englewood cliffs.

Millington R. (1959). Gas diffusion in porous media. *Science, Volume. 130,* p. 100-102 tiré de (Thiery, 2007).

Mjahad, S. (2012). Impact de la fissuration sur les propriétés de rentention d'eau et de transport de gaz.Application au stockage profond des déchets radioactifs.

Monlouis-Bonnaire, J.P., Perrin, B., and Verdier, J. (2004). Prediction of the relative permeability to gas flow of cement based materials. Cem. Concr. Res. *Volume 34*, 737–744.

Morandeau, A., Sellier, A., Denis, R., Rapporteur, D., Examinateur, B.H., and Scrivener, K. (2014). Carbonatation atmosphérique des systèmes cimentaires à faible teneur en portlandite.Université Paris-Est.

Mounanga, P. (2003). Étude experimentale du comportement de pates de ciment au tres jeune âge : hydratation, retraits, proprietes thermophysiques. 245.

Mualem, Y. (1976). Wetting front pressure head in the infiltration model of Green and Ampt. Water Resour. Res. *12*, 564–566.

N

NF EN ISO 1257 (2013). Hygrothermal performance of building materials and products - Determination of hygroscopic sorption properties. 28.

NF P18-427 (1996). NF P18-427 - Béton - Détermination des variations dimensionnelles entre deux faces.

NF P18-459 (2010). NF P18-459 - Mars 2010.

Nguyen, P.T.M., Do, D.D., and Nicholson, D. (2011). On the cavitation and pore blocking in cylindrical pores with simple connectivity. J. Phys. Chem. B *115*, 12160–12172.

Nguyen, H., Rahimi-Aghdam, S., and Bažant, Z.P. (2020). Unsaturated nanoporomechanics. Proc. Natl. Acad. Sci.

Nilsson, L.O. (2002). Long-term moisture transport in high performance concrete. Mater. Struct. Constr. *35*, 641–649.

NIST Chemistry WebBook (2018). NIST chemistry webbook,thermophysical properties of fluid systems.

O

Obeid, W. (2001). Mathematical formulation of thermo hygro mechanical coupling problem in non-saturated porous media. Comput. Methods Appl. Mech. Eng. *Volume 190*, p5105-5122.

Ollivier, J. and Torrenti, J. (2008). La structure poreuse des bétons et les propriétés de transfert. La Durabilité Des Bétons p51-133.

Ožbolt, J., Oršanić, F., and Balabanić, G. (2016). Modeling influence of hysteretic moisture behavior on distribution of chlorides in concrete. Cem. Concr. Compos. *67*, 73–84.

P

Pan, H., Ritter, J. a, and Balbuena, P.B. (1998). from the Clausius - Clapeyron Equation. *7463*, 6323–6327.

Parrott, L.J. (1974). Lateral strains in hardened cement paste under short- and long-term loading. Mag. Concr. Res. *26*, 198–202.

Pellenq, R.J.M., Coasne, B., Denoyel, R.O., and Coussy, O. (2009). Simple phenomenological model for phase transitions in confined Geometry. 2. Capillary condensation/evaporation in cylindrical mesopores. Langmuir *25*, 1393–1402.

Pereira, J.-M., Coussy, O., Alonso, E.E., Vaunat, J., and Olivella, S. (2010). Is the degree of saturation a good candidate for Bishop's X parameter? Alonso, E.E., Gens, A. Unsaturated Soils—Proceedings 5th Int. Conf. Unsaturated Soils 913–919.

Pezzani, P. (1992). Propriétés thermodynamiques de l'eau (Editions T.I. | Techniques de l'Ingénieur).

Picandet, V. (2001). Influence d'un endommagement mécanique sur la perméabilité et sur la diffusivité hydrique des bétons.

Pickett, G. (1942). The effect of change in moisture-content on the crepe of concrete under a sustained load. ACI J. Proc. *38*.

Pickett, G. (1945). Modification of the brunauer-emmett-teller theory of multimolecular adsorption. J. Am. Chem. Soc. *67*, 1958–1962.

Pinson, M.B. (2015). Hysteresis from Multiscale Porosity : Modeling Water Sorption and Shrinkage in Cement Paste - The MIT Faculty.

Powers, T.C. (1968). The thermodynamics of volume change and creep. Matériaux Constr. *1*, 487–507.

Powers, T.C., and Brownyard, T.L. (1947). Studies of the physical properties of hardened portland cement paste. Res. Lab. Portl. Cem. Assoc.

Poyet, S. (2013). Determination of the intrinsic permeability to water of cementitious materials: Influence of the water retention curve. Cem. Concr. Compos. *35*, 127–135.

Poyet, S. (2016). Describing the influence of temperature on water retention using van Genuchten equation. Cem. Concr. Res. *84*, 41–47.

Poyet, S., and Charles, S. (2009). Temperature dependence of the sorption isotherms of cement-based materials: Heat of sorption and Clausius-Clapeyron formula. Cem. Concr. Res. *39*, 1060–1067.

Poyet, S., Trentin, K., and Amblard, E. (2016). The use of sorption balance for the

characterization of the water retention curve of cement-based materials. J. Adv. Concr. Technol. *14*, 354–367.

Poyet S. (2016). Experimental investigation of the effect of temperature on the first desorption isotherm of concrete.

R

Rahimi-Aghdam, S., Masoero, E., Rasoolinejad, M., and Bažant, Z.P. (2019). Century-long expansion of hydrating cement counteracting concrete shrinkage due to humidity drop from selfdesiccation or external drying. Mater. Struct. Constr. *52*.

Rahman, S.F., and Grasley, Z.C. (2017). The significance of pore liquid pressure and disjoining pressure on the desiccation shrinkage of cementitious materials. Int. J. Adv. Eng. Sci. Appl. Math. *9*, 87–96.

Rahoui, H. (2018). Contribution à la compréhension de l'action des agents réducteurs de retrait dans les matériaux cimentaires: étude expérimentale et modélisation. www.Theses.Fr.

Ranaivomanana (2010). Transferts dans les milieux poreux réactifs non saturés : application à la cicatrisation de fissure dans les matériaux cimentaires par carbonatation. Laboratoire Matériaux et Durabilité des Constructions (LMDC)

Reid, R. (1987). The properties of gases and liquids (mcgraw-hill). tiré de (Chhun, 2017).

Reviron, N. (2009). Etude du fluage des bétons en traction . Application aux enceintes de confinement des centrales nucléaires à eau sous pression. p244.

Robens, E., Benzler, B., Büchel, G., Reichert, H., and Schumacher, K. (2002). Investigation of characterizing methods for the microstructure of cement. Cem. Concr. Res. *32*, 87–90.

Rougelot, T., Skoczylas, F., and Burlion, N. (2009). Water desorption and shrinkage in mortars and cement pastes: Experimental study and poromechanical model. Cem. Concr. Res. *39*, 36–44.

Rouquerol, F. et al. (2003). Texture des matériaux pulvérulents ou poreux. Tech. l'Ingénieur *P1050*, 1–24.

S

Sakata, K. (1983). A study on moisture diffusion in drying and drying shrinkage of concrete. Cem. Concr. Res. *13*, 216–224.

Scherer, G. (1986). Dilatation of porous glass. J. Am. Ceram. Soc. *69*, 473–480.

Schulman, R.D., Trejo, M., Salez, T., Raphaël, E., and Dalnoki-Veress, K. (2018). Surface energy of strained amorphous solids. Nat. Commun. *9*, 8–13.

Sellier, A., and Buffo-Lacarrière, L. (2009). Vers une modélisation simple et unifiée du fluage propre, du retrait et du fluage en dessiccation du béton. Eur. J. Environ. Civ. Eng. *13*, 1161–1182.

Sémété, P., Février, B., Le Pape, Y., Delorme, J., Sanahuja, J., and Legrix, A. (2017). Concrete desorption isotherms and permeability determination: effects of the sample geometry. Eur. J. Environ. Civ. Eng. *21*, 42–62.

Setzer, M.J., Duckheim, C., Liebrecht, A., and Kruschwitz, J. (2006). The solid-liquid gel-system of hardened cement paste. 1–16.

Setzer, M. (1996). The Munich model – An example for modern materials science in civil engineering. Advances in Building Materials Science, EADIFICATIO Publishers.

Shahraeeni, E., Lehmann, P., and Or, D. (2012). Coupling of evaporative fluxes from drying porous surfaces with air boundary layer: Characteristics of evaporation from discrete pores. Water Resour. Res. *Volume 48*.

Shuttleworth, R. (1950). The surface tension of solids. Proc. Phys. Soc. Sect. A *63*, 444–457.

Soleilhet, F. (2018). Etudes expérimentales et numériques des matériaux cimentaires sous sollicitations hydro-mécaniques - HAL Id : tel-01818777.

Soliman, A.M., and Nehdi, M.L. (2011). Effect of drying conditions on autogenous shrinkage in ultra-high performance concrete at early-age. Mater. Struct. Constr. *44*, 879–899.

T

Tazawa, E., and Miyazawa, S. (1995). Chemical shrinkage and autogenous shrinkage of hydrating cement paste. *11*, 296–300.

Tenchev, R.T (2001). Finite element analysis of coupled heat and moisture transfer in concrete subjected to fire. Numer. Heat Transf. Part A Appl. *39*, 685–710.

Thiery, M., Baroghel-Bouny, V., Bourneton, N., Villain, G., and Stéfani, C. (2007). Modélisation du séchage des bétons. Rev. Eur. Génie Civ. *Volume 11*, p541-577.

Thiéry, M. (2005). Modélisation de la carbonatation atmosphérique des bétons – Prise en compte des effets cinétiques et de l'état hydrique.

Thomas, H.a. (1995). Fully coupled analysis of heat, moisture, and air transfer in unsaturated soil. J. Eng. Mech. 121

Torquato, S., and Stell, G.R. (1982). An equation for the latent heat of vaporization. Ind. Eng. Chem. Fundam. *21*, 202–205.

Torrenti, J.M., and Granger, L. (1997). Modélisation du retrait du béton en ambiance variable.

Tran Le, A.(2016). Etude des transferts hygrothermiques dans le béton de chanvre et leur application au bâtiment (sous titre : simulation numérique et approche expérimentale). HAL Id : tel-00590819.

Tsivilis, S., Tsantilas, J., Kakali, G., Chaniotakis, E., and Sakellariou, A. (2003). The permeability of portland limestone cement concrete. Cem. Concr. Res. *Volume 33*, p1465-1471.

V

Van Genuchten, M.T., and Nielsen, D.R. (1985). On describing and predicting the hydraulic properties of unsaturated soils. Ann. Geophys. *3*, p615-628.

Van Genuchten, M.T. (1980). A closed-form equation for predicting the hydraulic conductivity of unsaturated soils.

Vandamme, M., Brochard, L., Lecampion, B., and Coussy, O. (2010a). Adsorption and strain: The CO2-induced swelling of coal. J. Mech. Phys. Solids *58*, 1489–1505.

Verdier, J. (2001). Contribution à la caractérisation de l'évolution du taux de fuite des enceintes de confinement du parc nucléaire. 299.

Villain, G., Baroghel-Bouny, V., Kounkou, C., and Hua, C. (2001). Mesure de la perméabilité aux gaz en fonction du taux de saturation des bétons. Rev. Française Génie Civ.

Volume 5, p251-268.

Vlahinić, I., Jennings, H.M., and Thomas, J.J. (2009). A constitutive model for drying of a partially saturated porous material. Mech. Mater. *41*, 319–328.

W

Weber, B., Ehrhardt, J.-J., and Thomy, A. (1988). Surface des solides. Tech. l'ingénieur *33*, 0–20.

Wittmann, F.H. (2008). Heresies on shrinkage and creep mechanisms. Proc. 8th Int. Conf. Creep, Shrinkage Durab. Mech. Concr. Concr. Struct. (CONCREEP 8) *8*, 3–9.

Wittmann, F. (1973). Interaction of hardened cement paste and water. Journal of American ceramic Society, 56(8), p. 409-415.

Wyrzykowski, M., Bella, C.D., and Lura, P. (2017). Prediction of drying shrinkage of cement-based mortars with poroelastic approaches - a critical review. Poromechanics 2017 - Proc. 6th Biot Conf. Poromechanics 579–586.

Z

Zhang, Y. (2018). Mechanics of adsorption–deformation coupling in porous media. J. Mech. Phys. Solids *114*, 31–54.

Zhang, J., Wang, J., and Han, Y. (2015). Simulation of moisture field of concrete with pre-soaked lightweight aggregate addition. Constr. Build. Mater. *96*, 599–614.

Zhou, Q., and Glasser, F.P. (2001). Thermal stability and decomposition mechanisms of ettringite at <120°C. Cem. Concr. Res. *31*, 1333–1339.

Zou, L., Gong, L., Xu, P., Feng, G., and Liu, H. (2016). Modified GAB model for correlating multilayer adsorption equilibrium data. Sep. Purif. Technol. *161*, 38–43.

APPENDIX

List of Figures

A.1. Experimental dynamic vapor sorption isotherm - scenario 2

In Chapter 2 –section 2.2.2.6, two correction scenarios for the isotherms tests were discussed, based on two hypothesis leading to a different estimation of the saturated density: scenario 1 corresponds to an insufficient resaturation of the 7x7x28cm and 7x7x3cm samples at the end of the test; while scenario 2 corresponds to a probable micro-crack formation in the 7x7x1cm and 7x7x3cm. Two desorption isotherms were then obtained.

In section 2.2.4, the dynamic vapor sorption desorption isotherms obtained with DVS (Dynamic Vapor Sorption) are compared with the desorption isotherms obtained with the SSS (Saturated Salted Solutions) method. This comparison was done in section 2.2.4 for scenario 1 in Fig. 2-33. The same comparison is done in this appendix here for the scenario 2 and is shown in Fig. A-1.

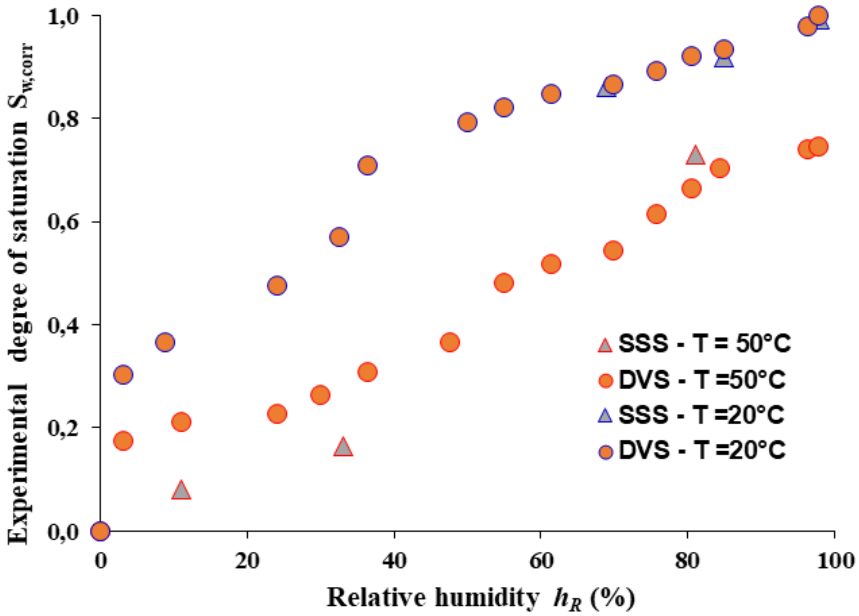

Fig. A-1 - The DVS isotherm $S_{w,corr}(h_R)$ compared with the SSS isotherm for the temperature of T=20°C and T=50°C and for the scenario 2

A.2. The modified Van–Genuchten model function of the capillary pressure

We recall that the Van Genuchten water retention model (Van Genuchten, 1980) is written in its initial form as in equation (2-21). It could be also written as a function of the capillary pressure as in equation (2-22) or a function of the relative humidity as in equation (2-23).

In chapter 2, section 2.3, a modification to the Van-Genuchten model was proposed. This consisted on considering equation 2-23 while adding a new parameter S_{100}. The latter parameter corresponds to the saturation degree for a relative humidity of 100%. By calibrating the modified form of the Van Genuchten model (equation 2-36) on SSS desorption isotherms of the F44Adj concrete, we presented the corresponding curves S_w (h_R) in Fig 2-38 and Fig 2-39. In the present appendix (Fig. A-2 and Fig. A-3), we show the same calibration done considering the Van Genuchten model as a function of the capillary pressure according to equation (A-1). This expression is implemented in *Code_Aster* where the unknown pressures are the capillary pressure P_c and the gas pressure P_G.

The fitting parameters (S_r, S_{100}, P_r, n) are also given in Fig. A-2 and Fig. A-3.

$$S_e = \frac{S_w - S_r}{S_{100} - S_r} = \left(1 + \left(\frac{P_C}{P_r}\right)^n\right)^{-(1-\frac{1}{n})} \qquad \text{(A-1)}$$

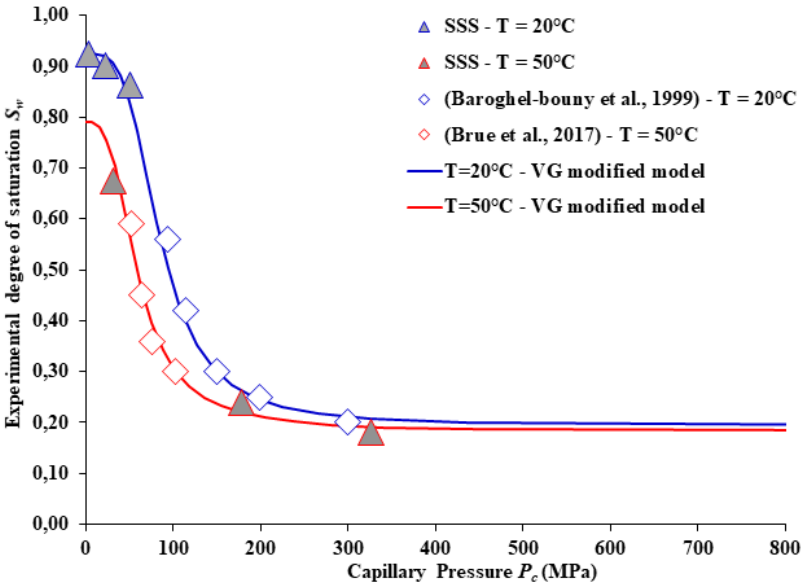

T	20°C	50°C
P_r (MPa)	75.58	51
n	3.759	3.759
S_{100}	0.924	0.79
S_r	0.195	0.182

Fig. A-2 - Calibrated SSS desorption isotherm of the F44Adj concrete with a modified Van Genuchten model at the temperatures of 20°C and 50°C for the considered scenario of insufficient saturation

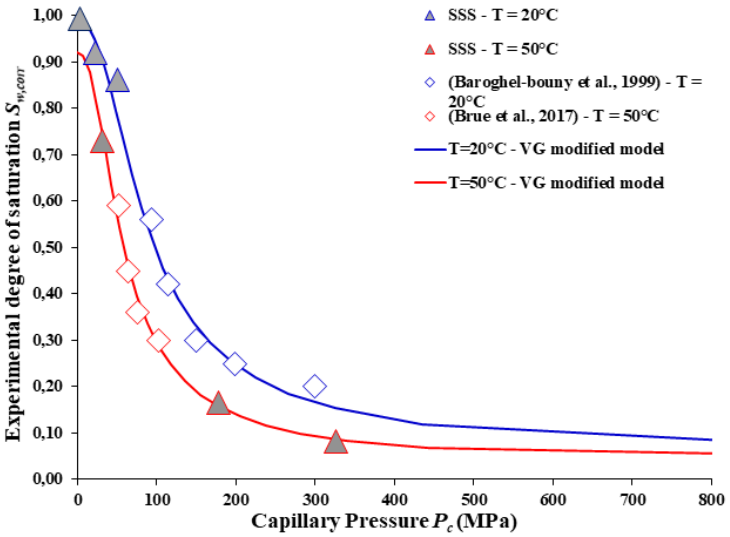

T	20°C	50°C
P_r (MPa)	65.30	43.24
n	2.353	2.353
S_{100}	0.988	0.921
S_r	0.05	0.03

Fig. A-3 - Calibrated SSS desorption isotherm of the F44Adj concrete with a modified Van-Genuchten model at the temperatures of 20°C and 50°C for the considered scenario of micro-cracks formation

A.3. The calibration of the dynamic vapor sorption isotherm - scenario 2

The experimental desorption isotherms of the F44Adj concrete obtained with the DVS method for the correction scenario 2 (Appendix 1 - Fig. A-1) are calibrated in this appendix with the modified Van Genuchten model (equation (2-37)). The desorption isotherms obtained with DVS were modeled using a Durner model (Durner, 1994), allowing us to better capture the abrupt variation of saturation at 30-40% relative humidity. For the temperature of 20°C, an order k=3 (k series of Van Genuchten curves) had to be taken in order to correctly model the whole desorption isotherm (see Fig. A-4); for T=50°C, an orderk= 2 is found to be sufficient (see Fig. A-5). The parameters of the two modified models used in Fig. A-4 and Fig. A-5 are given in Table 1.

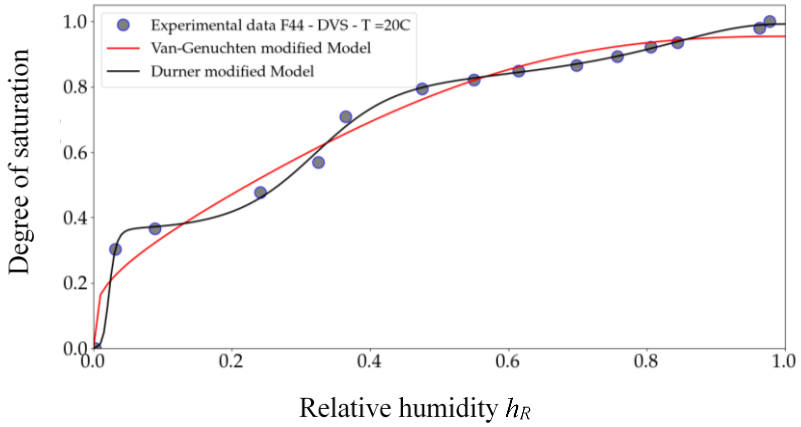

Fig. A-4 - Calibrated DVS desorption isotherm of the F44Adj concrete with a modified Van Genuchten model and (Durner, 1994) model at the temperature of 20°C - scenario 2

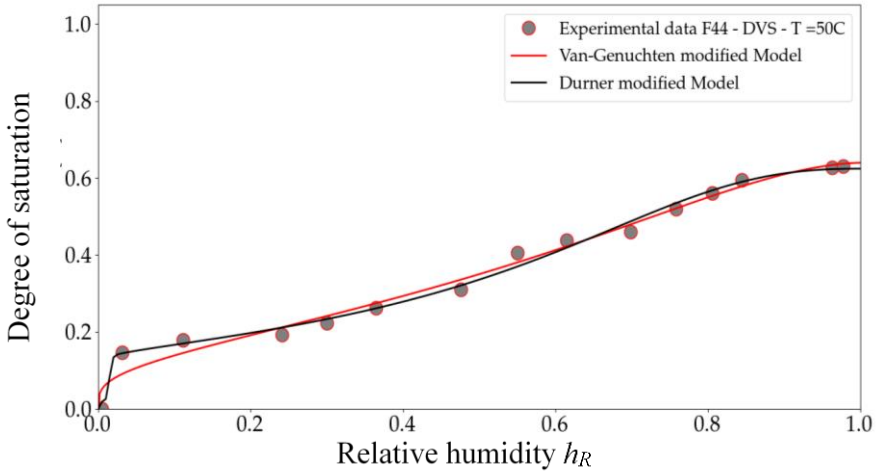

Fig. A-5 - Calibrated DVS desorption isotherm of the F44Adj concrete with a modified Van Genuchten model and (Durner, 1994) model at the temperature of 50°C - scenario 2

The Van Genuchten modified model		
T	**20°C**	**50°C**
c	0.99	2.59
n	2.145	1.679
S_{100}	0.954	0.64
S_r	0.00	0.00

The (Durner, 1994) modified model		
T	**20°C**	**50°C**
S_{100}	0.99	0.62
S_r	0.00	0.00
c_1	0.90	2.44
n_1	6.88	2.29
c_2	0.27	0.24
n_2	18.80	38.83
c_3	5.01	-
n_3	2.21	-
w_1	0.42	0.82
w_2	0.36	-

Table 1 – The Van Genuchten and (Durner, 1994) modified models parameters

A.4. The impact of diffusion on the drying kinetic at T=20°C

In chapter 3 – section 3.3.2.6, the impact of diffusion (Fick law) on the drying kinetic is studied. In order to test the sensibility of the results to the coefficient D_{v0} of equation (3-23), this parameter is taken equal to 1 rather than to $2.33 \cdot 10^{-5}$ m^2/s at T=20°C. This would mean multiplying the diffusion coefficient D_{vp} in equation (3-23) by a factor of approximately 10^5. The intrinsic permeability was again calibrated on the evolution of the saturation degree using the new diffusion parameter. The relative permeability function is that given by (Mualem, 1976).

The calibration is shown in Fig 3-32 and Fig 3-33 for the temperature T=50°C. For the temperature of T=20°C, the increase in the diffusion coefficient had no impact on the calibrated permeability, as shown in Fig. A-6.

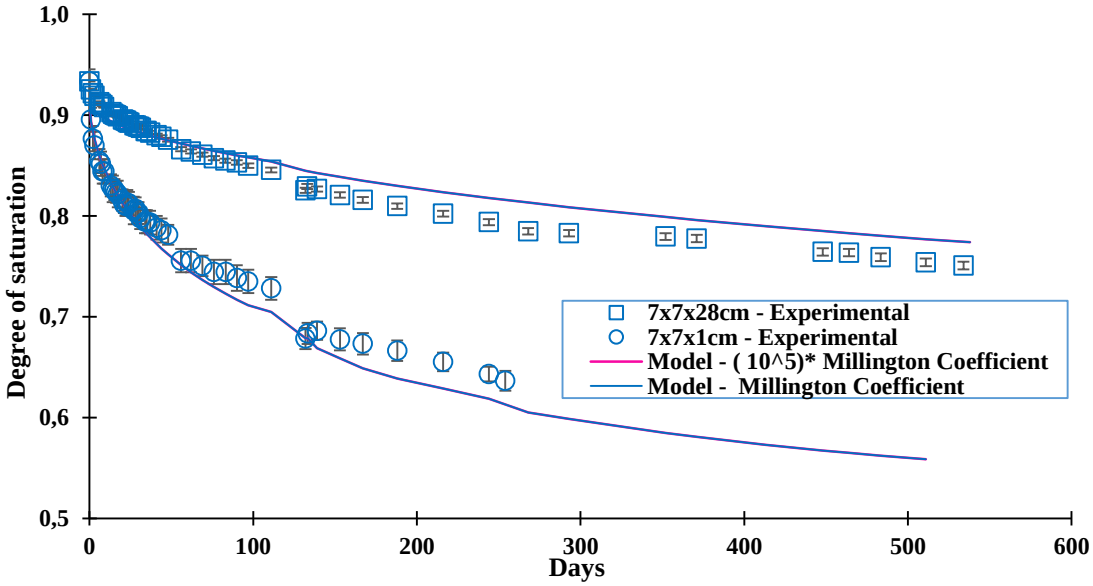

Fig. A-6 – Calibration of the intrinsic permeability for a temperature T=20°C with two different values of the diffusion coefficient.

A.5. 3D Calculation Comparison of an axisymmetric vs 3D simulation of the drying tests

The optimal set of transfer parameters (intrinsic and relative permeability) and boundary conditions (mass exchange coefficient) found on axisymmetric geometries in Chapter 3 - section 3.3.2 were also tested on the 3D geometries. The axisymmetric and 3D model results in termes of saturation degre are compared in Fig. A-7 and Fig. A-8 for T=20°C and T = 50°C respectively.

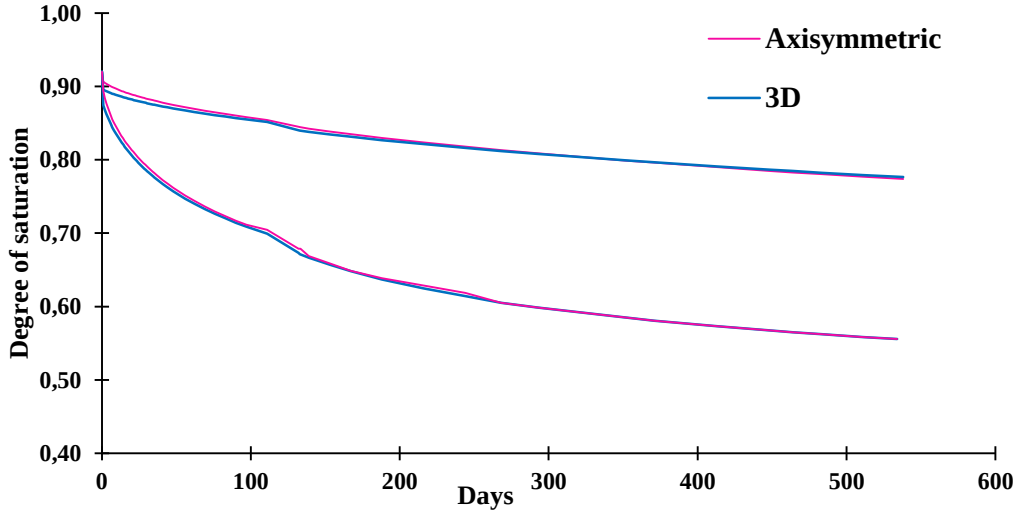

Fig. A-7 – Comparison of the numerical solution for T=20°C, h_R = *50%* executed on an axisymmetric model vs a 3D model

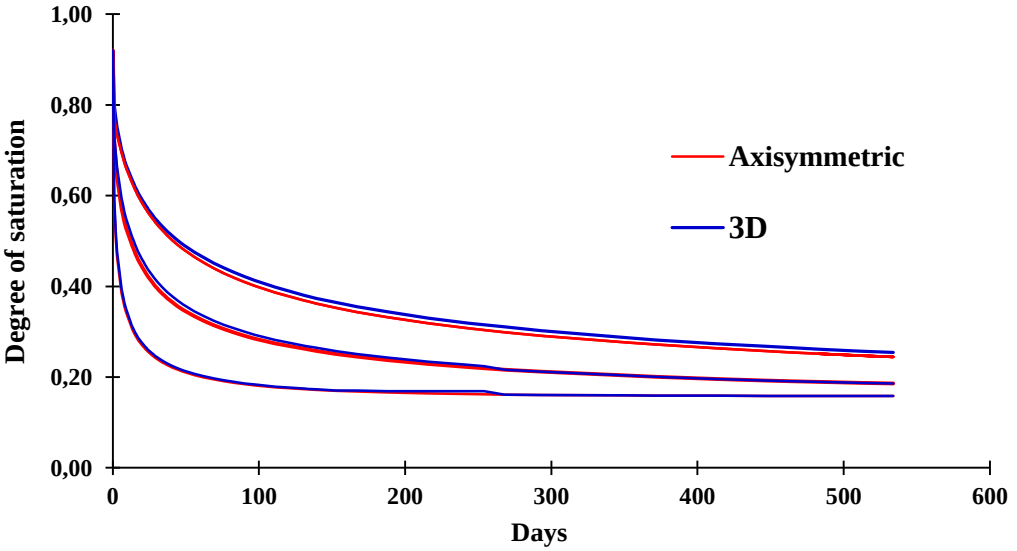

Fig. A-8 - Comparison of the numerical solution for T=50°C, h_R = *30%* executed on an axisymmetric model vs a 3D model

Fig. A-7 and Fig. A-8 shows that the numerical solutions obtained with axisymmetric meshes are very close to those obtained with a 3D meshes. This verifies the accuracy of the solutions obtained with the calibrations done in section 3.3.2 on axisymmetric meshes.

A.6. Homothetic variation verification

In this appendix, we verify the previous indication that states that any isotropic homothetic variation of the pore dimension by a factor (1+$\lambda/3$) will induce a volume increase of $(1+\lambda)$ and a surface increase of $(1+\frac{2\lambda}{3})$. The proof is shown here in the particular cases of a sphere or a cylinder. For this purpose, let us consider first a spherical pore with radius r and let us note the factor $\lambda/3$ as β. The proof is done through the following steps.

1) The initial volume of the pore is $V_i = \frac{4}{3}\pi r^3$ and its initial surface is $S_i = 4\pi r^2$
2) If we consider an isotropic homothetic variation of the pores by a factor $(1+\beta)$ then the final volume of the sphere will be equal to $V_f = \frac{4}{3}\pi(r(1+\beta))^3 = \frac{4}{3}\pi r^3(1+\beta)^3$. If we consider only the first order terms, we could write $V_f = \frac{4}{3}\pi r^3(1+3\beta)$ and thus the increase of the volume of the sphere is of $(1+3\beta)$.
3) The final surface is $S_i = 4\pi\big(r(1+\beta)\big)^2 = 4\pi r^2(1+\beta)^2$. If we consider only the first order terms, we could write $S_f = 4\pi r^2(1+2\beta)$ and thus the increase of the surface of the sphere is of $(1+2\beta)$.

The same demonstration can be done for pore with a shape of an infinite cylinder with a radius r and a height h, with the following steps:

1) The initial volume of the pore is $V_i = \pi r^2 h$ and its initial surface is $S_i = 2\pi r h$
2) If we consider an isotropic homothetic variation of the pores by a factor $(1+\beta)$ then the final volume of the cylinder will be equal to $V_f = \pi(r(1+\beta))^2(h(1+\beta)) = \pi r^2 h(1+\beta)^3$. If we consider only the first order terms, we could write $V_f = \pi r^2 h(1+3\beta)$ and thus the increase of the volume of the cylinder is of $(1+3\beta)$.
3) The final surface is $S_i = 2\pi(r(1+\beta))(h(1+\beta)) = 2\pi r h(1+\beta)^2$. If we consider only the first order terms, we could write $S_f = 2\pi r h(1+2\beta)$ and thus the increase of the surface of the cylinder is of $(1+2\beta)$.

A.7. New poromechanical model – alternative BJH method

In this appendix, we show the results obtained when we consider that for a certain value of relative humidity h_R near 0.3, cavitation will take place (as stated in (Maruyama et al., 2018)). Below this value of relative humidity, all pores will be considered unsaturated. In terms of the model parameters, this corresponds to fixing $S_L(h_R) = 0$ and $\omega_G(h_R) = 1$ for a relative humidity smaller than approximately 0.3.

Concerning the experimental data of (Maruyama et al., 2018), the complete desaturation of pores is considered for a relative humidity h_R *=0.3*. This value has been chosen based on previous observations (refer to Fig 4-13: when the relative humidity reaches a value near 0.3, the HCP is left with a value of S_L near zero). As done previously, for the experimental data of (Maruyama et al., 2018), the two scenarios *Sc1* (Fig. A-9) and *Sc2 (*Fig. A-10*)* were equally tested. The obtained curves $S_L(h_R)$ and $\omega_G(h_R)$ from the BJH computation are presented respectively in Fig. A-9-b and Fig. A-10-b. The calculated drying shrinkage strains are shown Fig. A-9-a for scenario *Sc1* and Fig. A-10-a for scenario *Sc2.* The equivalent pore pressure and the corresponding contributions are shown in Fig. A-9-b and Fig. A-10-b respectively for scenarios *Sc1* and *Sc2*.

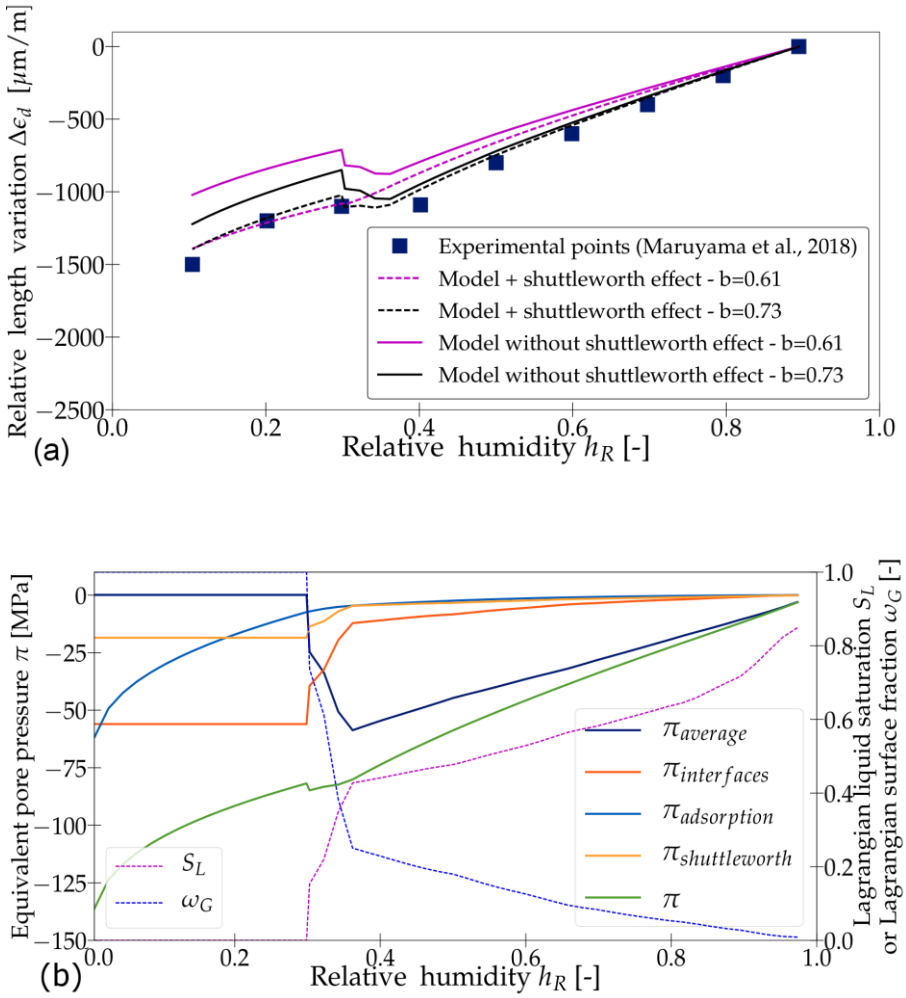

Fig. A-9–Results for the experimental data of (Maruyama et al., 2018) with the calculation scenario *Sc1*: (a) Calculated relative length variations– (b) Contributions to the equivalent pore pressure

Regarding the experimental results of (Baroghel-Bouny et al., 1999), the BJH calculation was stopped at a relative humidity h_R of 0.33. Below this value, pores are assumed to be totally unsaturated. This value has been chosen based on previous observations (see Fig 4-14: when the relative humidity reaches 0.33, the studied concrete is left with a very small amount of liquid water). The BJH curves $S_L(h_R)$ and $\omega_G(h_R)$ and model results are shown in Fig. A-11. From the previous results, we can conclude that if the BJH computation was stopped at a value of relative humidity h_R near 0.35 and total desaturation of pores was assumed for this value, this may lead (as seen in Fig. A-9) to a less satisfactory prediction of the drying shrinkage strains when neglecting the Shuttleworth effect and considering a value of b near 0.7. Therefore, the BJH method (where the BJH computation is maintained until approaching 0% of relative humidity) should be retained for further model predictions.

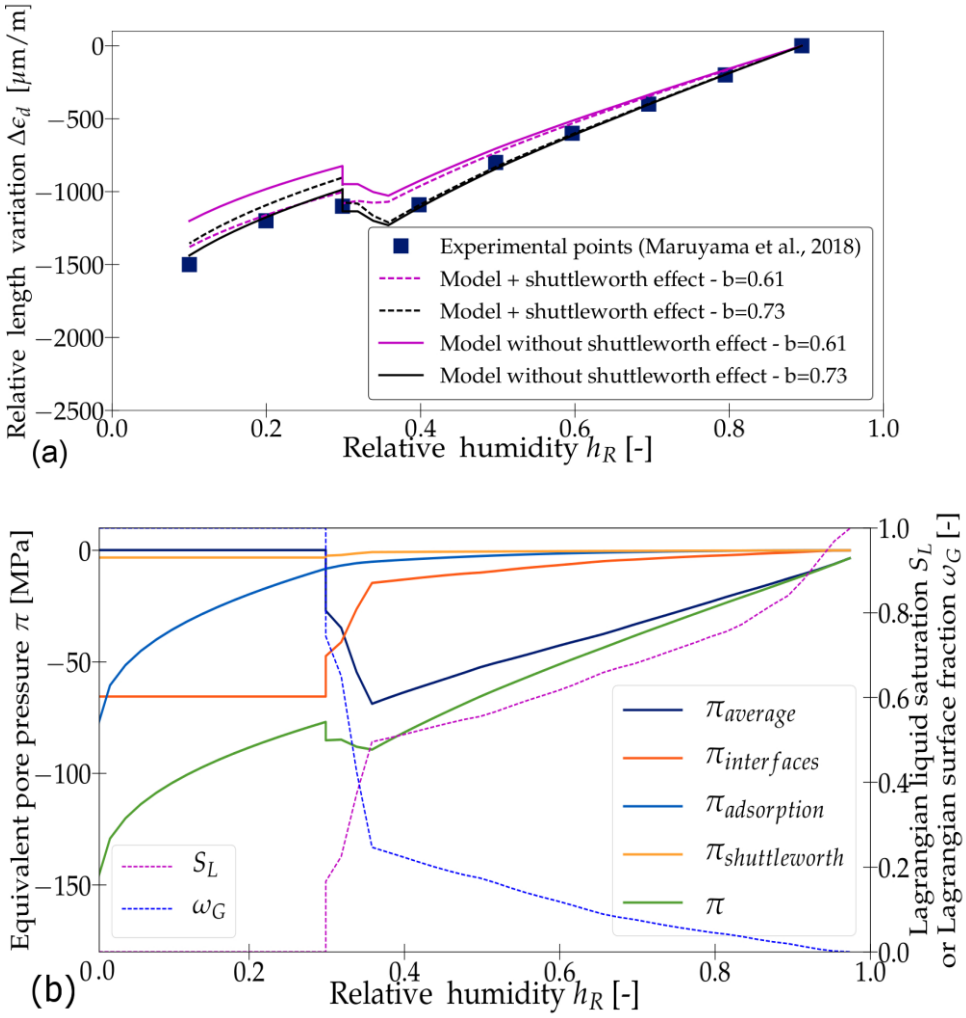

Fig. A-10– Results for the experimental data of (Maruyama et al., 2018) with the calculation scenario *Sc2*: (a) Calculated relative length variations– (b) Contributions to the equivalent pore pressure

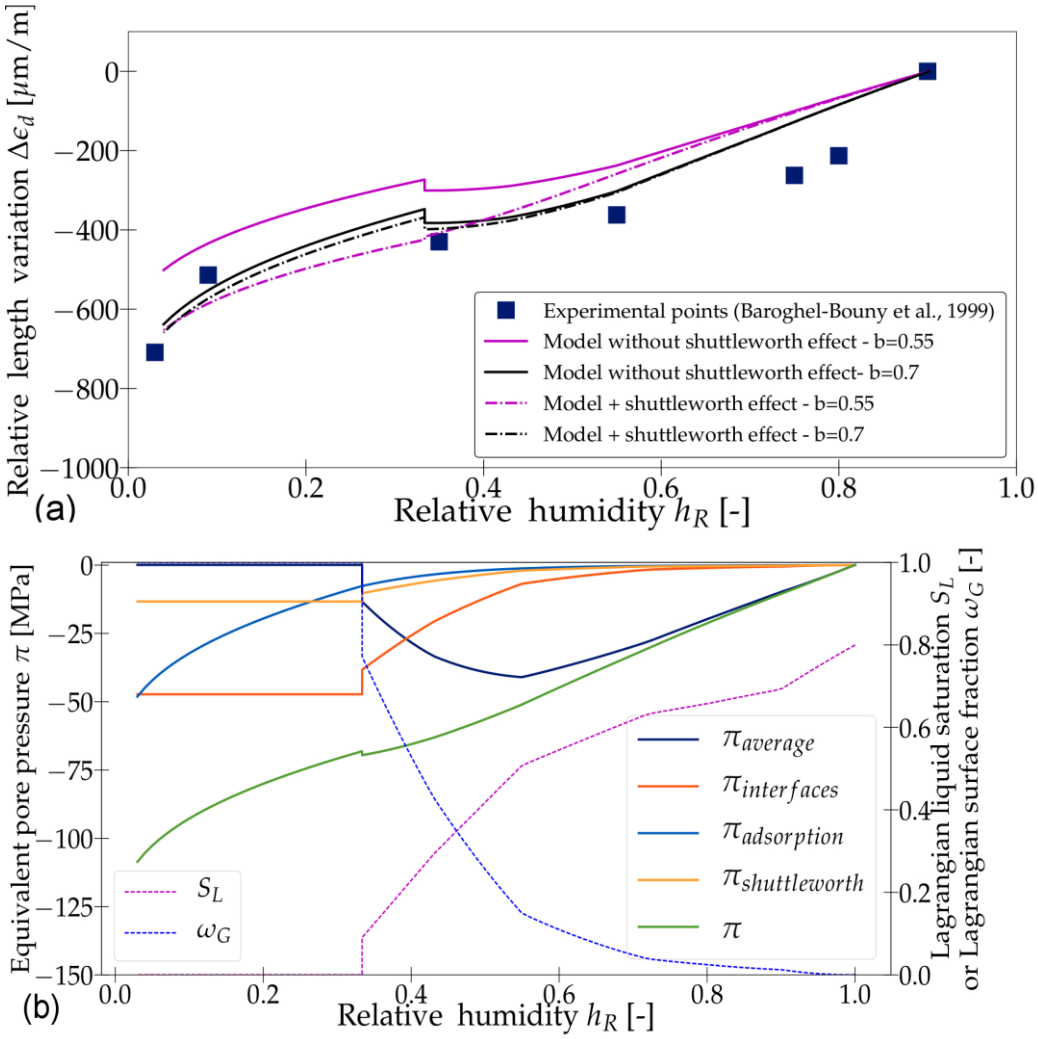

Fig. A-11– Results for the data of (Baroghel-Bouny et al., 1999): (a) Calculated relative length variations – (b) Contributions to the equivalent pore pressure

A.8. New poromechanical model implemented in *Code_Aster*

```
#*******************************************************************
# Concrete F44Adj - simulation on the sample 7x7x28cm
#*******************************************************************
DEBUT(PAR_LOT='NON');
perm = 4.5E-24
p=0.5
q=2
# PARAMETERS OF VAN GENUCHTEN #
SRCOQ_BAR = 0.05
SRCOQ= 0.05
NCOQ_BAR = 2.353
MCOQ_BAR =1-1./NCOQ_BAR
PRCOQ_BAR = 6.53E7
S100_BAR = 0.988
FACK_BAR = (S100_BAR-SRCOQ)/(1-SRCOQ)

#*********************************************************
### MESH DEFINITION
#*********************************************************
mesh_BAR  =  LIRE_MAILLAGE(UNITE=20)
mesh_BAR  = MODI_MAILLAGE(reuse=mesh_BAR,
                          MAILLAGE=mesh_BAR,
           ORIE_PEAU_3D=_F(GROUP_MA=('HAUT', 'BAS','GAUCHE',
                            'DROITE','AVANT', 'ARRIERE',),),);

#*********************************************************
### DEFINITION OF THE FLUIDS CHARACTERISTCS
#*********************************************************
VISCOLIQ=DEFI_CONSTANTE(VALE=9.94E-4)
VISCOGAZ=DEFI_CONSTANTE(VALE=1.13E-05
RHOW = 998.
RHOA = 1.2
KINT = DEFI_CONSTANTE (VALE=perm,);

#*********************************************************
### MATERIAL DENSITY AND POROSITY
#*********************************************************
poro_coq_BAR = 0.075
MAMOLVAP = 0.018
R = 8.315
SINI_BAR = 0.92
```

```
RHOH_BAR = 2503

#************************************************************
### HYDRO MECHANICAL COUPLING PARAMETERS
#************************************************************
BIOCOQ = 1
Nu = 0.2
Ebet = 44E9

#************************************************************
### REFERENCE VALUES
#************************************************************
TREF = 273.
P2REF = 1.E5

#************************************************************
### Van Genuchten/Mualem
#************************************************************
LI1=DEFI_LIST_REEL(DEBUT=0,
                        INTERVALLE=(_F(JUSQU_A=1.E6,NOMBRE=100,),
                                    _F(JUSQU_A=1.E7,NOMBRE=100,),
                                    _F(JUSQU_A=1.E8,  NOMBRE=100,),
                                    _F(JUSQU_A=1.E9,NOMBRE=100,),),);
LI_BAR=DEFI_LIST_REEL(DEBUT=SRCOQ_BAR+0.001,
                      INTERVALLE=_F(JUSQU_A=0.999,PAS=1.E-2,),);

SLO_BAR=FORMULE(NOM_PARA='PCAP',VALE='((S_100-SR_COQ)*((1+(PCAP/(PR_COQ))**N_COQ)**(-
M_COQ)))+SR_COQ',S_100=S100_BAR,SR_COQ=SRCOQ,PR_COQ=PRCOQ_BAR,N_COQ=NCOQ_BAR,M_COQ=MCO
Q_BAR)


SATU_BAR=CALC_FONC_INTERP(FONCTION=SLO_BAR,
                        LIST_PARA=LI1,NOM_PARA='PCAP',
                        PROL_DROITE='LINEAIRE',PROL_GAUCHE='LINEAIRE',  INFO=2,);
KL_BAR=FORMULE(NOM_PARA='SAT',VALE='((((SAT-SR_COQ)/(S_100-SR_COQ))*FA_CK)**(p_))*(1-
((1-((((SAT-SR_COQ)/(S_100-
SR_COQ))*FA_CK)**(1./M_COQ)))**(M_COQ)))**q_',S_100=S100_BAR,SR_COQ=SRCOQ,p_=p,FA_CK=F
ACK_BAR,M_COQ=MCOQ_BAR,q_=q)


PKL_BAR=CALC_FONC_INTERP(FONCTION=KL_BAR,
                        LIST_PARA=LI_BAR,NOM_PARA='SAT',
                        PROL_DROITE='CONSTANT',PROL_GAUCHE='CONSTANT',  INFO=2,);


KG_BAR=FORMULE(NOM_PARA='SAT',VALE='((1-(((SAT-SR_COQ)/(S_100-
SR_COQ))*FA_CK))**(p_))*((1-((((SAT-SR_COQ)/(S_100-
SR_COQ))*FA_CK)**(1./M_COQ)))**(q_*M_COQ))
',S_100=S100_BAR,SR_COQ=SRCOQ,p_=p,FA_CK=FACK_BAR,M_COQ=MCOQ_BAR,q_=q)
```

```
PKG_BAR=CALC_FONC_INTERP(FONCTION=KG_BAR,
                         LIST_PARA=LI_BAR,NOM_PARA='SAT',
                         PROL_DROITE='CONSTANT',PROL_GAUCHE='CONSTANT',INFO=2,);


#************************************************************
### SATURARATED VAPOR PRESSURE
#************************************************************
PVSAT = 2295.  # FORMULE DOC R P. 26 à 20 degree

PC0_BAR
= Pcdesat (PRCOQ_BAR,SRCOQ_BAR,NCOQ_BAR,SINI_BAR,S100_BAR)
PVCOQ_BAR = PVSAT * exp(-PC0_BAR*MAMOLVAP/RHOW/R/TREF)


#************************************************************
### INITIAL STATE
#************************************************************
TINI = 20
PGZ0 = 1.E5
P20 = PGZ0 - P2REF


#************************************************************
## TIME LIST
#************************************************************
T1H = 60.*60.
T1J = 24.*T1H
INST_BA = DEFI_LIST_REEL(VALE=(0     ,200,500,700,1000,3600,7200,10800      ,25200
    ,32400,43200,57600,72000,  86400, 172800 ,259200,     518400,      604800,
    691200,      777600,      1159200,     1245600,     1332000,     1418400,
    1504800,     1765800      ,1853100     ,1934100     ,2023200     ,2109600,
    2368800      ,2455200,    2541600,     2628000,     2714400,     2973600
    ,3024000     ,3196800,    3542400,     3801600      ,4147200     ,4838400
    ,5356800     ,5961600,    6566400      ,7171200,    7776000      ,8380800
    ,9590400,    11404800     ,11491200,   12009600,    13219200,    14428800
    ,16243200    ,18662400    ,21081600,   23155200     ,25315200,   30412800),)


TIME_BAR=DEFI_LIST_INST(    ECHEC=_F(SUBD_NIVEAU=6,  SUBD_PAS_MINI=0.0,
                                     SUBD_PAS=6,SUBD_METHODE='MANUEL',
                                     ACTION='DECOUPE',  EVENEMENT='ERREUR',),


#************************************************************
### DIFFUSION PARAMETERS
#************************************************************
# Fick mélange gazeux
FICKBET=DEFI_CONSTANTE(VALE=2.33E-5,);


# Fick mélange liquide
FadBET=DEFI_CONSTANTE(VALE=1.0E-10,);
```

```
# Coefficient de Henry pour la dissolution
KHENRY=DEFI_CONSTANTE(VALE=1.30719E05,);#CR 6125-1715-2017-04002

FVP_S = FORMULE(VALE='((0.075)**(4./3))*(( 0.999-SAT)**(10./3))',
                NOM_PARA='SAT',);
FVPS_BAR=CALC_FONC_INTERP(FONCTION=FVP_S,
                      LIST_PARA=LI_BAR,  NOM_PARA='SAT',
                      PROL_DROITE='CONSTANT',PROL_GAUCHE='CONSTANT',INFO=2,);

FA_S = FORMULE(VALE=' SAT',NOM_PARA='SAT',);
FAS_BAR=CALC_FONC_INTERP(FONCTION=FA_S,
                     LIST_PARA=LI_BAR,
                     NOM_PARA='SAT',PROL_DROITE='CONSTANT',
                     PROL_GAUCHE='CONSTANT',  INFO=2,);
ALPHAL = DEFI_CONSTANTE(VALE=1.5e-04)

#************************************************************
# INITIAL ENTHALPY AND EFFECTIVE STRESS
#************************************************************
ENT11_BAR = -PC0_BAR / RHOW
ENT12 = 2500800 - (2443 * TINI)
SITOT = 0.
SIPbet_BAR =-BIOCOQ*(-31.94E+06)
SIEFbet_BAR = SITOT -SIPbet_BAR

#************************************************************
# BJH PARAMETERS
#************************************************************
SBJH = DEFI_FONCTION(NOM_PARA = 'PCAP',
INTERPOL  =  'LIN',PROL_DROITE  =  'CONSTANT',PROL_GAUCHE  =  'CONSTANT',VALE  =  (0.0,
0.98808922634100005, 1374658.7896400001, 0.988027921709, etc,),)
wBJH = DEFI_FONCTION(NOM_PARA = 'PCAP',
INTERPOL = 'LIN',PROL_DROITE = 'CONSTANT',    PROL_GAUCHE = 'CONSTANT', VALE = ( 0.0,
2.6750881985200002e-10, 1374658.7896400001, 2.7026254750900002e-10, etc,),)
EP = DEFI_FONCTION(NOM_PARA = 'PCAP',
 INTERPOL = 'LIN',  PROL_DROITE = 'CONSTANT',  PROL_GAUCHE = 'CONSTANT', VALE = (0.0,
4.1141361467899999e-09, 1374658.7896400001, 1.3480095918e-09, etc,),)

#************************************************************
# MATERIAL DEFINITION
#************************************************************
BETONBAR = DEFI_MATERIAU(
    COMP_THM='LIQU_AD_GAZ_VAPE',
    ELAS=_F(ALPHA=1.14e-05, E=Ebet, NU=Nu),
```

```
    THM_AIR_DISS=_F(COEF_HENRY=KHENRY, CP=1000.0),
    THM_DIFFU=_F(BIOT_COEF=BIOCOQ,
        CP=815,#!! À VERIFIER
        D_LB_S=DLSRB,
        FICKA_S=FAS_BAR,
        FICKA_T=FICKBET,
        FICKV_S=FVPS_BAR,
        FICKV_T=FadBET,
        PERM_IN=KINT,
        RHO=RHOH_BAR,
        R_GAZ=8.315,
        EPAI=EP,
        A0 =62164189.9206,
        SHUTTLE=0.0,
        S_BJH = SBJH,
        W_BJH=wBJH,
        SATU_PRES=SATU_BAR,
        D_SATU_PRES=DSAT_BAR,
        PERM_LIQU=PKL_BAR,
        D_PERM_LIQU_SATU=PDKL_BAR,
        PERM_GAZ=PKG_BAR,
        D_PERM_SATU_GAZ=PDKG_BAR,
        D_PERM_PRES_GAZ=ZERO,     ),
    THM_GAZ=_F(CP=1000.0, D_VISC_TEMP=ZERO, MASS_MOL=0.028, VISC=VISCOGAZ),
    THM_INIT=_F(PORO=poro_coq_BAR,    PRE1=0.0,    PRE2=P2REF,    PRES_VAPE=PVCOQ_BAR,
TEMP=TREF,),
    THM_LIQU=_F(ALPHA=ALPHAL,
        D_VISC_TEMP=ZERO,
        RHO=RHOW,
        UN_SUR_K=4.5e-10,
        VISC=VISCOLIQ),
    THM_VAPE_GAZ=_F(D_VISC_TEMP=ZERO, MASS_MOL=0.018, VISC=VISCOGAZ))


mat_BAR = AFFE_MATERIAU(AFFE=_F(MATER=(BETONBAR, ), TOUT='OUI'), MAILLAGE=mesh_BAR)


modelBAR  =  AFFE_MODELE(AFFE=_F(MODELISATION=('3D_THH2MS',  ),  PHENOMENE='MECANIQUE',
TOUT='OUI'),MAILLAGE=mesh_BAR)


#************************************************************
# INITIAL STATE
#************************************************************
DEPL0BAR = CREA_CHAMP(AFFE=(_F(NOM_CMP=('PRE1', ), TOUT='OUI', VALE=(PC0_BAR, )),
         _F(NOM_CMP=('TEMP',         ),         TOUT='OUI',         VALE=(TINI,         ))
),MAILLAGE=mesh_BAR,OPERATION='AFFE',TYPE_CHAM='NOEU_DEPL_R',)
```

```
SIG0_BAR = CREA_CHAMP(
    AFFE=_F(NOM_CMP=('SIXX', 'SIYY', 'SIZZ', 'SIPXX', 'SIPYY', 'SIPZZ', 'SIXY', 'SIXZ',
            'SIYZ', 'SIPXY', 'SIPXZ', 'SIPYZ', 'M11', 'FH11X', 'FH11Y', 'M12',
            'FH12X', 'FH12Y', 'M21', 'FH21X', 'FH21Y', 'M22', 'FH22X', 'FH22Y',
            'ENT11', 'ENT12', 'ENT21', 'ENT22', 'QPRIM', 'FHTX',),
        TOUT='OUI',
                VALE=(SIEFbet_BAR, SIEFbet_BAR, SIEFbet_BAR, SIPbet_BAR, SIPbet_BAR,
                SIPbet_BAR, 0.0, 0.0, 0.0, 0.0, 0.0, 0.0, 0.0, 0.0, 0.0, 0.0, 0.0, 0.0,
                0.0, 0.0, 0.0, 0.0,0.0, 0.0, ENT11_BAR, ENT12, 0.0, 0.0, 0.0, 0.0,
                0.0)),
    MODELE=modelBAR,OPERATION='AFFE',
    PROL_ZERO='OUI',TYPE_CHAM='ELGA_SIEF_R)


#*********************************************************
# LOAD
#*********************************************************
T_moy = DEFI_FONCTION(NOM_PARA = 'INST',INTERPOL = 'LIN',PROL_DROITE = 'CONSTANT',
                              PROL_GAUCHE = 'CONSTANT',
                              VALE = (0.0,19.08,  10200,19.0684000000001,etc,),)


PCHYGRO = DEFI_FONCTION(NOM_PARA = 'INST',INTERPOL = 'LIN',PROL_DROITE = 'CONSTANT',
                                PROL_GAUCHE = 'CONSTANT',
VALE=(0,80051783,9591360,80051783,11403660,99182665.55,11404800,93666311,11491200,9502
4432.17,),)


DXx = DEFI_CONSTANTE(VALE=0.0,);
DYy = DEFI_CONSTANTE(VALE=0.0,);
CHARGBAR = AFFE_CHAR_CINE_F(
MECA_IMPO=(_F(DY=DYy, GROUP_MA=('ARRIERE', )), _F(TEMP=T_moy, TOUT='OUI'), _F(DX=DXx,
GROUP_MA=('GAUCHE', ),) ,),
 MODELE=modelBAR,)
SECH_BAR=AFFE_CHAR_CINE(MODELE=modelBAR,
MECA_IMPO= (_F(GROUP_MA=('HAUT','DROITE','BAS'), PRE1=PCHYGRO, ),


#*********************************************************
#SIMULATION WITH THE NEW POROMECHANICAL MODEL - HYDR_TABBAL
#*********************************************************
  RESU_BAR = STAT_NON_LINE(
    CHAM_MATER=mat_BAR,
    COMPORTEMENT=_F(
        RELATION='KIT_THH2M',
        RELATION_KIT=('HYDR_TABBAL', 'LIQU_AD_GAZ_VAPE', 'ELAS'),
        TOUT='OUI'),
    CONVERGENCE=_F(ITER_GLOB_MAXI=50,),
    ETAT_INIT=_F(DEPL=DEPL0BAR, SIGM=SIG0_BAR),
```

```
    EXCIT=(_F(CHARGE=CHARGBAR),
           _F(CHARGE=SECH_BAR),),
    INCREMENT=_F(LIST_INST=TIME_BAR),
    METHODE='NEWTON',
    MODELE=modelBAR,
    NEWTON=_F(),
    OBSERVATION=F(NOEUD=('N1', ), NOM_CHAM='DEPL', NOM_CMP=('PRE1', 'PRE2')),),
    SOLVEUR=_F(METHODE='MUMPS'))
FIN();
```

A.9. Modification of the expression of the relative permability

In this appendix, a modification of the expression of relative humidity is proposed and presented in section 4.2.4.1. This modification consists on considering that the relative permeabilities K_{rl} and K_{rg} are linked to the amount of liquid water S_L instead of the total amount of water S_w.

A comparison of the expression of $K_{rl}(S_L)$ (given in equation 4-56) and $K_{rl}(S_w)$ (given in equation 3-32) is shown in Fig. A-12 for the temperature of 20°C and in Fig. A-14 for T=50°C. The corresponding isotherms are given in Fig 2-39.

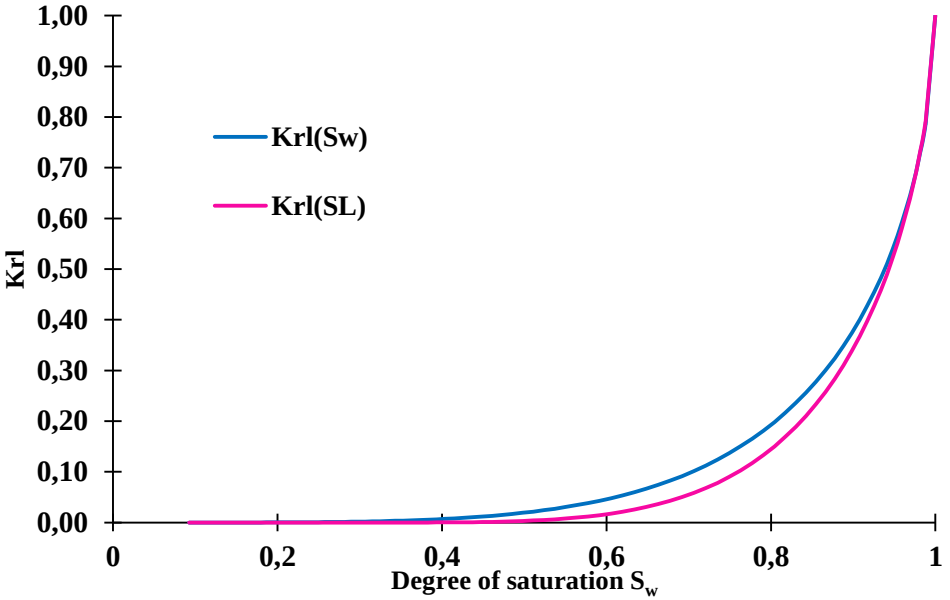

Fig. A-12– Comparison of the expression of relative permeability $K_{rl}(S_L)$ (given in equation 4-56) and $K_{rl}(S_w)$ (given in equation 3-32) - T=20°C.

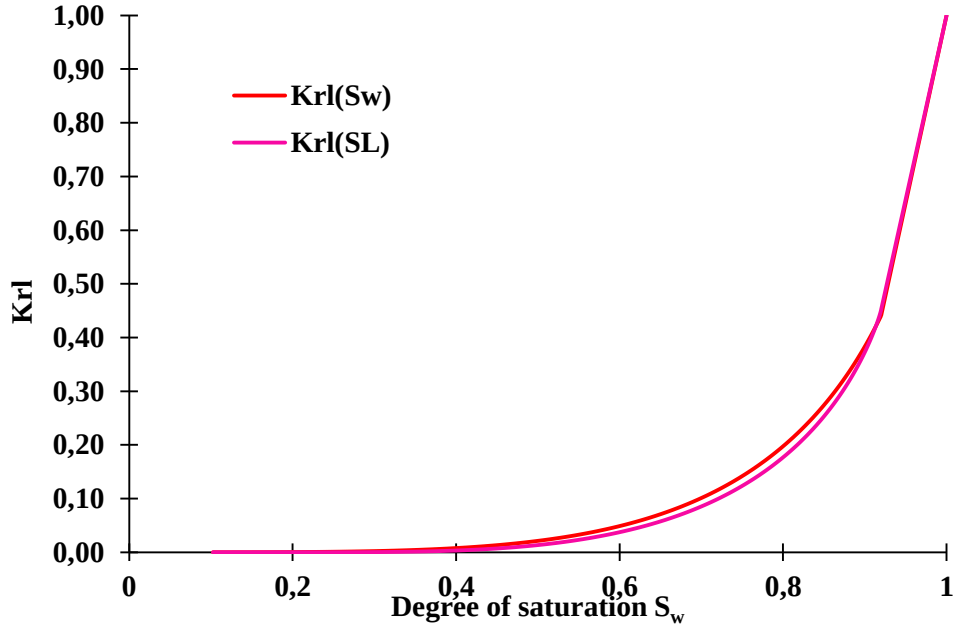

Fig. A-13– Comparison of the expression of relative permeability $K_{rl}(S_L)$ (given in equation 4-56) and $K_{rl}(S_w)$ (given in equation 3-32) - T=50°C.

New simulations, performed to calibrate the intrinsic permeability of the concrete, are run while considering that the expressions of K_{rl} and K_{rg} are linked to S_L. The obtained results for T=20°C are shown in Fig. A-14. A value of $6.4 \cdot 10^{-24}$ m^2 was fitted assuming $K_{rl}(S_L)$ and $K_{rg}(S_L)$ (functions of S_L) Compared to the previous simulations with $K_{rl}(S_w)$ and $K_{rg}(S_w)$ (relative permability as a finction of the experimental saturation degree S_w), a negligible difference in results is shown (Fig. A-14).

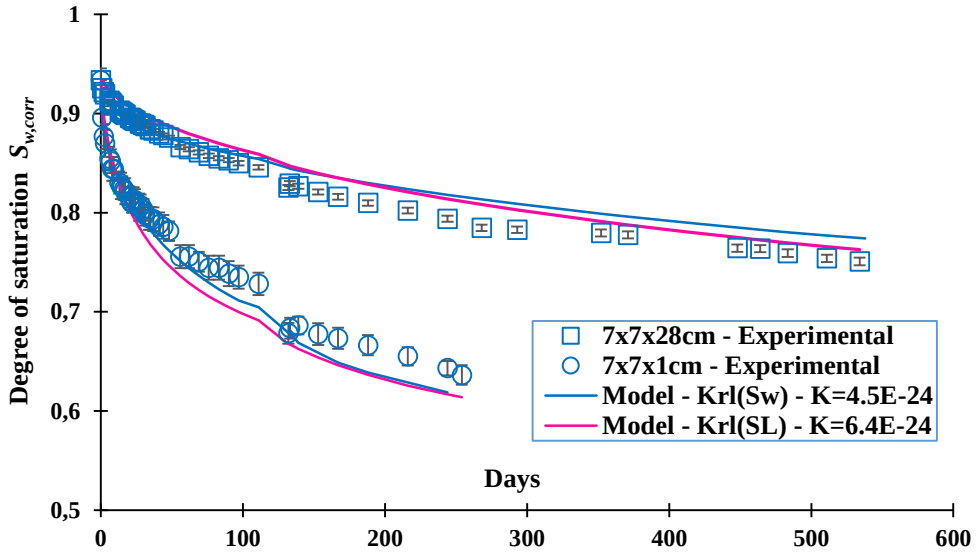

Fig. A-14– Comparison of the calibration of the saturation degree evolution when $K_{rl}(S_L)$ vs when $K_{rl}(S_w)$ – For T=20°C.

The same comparison is done for T=50°C in Fig. A-15. It is seen that when $K_{rl}(S_L)$ and $K_{rg}(S_L)$ are considered, the model fail to correctly describe the drying kinetic at T=50°C.

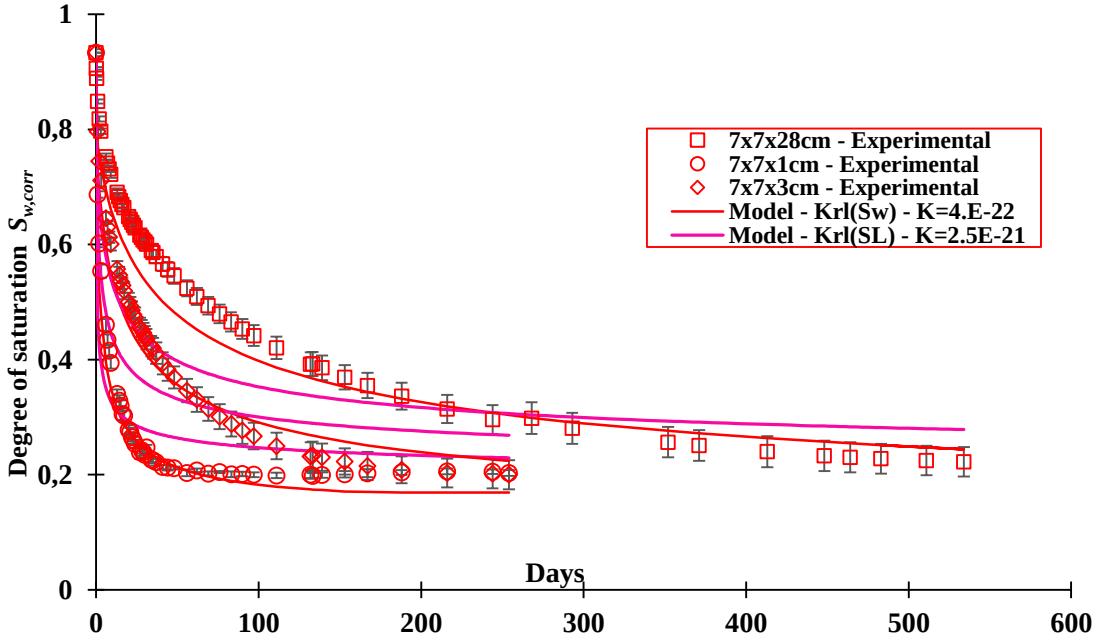

Fig. A-15– Comparison of the calibration of the saturation degree evolution when $K_{rl}(S_L)$ vs when $K_{rl}(S_w)$ – For T=50°C.

A.10. Fit of the Biot coefficient to include autogenous shrinkage strains at T=50°C

This appendix shows the fit of the Biot coefficient of the poromechanical model, in order to account for both autogenous and drying shrinkage occurring in the concrete submitted to a condition of T=50°C and h_R = 30%.

The experimental curves shown in Fig. A-16 corresponds to the sum of autogenous strains and drying strains (presented in Fig 4-23 – Chapter 4). The fitted value of the Biot coefficient is of b=0.6. This value is considered in order to model the drying behavior of the concrete package in Chapter 5.

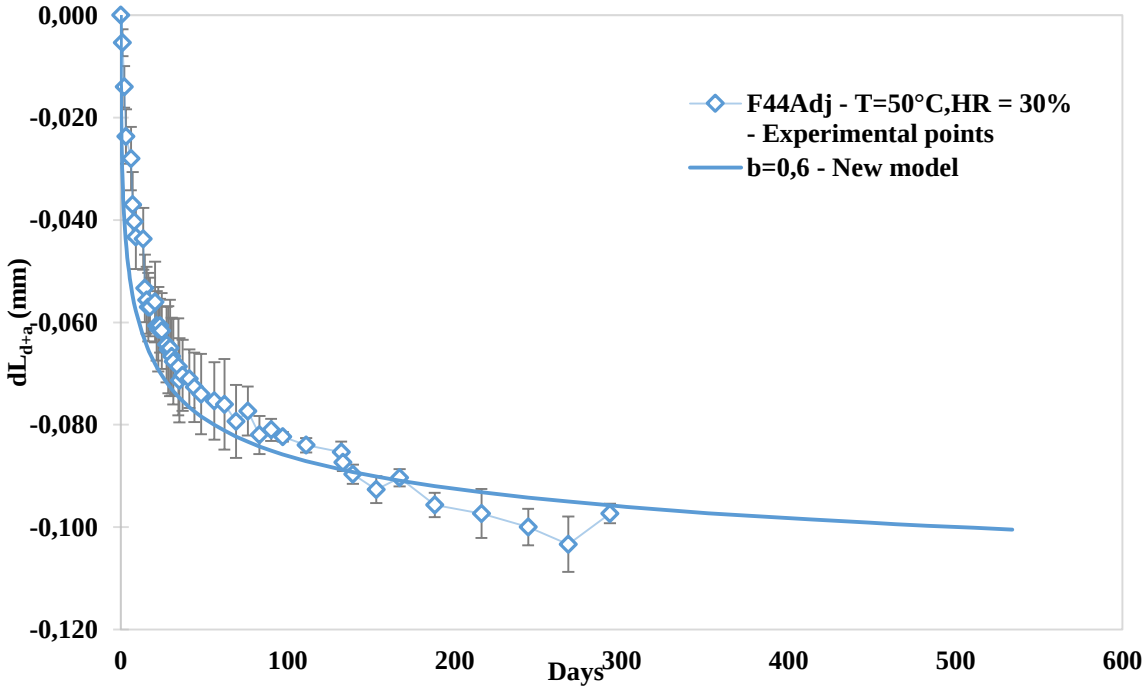

Fig. A-16– For T=50°C – Calibration of the Biot coefficient.